

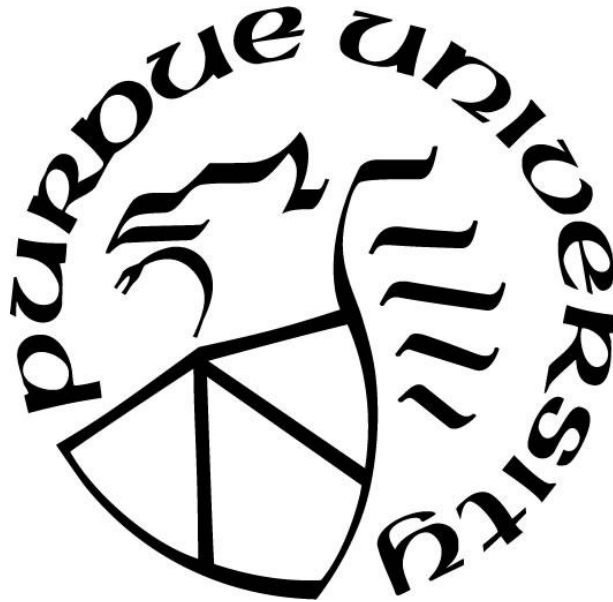
**SMALL-SCALE MECHANICAL BEHAVIORS OF ZIRCONIA
PROCESSED BY DIFFERENT TECHNIQUES**

by
Jaehun Cho

A Dissertation

*Submitted to the Faculty of Purdue University
In Partial Fulfillment of the Requirements for the degree of*

Doctor of Philosophy



School of Materials Engineering

West Lafayette, Indiana

August 2020

THE PURDUE UNIVERSITY GRADUATE SCHOOL
STATEMENT OF COMMITTEE APPROVAL

Dr. Xinghang Zhang, Chair

School of Materials Engineering

Dr. Haiyan Wang

School of Materials Engineering

Dr. R. Edwin García

School of Materials Engineering

Dr. Kenneth H. Sandhage

School of Materials Engineering

Approved by:

Dr. David F. Bahr

Dedicated to my parents: Sangyong Cho and Geumsoon Shin

ACKNOWLEDGMENTS

Firstly, I would like to thank my advisor, Dr. Xinghang Zhang, for his excellent guidance, encouragement, instruction, and support throughout my Ph.D. study. I was very fortunate to meet him and became one of his students. I would not be able to grow and become a mature and independent researcher without his meticulous teaching and advice. Besides, I would like to express sincere appreciation to Dr. Haiyan Wang for allowing me to work with her and her students on an exciting research project. I also would like to thank Dr. R. Edwin García and Dr. Kenneth H. Sandhage, for their academic guidance and precious advice during my Ph.D. study. I also want to thank the staff of Materials Engineering at Purdue University, Rosemary Son, Vicki Cline, Stacey Coar, Tim VanMeter, Jameson Root, and Darren Pauly for their technical, administrative, and academic supports. I also acknowledge immense help from Dr. Christopher J. Gilpin, Robert Seiler, and Laurie Mueller in the Life Science Microscopy Facility at Purdue University.

I appreciate my teammates from Dr. Zhang's and Dr. Wang's groups for collaboration and encouragement. They are: Zhe Fan, Jin Li, Sichuang Xue, Qiang Li, Cuncai Fan, Ruizhe Su, Jie Ding, Zhongxia Shang, Yifan Zhang, Tongjun Niu, Bo Yang, Tianyi Sun, Nick Richter, Ben Stegman, Jie Jian, Jijie Huang, Han Wang, Xingyao Gao, Zhimin Qi, Xing Sun, Bruce Zhang, Xuejing Wang, Shikhar Misra, Matias Kalaswad, Robynne Paldi, Di Zhang, Xin Li Phuah, Zihao He, Bethany Rutherford, Juncheng Liu, Hongyi Dou, and Juanjuan Lu. I also want to thank my friends in Materials Engineering for a strong fellowship: Kyungjean Min, Sunghwan Hwang, Kyungho Kim, Changeun Kim, Taehoo Chang, Hyeyoung Son, Gyuchul Park, Sungho Yook, Pilsun Yoo, Hyungyung Jo, and Michael Taejoon Park.

I also thank my research collaborators: Dr. Amiya Mukherjee, Dr. Stephen Hellberg, Dr. Noam Bernstein, Dr. Troy B. Holland, Dr. Yiquan Wu, Dr. Wolfgang Rheinheimer, Jack M. Lopez, William J. Jarosinski, Dr. M. M. Gentleman, Dr. Vaishak Viswanathan, Dr. Harry Charalambous, Dr. Shikhar Jha, Dr. Thomas Tsakalakos, and Dr. K. S. N. Vikrant.

Last but not least, I would like to thank my parents and sister for their understanding and unconditional love.

The research in this thesis was financially supported by the Office of Naval Research N00014-17-1-2087 and N0014-16-1-2778.

TABLE OF CONTENTS

TABLE OF CONTENTS.....	5
LIST OF TABLES.....	9
LIST OF FIGURES	10
ABSTRACT.....	23
CHAPTER 1. INTRODUCTION	24
1.1. Polymorphism of ZrO ₂	24
1.2. Martensitic transformation.....	25
1.2.1. Effect of temperature on martensitic transformation	27
1.2.2. Effect of grain size on martensitic transformation	28
1.3. Several types of transformation-toughened ZrO ₂ -bearing ceramics.....	30
1.3.1. Magnesia-partially stabilized zirconia	31
1.3.2. Yttria-tetragonal zirconia polycrystal.....	32
1.3.3. Zirconia toughened alumina.....	35
1.4. Mechanical behavior of stabilized ZrO ₂ at mesoscale	35
1.4.1. Magnesia-partially stabilized zirconia at mesoscale	35
1.4.2. Mesoscale mechanical behavior of Y-TZP	38
1.5. Mechanical behavior of stabilized ZrO ₂ at microscale	40
1.5.1. The effect of the tetragonal phase in mechanical behavior	40
1.5.2. Orientation dependent martensitic transformation.....	42
1.5.3. Shape memory and superelasticity	46
1.5.4. Size effect on shape memory behavior	47
1.6. Consolidation methods.....	48
1.6.1. Flash sintering	49
1.6.1.1. Experimental setup	49
1.6.1.2. Flash sintering mechanisms.....	50
1.6.2. Spark plasma sintering	55
1.6.2.1. Heating rate.....	56
1.6.2.2. Pressure.....	58
1.6.2.3. Current	60

1.6.3.	Hot pressing.....	61
1.6.4.	Thermal barrier coatings	62
1.6.4.1.	Air plasma spray	64
1.6.4.2.	E-beam physical vapor deposition.....	65
1.6.4.3.	Detonation gun thermal spray.....	66
1.7.	Motivation and Objective.....	67
CHAPTER 2. EXPERIMENTAL		69
2.1.	Processing techniques	69
2.1.1.	Powder preparation	69
2.1.2.	Flash sintering	71
2.1.3.	Spark plasma sintering	72
2.1.4.	Air plasma spray and detonation gun thermal spray	73
2.2.	Microstructure Characterization.....	73
2.2.1.	Scanning electron microscope.....	73
2.2.2.	Transmission electron microscope	74
2.3.	Micromechanical properties.....	75
2.3.1.	<i>In-situ</i> micropillar compression	75
2.3.2.	Vickers hardness	76
CHAPTER 3. HIGH TEMPERATURE DEFORMABILITY OF DUCTILE FLASH SINTERED CERAMICS BY IN-SITU COMPRESSION.....		78
3.1.	Overview	78
3.2.	Introduction	78
3.3.	Experimental	80
3.3.1.	Flash sintering	80
3.3.2.	TEM sample preparation.....	80
3.3.3.	Microcompression test	80
3.3.4.	Finite element analysis	81
3.4.	Results	82
3.4.1.	Microstructural characterization.....	82
3.4.2.	Preexisting dislocations.....	86
3.4.3.	<i>In-situ</i> microcompression tests.....	89

3.4.4.	Temperature dependence of deformation mechanisms	91
3.4.5.	Martensitic transformations.....	94
3.4.6.	Cyclic loading tests	95
3.4.7.	Finite element method analysis on stress field distribution for dislocations.....	97
3.5.	Discussion	99
3.6.	Conclusions	105
CHAPTER 4. STUDY OF DEFORMATION MECHANISMS IN FLASH-SINTERED YTTRIA-STABILIZED ZIRCONIA BY IN-SITU MICROMECHANICAL TESTING AT ELEVATED TEMPERATURES		
106		
4.1.	Overview	106
4.2.	Introduction	106
4.3.	Experimental procedures.....	107
4.4.	Results	108
4.5.	Discussion	117
4.6.	Conclusions	122
CHAPTER 5. IN-SITU HIGH TEMPERATURE MICROMECHANICAL TESTING OF ULTRAFINE GRAINED YTTRIA-STABILIZED ZIRCONIA PROCESSED BY SPARK PLASMA SINTERING		
123		
5.1.	Overview	123
5.2.	Introduction	123
5.3.	Materials and methods	125
5.4.	Results	128
5.5.	Discussions.....	139
5.5.1.	Transformation induced toughening	139
5.5.2.	Evolution of deformation mechanisms at 400°C.....	143
5.5.3.	The evolution of deformation mechanism at 670°C.....	146
5.6.	Conclusions	148
CHAPTER 6. COMPARISION OF TEMPERATURE DEPENDENT DEFORMATION MECHANISMS OF 8YSZ THERMAL BARRIER COATINGS PREPARED BY AIR-PLASMA-SPRAY AND D-GUN THERMAL SPRAY: AN IN SITU STUDY.....		
150		
6.1.	Overview	150

6.2.	Introduction	150
6.3.	Experimental Procedures	152
6.3.1.	TBC depositions	152
6.3.2.	Microstructure characterizations	153
6.3.3.	Micropillar fabrications	154
6.3.4.	<i>In situ</i> microcompression tests	154
6.4.	Results	155
6.5.	Discussion	165
6.5.1.	Pillar fabrication and microstructure difference in APS and DVC coatings.....	165
6.5.2.	Room temperature deformability of APS and DVC pillars	167
6.5.3.	Comparison of mechanical behavior of APS vs. DVC 8YSZ at elevated temperatures	168
6.6.	Conclusions	170
CHAPTER 7. MICROMECHANICAL PROPERTIES OF MAGNESIA-PARTIALLY STABILIZED ZIRCONIA (MG-PSZ) PREPARED BY SPARK PLASMA SINTERING		171
7.1.	Overview	171
7.2.	Introduction	171
7.3.	Materials and methods	172
7.4.	Results	174
7.5.	Discussion	182
7.6.	Conclusions	183
CHAPTER 8. CONCLUSIONS AND FUTURE WORK		184
8.1.	Conclusions	184
8.2.	Comparison of deformation mechanisms for FS 3YSZ and SPS 3YSZ.....	185
8.3.	Future work	187
8.3.1.	Mechanical behavior of flash sintered ZnO	188
8.3.1.1.	Flash sintering of ZnO	188
8.3.1.2.	Mechanical testing	191
8.3.1.3.	Post-mortem TEM analysis	194
REFERENCES		200

LIST OF TABLES

Table 2.1. Chemical composition of non-stabilized ZrO ₂ and 3YSZ from Torso Corp.....	69
Table 3.1. Elastic properties of tetragonal zirconia [15].....	81
Table 3.2. The elastic compliance constants for tetragonal ZrO ₂ [163].	83
Table 4.1. Compositions of chemicals in 3YSZ (Provided by Tosoh corp.)	108
Table 4.2. Flow stress, yield strength and threshold stress at each temperature and strain rate.	118
Table 4.3. Activation energy of grain boundary and lattice diffusion for Zr, Y, O, and oxygen vacancy (V _o).....	121

LIST OF FIGURES

Figure 1.1. Schematic representation of (a) cubic, (b) tetragonal, and (c) monoclinic ZrO ₂ [1].	25
Figure 1.2. An example of phase transformation of ZrO ₂ caused by a thermal cyclic. (a-b) Cubic phase (C) transforms into a thermally stable tetragonal phase (T ^ˆ) at room temperature on cooling. (c-e) Thermally unstable T and C form on heating of T ^ˆ phase due to Y segregation along grain boundaries [15].	26
Figure 1.3. Free energy change required for martensitic transformation to occur as a function of temperature. Embedded dopant plays a role in increasing the free energy barrier as much as the strain energy change. As such, lower temperatures than <i>M_s</i> are required to obtain monoclinic ZrO ₂ [17].	28
Figure 1.4. (a) Measured and calculated <i>M_s</i> of 12 mol% CeO ₂ -doped ZrO ₂ as a function of grain size. (b) The presence of the martensitic transformation zone near a crack tip. The bigger grain size exhibits the larger transformation zone [17].	30
Figure 1.5. (a) Bright-field TEM micrograph of PSZ showing lenticular-shaped tetragonal precipitates in cubic matrix. (b) SEM image of TZP, and (c) ZTA [1].	31
Figure 1.6. A phase diagram of the MgO-ZrO ₂ system. The highlighted region is the commonly used composition for industrial applications [1].	32
Figure 1.7. A phase diagram of the Y ₂ O ₃ -ZrO ₂ system [1].	34
Figure 1.8. (a) Flexural strength of Mg-PSZ aged at 1100°C for 16 and 40 hrs. (b) Flexural strength and fracture toughness of Mg-PSZ as a function of monoclinic content on polished surface [36].	36
Figure 1.9. An indent mark and microstructure change in the surrounding region on Mg-PSZ aged for different time: (a) 2h, (b) 16 h, (c) 40 h [36].	37
Figure 1.10. A stress-strain curve for the compression test on Mg-PSZ and acoustic emission counts as a function of strain [37].	38
Figure 1.11. (a) Stress-strain behavior of YSZ tested at 23, 400, and 800°C with a strain rate of 1×10 ⁻⁵ s ⁻¹ . (b) Differential interference contrast view after compression at 23°C with a strain rate of 10 ⁻⁵ s ⁻¹ , showing surface rumpling by the martensitic transformation. (c) SEM micrograph of YSZ deformed at 800°C with a strain rate of 10 ⁻⁵ s ⁻¹ , showing the evidence of grain boundary sliding by intergranular crack and visible grain boundaries in the deformed area. (d) High-magnification SEM image showing cavitation along the grain boundaries [39].	39
Figure 1.12. (a) SEM image of hydrothermally degraded 3YSZ. Micropillars were fabricated in the upper region, which contains the monoclinic phase dominantly. (b) metastable tetragonal dominant micropillar (c) monoclinic dominant micropillar. (d) Stress-strain curves for the microcompression tests on DEG and AS specimens with different diameters. X-shaped mark on the curves stands for catastrophic failure.	42

Figure 1.13. (a) SEM image of 5 mol % TiO ₂ doped 2YSZ showing large grain size enough to fabricate a single crystal micropillar. (b) EBSD map of 5 mol % TiO ₂ doped 2YSZ. (c-d) low and high magnification of a micropillar retaining a single orientation. (e) schematic representation of the micropillar compression test [46].	43
Figure 1.14. (a) Stereographic triangle of tetragonal ZrO ₂ . Round, cross, and triangle-shaped marks represent transformed, fractured, and slipped micropillars, respectively. (b) Slipped micropillar after compression with a corresponding load-displacement curve. (c) transformed micropillar after compression with a corresponding load-displacement curve. Plateau represents transformation induced displacement-burst. (d) fractured micropillar after compression with a corresponding load-displacement curve [46].	44
Figure 1.15. (a) Measured critical stress at which martensitic transformation takes place versus the maximum Schmid factor. The phase transformation takes place at lower critical stress when the Schmid factor is larger than 0.3. (b) SEM images of a micropillar that exhibits both transformation and crack due to the intermediate level of the Schmid factor [46].	45
Figure 1.16. (a) Stress-strain curve for a microcompression test on oligocrystalline micropillar showing superelasticity owing to the martensitic transformation. Sudden increase of strain (plateau regions) is due to the forward and reverse transformation during loading and unloading, respectively. (b) Stress-strain curves for the cyclic loading tests. The curves become stabilized as the cyclic tests proceed. (c) SEM image of the micropillar before compression. (d) SEM image of the micropillar after compression. (e) SEM image of the micropillar after heating at 500°C for 2 h. It exhibits a shape memory effect [14].	47
Figure 1.17. (a-c) A schematic representation of micropillars with different diameters (d = grain size). (d-f) SEM images of compressed micropillars. A micropillar with a smaller diameter exhibits plastic deformation due to the martensitic transformation. A micropillar with larger diameter fails due to mismatch stress among grains during the martensitic transformation. (g-i) Corresponding load-displacement curves. Strain bursts result from the martensitic transformation [45].	48
Figure 1.18. A flash sintering set up with a green body of (a) dog-boned shape, (b) cylindrical shape, and (c) rod shape.	50
Figure 1.19. Plots of (a) electric field, (b) current density, and (c) powder density as a function of time during a typical flash sintering experiment.	51
Figure 1.20. Flash sintered single-crystal 8YSZ (100) showing electrochemical blackening from (a) plan-view and (b) cross-sectional view [90].	54
Figure 1.21. 8YSZ subjected to 50 A/cm ² showing the abnormal grain growth on the cathode side [95].	54
Figure 1.22. A schematic representation of SPS.	56
Figure 1.23. SEM micrographs of Al ₂ O ₃ prepared by SPS at a heating rate of (a) 2 °C/min and (b) 100 °C/min [113].	57
Figure 1.24. (a) The effect of applied pressure on the relative density of fine- and coarse-grained ZrO ₂ [119]. (b) The effect of applied pressure on the sintering temperatures to achieve a 95% relative density of ZrO ₂ [120].	60

Figure 1.25. A schematic representation of a thermal barrier coated turbine blade [12].	64
Figure 1.26. SEM images of APS TBC from (a) plan-view and (b) cross-sectional view showing a high density of pores and cracks.	65
Figure 1.27. A cross-sectional SEM image of EBPVD TBC showing columnar grains on top of equiaxed grains at the interface of the top-coat and bond-coat.	66
Figure 1.28. SEM images of DVC TBC prepared by detonation gun thermal spray from (a) plan-view and (b) cross-sectional view showing dense microstructure and vertical cracks.	67
Figure 1.29. A plot of Vickers hardness for TBCs prepared by detonation gun thermal spray, EBPVD, APS, and suspension plasma spray.	67
Figure 2.1. XRD patterns from 3YSZ raw powder (Tosoh TZ-3Y-E) and typical tetragonal ZrO ₂ indexed by PDF#83-0113.	70
Figure 2.2. (a) Vertical high energy planetary ball mill and (b) chiller used in this thesis.	71
Figure 2.3. A schematic representation of an experimental setup for flash sintering.	72
Figure 2.4. SPS system in Purdue University	72
Figure 2.5. FEI Quanta 3D FEG Dual Beam SEM/FIB in Purdue University.	74
Figure 2.6. FEI Talos 200X TEM/STEM in Purdue University.	75
Figure 2.7. Micropillar and <i>In-situ</i> nanoindentation system used in this study.	76
Figure 3.1. STEM micrograph. a A STEM micrograph of the flash-sintered 3YSZ showing several triple junctions among grains. Scale bar, 60 nm. b-c The EDS mapping of zirconium and yttrium. Note that zirconium and yttrium are nearly uniformly distributed throughout the grains. The grain boundaries appear to have slight deficiency in zirconium. Scale bar, 60 nm.	82
Figure 3.2. Relative density comparing to theoretical value as a function ramping temperature during flash sintering. 3YSZ was sintered at a constant heating rate of 25°C/min under an electrical field of 1.5, 15, and 150 V/cm. Flash sintering under an electric field of 150 V/cm took place at 1,150-1,200°C in a few seconds.	84
Figure 3.3. XRD patterns of flash sintered 3YSZ at an electrical field of 150 V/cm, showing dominant metastable tetragonal phase and crystallographic plane indices.	84
Figure 3.4. The determination of the residual stress using the Williamson-Hall analysis.	85
Figure 3.5. Microstructure of flash-sintered 3YSZ. a SEM images of the unpolished flash-sintered 3 YSZ. The average particle size is ~ 1 μm. Scale bar, 3 μm. b Bright-field TEM micrograph showing subgrains with grain boundaries and defects generated during flash sintering (labeled by black arrows) and nanopores (~1.4%) (indicated by red arrows). The inserted SAD pattern shows diffraction rings. Scale bar, 200 nm. c A STEM micrograph showing a dislocation array inside a grain in the flash sintered 3YSZ. The dislocation array was generated in a bottleneck region of the grain as indicated by red arrows. Scale bar, 100 nm. d-e Bright-field (BF) and dark-field (DF) TEM micrographs showing the dislocation array in the boxed region in c . Scale bar, 50 nm. f-i	

Numerous BF TEM images of the flash sintered 3YSZ showing the existence of dislocations and dislocation arrays in grains. Scale bar, 50 nm. 85

Figure 3.6. Grain size distribution. **a** Agglomerated particle size distribution and **b** subgrain size distribution of flash- sintered 3YSZ calculated by systematic grain intercept method. The average grain size and subgrain size are 0.87 μm and 159 nm, respectively. The density of flash-sintered ceramic is $\sim 98\%$ 86

Figure 3.7. Bright-field TEM images of flash-sintered 3YSZ under an electric field of 150 V/cm indicating the existence of grains with significant internal defects. Many of these internal defects appear to be high-density dislocation networks. Scale bar, 200 nm. 87

Figure 3.8. Bright-field TEM micrographs. **a-f** Bright-field TEM images of the flash sintered 3YSZ showing the existence of dislocations and dislocation arrays in grains. Dislocation arrays were frequently observed near triple junctions. Dislocations may arise from the large stress concentration near triple junctions induced during flash-sintering of 3YSZ. Scale bar, 50 nm... 88

Figure 3.9. Bright field TEM images of 3YSZ processed under 1.5 V/cm and 15 V/cm showing nanograins. **a-b** 3YSZ sintered under 1.5 V/cm. Scale bar, 100 nm. **c-d** 3YSZ sintered under 15 V/cm. Scale bar, 100 nm. Dislocations and dislocation arrays rarely exist inside the grains unlike 3YSZ sintered under 150 V/cm. 89

Figure 3.10. Uniaxial *in situ* microcompression tests on the flash sintered 3YSZ at room temperature and 400°C at a constant strain rate of $5 \times 10^{-3} \text{ s}^{-1}$. **a-d** SEM images during *in situ* compression test of micropillars at different strain levels at 25°C. No crack can be detected until a true strain of 8%. At the strain of 9%, the pillar experienced brittle catastrophic fracture. Scale bar, 2 μm . **e-h** For micropillars tested at 400°C, cracks nucleated at smaller strain, $\sim 4\%$. Crack density increased with compressive strain. However, cracks propagated downward gradually and slowly without catastrophic failure. Scale bar, 2 μm . **i** The corresponding true stress-strain curve shows that the flow stress exceeds 3.5 GPa for pillars tested at 25°C. In comparison, the pillar tested at 400°C has a flow stress of 2 GPa and higher elastic modulus. 90

Figure 3.11. SEM images of the flash sintered 3YSZ micropillars before and after compression tests from 25°C to 600°C and corresponding mechanical properties. **a-d** When tested at 200°C and below, the pillar fractures in a brittle manner (into 2 major sections) at very large true strain. Scale bar, 2 μm . **e-j** When tested at 400-600°C, multiple cracks formed and propagated slowly into the pillars, leading to formation of the cauliflower type of pillar tops. At 600°C, crack density and propagation distance were substantially reduced. Scale bar, 2 μm . **k** Corresponding true stress-strain curves of pillars tested at different temperatures. Black arrows indicate the ultimate compressive strength (UCS) of the pillars. Partial unloading at 0.5 and 1% strains were performed to investigate the apparent elastic moduli of pillars tested at different temperatures. A stress-strain curve for 3YSZ sintered without the electrical field is shown as reference. **l** Ultimate compressive strength (UCS) decreases monotonically with increasing test temperature. The elastic modulus increases with test temperature up to 400°C and decreases thereafter. Meanwhile, the critical strain at which the first crack nucleation takes place decreases with temperature to a minimum of 4.5% strain at 400°C and increases thereafter to 7.5% when tested at 600°C. 400°C is the onset temperature where a different inelastic deformation mechanism begins to operate. Zone 1 represents phase transformation toughening from room temperature to 400°C. Zone 2 corresponds to dislocation creep dominant plasticity above 400°C..... 92

Figure 3.12. Repeatability of true stress-strain curves for 3 YSZ tested at **a** 25°C, **b** 200°C, **c** 400°C, **d** 500°C, and **e** 600°C. Five microcompression tests were carried out to check repeatability of the tests. Flow stresses in most studies show good agreement. Unloading studies at 0.5 and 1% strain were carried out to measure the apparent elastic moduli at each temperature..... 93

Figure 3.13. TEM analyses of a 3 YSZ pillar tested at room temperature. **a-b** The SEM image of the pillar before and after compression test at room temperature. Scale bar, 2 μm . **c** The corresponding stress-strain curve showing a flow stress of 4 GPa and a fracture strain of $\sim 6\%$. **d** Bright-field XTEM image of the fractured pillar. Scale bar, 500 nm. **e-f** Bright-field XTEM images of the pillar showing ultrafine grains near fracture surface. Grains 1-3 were chosen to identify phase transformation. Scale bar, 200 nm. **g-i** Selected area electron diffraction (SAED) patterns showing that grains 1-3 have monoclinic zirconia phase examined along respective zone axis of [101], [132], and [112]. 95

Figure 3.14. Cyclic loading and following monotonic compression tests at a strain rate of $5 \times 10^{-3} \text{ s}^{-1}$ at 25°C and 400°C and the corresponding stress-strain curves. **a** and **f** SEM images of micropillars before cyclic loading tests. Scale bar, 2 μm . **b** and **g** SEM micrographs of micropillars after 30 cyclic loading tests. The cyclic stress-strain curves are shown as blue curves. **c** and **h** After the first monotonic compression tests highlighted in red curves. **d** After the second monotonic compression test highlighted in green. The 27th loading-unloading curves at each temperature shown in orange color and enlarged in the inserted stress-strain curves clearly show the hysteresis loops. The upper portion of a loading-unloading curve is enlarged in a circle to illustrate the stress relaxation for 1 second of holding at 400°C..... 96

Figure 3.15. Peach-Köhler force distribution in the vicinity of grain boundaries. **a** Original microstructure. Scale bar, 60 nm. **b** Zoom-in region around a selected grain corner highlighted in the black-box region. Assigned Euler angle orientations are, for the bottom grain, $(\alpha, \beta, \gamma) = (0, 0, 0)$, for the top-right grain, $(\alpha, \beta, \gamma) = (0, 45, 0)$ and for the top-left grain, $(\alpha, \beta, \gamma) = (45, 45, 0)$. For the BCT system, $b = 3.16[111] \text{ \AA}$ and dislocation line, $\xi = [110]$, **c-d** The Peach-Köhler forces for a polycrystal subjected to a -200MPa in-plane vertical compression for plane strain conditions at selected locations. The maximum magnitude of the force per unit length on the test dislocations is $|F|=0.059 \text{ N/m}$. For this particular Burgers vector and line direction, the resultant force field favors dislocations to pile up in the abutting grains, making grain boundaries and corners sources and sinks of dislocations. 98

Figure 3.16. Summary of Peach-Köhler forces for microstructure shown in Fig. 3.14a. Each inset shows a different test dislocation line: **a** $b = 3.16111 \text{ \AA}$ and $\zeta = 111$, **b** $b = 3.16111 \text{ \AA}$ and $\zeta = 110$, **c** $b = 3.16111 \text{ \AA}$ and $\zeta = 110$, **d** $b = 3.16111 \text{ \AA}$ and $\zeta = 110$, **e** $b = 3.16111 \text{ \AA}$ and $\zeta = 101$, **f** $b = 3.16111 \text{ \AA}$ and $\zeta = 011$, **g** $b = 3.16111 \text{ \AA}$ and $\zeta = 100$, **h** $b = 3.16111 \text{ \AA}$ and $\zeta = 010$, and **i** $b = 3.16111 \text{ \AA}$ and $\zeta = 001$. In all cases, grain corners and boundaries become sources or sinks for dislocations. 99

Figure 3.17. Stress relaxation as a function strain at room temperature and 400°C during one second holding segment of cyclic loading and unloading tests. 105

Figure 4.1. Microstructure and strain rate jump tests on the flash sintered 3YSZ. (a-b) Bright field TEM micrographs of the flash sintered 3YSZ showing (a) ultrafine grains and (b) an array of preexisting dislocations. (c-e) SEM snapshots of the pillars tested at 450, 550, and 650°C at 0, 3%,

6%, and final strains (11-12%). Several cracks propagated from the top surface of the pillar. Crack length and density reduce as test temperature rises. 110

Figure 4.2. Stress-strain curves for strain rate jump tests on the flash sintered 3YSZ at 450, 550, and 650°C. Stress-strain curves for three strain rate jump tests at (a) 450°C, (b) 550°C, and (c) 650°C. Strain rate of $5 \times 10^{-4} \text{ s}^{-1}$ was employed in the elastic region. Strain rates of $3 \times 10^{-3} \text{ s}^{-1}$, $1 \times 10^{-2} \text{ s}^{-1}$, $5 \times 10^{-2} \text{ s}^{-1}$, and $3 \times 10^{-1} \text{ s}^{-1}$ were utilized in the plastic region to obtain flow stresses at each temperature. The flow stresses increase with increasing strain rate and decreasing temperature. 111

Figure 4.3. Data processing from strain rate jump tests on the flash sintered 3YSZ at 450, 550, and 650°C before considering the presence of the threshold stresses. (a) Effect of strain rates on flow stress at each temperature. Note that the natural logarithm of both strain rate and flow stress is taken and plotted. The slopes represent strain rate sensitivity (m). (b) Temperature dependence of strain rate at a flow stress of 2 GPa. The activation energy for the underlying deformation mechanism turns out to be $347 \pm 151 \text{ kJ/mole}$. (c) Flow stress versus the normalized strain rate. The slope indicates the stress exponent (n). The abnormally high stress exponent (30.2) implies the existence of the threshold stress. 113

Figure 4.4. The determination of the threshold stress for the flash sintered 3YSZ at 450, 550, and 650°C. (a) The determination of the threshold stress with a stress exponent of 1. The actual data points are significantly deviated from the linear regression lines as indicated by the curved dash lines. (b) The determination of the threshold stress with a stress exponent of 2. The actual data shows better linear fit than those with a stress exponent of 1, but still deviates from the linear regression lines by exhibiting positive upward curvature. (c) The determination of the threshold stress with a stress exponent of 7. The linear regression lines match well with the actual data. The extrapolation of the linear line to zero strain rate describes the threshold stress. 115

Figure 4.5. Corrected data processing from strain rate jump tests on the flash sintered 3YSZ at 450, 550, and 650°C in consideration of the presence of the threshold stress. (a) The corrected flow stress as a function of strain rates at each temperature. The strain rate sensitivities after the correction increase to 0.15. (b) Temperature dependence of strain rate at a flow stress of 500 MPa. The activation energy is estimated to be $145 \pm 74 \text{ kJ/mole}$. (c) The corrected flow stress versus the normalized strain rate. The data correction with an imposed stress exponent of 7 returns the stress exponent of 6.7. 116

Figure 5.1. Displacement vs. time curves at RT, 400, and 670°C. The slopes of curves (drift rate) are less than 0.7 nm/s in every case. 127

Figure 5.2. XRD patterns of spark plasma sintered 3YSZ with crystallographic plane indices. It is shown that metastable tetragonal zirconia is a dominant phase without evident cubic and monoclinic zirconia phase. 129

Figure 5.3. The determination of the residual stress in SPS YSZ using the Williamson-Hall analysis. 129

Figure 5.4. Microstructure of SPS 3YSZ and grain size analysis. (a) An SEM image of a typical unpolished region showing agglomerated grains. (b) A bright-field TEM micrograph showing ultrafine grains, and the inserted SAD pattern shows continuous rings of the tetragonal phase. (c) A high-resolution TEM image showing a clear triple junction without glassy phase along the grain

boundaries. (d) Grain size distribution determined by the intercept method showing the average grain size of ~ 175 nm. 130

Figure 5.5. Comparison of morphology evolution and stress-strain behaviors of micropillars during *in-situ* compression tests at 25, 400, and 670°C. (a₁-a₄) At 25°C, cracks were nucleated at a strain of 6%, and the pillar fractured in a brittle manner right after the crack nucleation. (b₁-b₄) The micropillars tested at 400°C show crack formation at a strain of 5~6%. However, cracks propagated downward slowly into the pillar without brittle failure. (c₁-c₄) When compressed at 670°C, the pillars deformed gradually and uniformly in the top portion of the pillars with little cracks. (d) The true stress-strain curve collected at 25°C deviates from its linearity at a strain of 4%, corresponding to a stress level of ~ 4 GPa. The yield strength and flow stress both decrease for pillars tested at elevated temperatures. The pillars tested at 670°C reached a constant flow stress of ~1.5 GPa until a strain of 30% without softening. Partial unloading was performed in all tests to obtain a reliable measurement of modulus. The white dash lines in the SEM micrographs indicate cracks. 131

Figure 5.6. SEM images of micropillars before and after microcompression tests at elevated temperatures up to 670°C. (a-b) When tests were conducted below 200°C, the micropillars exhibit brittle fracture at a strain of 4-7%. (c-d) Transitions of deformation mechanisms were observed in pillars tested at 400 and 600°C. Several cracks nucleated from the top of the pillars and propagated slowly downward into the pillars. (e) The pillars tested at 670°C showed significantly enhanced plastic flow ability. The deformation was mainly accommodated by the top half of the pillar, and the crack propagation speed was greatly reduced. 132

Figure 5.7. Stress-strain curves for SPS 3YSZ micropillars tested *in-situ* at different temperatures at a strain rate of 5×10^{-3} /s. Numerous tests were carried out to check the reproducibility of the experimental results at (a) 25°C, (b) 200°C, (c) 400°C, (d), 600°C, and (e) 670°C. (f) Comparison of stress-strain curves at different temperatures. Partial unloading at displacement of 60 and 120 nm was conducted to measure the apparent elastic modulus of SPS 3YSZ at different temperatures. 133

Figure 5.8. Top (left panel) and side (right panel) views of pillars tested at 25, 400, and 670°C. (a-b) For the pillars tested at 25°C, transgranular fracture with several shear bands (black arrows) was observed. Surface rumpling in the boxed region was observed due to martensitic phase transformation. (c-d) When tested at 400°C, fracture surface reveals individual equiaxed grains highlighted in the white box. (e-f) Little fracture was detected for the pillars tested at 670°C. After compression to a true strain of 30%, surface roughening in the boxed region can be seen as shown in the box. 134

Figure 5.9. TEM analyses of the 3YSZ pillars tested at room temperature and 400°C. (a) Bright-field XTEM image of the deformed pillar at room temperature. Grains 1-3 were chosen to identify the phase transformation. (b-d) Selected area electron diffraction (SAED) patterns showing that grains 1-3 have monoclinic zirconia phase examined along respective zone axis of [100], [112], and [101]. (e) Bright-field XTEM image of the deformed pillar at 400°C. (f) Top portion of the deformed pillar showing gaps along grain boundaries induced by grain boundary sliding (indicated by red arrows). (g) Intergranular fracture in the middle section of the deformed pillar. (h) The bottom portion of the deformed pillar shows no grain boundary gaps. 136

Figure 5.10. Cross section FIB ion microscopy images of the compressed pillars. (a) The cross-sectional view of the pillar tested at 400°C at a strain of 9% shows crack propagation path and

cavities generated along the grain boundaries due to mechanical test. (b) For the pillar tested 670°C, no obvious crack was observed. Elongated grains with numerous nanoscale cavities indicated by blue and red arrows, respectively in the top half of the pillar were resolved. 137

Figure 5.11. TEM images of the pillar after compression test at 670°C. (a) BF TEM images of the deformed pillar showing the location of the grains in Fig. (b) and Fig 5.12. (b) Arrays of dislocations within grains were verified (marked by orange arrows). (c) High resolution TEM image of the grain retaining arrays of dislocations with selected area diffraction pattern of the grain examined along [100] zone axis. (d) FFT processed high resolution TEM image shows the presence of abundant dislocations along (022) plane. 138

Figure 5.12. TEM images of the compressed pillar at 670°C showing the deformation induced monoclinic zirconia. (a) SAD pattern with continuous rings indicates dominant tetragonal phase with monolithic diffraction spots arising from a few grains that underwent martensitic transformations. (b) Bright-field TEM image of a grain with monoclinic phase shows martensite lath and stacking faults. (c) SAD pattern of the grain with monoclinic phase. (d) High resolution TEM image and the inserted FFT confirms the presence of stacking faults. 139

Figure 5.13. Stress-strain curves for the micropillars with a diameter of (a) 3 μm (b) 1.5 μm and (c) 0.7 μm. As the diameter of micropillars increases, fracture strain and peak stresses increase. Fracture events are indicated by X-shaped cross. 141

Figure 5.14. Cyclic loading tests at a strain rate of $5 \times 10^{-3} \text{ s}^{-1}$ at room temperature. 5th, 11th, and 19th loading and unloading curves are highlighted in red to show hysteresis loops. 142

Figure 5.15. Microcompression test on a pillar with high aspect ratio at room temperature. (a) Before the compression test. (b) The pillar experienced a strain of 5% and bent without any crack owing to martensitic transformation, which prevents crack propagation upon loading. (c) After elimination of loading, the deviatoric strain was partially recovered due to reverse martensitic transformation (monoclinic to tetragonal zirconia). Partial shape recovery implies that the test temperature is between austenite start and finish temperature. 143

Figure 5.16. Mechanical properties of SPS 3YSZ as a function of test temperatures. (a) The apparent elastic modulus (red curve) increases with increasing temperature up to 200°C and decreases thereafter. The ultimate compressive strength (UCS) decreases monotonically with the increasing test temperature. (b) The critical strain at which the first crack occurs for the onset of crack nucleation decreases slightly with test temperature up to 400°C, due to the gradual suppression of martensitic transformation. Beyond 400°C, the critical strain increases monotonically with test temperature and the dominant deformation mechanism changes. 144

Figure 5.17. SEM images of compressed pillars at 200 and 600°C. (a) Pillars tested at 200°C fractured catastrophically. Fracture arises mainly from transgranular cracking, but intergranular cracking was also observed. (b) For pillars tested at 600°C, no significant fracture was appreciable. It appears that the strain was accommodated by change in internal structure based on the observation of elongated grains. 145

Figure 5.18. Energy dispersive X-ray spectroscopy images. (a) Scanning TEM image of 3YSZ showing clear grains and pore. (b) EDS mapping of zirconium. (c) EDS mapping of yttrium showing yttrium segregation along the grain boundaries which may promote grain boundary sliding as temperature increases. 145

Figure 6.1. XRD patterns of APS and DVC 7 YSZ coatings. (a) The dominant phase is tetragonal prime (t') zirconia for both TBCs, which is not transformable to monoclinic phase upon compression owing to higher yttria concentration (8 wt%) and high rate deposition. (b) A magnified view of XRD patterns in the range of 72 to 76° clearly distinguish the t' phase from tetragonal (t) and cubic (C) zirconia. 155

Figure 6.2. TEM images of APS and DVC YSZs showing grain sizes and preexisting cracks with inserted selected area diffractions. (a) Bright-field TEM image of APS TBC with preexisting cracks. Grain intercept method reveals an average grain size of 323 ± 111 nm. (b) TEM micrograph of DVC YSZ with clearly resolved intergranular cracks. The average grain size is 169 ± 45 nm. 156

Figure 6.3. (a-b) Plan-view SEM images of APS and DVC TBCs after polishing. (c-d) Cross-section SEM images of APS and DVC TBCs after polishing. 157

Figure 6.4. SEM snapshots of micropillars ($\sim 1.5 \mu\text{m}$ in diameter and $\sim 3.3 \mu\text{m}$ in height) during *in-situ* compression tests at room temperature at a constant strain rate of $5 \times 10^{-3} \text{ s}^{-1}$ showing typical morphology evolutions at different strain levels. (a₁-a₄) For the micropillars of APS TBC, no cracks were observed at a strain of 6%, but the pillar fractured into two major pieces right after the crack nucleation at a strain of 7.5%. (b₁-b₄) The DVC YSZ micropillars exhibit crack nucleation at a strain of 6%. However, cracks slowly propagated downward into the pillar rather than showing a catastrophic failure. (c) The stress-strain curve for APS YSZ exhibits a sudden load drop after reaching an ultimate compressive strength of 5.8 GPa. On the other hand, the stress-strain curve for DVC YSZ shows an ultimate compressive strength of 6 GPa at a strain of 7.5% followed by gradual softening to a strain of 10%. See Supplementary Videos 1 and 2 for greater details.... 158

Figure 6.5. Typical morphology evolutions of APS and DVC YSZ micropillars during *in-situ* compression tests at 500°C . (a₁-a₄) For the APS micropillar, a few prominent cracks were generated at a strain of 14%. The large plastic strain was accommodated mainly by the dilation of the top section of the pillar. (b₁-b₄) For the DVC micropillar, cracks were nucleated at an early stage (7% strain), but gradually and slowly propagated into the pillar such that no catastrophic failure was observed. (d) The corresponding stress-strain curves show the flow stresses for APS and DVC TBCs are ~ 1.2 and ~ 1.6 GPa, respectively. The stress-strain curve for DVC TBC exhibits local load drops induced by cracks during the compression test. See Supplementary Videos 3 and 4 for greater details. 159

Figure 6.6. SEM images of the pillars compressed at 500°C showing typical deformation-induced morphology changes. (a) APS pillar compressed to a strain of 23% contains a few small cracks in the prominently dilated pillar top. The orange box revealed a high-density of deformation bands. (b) For the DVC pillar compressed to a strain of 23%, large cracks highlighted in the orange box propagated vertically into the pillar, which did not show significant pillar top dilation. 159

Figure 6.7. TEM analyses of the APS TBC pillar compressed at room temperature. (a) Bright-field XTEM image of the fractured pillar. (b) A grain of the fractured pillar showing dislocations and dislocation strain field obtained by two beam condition diffraction. (c) SAD pattern of a grain in examined along $[111]$ zone axis. Three $\{112\}$ tetragonal variants were chosen to investigate the relative incidence of each tetragonal variant. (d-f) Dark-field TEM images of the pillar top showing three tetragonal variants (112), (121), and (211). 160

Figure 6.8. TEM analyses of the DVC TBC pillar compressed at room temperature. (a) Bright-field XTEM image of the fractured DVC pillar. (b) A region of the fractured pillar containing a high density of stacking faults. (c) High resolution TEM images and the inserted FFT confirming the occurrence of stacking faults. (d) SAD pattern of the grain in Figure 6.8(b) observed along [111] zone axis. (e-g) Dark-field TEM images of the pillar top showing relative incidence of three tetragonal variants..... 161

Figure 6.9. TEM analyses of the APS TBC pillar compressed at 500°C. (a) Bright-field XTEM image of the upper half of the deformed pillar. (b) A region of the deformed pillar showing a high density of dislocations. (c) SAD pattern examined along [111] zone axis. Three {112} tetragonal twin variants were chosen to investigate the appearance of each tetragonal variant. (d-e) Dark-field TEM images of the pillar top showing two tetragonal variants (112) and (121). (f) The third tetragonal variant (211) is largely absent..... 162

Figure 6.10. TEM analyses of the DVC TBC pillar deformed at 500°C. (a) Bright-field XTEM image showing overall structure of the deformed pillar containing cracks. (b) Fractured region of the deformed pillar containing a high-density of stacking faults. (c) High resolution TEM of stacking faults with inserted FFT. (d) SAD pattern showing {112} planes examined along the [111] zone axis. Three {112} tetragonal variants were selected to conduct dark-field TEM experiments. (e-g) Dark-field TEM images of the pillar top showing the absence of one tetragonal variant in the deformed pillar top attributed to ferroelastic domain switching to the other two tetragonal variants (e and f). 163

Figure 6.11. SAD patterns on the APS and DVC pillars tested at 25 and 500°C. No cubic and monoclinic phases were observed..... 164

Figure 6.12. Numerous stress-strain curves for the numerous APS and DVC micropillars tested at room temperature and 500°C at a strain rate of $5 \times 10^{-3} \text{ s}^{-1}$. The X-shaped mark represents the fracture strain. (a) The APS micropillars compressed at room temperature show scattered fracture strengths (0.6 ~ 6.6 GPa) resulting from preexisting cracks and pores. (b) For the DVC pillars tested at room temperature, fracture strengths are less dispersed, ranging from 3.9 to 6.6 GPa. (c) For the APS TBC pillars tested at 500°C, the variation of fracture strengths decreases significantly, and the average fracture strength is ~ 1.2 GPa. (d) The DVC TBC pillars tested at 500°C also shows less variable fracture strengths (1.3 ~ 1.8 GPa) compared to that at room temperature with an average fracture strength of 1.6 GPa..... 165

Figure 6.13. SEM images of (a) APS and (b) DVC pillars showing preexisting pores and cracks. In general, pore and crack sizes of APS TBC pillars are larger than those of DVC TBC pillars. 166

Figure 7.1. XRD patterns and microstructure analyses of Mg-PSZ processed by spark plasma sintering at 1700°C and 1850°C. (a-b) XRD patterns of Mg-PSZ sintered at 1700°C and 1850°C, and subsequently heat-treated at 1100°C for different aging times (0, 0.5, 2, 4, and 8 hrs). For both samples, t-phase starts showing up after 2 hr aging and m-phase emerges after 4 hr aging. (c) Phase stability ratio of two samples as a function of aging time. A ratio of c- and t-phases to m-phase in the sample sintered at 1700°C decreases significantly after 8hr aging. (d-f) SEM micrograph, inverse pole figure and KAM map of Mg-PSZ sintered at 1700°C. The average grain size is $7 \mu\text{m}$ and significant residual stress is observed within grain interiors. (g-i) SEM micrograph, inverse

pole figure and KAM map of Mg-PSZ sintered at 1850°C. The average grain size is determined to be 30 μm and residual stress is predominant along grain boundaries. 176

Figure 7.2. Determination of the residual stress in as-sintered Mg-PSZ at (a) 1700 and (b) 1850°C. Plots of d spacing of the (311) plane versus $\sin^2(\Psi)$ yields the tensile residual stress of 472 MPa and 226 MPa for 1700Mg-PSZ and 1850Mg-PSZ, respectively. m is the slope of the linear regression line and d_0 is the unstressed d spacing of the (311) plane. 177

Figure 7.3. TEM micrographs of as-sintered Mg-PSZ at 1700°C. (a-b) Bright-field TEM micrographs of as-sintered Mg-PSZ showing clear c-matrix with low density of precipitates and bend contours. (c-d) HRTEM micrographs showing the existence of t- and m-precipitates. (e-h) HADDF image and EDS map of as-sintered Mg-PSZ showing uniform distribution of Mg throughout the specimen. 178

Figure 7.4. TEM micrographs of Mg-PSZ sintered at 1700°C followed by 2 hr aging. (a) Low-magnification bright-field TEM image showing the presence of lenticular precipitate indicated by orange arrows. (b) Bright-field TEM micrograph of precipitates from an inserted box in Fig. (a), showing two precipitates embedded in c-matrix. (c) HRTEM micrograph from the precipitate of Fig. (b), showing the presence of t- and m-phases, confirmed by the inserted FFTs. (d-g) High-angle annular dark field (HAADF) image and EDS map of 2 hr aged Mg-PSZ showing Mg deficiency in precipitates. 179

Figure 7.5. TEM micrographs of Mg-PSZ sintered at 1700°C followed by 4 hr aging. (a) Low-magnification bright-field TEM image showing the presence of lenticular precipitate (indicated by orange arrows) and monoclinic variants. (b) HRTEM micrograph of monoclinic variants showing twin-relation as evidenced by an inserted FFT. (c) HRTEM micrograph of c-matrix site showing the presence of t- and o-phases, confirmed by inserted FFTs. (d) HRTEM image of the lenticular precipitate, consisting mainly of m-phases confirmed by the inserted FFTs. (e-h) HAADF image and EDS map showing the enrichment of Zr and deficiency of Mg in precipitates. 180

Figure 7.6. TEM micrographs of Mg-PSZ sintered at 1700°C and subsequently aged for 4 hrs. (a-b) Bright-field TEM micrographs showing the presence of twin-related monoclinic variants along grain boundaries. 180

Figure 7.7. Microindentation hardness and fracture toughness as a function of aging time for Mg-PSZ prepared by spark plasma sintering at (a) 1700 and (b) 1850°C. Hardness of Mg-PSZ decreases monotonically with increasing aging time for both specimens. Fracture toughness reaches to the highest value when aged for 4 hrs and decreases thereafter. 181

Figure 8.1. Critical strain versus test temperature for FS and SPS 3YSZ. 187

Figure 8.2. Flash sintering conditions and microstructure of the flash-sintered ZnO. (a) An electric field of 60 V/cm was applied to the ZnO green body under the isothermal condition (700°C). After the onset of flash sintering, a current density of 10 A/cm² was applied for 60 s. (b) The power-spike and abrupt linear shrinkage were observed at the onset of flash sintering. (c) The XRD pattern of the sintered ZnO reveals a typical wurtzite crystal structure. (d) SEM micrograph of the as-sintered ZnO from the positive side showing the typical granular morphology. (e) TEM micrograph showing grains with an average grain size of 1.3 μm , and nanovoids at the grain boundaries. (f) Inverse pole figure crystal orientation map shows the polycrystalline nature of the sintered ZnO with high angle grain boundaries. (g) Geometrically necessary dislocation (GND)

map shows the average GND density of the flash-sintered ZnO at the positive side is $1.2 \times 10^{12} m^{-2}$ 189

Figure 8.3. Sintering parameter and microstructure of the conventionally sintered ZnO. (a) Green body ZnO was heated at a heating rate of 10 °C/min and held at 1100°C for 1 min. (b) XRD pattern of the CS ZnO shows no considerable difference in texture and peak position when compared to the FS ZnO. (c-d) SEM and bright-field TEM micrographs of the CS ZnO show a larger grain size ($\sim 2 \mu m$) than the FS ZnO. (f-g) Inverse pole figure and GND map of CS ZnO showing average GND density of $1.10 \times 10^{12} m^{-2}$ 190

Figure 8.4. Microstructure of the FS ZnO at the negative and positive sides. (a) SEM image of the FS ZnO at the negative side. (b) BF TEM image of as-sintered ZnO grains at the negative side. (c-d) TEM micrographs of the FS ZnO at the positive side show stacking faults and grain size similar to the negative side..... 191

Figure 8.5. *In-situ* microcompression tests on flash-sintered (FS) and conventionally sintered (CS) ZnO at 25, 200, 400, and 600°C. (a) The FS ZnO micropillars have higher flow stress (1.2 GPa) than that of the CS ZnO micropillar at 25°C. SEM snapshots of the FS ZnO pillar reveal cracks generated at a strain of 10% and their downward propagation without a significant crack deflection. (b) The flow stress of the FS ZnO decreased to 0.7 GPa when tested at 200°C. The flow stress of the FS ZnO micropillars tested at 200°C is comparable to that of the CS ZnO micropillar. SEM snapshots show the crack deflections along grain boundaries. (c) The CS and FS pillars tested at 400°C show similar flow stress, ~ 0.6 GPa and the stress-strain curves of the FS pillars have much less serrations. Multiple small cracks along grain boundaries were observed. (d) At 600°C, significant serrations were observed on the flow stress-strain curve of the CS pillars. Whereas there are much less serrations on the flow stress of FS ZnO pillars, and intergranular cracks emerged when $\epsilon = 5\%$. Crack density increased rapidly when $\epsilon = 5\%$ 193

Figure 8.6. SEM micrographs of the CS ZnO micropillars before and after compression tests at room temperature to 600°C. (a) SEM image shows pillar morphology after compression at room temperature. No high density of crack was observed. (b) After compression at 200°C, both intergranular crack and shear-offset formation were observed. (c) The pillar tested at 400°C shows intergranular fracture near top and severe dilation of the pillar at bottom. (d) After 600°C test, intergranular fracture near top was observed..... 194

Figure 8.7. Microstructure of the FS ZnO micropillar compressed at room temperature (to a strain of 14%). (a) Bright-field (BF) TEM image shows the upper half of the pillar exhibits a high density of defects and transgranular cracks. The lower half of the pillar remains relatively intact. (b) Dark-field (DF) TEM image of a grain in the upper region of the pillar shows a high density of dislocations near a grain boundary. (c) High resolution TEM micrograph along the [1213] zone axis shows the low angle grain boundary (9°) with a high density of dislocations. (d) Processed high resolution TEM image shows the existence of abundant dislocations along (1010) planes near the grain boundary. (e) Inverse pole figure of the fractured pillar confirms the transgranular cracking and polycrystalline grains. (f) Kernel average misorientation (KAM) map shows high degree of misorientation within grains near the fracture surface. (g) GND map shows the average GND density of $1.97 \times 10^{12} m^{-2}$ after the compression test. A high density of GNDs is observed near the fracture surface, crack tips, and grain boundaries..... 195

Figure 8.8. TEM post-analyses of the CS ZnO micropillar compressed at room temperature. (a) BF TEM micrograph shows an obvious transgranular crack. (b) A grain near the pillar top has a high density of defects. (c) Weak-beam DF TEM image reveals that the high-density dislocations. (d) DF TEM image also shows dislocations near a grain boundary. (e-f) High resolution and processed TEM micrographs confirm the presence of dislocations. (g-h) Inverse pole figure and GND map of CS ZnO micropillar showing high density of GND near a crack-tip. Average GND density is determined to be $1.24 \times 10^{12} m^{-2}$ 196

Figure 8.9. TEM analyses of the FS ZnO micropillar compressed at 400°C. (a) BF TEM image shows prominent dilation of the upper half of the tested pillar. Local grain separations are indicated by green arrows. (b) DF TEM image of a grain in the upper deformed region shows a high density of dislocations. (c-d) High resolution and FFT processed TEM micrographs along the [0001] zone axis show high-density dislocations. (e) Inverse pole figure of the compressed pillar shows insignificant changes in the grain shape after the compression test. (f) KAM map shows a high degree of misorientation within grains in the upper half of the deformed pillar. (g) The average GND density of the pillar is $1.65 \times 10^{12} m^{-2}$ when tested at 400°C. 197

Figure 8.10. Microstructure of the FS ZnO micropillar deformed at 600°C. (a) TEM micrograph shows obvious dilation of the pillar top. No significant grain separation was observed. (b-d) TEM micrographs near the pillar top show dislocation networks, dislocation arrays, and stacking faults. (e) Inverse pole figure reveals elongated grains (indicated by green arrows) at the upper half of the pillar. (f) KAM map shows misorientation within the grains localized near the pillar top. (g) Average GND density of the deformed pillar is $1.16 \times 10^{12} m^{-2}$, comparable to that of as-sintered ZnO. 198

Figure 8.11. TEM post-analyses of the CS ZnO micropillar compressed at 600°C. (a) BF TEM micrograph of the tested pillar shows the overall pillar morphology and obvious dilation at the pillar top. (b-d) A high density of dislocations was observed by BF TEM and STEM micrographs near a top portion of the compressed pillar. (e-f) Inverse pole figure and GND map of the CS micropillar showing the presence of nanograins near pillar top. Average GND density is calculated to be $1.08 \times 10^{12} m^{-2}$ 199

Figure 8.12. Variations of critical strain, GND density, and flow stress with test temperatures. (a) The critical strain to detect cracks (blue triangle) and GND density (red square) decrease as test temperature increases. (b) Flow stress (at a strain of 8%) for the flash-sintered and conventional ZnO decreases with increasing test temperature. After 200°C, strength reduction is insignificant for both types of ZnO specimens. 199

ABSTRACT

Zirconium oxide (zirconia, ZrO_2) is one of the essential structural ceramics for industrial applications due to its superb strength and fracture toughness. ZrO_2 has three main polymorphs: cubic, tetragonal, and monoclinic phase, depending on temperature, type, and concentration of dopants. Stabilized zirconia with metastable tetragonal phase can transform into monoclinic phase with $\sim 4\%$ volume expansion under an applied external stress. The tetragonal-to-monoclinic transformation can hinder crack propagations by generating a compressive stress field near crack field, thereby enhancing fracture toughness. In addition, other deformation mechanisms such as dislocation activities, crack deflection, and ferroelastic domain switching can further enhance its deformability. Bulk ZrO_2 is typically prepared by sintering at high temperatures over a long period of time. Recently, field-assisted sintering techniques such as flash sintering and spark plasma sintering have been applied to effectively sinter ZrO_2 . These techniques can significantly decrease sintering temperature and time, and more importantly introduce a large number of defects in the sintered fine grains.

The miniaturization of sample dimension can alter the mechanical properties of materials by increasing the surface-to-volume ratio and decreasing the likelihood of retaining process-induced flaws. The knowledge of mechanical properties of ZrO_2 at micro and nanoscale is critical in that superelasticity and shape memory effect of ZrO_2 can be utilized for applications of actuation, energy-damping, and energy-harvesting at small scale. Here, we performed *in-situ* microcompression tests at various temperatures inside a scanning electron microscope to examine and compare the mechanical properties of ZrO_2 prepared by flash sintering, spark plasma sintering, plasma spray, and thermal spray. Detailed microstructural analyses were conducted by transmission electron microscopy. The unique microstructures in ZrO_2 prepared by field-assisted sintering largely improved their plasticity. Temperature and processing technique-dependent underlying deformation mechanisms and fracture behavior of ZrO_2 are discussed.

CHAPTER 1. INTRODUCTION

Zirconium oxide (zirconia, ZrO_2) is one of the widely used structural ceramics for industrial applications. There are many techniques to consolidate ZrO_2 powder, including conventional firing, spark plasma sintering, flash sintering, hot pressing, air plasma spray, e-beam physical vapor deposition, and thermal spray. This thesis discusses the effects of some of these processing techniques (with the focus on flash sintering and spark plasma sintering) on the mechanical response of ZrO_2 , especially at the micrometric scale. This chapter provides a background review on the microstructure and meso-scale and micro-scale mechanical properties of ZrO_2 prepared by various techniques.

1.1. Polymorphism of ZrO_2

ZrO_2 is a white crystalline oxide material that has three main polymorphs depending on temperatures at ambient pressure: cubic, tetragonal, and monoclinic ZrO_2 . Cubic ZrO_2 is the high-temperature phase, existing beyond 2370°C , and has the fluorite structure ($Fm\bar{3}m$) with a lattice parameter of 5.139 \AA , as shown in Fig. 1.1a [1]. Tetragonal ZrO_2 ($P4_2/nmc$, Fig. 1.1b) is present at intermediate temperatures ($1200^\circ\text{C} - 2370^\circ\text{C}$) and has a lattice parameter of 3.601 \AA for a constant and 5.179 \AA for c constant. The low-temperature phase, monoclinic ZrO_2 ($P2_1/c$, $< 950^\circ\text{C}$, Fig. 1.1c) has a lattice constant of $5.313 \times 5.213 \times 5.147 \text{ \AA}$ and $\beta = 99.2^\circ$. Although ZrO_2 has compelling mechanical, chemical, physical, and thermal properties, it was of less industrial importance primarily due to phase transformation from tetragonal to monoclinic ZrO_2 at $\sim 950^\circ\text{C}$ upon cooling. [1]. A volume expansion of $\sim 4.5\%$ occurs during the phase transformation and the large volume change in ZrO_2 can cause a catastrophic failure in its service. However, in 1975, it was found that the phase transformation can be hindered by adding lower valence oxides such as Y_2O_3 , MgO , CaO , and CeO_2 in ZrO_2 matrix [2–4]. Consequently, the metastable tetragonal and cubic ZrO_2 , namely stabilized zirconia, is obtained at room temperature. Stabilized tetragonal and cubic ZrO_2 have the same structure as that in pure ZrO_2 , but they contain dopant cations and oxygen vacancies to keep the charge balance [5]. The presence of oxygen vacancies plays a pivotal role in stabilizing metastable phases at room temperature by allowing the relaxation of the cations and anions to occur [6]. Depending on the concentration and type of dopants, distinct phases of

ZrO₂ can be produced: partially stabilized-zirconia (PSZ, tetragonal ZrO₂ precipitates in cubic ZrO₂ matrix), tetragonal zirconia polycrystal (TZP), and cubic zirconia [7].

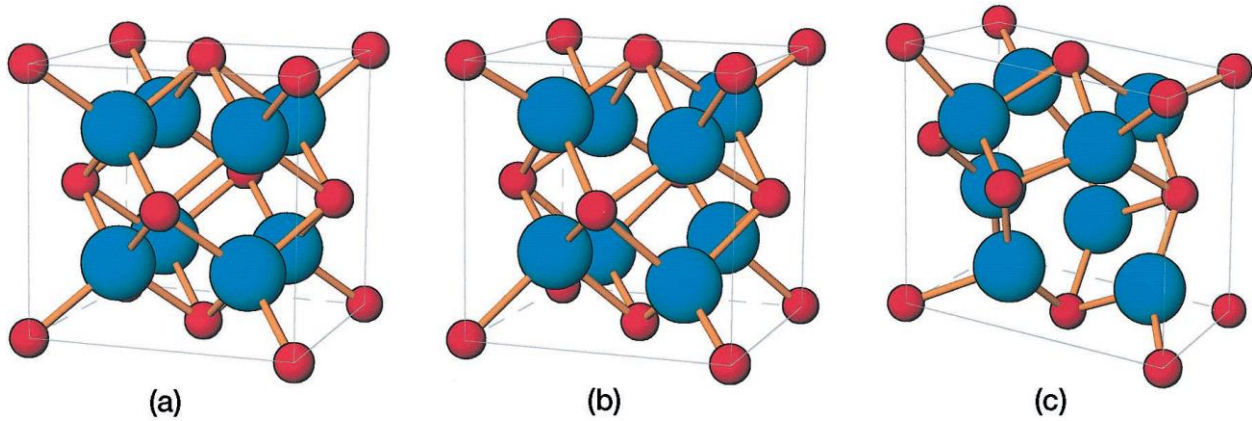


Figure 1.1. Schematic representation of (a) cubic, (b) tetragonal, and (c) monoclinic ZrO₂ [1].

1.2. Martensitic transformation

Although most of ceramics feature high strength and extremely low deformability [8], tetragonal ZrO₂ shows both great strength and fracture toughness owing to martensitic transformation occurring near a crack tip where stress is concentrated [9–11]. The martensitic transformation in the ZrO₂ system refers to the phase transformation of tetragonal ZrO₂ (austenite) to monoclinic ZrO₂ (martensite), which is induced either by mechanical stress or heating and accompanies 4.5% volume expansion [11]. When the phase transformation is mechanically induced, the consequent volume expansion can generate a compressive strain field that can retard crack propagation, thereby enhancing the fracture toughness. Therefore, stabilized ZrO₂ with the superb mechanical properties has been used for various applications such as engineering components, medical devices, oxygen sensors, shape memory devices, thermal barrier coatings, and fuel cells [12–14].

The martensitic transformation features a diffusion-less lattice shift. The shift occurs within a temperature range starting from martensite start temperature (M_s) to martensite finish temperature (M_f) rather than occurring at a specific temperature [11]. Fig. 1.2 demonstrates a possible failure scenario for yttria stabilized zirconia (YSZ) during a thermal cycling owing to a series of phase transformations [15]. During the sintering of YSZ at high temperatures, a stable cubic phase (C) is formed (Fig. 1.2a). Thermally stable tetragonal ZrO₂ (T⁺ in Fig. 1.2) can be

introduced by the cooling process (Fig. 1.2b). As temperature rises, the thermodynamic stability of T^* decreases, and it decomposes into unstable tetragonal (T) and C (Fig. 1.2c and 1.2d). As Y segregates along grain boundaries, lattices near grain boundaries have high enough concentration of Y to stabilize C phase, while Y-deficient lattices becomes T with a high tetragonality [16]. As a result, T loses its stability at room temperature. Finally, thermally induced monoclinic phase (M) accompanying large volume expansion forms from T upon cooling and causes material degradation, such as crack formation and delamination (Fig. 1.2e).

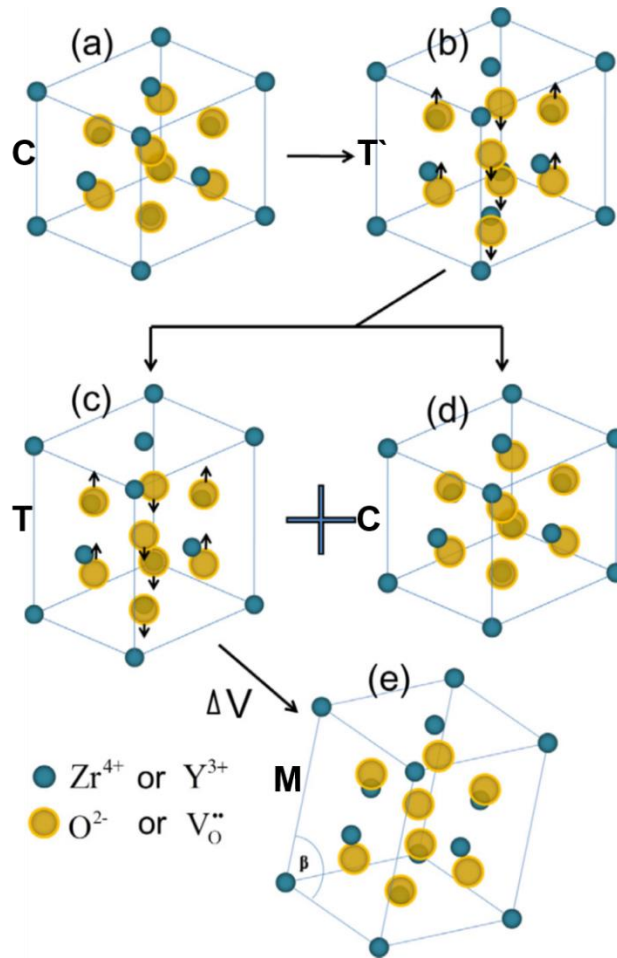


Figure 1.2. An example of phase transformation of ZrO_2 caused by a thermal cyclic. (a-b) Cubic phase (C) transforms into a thermally stable tetragonal phase (T^*) at room temperature on cooling. (c-e) Thermally unstable T and C form on heating of T^* phase due to Y segregation along grain boundaries [15].

Activation of martensitic transformation is known to be strongly dependent on temperature and grain size [17]. Tetragonal ZrO_2 should be stable enough to retain its phase at room

temperature, but, reversely, it should easily transform into monoclinic ZrO₂ under a mechanical loading. Therefore, the retention of the optimal grain size in consideration of environmental temperature plays a key role in enhancing the mechanical properties of ZrO₂.

1.2.1. Effect of temperature on martensitic transformation

The temperature dependence of the martensitic transformation can be thermodynamically described [17,18]. The total Gibbs free energy change for martensitic transformation per unit volume (ΔF_0) can be expressed as [17],

$$\Delta F_0 = \Delta F_{CH} + \Delta U_e + \Delta U_s - \Delta U_I \quad (1.1)$$

where ΔF_{CH} is the chemical-free energy change, ΔU_e the strain energy change, ΔU_s the surface energy change, and ΔU_I the change in free energy associated with an applied stress. This mechanical term should be larger than the first three terms on the right-hand side of Eq. 1.1 for the martensitic transformation to occur. The chemical-free energy term is written as [17],

$$\Delta F_{CH} = \Delta S_m(T_o - T) \quad (1.2)$$

where ΔS_m is entropy change associated with martensitic transformation and T_o is the temperature at which tetragonal phase without matrix constraint transforms into monoclinic ZrO₂. ΔU_s is assumed to be negligible. ΔU_e is associated with volume expansion of embedded particles against matrix constraint. M_s is lower than T_o due to the presence of dopants in the matrix, and thus an additional free energy change ($\Delta S_m(M_s - T_o)$) is given and should be overcome for the tetragonal phase to transform into monoclinic ZrO₂ (Fig. 1.3). The total free energy change in the presence of dopants is expressed as [17],

$$\Delta F_0 = \Delta S_m(M_s - T) - \Delta U_I. \quad (1.3)$$

The mechanical energy change can be rewritten as,

$$\Delta U_I = \sigma_a \epsilon^T \quad (1.4)$$

where σ_a is the applied stress and ϵ^T is the transformation strain. The critical stress (σ_c^T) above which martensitic transformation occurs can be expressed as [17],

$$\sigma_a = \sigma_c^T = \frac{\Delta S_m(M_s - T)}{\epsilon^T}. \quad (1.5)$$

When $T = M_s$, spontaneous martensitic transformation starts without external stress ($\sigma_c^T = 0$). As T increases, Eq. (1.3) shows that the chemical energy change also increases (note that $\Delta S_m < 0$), thereby requiring a more substantial external stress to overcome the free energy barrier for the

martensitic transformation to occur. Also, the critical stress increases with the decrease in M_s at a given temperature.

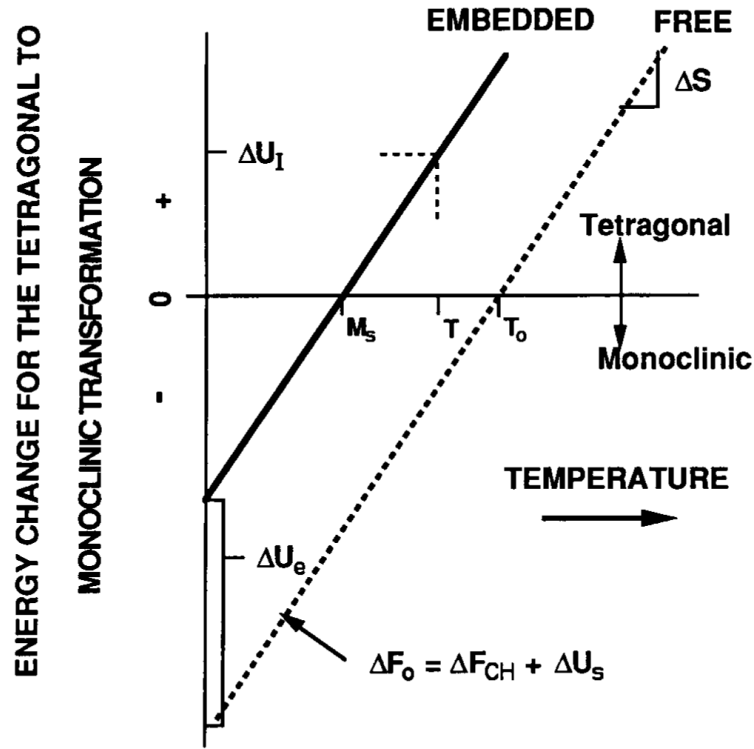


Figure 1.3. Free energy change required for martensitic transformation to occur as a function of temperature. Embedded dopant plays a role in increasing the free energy barrier as much as the strain energy change. As such, lower temperatures than M_s are required to obtain monoclinic ZrO_2 [17].

1.2.2. Effect of grain size on martensitic transformation

For the martensitic transformation to occur at a lower stress, (a) a test temperature needs to decrease to M_s or (b) M_s should increase to a test temperature. The factors affecting M_s are the degree of tetragonality and grain size [17,19,20]. The martensitic transformation of ZrO_2 with a higher tetragonality can occur at lower mechanical loading due to the increase in M_s [19]. The degree of tetragonality is affected by the type and concentration of dopant. It was reported that TiO_2 provides the highest tetragonality followed by CeO_2 and Y_2O_3 [7]. If the dopant type is the same, a lower concentration provides the higher tetragonality [7,19]. The role of grain size is directly associated with an internal residual stress. As temperature decreases during the cooling

process, a local mismatch stress concentrated at grain corners and grain boundaries forms due to an anisotropy in crystallographic thermal expansion coefficients ($\alpha_a \neq \alpha_c$) along with lattice misorientation [17]. It is known that the internal residual stress (σ_i) increases with the increase in the grain size (d) and the decrease in the distance from the grain corner (r) [17]:

$$\sigma_i = \sigma_{TEA} \frac{d}{r} \quad (1.6)$$

where σ_{TEA} is the local mismatch stress at the grain corners and proportional to $\Delta\alpha\Delta T$. Based on the Eqs. (1.5) and (1.6), the applied stress for the martensitic transformation to occur in the presence of the internal residual stress can be expressed as,

$$\sigma_a = \sigma_c^T - \sigma_i = \frac{\Delta S_m(M_s - T)}{\epsilon^T}. \quad (1.7)$$

The critical stress without the internal residual stress is given by,

$$\sigma_c^T = \frac{\Delta S_m(M_s^o - T)}{\epsilon^T} \quad (1.8)$$

where M_s^o is martensitic start temperature without internal residual stress. Substituting Eq. (1.7) with (1.6) and (1.8) yields,

$$M_s = M_s^o - \frac{\sigma_{TEA}\epsilon^T}{\Delta S_m r_{crt}} d \quad (1.9)$$

where r_{crt} is the critical radius for the nucleation of monoclinic phase. The linear grain size dependence of M_s can be appreciated in Eq. (1.9). M_s increases with the increase in the grain size given that ΔS_m is a negative value. The increase in M_s allows the martensitic transformation to start at a lower applied stress, as shown in Eq. (1.5). The grain size dependence of M_s and the martensitic transformation was also shown experimentally (Fig. 1.4). Different grain size of tetragonal ZrO₂ doped by 12 mol% CeO₂ was prepared, and martensitic start temperature was measured by a dual rod dilatometer [17]. Fig. 1.4a shows the good agreement between the calculated M_s and the experimentally measured M_s . Fig. 1.4 exhibits the experimental evidence for the effect of grain size on M_s by showing transformation zone. It shows that the larger grain size triggers more martensitic transformation attributed to the decreasing M_s .

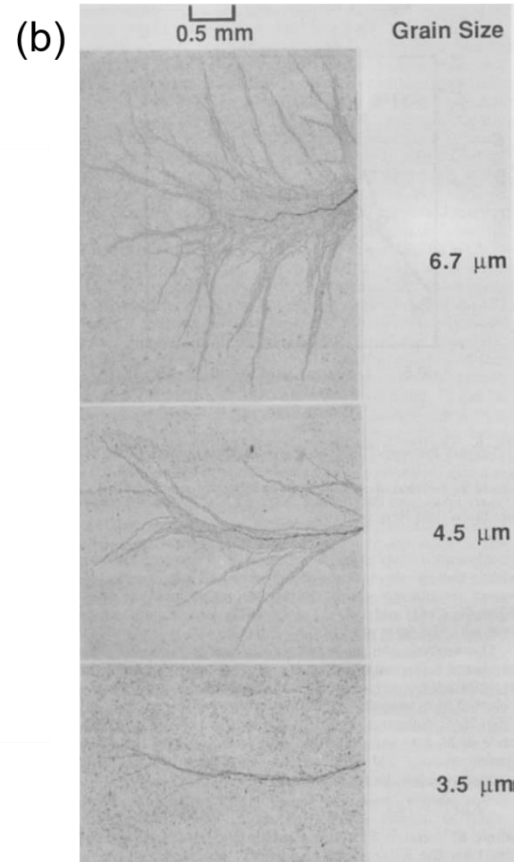
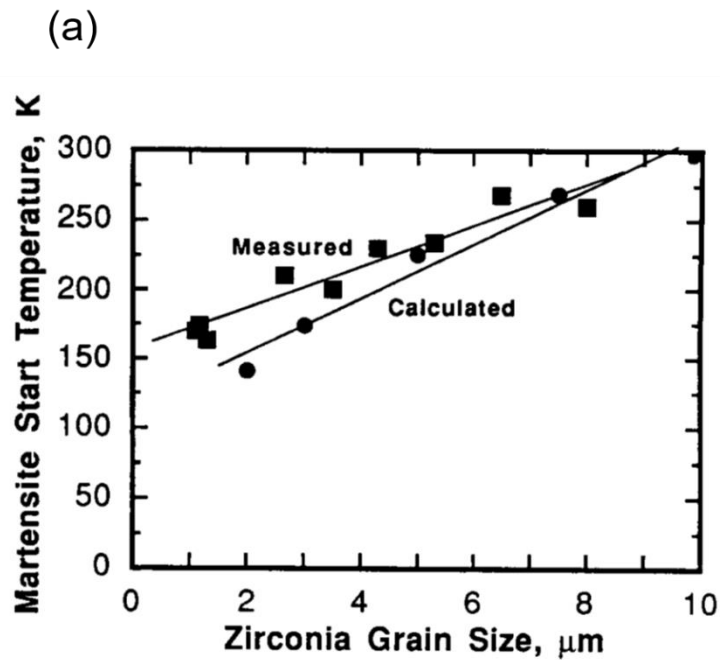


Figure 1.4. (a) Measured and calculated M_s of 12 mol% CeO_2 -doped ZrO_2 as a function of grain size. (b) The presence of the martensitic transformation zone near a crack tip. The bigger grain size exhibits the larger transformation zone [17].

1.3. Several types of transformation-toughened ZrO_2 -bearing ceramics

Several types of ceramics containing tetragonal ZrO_2 can be synthesized to enhance the fracture behavior. For example, tetragonal ZrO_2 precipitates are embedded in cubic ZrO_2 by doping MgO as shown in transmission electron microscopy (TEM) image (Fig. 1.5a), and this type of ceramic is called as magnesia-partially stabilized zirconia (Mg-PSZ). Fig. 1.5b shows a scanning electron microscopy (SEM) image of a single phase of tetragonal ZrO_2 , also known as tetragonal zirconia polycrystal (TZP). A composite of tetragonal ZrO_2 and Al_2O_3 named zirconia toughened alumina (ZTA) is one of commonly used transformation-toughened ceramics and the typical microstructure of ZTA is shown in Fig. 1.5c. This subsection describes the microstructural characteristics of Mg-PSZ, TZP, and ZTA.

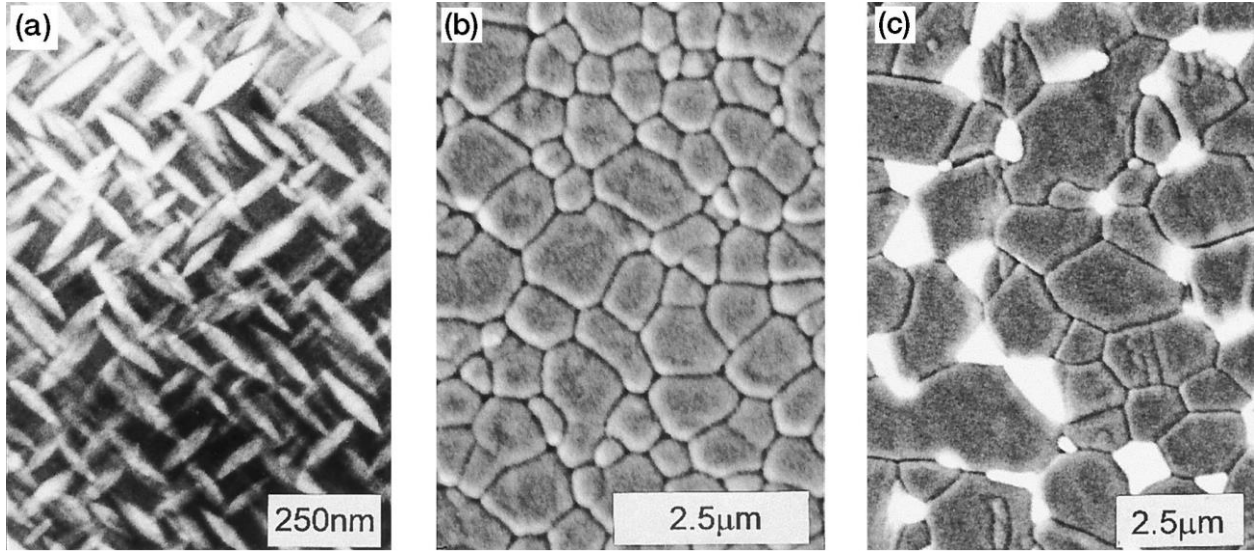
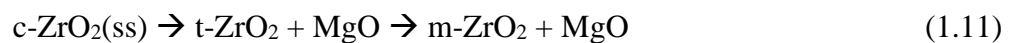


Figure 1.5. (a) Bright-field TEM micrograph of PSZ showing lenticular-shaped tetragonal precipitates in cubic matrix. (b) SEM image of TZP, and (c) ZTA [1].

1.3.1. Magnesia-partially stabilized zirconia

MgO is one of the most interesting dopants in that it can provide complicated microstructures and intriguing mechanical properties, dependent on its thermal treatment and MgO concentration [1]. 9 ~ 10 mol % MgO with balanced ZrO₂ is the most commonly used composition for industrial applications to obtain Mg-PSZ, highlighted in the MgO-ZrO₂ phase diagram (Fig. 1.6). Mg-PSZ has a lenticular shape of dispersed tetragonal ZrO₂ precipitates in a cubic phase matrix. This unique combination can provide both high strength and fracture toughness that result from the cubic matrix and tetragonal precipitates, respectively [1]. A cubic solid solution of the MgO-ZrO₂ compound can be acquired at a sintering temperature of $\geq 1700^{\circ}\text{C}$, as shown in the phase diagram. The nanosized tetragonal ZrO₂ precipitates in the cubic solid solution can form upon the subsequent furnace cooling. Since martensitic start temperature is much below room temperature when tetragonal ZrO₂ precipitates are in nanoscale, further heat-treatments are required to increase the size and density of tetragonal ZrO₂ precipitates to the point that the martensitic transformation can occur under a low external stress. There exist two possible aging methods: eutectoid aging (1240°C - 1400°C) through the reaction in Eq. 1.10 or subeutectoid aging (<1240°C) through the reaction in Eq. 1.11 [21];



where c-ZrO₂(ss), t-ZrO₂, and m-ZrO₂ are cubic solid solution, tetragonal, and monoclinic zirconia, respectively. The eutectoid aging of the cubic solid solution can provide diffusion-controlled tetragonal ZrO₂ nucleation and coarsening, but this process has a sluggish nature [22]. On the other hand, the subeutectoid aging can produce tetragonal precipitates more rapidly due to a higher degree of undercooling. The process results in the formation of unfavorable monoclinic ZrO₂ at the expense of t-ZrO₂. However, it produces one of the toughest ceramics owing to the presence of δ phase (Mg₂Zr₅O₁₂), which can grow at a tetragonal ZrO₂ interface. δ phase can build considerable strain on tetragonal ZrO₂ which facilitates the transformation to monoclinic ZrO₂, thereby retarding crack propagation.

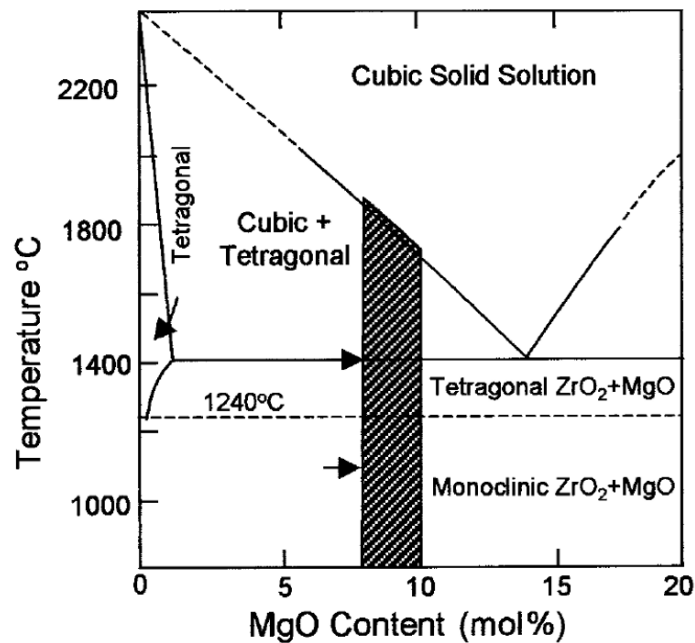


Figure 1.6. A phase diagram of the MgO-ZrO₂ system. The highlighted region is the commonly used composition for industrial applications [1].

1.3.2. Yttria-tetragonal zirconia polycrystal

TZP has a single-phase tetragonal ZrO₂ stabilized by dopants like Y₂O₃ or CeO₂. Y₂O₃ is known as the most attractive dopant in that ~ 3 mol % Y (equivalent to 1.5 mol % Y₂O₃) is enough to fully stabilize the tetragonal phase at room temperature, as shown in a phase diagram of the Y₂O₃-ZrO₂ system (Fig. 1.7) [1,23]. Hence, extensive research has been currently dedicated to YSZ, also known as Y-TZP. When prepared by conventional firing, the grain size of 3 mol %

yttria doped zirconia (3YSZ) ranges 0.5 ~ 2 μm in general. The grain coarsening of 3YSZ is limited due to the chemical segregation of Y along grain boundaries, and thus inhibits grain boundary migration (solute-drag effect). 3YSZ retains a matrix with a single phase tetragonal ZrO_2 whose tetragonality is high enough to allow transformation-toughening to occur under a mechanical loading. The tetragonality that directly impacts the fracture toughness of YSZ is an adjustable factor through altering dopant concentration and grain size. Hence, several attempts have been made to tailor the chemistry of Y concentration in ZrO_2 matrix for better fracture behavior. A fracture toughness of $\sim 17 \text{ MPa}\cdot\sqrt{\text{m}}$ was achieved by decreasing Y_2O_3 concentration to 1 mol % in nanocrystalline YSZ ($\sim 90 \text{ nm}$) [20]. Grain refinement is necessary here to maintain the tetragonal phase because it reduces internal stress in grains that would otherwise trigger the spontaneous transformation at room temperature. A small amount of the stabilizer, together with grain refinement, can maximize tetragonality to the point just before spontaneous phase transformation, such that a low stress can activate the transformation toughening. Furthermore, the grain refinement can provide additional advantages such as higher strength and more crack deflection. Another way to enhance the fracture behavior of YSZ is to add a different type of dopant in the YSZ matrix. For example, the addition of Ta_2O_5 as a dopant in YSZ can distort tetragonal lattice, thereby enhancing the transformability of YSZ [19,24]. Since YSZ with transformable tetragonal ZrO_2 has a superior fracture toughness owing to the martensitic transformation, it can be used for structural applications such as industrial components and dental blocks.

Meanwhile, it is also possible to stabilize ZrO_2 in the form of PSZ using Y_2O_3 , as shown in the highlighted region of the phase diagram (Fig. 1.7). Y_2O_3 -stabilized PSZ is often referred to as Y-PSZ. Despite thermodynamically feasible, Y_2O_3 is often not preferred as a stabilizer to fabricate PSZ due to the requirement of ultra-high temperatures ($\sim 2000^\circ\text{C}$) to form the cubic solid solution, higher than the temperature required for Mg-PSZ to form the cubic solid solution ($\sim 1700^\circ\text{C}$). Secondly, the aging treatment of the cubic solid solution to grow tetragonal ZrO_2 precipitates is performed at $1300\text{-}1400^\circ\text{C}$ and it has the kinetically sluggish nature [1]. Therefore, it is more favored to use Y_2O_3 as a stabilizer for Y-TZP rather than for Y-PSZ.

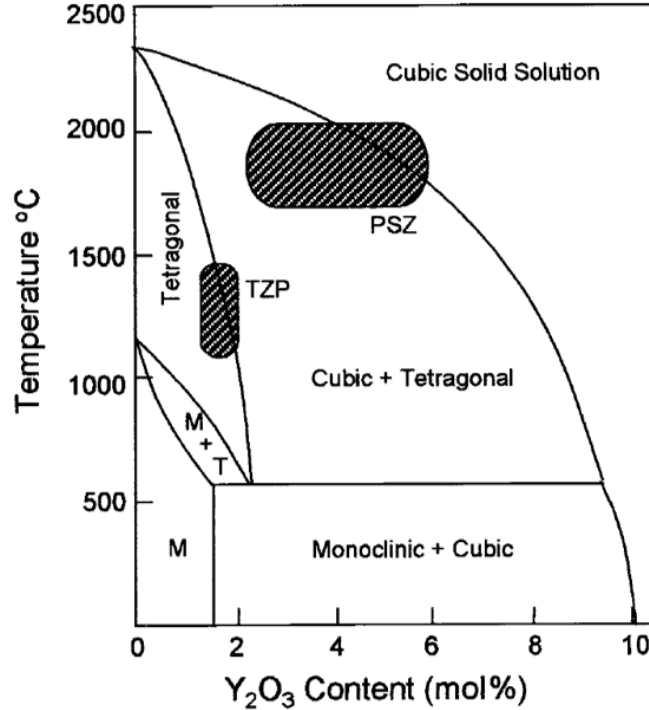


Figure 1.7. A phase diagram of the Y₂O₃-ZrO₂ system [1].

In the Y-TZP system, as the concentration of Y₂O₃ increases to ~ 4.5 mol% (~7 wt %), the matrix is still tetragonal ZrO₂, but its tetragonality decreases to the point where no more stress-induced transformation occurs. This type of tetragonal ZrO₂ is called as the metastable tetragonal prime phase (*t'*). Despite the absence of transformation toughening, the *t'* phase still exhibits a fairly good fracture behavior. For example, 7-8 wt % Y₂O₃ stabilized zirconia (7YSZ) exhibits a fracture toughness of ~ 3 MPa·√m, more than twice the toughness of a single-phase cubic ZrO₂ (~ 1.2 MPa·√m) [25]. This can be attributed to the ability of the *t'* structure to ferroelastically toughen the material [26–29]. The improvement of fracture toughness of 7YSZ can also be achieved by adding an additional dopant to the YSZ matrix. For example, the addition of TiO₂ in the 7YSZ matrix can enhance the fracture toughness by two folds as the increased tetragonality of *t'* provides more efficient ferroelastic toughening [26,30]. The presence of the *t'* phase in 7YSZ maintains its high-temperature stability by suppressing the equilibrium tetragonal-to-monoclinic phase transformation under the harsh environment (high temperature and pressure) due to the low tetragonality, and yet it exhibits relatively good fracture behavior. The aforementioned properties allow 7YSZ to be an excellent candidate for thermal barrier coating (TBC) applications that require high thermal stability and superb resistance to foreign object damage. Besides, YSZ has a low

thermal conductivity and a high coefficient of thermal expansion (CTE) that matches well with a metallic substrate [12,31–34].

1.3.3. Zirconia toughened alumina

ZTA usually consists of 10-80 wt % Al_2O_3 with the balanced ZrO_2 . The brittle nature of Al_2O_3 can be mitigated by the presence of ZrO_2 in the matrix, and thus ZTA can retain the high strength together with high fracture toughness comparable to that of Mg-PSZ and TZP. In general, the phase of ZrO_2 in ZTA can be either monoclinic or tetragonal ZrO_2 . In the case of monoclinic ZrO_2 in the ZTA system, the high fracture toughness can be obtained by microcrack toughening. When Y_2O_3 or CeO_2 stabilizes ZrO_2 in ZTA, high toughness can be achieved by the transformation toughening. Tsukuma *et al.* fabricated $\text{Al}_2\text{O}_3/\text{Y-TZP}$ (3 mol%) composite with a volume ratio of 7:3 using hot isostatic pressing [35]. The composite showed a bending strength of 1.6 GPa and fracture toughness of $\sim 6.5 \text{ MPa} \cdot \sqrt{m}$. They also prepared $\text{Al}_2\text{O}_3/\text{Ce-TZP}$ (12 mol%) composite with a volume ratio of 7:3 by means of conventional firing and observed the bending strength of 850 MPa and toughness of $8.5 \text{ MPa} \cdot \sqrt{m}$, comparable to those of a single-phase TZP. Thanks to high strength and fracture toughness that are usually mutually exclusive, ZTA has been utilized for cutting tools, grinding media, and dental applications.

1.4. Mechanical behavior of stabilized ZrO_2 at mesoscale

1.4.1. Magnesia-partially stabilized zirconia at mesoscale

Mg-PSZ is one of the toughest ceramics known to the society. The inelastic behavior of Mg-PSZ results from many factors that include transformation toughening, ferroelastic domain switching, crack deflection, crack bowing, and microcrack toughening. For example, subeutectoid-aged Mg-PSZ can exhibit a fracture toughness as high as $14 \text{ MPa} \cdot \sqrt{m}$ with a flexural strength of 800 MPa owing to the transformation toughening [36]. Swain measured flexural strength and fracture toughness using a four-point bending test and Vickers indentation test, respectively [36]. As-fired Mg-PSZ (9.4 mol%) with nanoscale tetragonal precipitates was aged at 1100°C for various times, such that the effect of aging times on thermomechanical properties of Mg-PSZ can be resolved. Fig. 1.8a shows the four-point bending tests on the as-fired Mg-PSZ, and the subeutectoid-aged Mg-PSZ at 1100°C for 16 and 40 hrs. The as-fired and 16 hr-aged Mg-PSZ

show linear elastic behavior and fractured at 500 and 600 MPa, respectively. The stress-strain curve for the 40 hr-aged specimen starts to detach at a strain of $\sim 0.18\%$ from the other two curves, indicating the occurrence of the inelastic deformation. Fig. 1.8b shows the flexural strength and fracture toughness as a function of monoclinic content on the polished surface of the specimens (polished surface monoclinic, PSM). The flexural strength reaches a maximum of 800 MPa at $\sim 12\%$ PSM and gradually decreases after that. The maximum fracture toughness of Mg-PSZ ($\sim 14 \text{ MPa} \cdot \sqrt{m}$) can be obtained at $\sim 20\%$ PSM, and it declines rapidly after that due to the lack of tetragonal precipitates. Fig. 1.9 shows 30 kg Vickers indentation marks on the 2 hr-aged, 16 hr-aged, and 40 hr-aged Mg-PSZ. As aging time increases, the surrounding deformation in the vicinity to the indent mark becomes more prominent. A high density of cracks propagating from the indent edge can be observed from the 2 hr-aged Mg-PSZ. On the other hand, a high degree of surface rumpling near the indent mark of the 16 and 40 hr-aged Mg-PSZ is observed, which results from the volume expansion induced by the tetragonal-to-monoclinic phase transformation. However, the microstructure difference among those specimens does not significantly affect the Vickers hardness ($\sim 10 \text{ GPa}$).

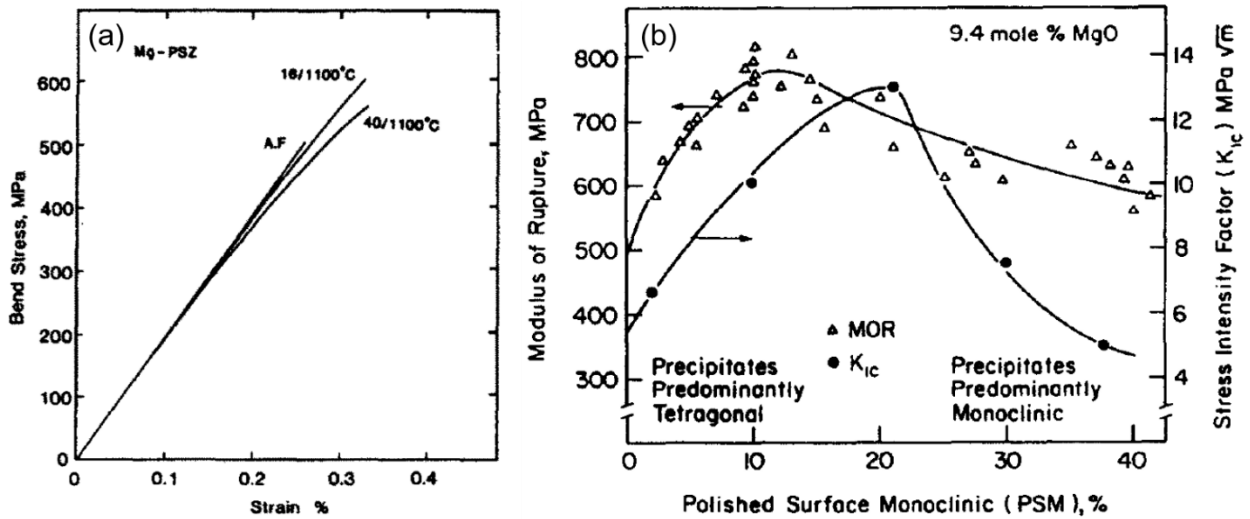


Figure 1.8. (a) Flexural strength of Mg-PSZ aged at 1100°C for 16 and 40 hrs. (b) Flexural strength and fracture toughness of Mg-PSZ as a function of monoclinic content on polished surface [36].

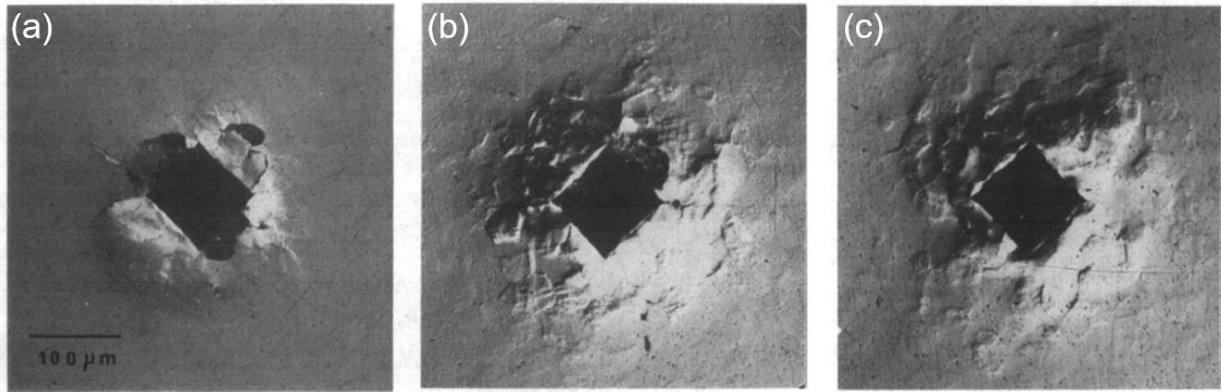


Figure 1.9. An indent mark and microstructure change in the surrounding region on Mg-PSZ aged for different time: (a) 2h, (b) 16 h, (c) 40 h [36].

Lankford carried out compression tests on Mg-PSZ with a fracture toughness of $8.5 \text{ MPa} \cdot \sqrt{m}$, a flexural strength of 600 MPa, and a Vickers hardness of 10.2 GPa [37]. The strain rate used in this test was 10^{-4} s^{-1} , and acoustic emission (AE) was utilized to resolve the compressive damage threshold. Fig. 1.10 shows a typical compression test on Mg-PSZ with a yield strength of 1190 MPa and an ultimate compressive strength of 1860 MPa. Acoustic emission occurs at the onset of microfracture at a strain of $\sim 2\%$. After yielded at $\sim 0.6\%$ strain, the plastic deformation region in the stress-strain curve is highlighted by a high degree of serration and high capability of work-hardening. Based on the assumption that the matrix phase of cubic ZrO_2 does not plastically flow, such a high inelastic behavior can be explained by the phase transformation of tetragonal precipitates. Lankford attributed the existence of the high toughness and serrated behavior of Mg-PSZ to the competition between the stress-induced and strain-induced phase transformation [37]. The stress-induced transformation can be triggered by elastic stress below the yield strength of the parent phase, whereas strain-induced transformation can occur when the parent phase undergoes slip after yield [38]. When Mg-PSZ retains the high tetragonality that results in the phase transformation under a low-stress level (or test temperature is slightly higher than M_s), stress-induced transformation can be dominant. When tetragonal ZrO_2 becomes over-stabilized due to the increase in temperature, strain-induced transformation can be favored. The serrated behavior in Fig. 1.10, thus, may be a consequence of competition between the two types of plasticity. Compression tests with a high strain rate (0.8 s^{-1}) can strengthen this assertion by showing higher yield strength (1619 MPa) and ultimate compressive strength (2073 MPa) [37]. Yield strength remains the same when stress-induced transformation solely contributed to the plasticity, whereas

strain-induced transformation is dependent on strain rate because the change in the parent phase in strain rate influences the thermally activated slip system.

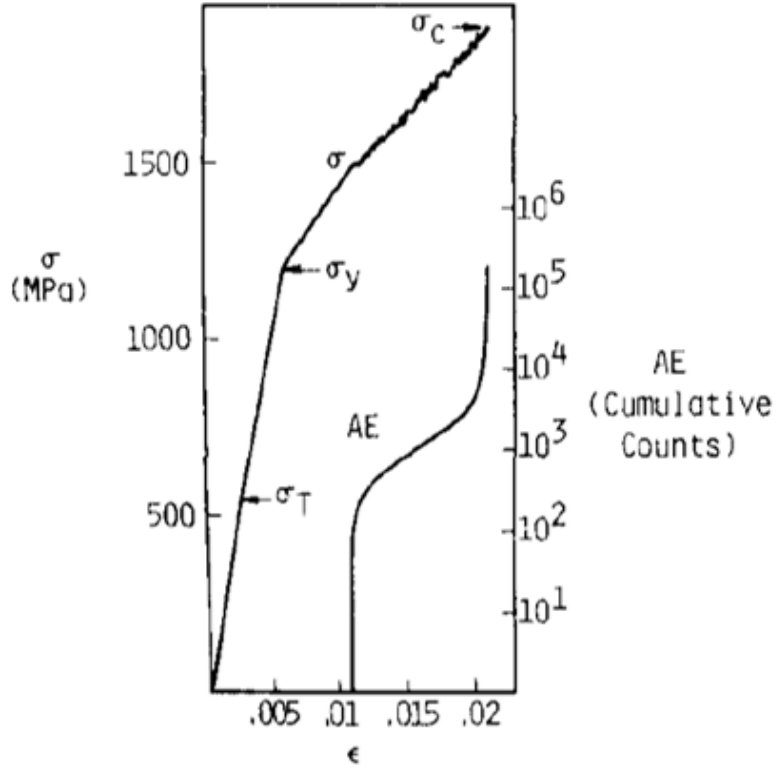


Figure 1.10. A stress-strain curve for the compression test on Mg-PSZ and acoustic emission counts as a function of strain [37].

1.4.2. Mesoscale mechanical behavior of Y-TZP

The mechanical behavior of polycrystalline Y-TZP (or YSZ) has been extensively studied after the way to stabilize tetragonal ZrO_2 was discovered. Especially, Lankford *et al.* investigated the deformation mechanism of polycrystalline YSZ at temperatures ranging from room temperature to 800°C [39]. The increase in test temperature results in strength and toughness reduction for YSZ due to the stabilization of the tetragonal phase [15]. Polycrystalline 3YSZ cylindrical compression specimens with 9 mm long and 4.5 mm diameter were prepared, and compression tests were carried out at different temperatures (Fig. 1.11). The specimen tested at 23°C with a strain rate of $10^{-5} s^{-1}$ exhibits a failure stress of 3.5 GPa and a failure strain of 3%. The high failure strain results from the martensitic transformation, as evidenced by Fig. 1.11b, showing surface rumpling due to the volume expansion. It appears that transformation induced-plasticity begins from 2.6 GPa,

where the curve loses its linearity. It is worthwhile to mention that the critical stress at which martensitic transformation initiates for mesoscale YSZ (2.6 GPa) is quite higher than that for microscale YSZ (~ 1 GPa), which will be shown in Chapter 1.5. When the critical stress is high enough to bring about the failure, the competition between transformation induced plasticity and the formation of crack takes place, and YSZ exhibits the early fracture as compared to microscale YSZ ($\sim 8\%$ failure strain). As the test temperature rises to 800°C , the strength decreases, and the specimen fails at 1.2 GPa. On the other hand, the deformability of YSZ increases as temperature increases by the thermally activated inelastic mechanism. Figs. 1.11c and d show SEM micrographs of YSZ deformed at 800°C , describing the evidence of grain boundary sliding by intergranular crack and visible grain boundaries in the deformed area. In contrast, it is hard to observe grain boundaries in the undeformed area.

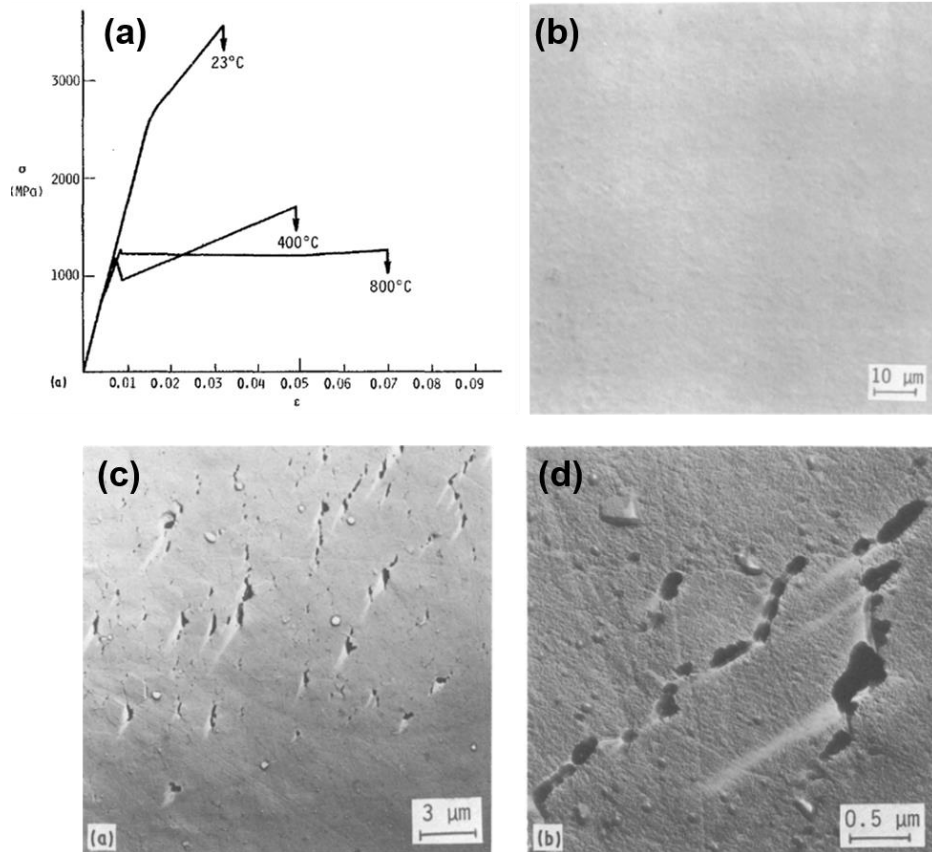


Figure 1.11. (a) Stress-strain behavior of YSZ tested at 23, 400, and 800°C with a strain rate of $1 \times 10^{-5} \text{ s}^{-1}$. (b) Differential interference contrast view after compression at 23°C with a strain rate of 10^{-5} s^{-1} , showing surface rumpling by the martensitic transformation. (c) SEM micrograph of YSZ deformed at 800°C with a strain rate of 10^{-5} s^{-1} , showing the evidence of grain boundary

sliding by intergranular crack and visible grain boundaries in the deformed area. (d) High-magnification SEM image showing cavitation along the grain boundaries [39].

1.5. Mechanical behavior of stabilized ZrO₂ at microscale

Currently, it is elucidated that miniaturization of stabilized ZrO₂ to the microscale permits the stress-induced transformation at a low external stress without fracture [14]. While stabilized ZrO₂ exhibits a failure strain of 3% at mesoscale, at microscale, stabilized ZrO₂ shows that of 8%. Also, superelasticity and shape memory effect are observed at microscale, attributed to the significantly enhanced effectiveness of the martensitic transformation and less population of intrinsic microcracks [40–47]. This discovery suggests a new paradigm for ceramic materials to be used in microelectromechanical and nanoelectromechanical systems [48].

Micropillar compression test is a unique technique to investigate the mechanical behavior of materials at a small scale, which ranges from micrometer to nanometer. Especially, when this technique applies to ceramic materials that are usually brittle in bulk size, the plastic flow of the brittle ceramic materials can be studied without applying a confining pressure via hydrostatic or gaseous medium [49]. The decrease in intrinsic defect population and strain gradients obtained by a miniaturization of specimen prevents brittle materials from premature failure, thereby permitting plastic flow [50]. Furthermore, the decrease in specimen size means the increase in surface area to volume ratio, leading that a relatively large ratio of free surface can relax the external stress [14].

1.5.1. The effect of the tetragonal phase in mechanical behavior

Camposilvan *et al.* compared the mechanical behavior between tetragonal YSZ and degraded YSZ to monoclinic phase at the microscale [51]. Monoclinic ZrO₂ was prepared by hydrothermal degradation in a pressure reactor. The transformation of the tetragonal-to-monoclinic phase occurred from the surface of the specimen and penetrated down to 13 μm (Fig. 1.12a). It turns out that the degraded (DEG) region consists of 85% monoclinic and 15% non-transformable cubic phase, which formed in the previous sintering process. The cross-sectional morphology of the DEG region is rough due to the monoclinic uplift and microcrack formed along the grain boundary. 0.3, 0.7, and 3.3 μm micropillars in the DEG region and as-sintered (AS) region were milled using a focused ion beam (FIB) to study the size effects. Figs. 1.12b and c show the metastable tetragonal and monoclinic dominant micropillars, respectively. Fig. 1.12d shows numerous stress-strain curves for the microcompression tests on DEG and AS specimens with different diameters. It is

observed that AS specimens composed of the transformable tetragonal phase exhibit high failure stress (6 ~ 7.5 GPa) and strain (6 ~ 8%). These values are incredibly high compared to their bulk counterpart, exhibiting the failure stress of ~ 4 GPa and the failure strain of ~3% [39]. It is also shown that the failure strain increases with the decrease in diameter. On the other hand, DEG micropillars exhibit a failure stress of 2 ~ 4 GPa and a failure strain of 2 ~ 4% except for a DEG 0.3 μm micropillar, showing ~ 6.5% failure strain. The degradation of mechanical properties in DEG pillars is attributed to: (a) loss of the martensitic transformation and (b) preexisting microcracks induced by volume expansion that occurred during the hydrothermal degradation. The reason for the DEG 0.3 μm micropillar to exhibit the exceptionally large failure strain is that the preexisting microcracks along the grain boundary are rare because the pillar size becomes smaller than the grain size (350 nm).

In summary, this study shows the effect of the martensitic transformation and preexisting microcracks in the mechanical properties of ZrO_2 at microscale. Interestingly, the monoclinic ZrO_2 exhibits the failure strain of ~ 4% at microscale, higher than that of 3% for tetragonal ZrO_2 at macroscale. Therefore, decreasing the specimen size to microscale plays a critical role in enhancing the toughness of ZrO_2 , by reducing the number of intrinsic cracks and relaxing external stress towards the free surface.

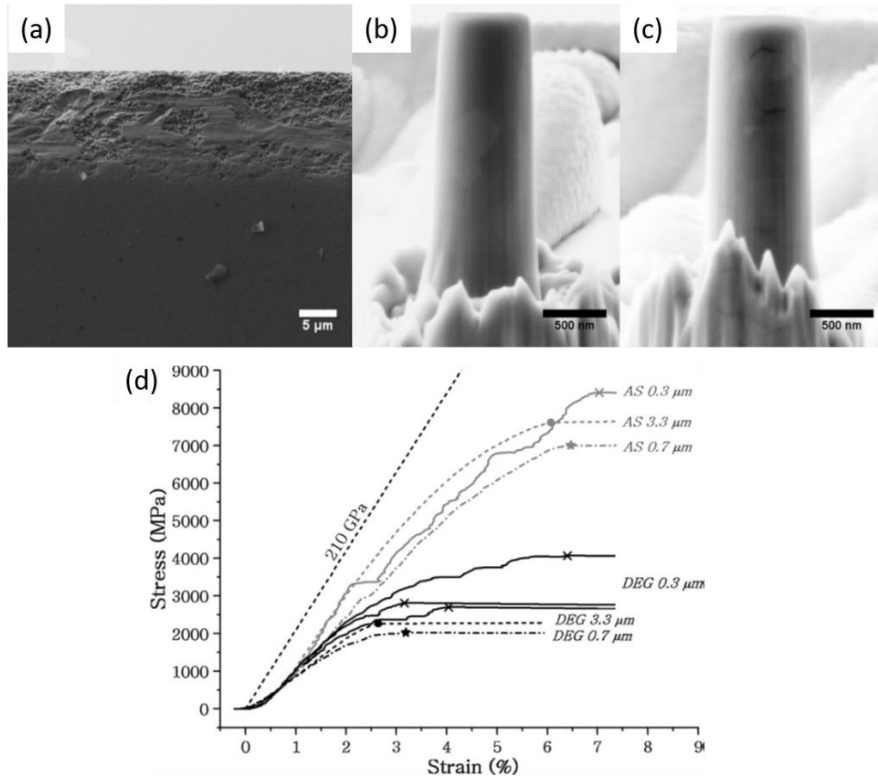


Figure 1.12. (a) SEM image of hydrothermally degraded 3YSZ. Micropillars were fabricated in the upper region, which contains the monoclinic phase dominantly. (b) metastable tetragonal dominant micropillar (c) monoclinic dominant micropillar. (d) Stress-strain curves for the microcompression tests on DEG and AS specimens with different diameters. X-shaped mark on the curves stands for catastrophic failure.

1.5.2. Orientation dependent martensitic transformation

The orientation dependence of the martensitic transformation is a crucial factor to maximize the mechanical properties of stabilized ZrO_2 . There are several studies on the orientation dependence study employing the nanoindentation technique, but the usage of nanoindentation limits our understanding of deformation mechanism, fracture morphology, and stress-strain relationship [52,53]. A simulation study for the orientation-dependent deformation mechanisms in single crystal YSZ shows that dominant deformation mechanisms (slip and transformation) are governed by crystallographic orientation [54].

Zeng *et al.* carried out microcompression tests on YSZ pillars with different orientations [46]. This study clearly shows the strong orientation dependence of deformation mechanisms that include slip, phase transformation, and fracture. The specimen prepared in the study is tetragonal ZrO_2 stabilized by 2 mol % Y_2O_3 and 5 mol % TiO_2 . The addition of TiO_2 in YSZ promotes grain

growth during the sintering process, such that it is relatively easy to fabricate a single crystal micropillar [55]. Fig. 1.13 shows tetragonal ZrO_2 with a grain size of $\sim 7 \mu m$ and crystallographic orientation for each grain analyzed by electron backscatter diffraction (EBSD). A micropillar was fabricated in a grain to obtain a single orientation (Figs. 1.13c and d). Fig. 1.13e shows a schematic representation of the microcompression test. For the martensitic transformation to happen to this micropillar, the mechanical energy should be larger than the sum of the chemical-free energy change, the surface energy change, and the strain energy change. The applied stress in the mechanical term can be expressed as,

$$\sigma_a = \frac{\sigma_{shear}}{\cos(\theta)\cos(\lambda)} \quad (1.12)$$

where θ and λ are an angle of applied stress with the glide plain and the glide direction, respectively. Since the mechanical term is a function of the Schmid factor (SF), the critical stress has a strong orientation dependence.

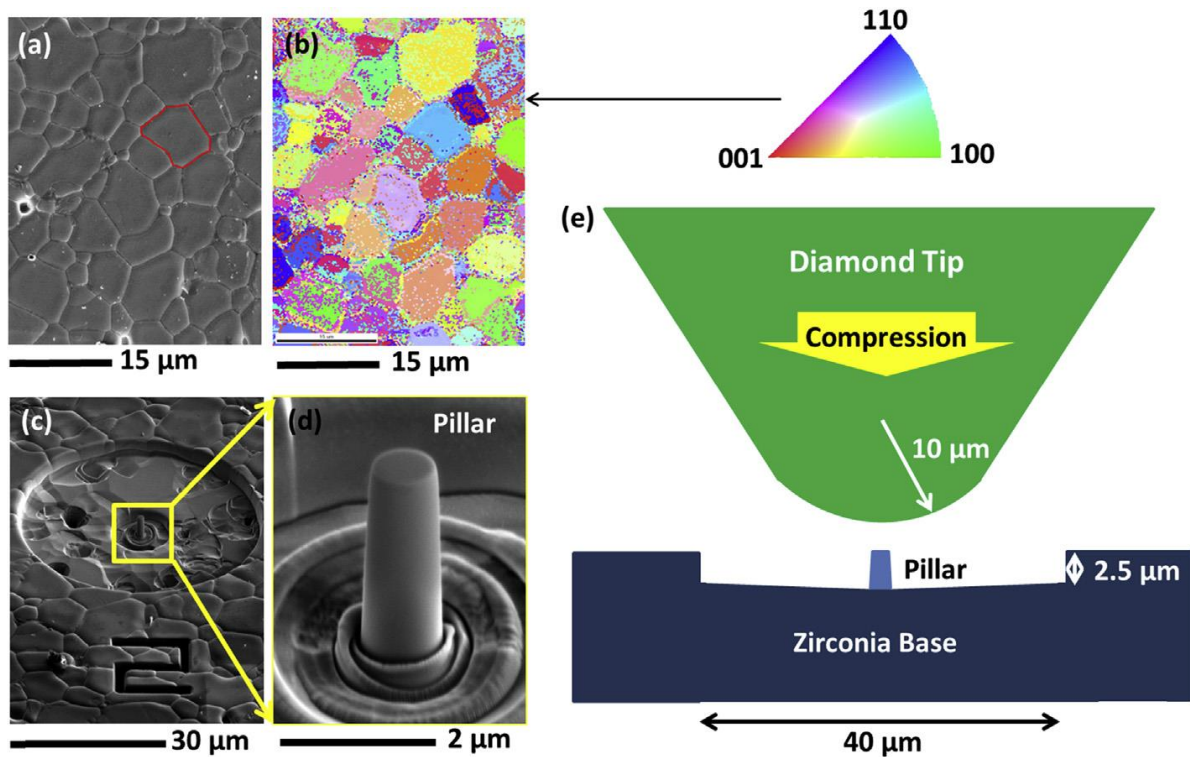


Figure 1.13. (a) SEM image of 5 mol % TiO_2 doped 2YSZ showing large grain size enough to fabricate a single crystal micropillar. (b) EBSD map of 5 mol % TiO_2 doped 2YSZ. (c-d) low and high magnification of a micropillar retaining a single orientation. (e) schematic representation of the micropillar compression test [46].

Fig. 1.14 shows the stereographic triangle of tetragonal ZrO_2 on which transformed, fractured, and slipped micropillars were marked. When slip takes place in a pillar, a plateau region forms followed by a load drop. On the other hand, the martensitic transformation features a sudden displacement plateau induced by volume expansion ($\sim 4\%$) and the subsequent loading increment. Martensitic band is also observed around the free surface of the micropillar after compression. A fractured micropillar exhibits a sudden load drop without a plateau region. Micropillars with orientations of $[100]$ and $[001]$ require immense stress to exhibit the transformation, and thus fracture takes place before the occurrence of the phase transformation. Micropillars with orientation of $[110]$ shows slip rather than the fracture and the martensitic transformation due primarily to the maximum resolved shear stress that can be obtained along $[110]$ orientation. However, micropillar along $[101]$ exhibits the early occurrence of the martensitic transformation.

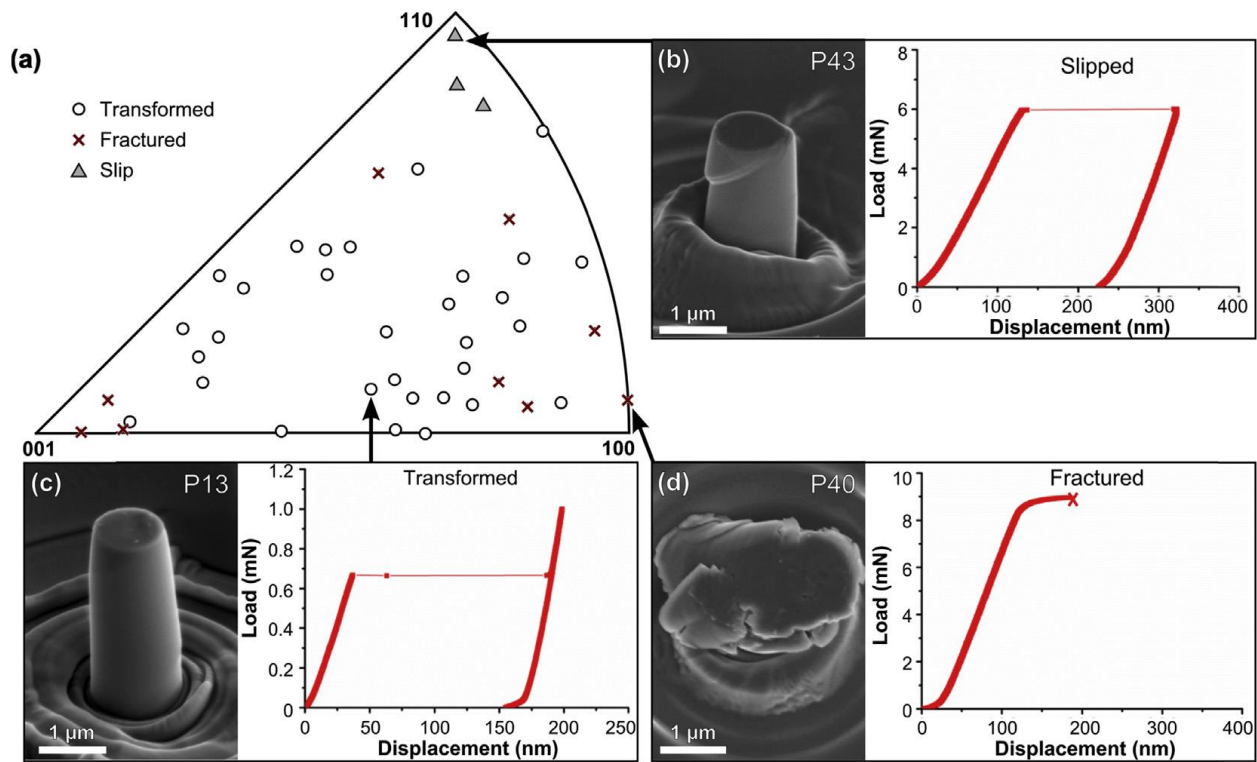


Figure 1.14. (a) Stereographic triangle of tetragonal ZrO_2 . Round, cross, and triangle-shaped marks represent transformed, fractured, and slipped micropillars, respectively. (b) Slipped micropillar after compression with a corresponding load-displacement curve. (c) transformed micropillar after compression with a corresponding load-displacement curve. Plateau represents transformation induced displacement-burst. (d) fractured micropillar after compression with a corresponding load-displacement curve [46].

Fig. 1.15 shows measured critical stresses as a function of maximum SF. If SF is larger than 0.3, a micropillar exhibits the martensitic transformation at a lower stress level, which is not enough to cause fracture and slip. When SF is less than 0.1, a micropillar only exhibits fracture or slip. For SF between 0.1 and 0.3, it appears that a micropillar exhibits both transformation and crack (Fig. 1.15b), meaning a gradual transition of the deformation mechanism. The stress level of the martensitic transformation and fracture for SF between 0.1 and 0.3 seems similar enough to trigger both deformation mechanisms simultaneously. The current study on the orientation dependence of mechanical properties of stabilized ZrO_2 is valid at room temperature. When the test is carried out much above M_s , the deformation mechanisms may be completely different. Hence, the investigation on the microscale-deformation mechanisms at the elevated temperature at which martensitic transformation is inoperable needs to be carried out for future applications. For example, the fracture can be retarded with the assistance of other inelastic deformation mechanisms such as grain boundary sliding and diffusional creep. Besides, ferroelastic domain switching induced by external stress is one of the possible deformation mechanisms for single crystal YSZ [56]. Given that ferroelastic domain switching can still be operable at high temperatures ($\sim 1000^\circ\text{C}$), it can be one of the governing deformation mechanisms as well.

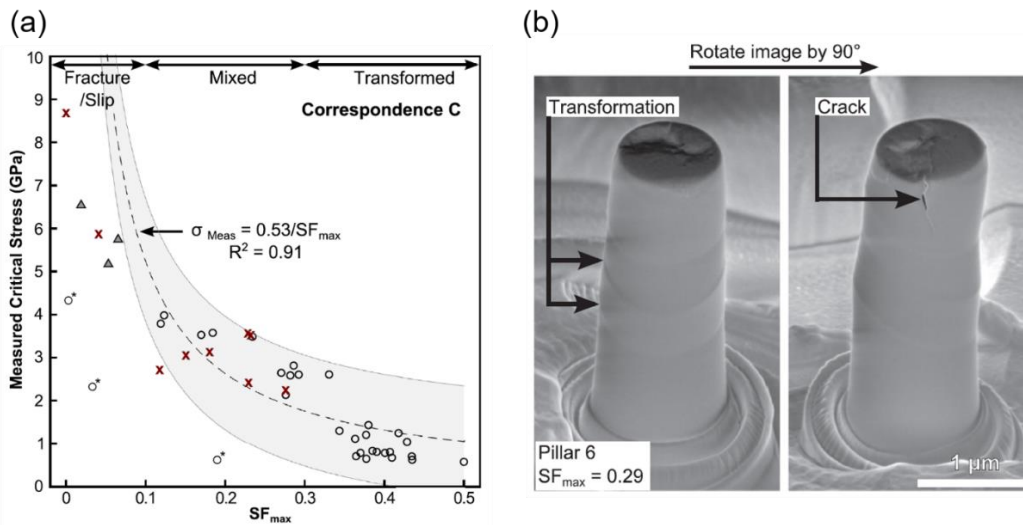


Figure 1.15. (a) Measured critical stress at which martensitic transformation takes place versus the maximum Schmid factor. The phase transformation takes place at lower critical stress when the Schmid factor is larger than 0.3. (b) SEM images of a micropillar that exhibits both transformation and crack due to the intermediate level of the Schmid factor [46].

1.5.3. Shape memory and superelasticity

The most exciting characteristic of tetragonal ZrO_2 is the shape memory effect owing to the martensitic transformation [14,57]. The shape memory effect is usually shown in metallic materials, whereas ceramic materials usually fail at a low stress before triggering the martensitic transformation. Although tetragonal ZrO_2 exhibits the shape memory effect, it fails at a strain of 2% after a few cycles of the transformation [57]. However, the miniaturization of tetragonal ZrO_2 can prevent it from cracking and eventually permit to reach a critical stress for the transformation to occur before fracture. Lai *et al.* showed the shape memory and superelasticity of cerium oxide doped YSZ at a small scale [14]. They fabricated micropillars retaining only several grains (also known as oligocrystalline) to increase stress relaxation towards the free surface and decrease mismatch stress among grains during the martensitic transformation. Microcompression tests were carried out on 1~2 μm diameter micropillars, and the results are shown in Fig. 1.16. Sudden strain bursts in plateau regions are attributed to the forward and reverse transformation resulting in ~ 4% volume expansion and contraction (Fig. 1.16a). The micropillar exhibits a linear behavior up to a critical stress level and a tremendous maximum strain (7%). During unloading, the micropillar exhibits the full recovery of 7% strain with several strain bursts due to reverse transformation. Fig. 1.16b shows stress-strain curves for the cyclic loading test. It shows that the curve becomes stabilized after 10 cycles as the cyclic tests proceed, and it can retain pristine shape up to 50 cycles without failure. Figs. 1.16c-e show 1 μm micropillar exhibiting shape memory effect. As an external load is applied, a micropillar plastically flows, which is rarely observed in ceramic materials at room temperature. After heating at 500°C for 2 h, the micropillar recovers its original shape through the reverse transformation.

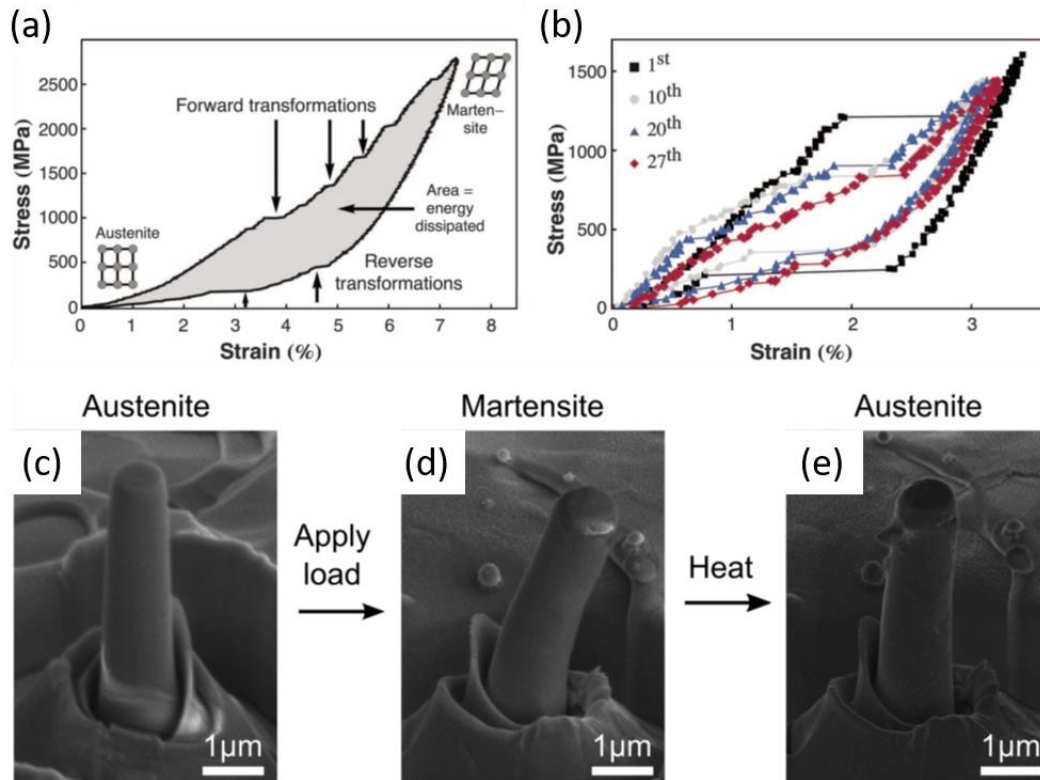


Figure 1.16. (a) Stress-strain curve for a microcompression test on oligocrystalline micropillar showing superelasticity owing to the martensitic transformation. Sudden increase of strain (plateau regions) is due to the forward and reverse transformation during loading and unloading, respectively. (b) Stress-strain curves for the cyclic loading tests. The curves become stabilized as the cyclic tests proceed. (c) SEM image of the micropillar before compression. (d) SEM image of the micropillar after compression. (e) SEM image of the micropillar after heating at 500°C for 2 h. It exhibits a shape memory effect [14].

1.5.4. Size effect on shape memory behavior

As a follow-up study on the shape memory effect of YSZ, the effect of micropillar size in the shape memory effect was carried out by Du *et al.* [45]. They prepared micropillars of tetragonal ZrO₂ with a diameter ranging from 0.5 to 3.0 μm . Fig. 1.17 shows a schematic representation of micropillars with different diameters. If the diameter is smaller than the average grain size (1.7 μm), the number of grains in the micropillar is only several, thereby exhibiting bending and significant plastic deformation due to the absence of mismatch stress among grains during the martensitic transformation. On the other hand, a micropillar with a diameter of 2.8 μm retains many grains and grain boundaries, which lead to mismatch stress during the martensitic transformation. Each grain has a different orientation, and thus the critical stress for the initiation

of the martensitic transformation is different. Thus, incommensurate transformation of different grains results in mismatch stress, leading to the development of intergranular crack.

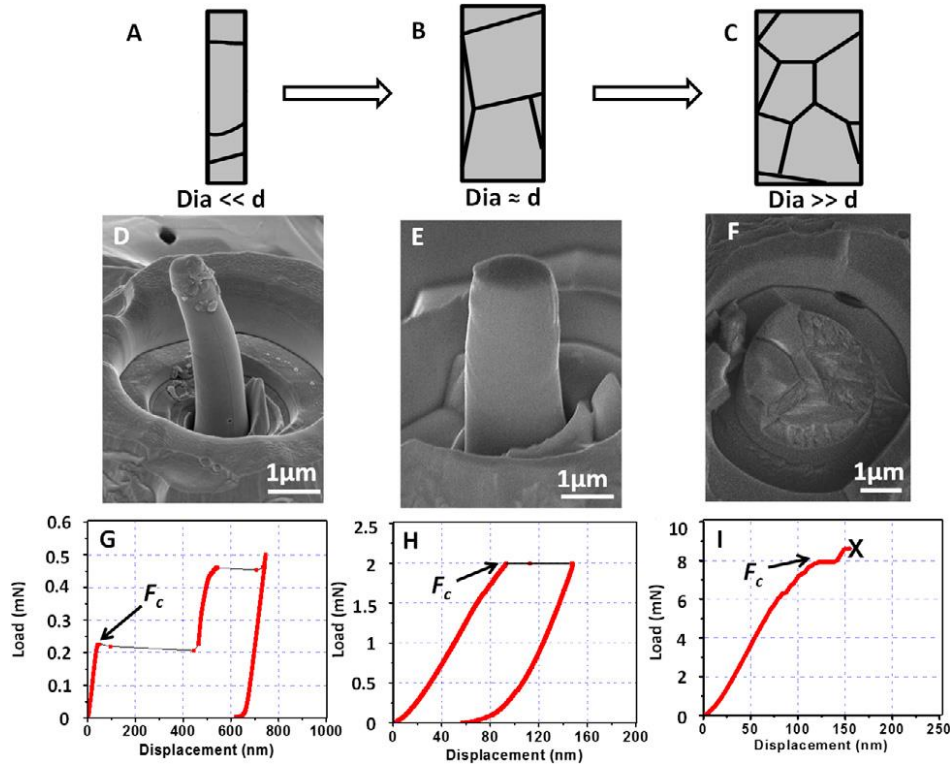


Figure 1.17. (a-c) A schematic representation of micropillars with different diameters (d = grain size). (d-f) SEM images of compressed micropillars. A micropillar with a smaller diameter exhibits plastic deformation due to the martensitic transformation. A micropillar with larger diameter fails due to mismatch stress among grains during the martensitic transformation. (g-i) Corresponding load-displacement curves. Strain bursts result from the martensitic transformation [45].

1.6. Consolidation methods

The conventional way to synthesize ceramic materials is to heat a powder compact at elevated temperatures below the melting point of major constituent for a few hours to trigger solid-state diffusion. Recently, attempts to develop several alternative consolidation methods have been made to (a) save energies by decreasing sintering temperature and sintering time and (b) enhance optic, electric, magnetic, and mechanical properties of ceramics by removing detrimental pores, nanovoids, and significantly reducing the grain size. So far, the most promising solutions appear to be the field-assisted sintering techniques that include flash sintering and spark plasma sintering.

This subchapter introduces several consolidation methods other than conventional firing and describes the principle of those sintering mechanisms.

1.6.1. Flash sintering

Cologna *et al.* reported the first validation of flash sintering in 2010, who fully densified a YSZ green body at 850°C in 5 s in support of a DC electric field [58]. Typically, YSZ can be consolidated at sintering temperatures of ~ 1400°C for several hrs. Flash sintering, one of the field-assisted sintering techniques, can considerably reduce furnace temperature as well as sintering time. Given that most ceramics have negative temperature coefficients of electrical resistance, the combination of furnace heating and electric field can yield a ultra-rapid densification when the material becomes electrically conductive at the onset of the flash event. Since the first report of flash sintering, many ceramic systems have been successfully prepared by flash sintering, which include YSZ, ZnO, TiO₂, CeO₂, SrTiO₃, BiFeO₃, MgTiO₃, Al₂O₃, and composite materials [59–68].

1.6.1.1. Experimental setup

An experimental setup for flash sintering requires a furnace, a power supply, and electrodes as shown in Fig. 1.18a. Two sides of a green body are connected by two electrodes with high electric conductivity, superb oxidation resistance, and high melting temperature. Several candidates for the electrodes that meet the aforementioned requirements are Pt, C, Ag, and Au. The shape of a green body can vary and affect the sintering behavior [69]. The most frequently used shape of the green body is dog-bone (Fig. 1.18a), cylinder (Fig. 1.18b), and rod (Fig. 1.18c). A moderate electric field applies to a green body placed in the furnace with a ramp heating (also known as stage I). Once a sudden increase of electric conductivity occurs at the onset of flash (Stage II), the voltage control mode is switched to the current control mode to prevent a thermal runaway (Stage III). Massive densification occurs at stage II, and the grain growth is favored at stage III.

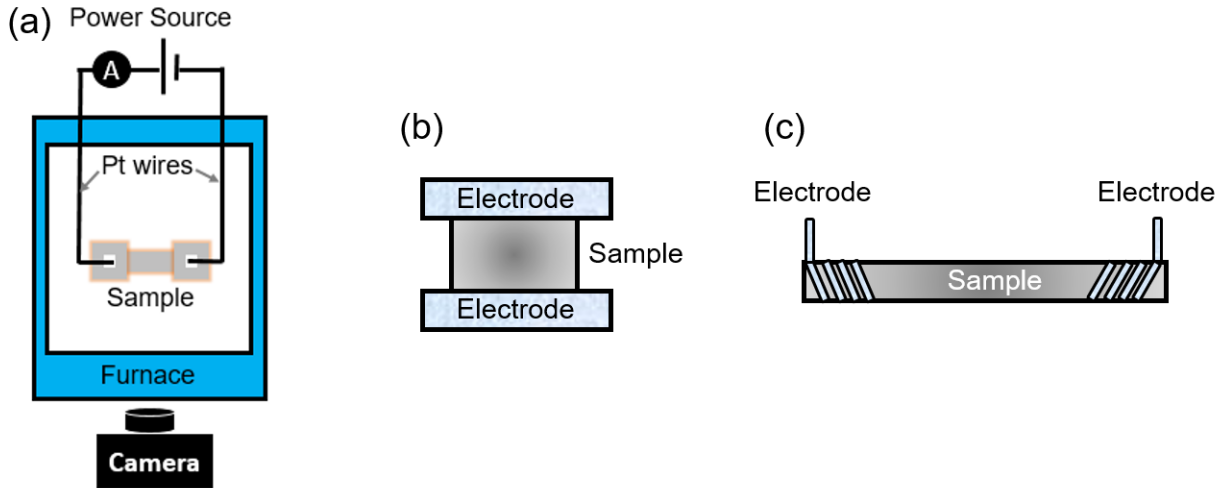


Figure 1.18. A flash sintering set up with a green body of (a) dog-boned shape, (b) cylindrical shape, and (c) rod shape.

1.6.1.2. Flash sintering mechanisms

Since most ceramics are electrically insulated at low temperatures, the power generated within the ceramic green body at stage I (Fig. 1.19) under the voltage control can be calculated by

$$w = E^2 / \rho \quad (1.13)$$

where w is the specific electric power dissipation in the sample, E is the electric field, and ρ is the resistivity of the sample. As the sample temperature increases in a furnace, the resistivity of the sample begins decreasing due to the negative temperature coefficients of electrical resistance, which, in turn, leads to the gradual increase in the power dissipation as shown in Fig. 1.19c. Once the sample temperature reaches the onset point, a large amount of current starts flowing across the specimen, and thus the sample flashes (stage II), as shown in Fig. 1.19b. The onset temperature of flash is strongly dependent on the electric field. In general, a higher electric field results in the onset of flash at lower furnace temperature. The specific power dissipation at the onset of flash can be given as,

$$w = EJ \quad (1.14)$$

where J is the current density. At stage II, the typical power dissipation at the onset is $10 \sim 50$ mW/mm³ [70], and a thermal runaway of Joule heating and rapid densification occur in the sample. After the voltage control switches to the current control (stage III), grain coarsening and the residual densification can occur. The power dissipation in this stage can be calculated as,

$$w = J^2 \rho. \quad (1.15)$$

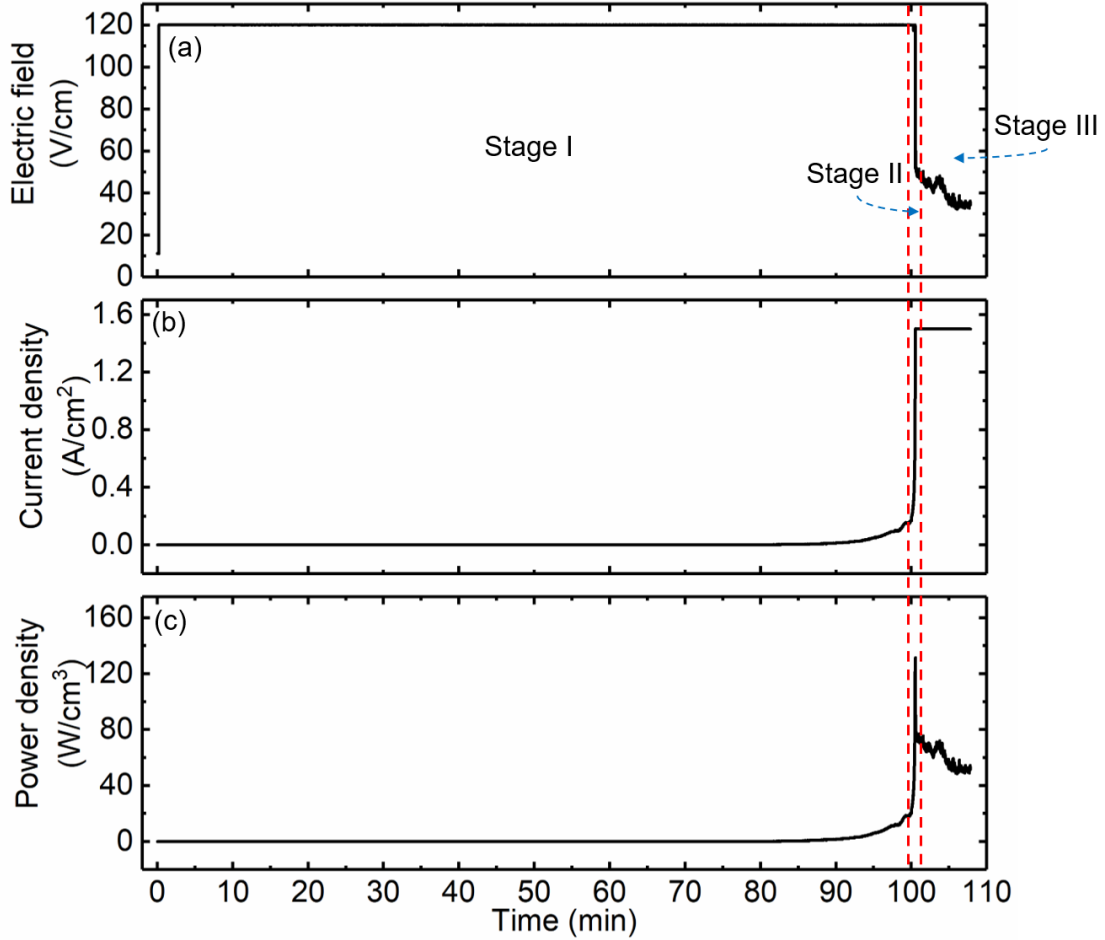


Figure 1.19. Plots of (a) electric field, (b) current density, and (c) powder density as a function of time during a typical flash sintering experiment.

Although the society reaches to the agreement that a thermal runaway of Joule heating causes the flash event, it is still not clear whether there exist other contributing factors to the concurrent occurrence of electrical carrier movement, rapid mass transport, and photoemission. Todd *et al.* and Zhang *et al.* introduced a simple concept in which the flash event occurs due to the competition between the heat generated by Joule heating and the heat dissipated from the sample [71,72]. Once the combination of the electric field and furnace temperature is such that electric current can flow across the specimen, Joule heating is produced in the sample. When the heat generated by Joule heating is higher than the heat dissipated from the sample, the sample temperature surplus from Joule heating can be considered as given by [73],

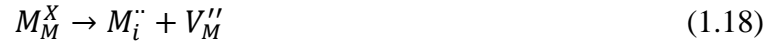
$$E^2 V \left. \frac{d\sigma}{dT} \right|_{T_s} > \frac{\partial \dot{Q}(T_s, T_f)}{\partial T_s} \quad (1.16)$$

where V is the volume of the sample, σ is the conductivity of the sample, T_s is the sample temperature, T_f is the furnace temperature, and $\dot{Q}(T_s, T_f)$ is the heat dissipation rate from the sample. The second derivative of Eq. 1.16 with respect to temperature yields

$$E^2 V \left. \frac{d^2 \sigma}{dT^2} \right|_{T_s} > \frac{\partial^2 \dot{Q}(T_s, T_f)}{\partial T_s^2}. \quad (1.17)$$

In the case where the heat generation rate by Joule heating is higher than the heat dissipation rate of the sample, the increase in the sample temperature will be maintained, which can, in turn, lead to a positive feedback loop or a thermal runaway of Joule heating. At this stage, the sample temperature precipitously increases at rapid heating rates ($>10^4$ °C/min), and the ultra-fast densification occurs in a few seconds [74].

The very first mechanism proposed to explain flash sintering was the formation of Frenkel defects [75–78]. The Frenkel pair forms when an atom leaves its site and resides in interstitial sites of the lattice. When the combination of electric field and temperature is such that interstitials and vacancies form by electric-field induced lattice disorder, the high density of Frenkel pair triggers an avalanche of defects. The reactions of Frenkel pair formation for an oxide system are given as,

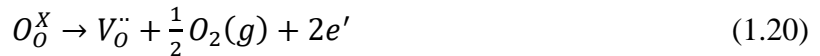


where M is the metal species, and V is the vacancy. The Frankel pairs produced by electrical potential can be ionized again to produce the neutral defects, electron holes, and electrons and migrate in response to the applied electric field. Interstitials generated from the reaction of defect ionization migrate to the pores, whereas neighboring grain boundaries or free surfaces absorb vacancies, and thus the rapid densification occurs. This hypothesis is attractive in that it can adequately explain concurrent phenomena occurring during the flash event. For example, Photoemission observed at stages II and III can be explained by the combination of electron holes and electrons [79,80]. However, direct experimental evidence to support this hypothesis is still lacking.

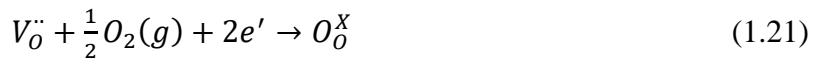
Another mechanism proposed for flash sintering is local grain boundary melting or overheating [81–84]. Grain boundaries have a high diffusion coefficient and space charge, which can lead to higher electrical resistance than a lattice counterpart [85]. Besides, at stage I, the interfacial neck area between two particles is much smaller than the grain interior, and thus the local current density increases abruptly in the necking area compared to the lattice counterpart [69]. If the power

dissipation at the interparticle region is high enough to melt grain boundaries, the electrical conductivity of the specimen may significantly increase two orders of magnitude more than a specimen without a melting phase [86]. The enhanced electrical conductivity can eventually induce the flash event of the specimen. The temperature gradient between grain boundaries and grain bulk can result in minimizing the grain boundary energy [87]. If hot grain boundaries migrate to cold grain bulk, the grain boundary energy increases, which is a thermodynamically unfavorable direction. Therefore, the driving force for grain growth is limited, and thus densification occurs in the absence of significant grain coarsening, which indeed is commonly observed in flash-sintered ceramics. As an experimental evidence of grain boundary melting during the flash, there are several reports on the formation of secondary phase along grain boundaries in flash-sintered ceramics. For example, Morisaki *et al.* observed grain boundary second phase in flash-sintered monoclinic ZrO₂ [88]. Uehashi *et al.* showed the formation of the secondary phase of BaTi₄O₉ in the grain boundary of flash-sintered BaTiO₃ [89].

Lastly, the improved mobility and electrical conductivity of ionic species due to the electrochemical reduction can be responsible for flash sintering. The electrochemical reaction was reported on flash-sintered cubic ZrO₂ (8YSZ) under DC polarization [90]. If the external electric field is higher than the intrinsic electrochemical reduction potential for ZrO₂, oxygen in the oxygen site at the anode gives up two electrons and creates an oxygen vacancy, as shown in Eq. 1.20 [91].



The electrons produced by the electrochemical reduction in cubic ZrO₂ flow through the external circuit. The positively charged oxygen vacancies created at the anode migrate towards the cathode across the sample in response to the electric field. The reverse reaction (Eq. 1.21) occurs between the electrode and the sample at the cathode to consume the products of the reaction in Eq. 1.20.



If the oxidation rate to restore the oxygen site is lower than the reduction rate due to Pt electrode limiting the access of oxygen gas, the charged oxygen vacancies start to accumulate at the cathode, and the new reaction to consuming the charged vacancies is triggered as given by,



The discharged oxygen vacancies incorporated in the lattice results in the reaction as given by



The formation of the reduced ZrO_2 is responsible for the electrochemical blackening (Fig. 1.20) that occurs at the cathode and propagates towards the anode at stages II and III.

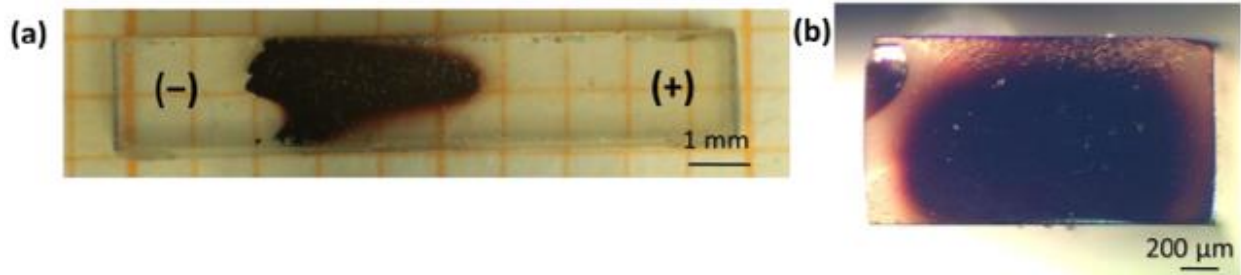


Figure 1.20. Flash sintered single-crystal 8YSZ (100) showing electrochemical blackening from (a) plan-view and (b) cross-sectional view [90].

The electrochemical reaction can explain the significant decrease in the electrical resistivity at the onset of flash. As the reduction reaction front (electrochemical blackening regime) propagates from the cathode to the anode, the electronic disorder forms, and thus results in the enhanced electrical conductivity [92]. Furthermore, the electrochemical reaction can be responsible for the enhanced mass transport. It was reported that the discharged oxygen vacancy and the reduced metal species produced under the electric field have the low migration energy, and thus it contributes to the rapid densification [83,93]. These ideas can be supported by (1) the direct measurement of the electric conductivity of reduced YSZ [94] and (2) the observation of grain size gradient across the electrodes in flash-sintered 8YSZ [95]. It was reported that the blacked YSZ has significantly higher electric conductivity than non-reduced YSZ [94]. Kim *et al.* reported that 8YSZ treated under DC electric field shows abnormal grain growth on the cathode side due to the migration energy reduction of the reduced species, as shown in Fig. 1.21 [95].

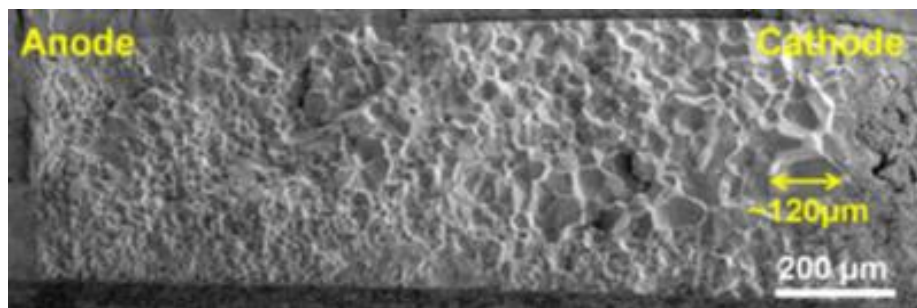


Figure 1.21. 8YSZ subjected to 50 A/cm^2 showing the abnormal grain growth on the cathode side [95].

1.6.2. Spark plasma sintering

Spark plasma sintering (SPS) utilizes an electric current and uniaxial pressure to consolidate metallic and ceramic powders. SPS is often referred to as several different names that include pulse electric current sintering (PECS), field-assisted sintering technique (FAST), plasma-assisted sintering (PAS), and electric pulse-assisted sintering (EPAC) [96]. As several names indicate, SPS features the use of high pulsed direct currents passing through a graphite die and a sample that can generate Joule heating. A raw powder is loaded in a graphite die (Fig. 1.22) and pulsed DC flows through the graphite die and the raw powder in the case where the sample is electrically conductive. In most case the SPS process is conducted in a low vacuum atmosphere ($10^{-2} \sim 10^{-3}$ torr) to prevent oxidation of graphite. The sintering temperature is measured by a pyrometer aiming at a hole of the graphite die (when the test temperature is $\geq 1000^{\circ}\text{C}$) or a k-type thermocouple inserted through a hole of a graphite punch (when the sintering temperature is $\leq 1000^{\circ}\text{C}$). Meanwhile, A pressure up to 1000 MPa can be applied to the powder in order to stimulate the consolidation process. The generated Joule heating from the graphite die offers a high heating rate of $\sim 1000^{\circ}\text{C}/\text{min}$, which enables to by-pass the grain coarsening regime (surface diffusion and evaporation-condensation dominant) at intermediate temperatures and ultimately reach to the densification regime at high temperatures, dominated by grain boundary and lattice diffusion of atoms. Hence, SPS enables the achievement of the theoretical density of materials with insignificant grain growth, and eventually reduces sintering time to less than an hour and decreases sintering temperature by $100 \sim 400^{\circ}\text{C}$ than that required for conventional sintering [97]. Due to the superb capability of SPS of consolidating materials efficiently in terms of sintering time and temperature, it has been utilized for a various class of materials such as metals, intermetallic, ceramics, and composites [98–102]. Furthermore, depending on sintering parameters such as the heating rate, pressure, and current, which directly impact on the microstructure, spark plasma sintered materials can exhibit much improved mechanical properties, optical properties, electrical properties, magnetic properties, and oxidation resistance [103–109].

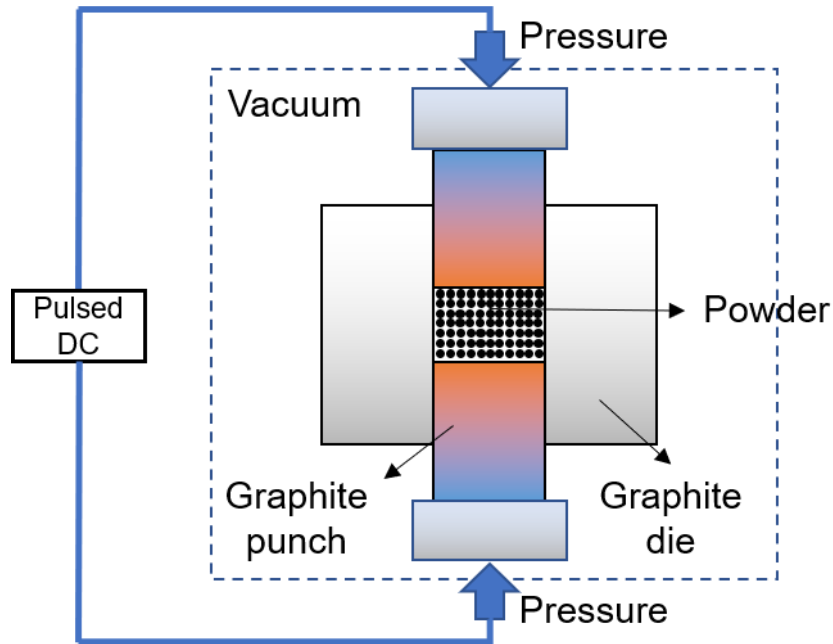


Figure 1.22. A schematic representation of SPS.

A distinctive feature of SPS over conventional sintering and hot-pressing is the existence of the electric current contributing densification in both thermal and non-thermal ways. The thermal nature of the electric current can provide gradient temperature distribution that results in thermal diffusion of vacancies, interparticle local melting, and thermal stress-induced dislocation creep, which eventually contributes to the rapid densification. Given that most ceramics have negative temperature coefficients of electrical resistance, the role of the electric current in densification is not limited to the generation of Joule heating. When the sample temperature is high enough for the electric current to flow through the sample, the current exerts a non-thermal effect that can directly influence the mass transport through the mechanisms of electroplasticity and electromigration [97]. Therefore, in this subchapter, not only heating rate and pressure, but the current effect on the microstructure is also discussed.

1.6.2.1. Heating rate

The effect of heating rate in the SPS has been investigated for many systems, and it produces somewhat conflicting results even in the same class of material. In many studies, the goal is to limit grain growth and achieve near full-density. Some studies on the heating rate effect on grain growth kinetics of Al_2O_3 show that the grain size decreases with increasing the heating rate [110–

112]. For example, Shen *et al.* showed the effect of heating rate on densification and grain growth of Al_2O_3 processed by SPS at various heating rates (50-600 $^\circ\text{C}/\text{min}$) and two maximum temperatures (1300 and 1400 $^\circ\text{C}$) [111]. When the heating rate is $\leq 350^\circ\text{C}/\text{min}$, fully dense Al_2O_3 was obtained, whereas porous structure was observed with the higher heating rates. Meanwhile, the grain size decreases with the increase in the heating rate, and this is more prominent at higher temperatures. For example, at 1300 $^\circ\text{C}$, the average grain size for Al_2O_3 sintered at a heating rate of 50 and 370 $^\circ\text{C}/\text{min}$ is 3 and 2 μm , respectively. When processed at 1400 $^\circ\text{C}$, the two heating rate shows even more obvious grain size difference, 9.5 and 4 μm at 50 and 370 $^\circ\text{C}/\text{min}$, respectively. The relatively better densification with the lower heating rates can be achieved due to the pulsed direct current passing through the particles at low temperatures. The pulsed direct current can produce spark discharges in gaps of the interparticle region and help the densification during the initial stage of the sintering. Once the sample temperature is high enough, grain boundary migration becomes dominant. On the contrary, some studies on spark plasma sintered Al_2O_3 show the conflicting results that the smaller grain size is observed with decreasing the heating rate [113,114]. For instance, Kim *et al.* investigated the effect of heating rate on grain size and transparency of Al_2O_3 [113]. When a heating rate of 100 $^\circ\text{C}/\text{min}$ is used, the average grain size was determined to be 0.55 μm . Meanwhile, the average grain size of 0.29 μm was observed under a heating rate of 10 $^\circ\text{C}/\text{min}$ (Fig. 1.23). The large grain size at the higher heating rate is attributed to the high density of defects generated by high heating rate and associated fast deformation. In addition, the large direct current produced at the higher heating rate helps to form the high-density defects that accelerate grain growth kinetics.

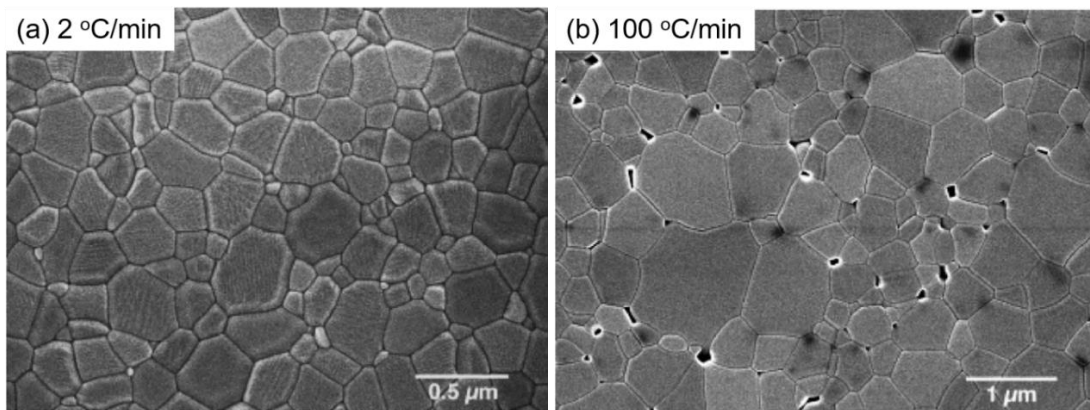


Figure 1.23. SEM micrographs of Al_2O_3 prepared by SPS at a heating rate of (a) 2 $^\circ\text{C}/\text{min}$ and (b) 100 $^\circ\text{C}/\text{min}$ [113].

The effect of the heating rate on the densification and grain growth of SiC was investigated [115,116] and showed conflicting results. Geophart *et al.* showed that higher heating rates caused a smaller grain size and lower density than lower heating rates [115]. These results may be attributed to pore-trapping effect and shorter processing time for the samples under a higher heating rate condition. On the other hand, Zhou *et al.* observed that a higher heating rate in the SPS yielded a larger grain size of SiC [116]. The pulsed direct current can generate an electric discharge between the particles and voids. The electric discharge-induced localized heating of the particles can facilitate rapid mass transport, and thus larger grain size is observed.

Lastly, cubic ZrO₂ stabilized by 8 mol% Y₂O₃ (8YSZ) was sintered by SPS, and the effect of heating rate was investigated [117,118]. In general, the grain size decreases with an increase in heating rate. For example, the average grain size of 60 nm was observed under a heating rate of 50 °C/min, while it decreases to 35 nm under a heating rate of 275 °C/min. Meanwhile, the heating rate shows an insignificant impact on the final density.

1.6.2.2. Pressure

Unlike the heating rate, the effect of pressure on grain growth and densification yields a consistent conclusion. An increase in pressure results in higher densification at the same temperature. The applied pressure can help decrease the sintering temperature without the sacrifice of densification, and thus limit grain growth. Applying the external pressure can be especially useful for nanometric powders that tend to agglomerate, because it can mechanically help the agglomerates rearranged and destructed. This process can enhance the packing density of particles, thereby accelerating densification. The external pressure is also associated with the driving force for sintering as given by [96],

$$\frac{d\rho}{(1-\rho)dt} = B\left(g\frac{\gamma}{x} + P\right) \quad (1.24)$$

where ρ is the density, t is time, B is a combined term of temperature and diffusion coefficient, g is the geometric constant, and γ is the surface energy, x is a term associated with particle size, and P is the external pressure. The right-hand side term of Eq. 1.24 is an intrinsic driving force for sintering associated with the curvature of particles and the external pressure. The relative contribution between the curvature and pressure to densification can be estimated by,

$$P = g\left(\frac{\gamma}{x}\right). \quad (1.25)$$

Eq. 1.25 determines the critical particle size above which the external pressure is more dominant than the curvature of particles. This implies that the applied pressure does not exert a significant impact on densification below the critical particle size. In other words, there exists a threshold stress above which the applied stress begins stimulating densification, and it is inversely related to particle size. For example, Skandan *et al.* showed that during the sintering of undoped ZrO₂ with an initial particle size of 6 nm, the applied pressure less than 35 MPa did not influence the densification, whereas the higher pressure significantly improved the final density (Fig. 1.24a) [119]. When the initial particle size is 12 nm, the threshold stress was determined to be 10 MPa. Anselmi-Tamburini *et al.* showed the effect of the pressure on the sintering temperature to achieve the 95% relative density of 8YSZ with an initial particle size of 6.6 nm [120]. The sintering temperature required to acquire the 95% relative density exponentially decreases with the increase in the applied pressure, as shown in Fig. 1.24b. For instance, the sintering temperature of 1350°C is necessary to achieve 95% of the theoretical density without the pressure, whereas 900°C is enough to fully consolidate 8YSZ with the applied pressure reaching 1 GPa. As the sintering temperature decreases with the increase in the applied pressure, the final grain size also decreases from 200 nm (1350°C and no pressure) to 16 nm (900°C and 1 GPa). Anselmi-Tamburini *et al.* also showed the effect of the applied pressure on the relative density and grain size of nanometric undoped ZrO₂ at the fixed temperature of 1200°C, holding time of 5 min, and heating rate of 200 °C/min [118]. When a pressure of 140 MPa is utilized, the full densification was achieved, whereas only 60% relative density was observed under a pressure of 20 MPa. Meanwhile, the pressure did not influence the final grain size, presumably due to the same maximum temperature.

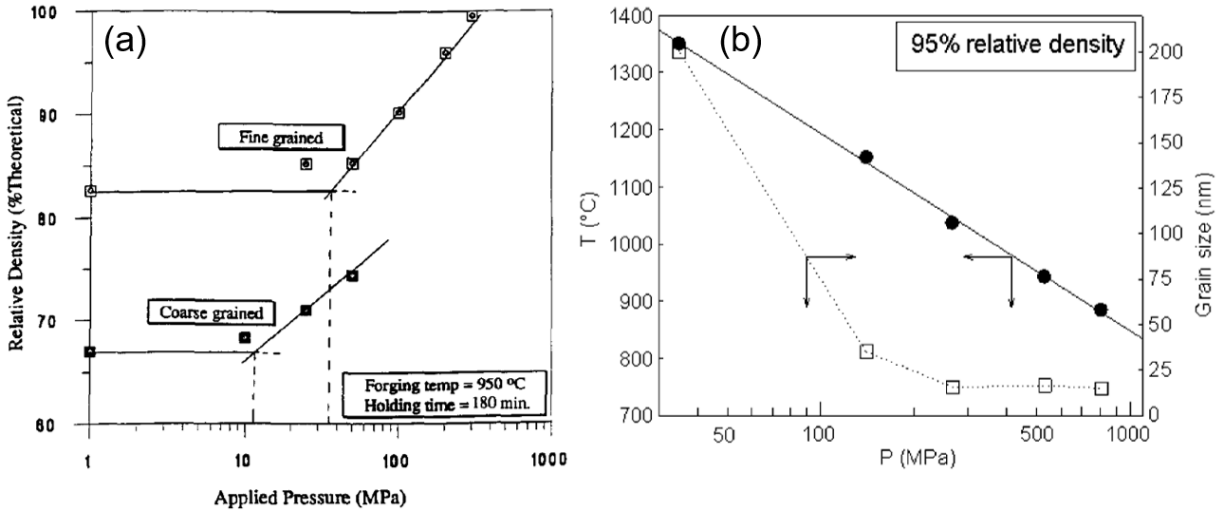


Figure 1.24. (a) The effect of applied pressure on the relative density of fine- and coarse-grained ZrO₂ [119]. (b) The effect of applied pressure on the sintering temperatures to achieve a 95% relative density of ZrO₂ [120].

1.6.2.3. Current

As mentioned earlier, a prominent feature of SPS over conventional sintering and hot-pressing technique is the use of an electric current that passes through a graphite die and a conducting sample. A sample processed in a conventional way is heated through the radiation in the enclosed furnace, whereas a spark plasma sintered sample is consolidated through the thermal conduction transferred from the graphite die. Other than the Joule heating effect of the current, there is a non-thermal effect of the current that improves the densification process in SPS. As the name indicates, electric discharge (spark) could happen at spaces between particles, thereby enhancing densification through cleansing CO₂ and H₂O adsorbed to the surface of particles [96]. However, this assertion is still under debate since it is difficult to observe the formation of plasma during the sintering process. Shen *et al.* suggested that spark discharges during Al₂O₃ sintering in SPS could occur on a microscopic level, which leads to the great enhancement of densification behavior [111]. The contribution of the spark discharges to densification can be made only at the initial stage of sintering because there are many gaps between the particles available for spark discharges to be generated. Once the sample reaches the state of a closed porosity, the grain boundary and lattice diffusion become dominant mechanisms for densification [121]. A similar idea was also suggested by Omori, who studied the sintering behavior of Al alloys, WC, polyimide, polymonomethylsilane, and CoSb₃ [122]. On the other hand, Wang *et al.* showed an inhomogeneous microstructure of

Al₂O₃ processed by SPS, attributed to Joule heating transferred from a graphite die [123]. They claimed that no electric discharge was observed due to the insulative nature of Al₂O₃. This argument is supported by Tomino *et al.* and Makino's works, which showed a negligible amount of current passing through Al₂O₃ in the SPS process even at high temperatures [124,125].

While the formation of an electric discharge during SPS is under debate, the contribution of an electric current to densification through the enhancement of mass transport reached the agreement. It was suggested that rapid mass transport could be realized through electromigration, an increase in point defect density, and a decrease in activation energy for defect migration [126,127]. Anselmi-Tamburini *et al.* showed the effect of an electric current in SPS on mass transport by measuring the thickness of MoSi₂ layer sandwiched by Mo and Si layers [128]. The growth rate of MoSi₂ layer showed a strong dependence of an electric current passing through the sample, which indicates that the current can indeed enhance mass transport of the migrating species. The activation energy for the formation of the reactant was the same as that in absence of the current, suggesting that the presence of the electric current did not alter the mechanism of mass transport. Hence, the presence of the current in the SPS system may enhance the density of point defects and the mobility of migrating species under the same mechanism of mass transport.

1.6.3. Hot pressing

The traditional manufacturing process of raw ceramic powders is to press the powder in a required shape, and then fire it at high temperatures. However, the development of a hot pressing technique (HP) allowed to combine the two separate processes of forming and firing into one step [129]. The raw powder can be loaded and pressed in a die uniaxially and simultaneously heated up to desired temperatures. This sintering process is very similar to SPS, but there exists no electric current passing through the die and sample for the HP technology. When the technique was developed 50 years ago, it was revolutionary in that HP can limit grain growth and yet allow it to achieve a full density at low temperatures. The application of pressure during the sintering process enhances mass transport through grain boundary sliding, diffusional creep, and plastic deformation, and achieves better densification than conventional firing [130,131]. Since the HP technique utilizes a uniaxial pressure that contains shear components, grain boundary sliding can occur, which eases the densification process. In comparison, hot isostatic pressing (HIP) also utilizes

pressure, but the hydrostatic pressure in the HIP process does not involve shear components, thereby being less effective than hot pressing in densification [132].

Bernard-Granger *et al.* prepared 3YSZ using HP and SPS and compared their sintering mechanisms [133–135]. In general, HP and SPS yielded pretty similar results of final grain size and relative density when they used the same temperature and holding time. For example, when 3YSZ was subjected to the sintering temperature of 1110-1125°C for 15 mins, the average grain size was ~ 85 nm, and a relative density was ~ 98% for both of hot-pressed and spark plasma sintered 3YSZ. For the hot-pressed 3YSZ, the stress exponent and the activation energy for the densification mechanism derived from the creep rate equations were determined to be 2 and 450 kJ/mol at low and medium temperatures, whereas the stress exponent of 1 and the activation energy of 280 kJ/mol were obtained at high-temperature regions. This result suggests that grain boundary sliding controlled by the interface reaction and lattice diffusion of cations (Zr^{4+} and Y^{3+}) is likely to be the dominant sintering mechanism at low and medium temperatures. On the other hand, at high temperatures, grain boundary sliding accommodated by diffusion of cations along grain boundaries is the densification mechanism for the hot-pressed 3YSZ. For the spark-plasma sintered 3YSZ, the stress exponent of 2 and the activation energy of 450 kJ/mol were obtained at a low-temperature region, indicating that the densification mechanism is grain boundary sliding accommodated by interface reaction and lattice diffusion of cations. At high temperatures (1050-1125°C), the stress exponent of 3-4.8 was determined, meaning that grain boundary sliding accommodated by dislocation climb is the densification mechanism. On the other hand, Langer *et al.* showed the sintering behavior of 8YSZ when processed by HP and SPS [136]. Under the same condition of sintering parameters such as heating schedule, pressure, atmosphere, and sample geometry, 8YSZ prepared by HP and SPS did not show any difference in densification and microstructures. The stress exponents of 8YSZ prepared by HP and SPS were calculated to be ~ 1, indicating that the densification mechanism of hot-pressed and spark plasma sintered 8YSZ was grain boundary diffusion of cations (Zr^{4+} and Y^{3+}) when test temperatures are $\leq 1300^\circ\text{C}$ [137].

1.6.4. Thermal barrier coatings

Nowadays, a long-term stance of the science and engineering community on material advancement is to create materials with enhanced properties, which aims at particular applications with high efficiency. A typical example includes the use of superalloy for high-thrust engines and

turbines operating at ultra-high temperatures ($\sim 1300^\circ\text{C}$). The application of TBCs on such a superalloy allows less energy consumption and extended service duration by protecting the substrate from foreign object damage (FOD) and minimize thermal exposure. Especially, the use of YSZ for the TBC applications can dramatically improve engine efficiency because it enables the engines to operate at higher temperatures than the melting point of the superalloys [12]. The benefit can be achieved by the fact that YSZ offers one of the lowest thermal conductivity of ~ 2.3 W/mK at $\sim 1000^\circ\text{C}$, primarily due to vacancy-induced phonon scattering [138]. Furthermore, YSZ has a high coefficient of thermal expansion (CTE) value ($11 \times 10^{-6} \text{ }^\circ\text{C}^{-1}$) comparable to that of the superalloy substrate ($14 \times 10^{-6} \text{ }^\circ\text{C}^{-1}$) [12]. The similar CTE values between the TBC and substrate can minimize thermal mismatch stress during thermal cycling, and thus enhance the structural reliability of the turbine engines. YSZ is one of a few materials that exhibit both high strength and fracture toughness, which is usually mutually exclusive. It has Young's modulus of 210 GPa and a hardness of 10-14 GPa [139]. For 7YSZ typically used for the TBC applications, the fracture toughness of $\sim 3 \text{ MPa}\cdot\sqrt{m}$ was reported owing to the toughening mechanism of ferroelastic domain switching [25].

Fig. 1.25 shows a schematic representation of a thermal barrier coated turbine blade consisting of a metal substrate, bond-coat, thermally grown oxide (TGO), and ZrO_2 top-coat [12]. The bond-coat is applied between the substrate and the ceramic topcoat to prevent a spallation failure in its service. NiCoCrAlY and NiCrAlY are typically used for the bond-coat application due to its superb oxidation resistance. Since the turbine engines undergo extreme environments ($\sim 1300^\circ\text{C}$) and the ceramic top-coats contain a high density of open pores and cracks, which facilitate oxygen penetration toward the bond-coat, the bond-coat can quickly oxidize underneath the ceramic top-coat. This oxidized layer, namely thermally grown oxide (TGO), is comprised of $\alpha\text{-Al}_2\text{O}_3$, and a meticulous design for the TGO layer is required for it to grow slowly and densely. In this subchapter, commercially available ways to deposit YSZ TBCs such as air plasma spray, e-beam physical vapor deposition, and detonation gun thermal spray are described.

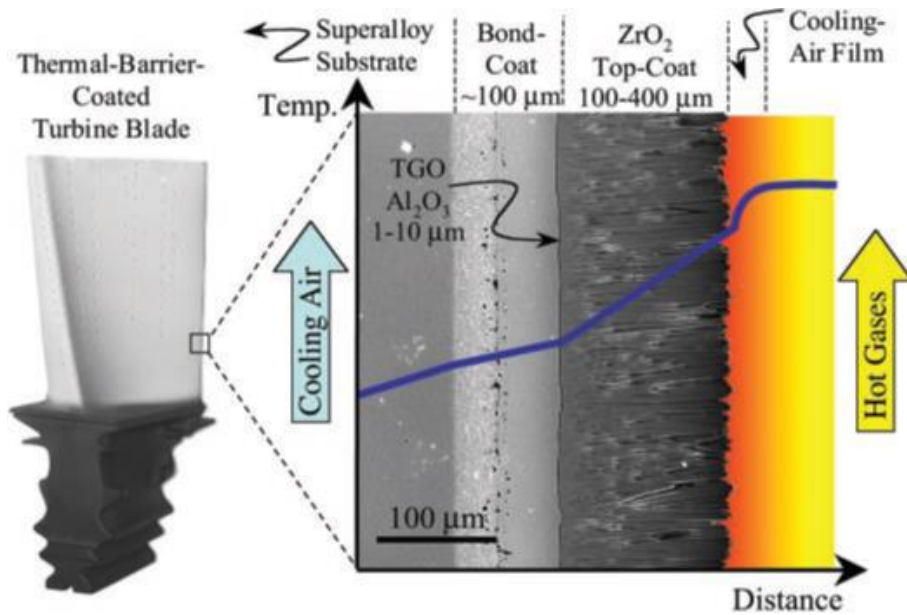


Figure 1.25. A schematic representation of a thermal barrier coated turbine blade [12].

1.6.4.1. Air plasma spray

Air plasma spray (APS) has a water-cooled W cathode and Cu anode with Ar gas introduced in the chamber to generate the plasma through the direct current [140]. The electric arc completes the circuit from the cathode to anode and forms the plasma with the maximum temperature of 15,000 K at a direct current torching power of 40 kW. The YSZ feedstock is completely melted in the flame and pushed to the metal substrate at a speed of 100-300 m/s [141]. In general, APS yields a low-density ceramic topcoat attributed to the slow particle velocity at the exit of the chamber. APS achieves a ceramic topcoat with a theoretical density of 75-85%. The reduced density results from the formation of pores and cracks in the form of horizontal splat boundaries that are introduced on purpose, as shown in Fig. 1.26. These pores and cracks can provide high strain tolerance and low thermal conductivity to the coating at high temperatures so that the spallation and delamination failure can be minimized [142]. However, the duration of the TBCs processed by APS is limited due to and the rapid increase in the defects and roughness of the metal-ceramic interface in its service. Therefore, the use of the APS TBCs is restricted to the less severe applications such as stator vanes, fuel vaporizers, and flame holders [12].

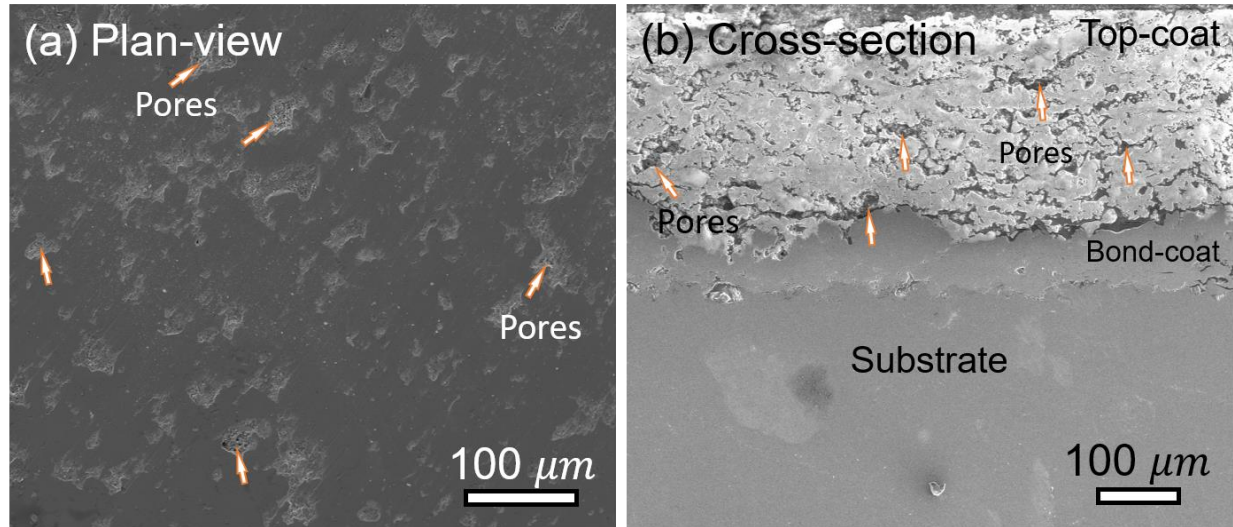


Figure 1.26. SEM images of APS TBC from (a) plan-view and (b) cross-sectional view showing a high density of pores and cracks.

1.6.4.2. E-beam physical vapor deposition

E-beam physical vapor deposition (EBPVD) for TBC applications consists of four main components, e-beam gun, Cu crucible containing the YSZ feedstock, metal substrate, and vacuum chamber [143]. The focused e-beam can melt the feedstock in the water-cooled Cu crucible, and the vaporized feedstock can condense onto the metal substrate. The EBPVD TBCs feature equiaxed grains at the interface of the bond-coat and top-coat underneath disconnected or loosely bonded columnar grains with a diameter of 2-10 μm as shown in Fig. 1.27. The separated columnar grains can provide the strain tolerance at high temperatures. However, due to the lack of the horizontal splat boundaries which causes the normal heat flow to the metal substrate, its thermal conductivity is somewhat higher than that of the APS TBCs ($\sim 1.5 \text{ W/m}\cdot\text{K}$ for APS TBCs vs $\sim 2.2 \text{ W/m}\cdot\text{K}$ for EBPVD TBCs) [143]. Because EBPVD can provide TBCs with a dense microstructure and smooth interface finish, it can be used in more severe applications than APS TBCs, such as high-pressure turbine section and rotating blades [142].

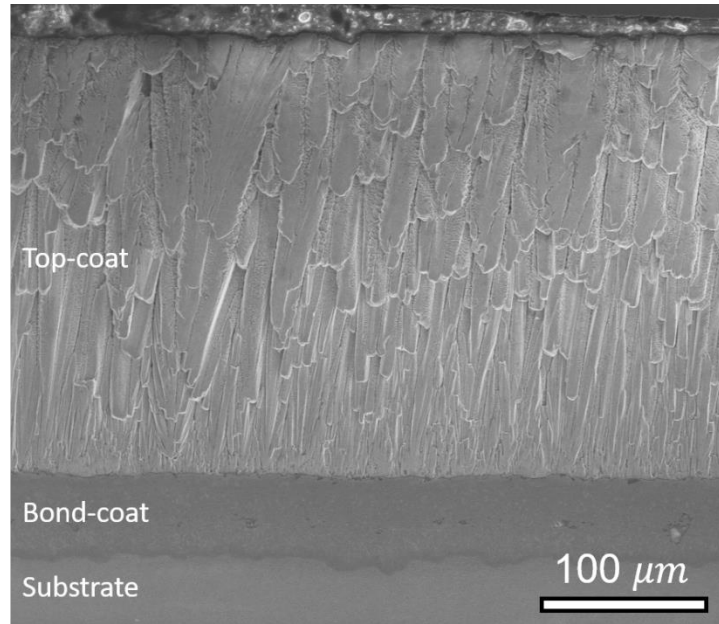


Figure 1.27. A cross-sectional SEM image of EBPVD TBC showing columnar grains on top of equiaxed grains at the interface of the topcoat and bond-coat.

1.6.4.3. Detonation gun thermal spray

Detonation gun thermal spray utilizes a mixture of oxygen and acetylene gas ignited by a spark in a chamber. The combustion can generate powerful detonation waves with a temperature of 4000°C and a velocity of 3500 m/s [144]. The ultrafast and hot gas stream can partially melt the YSZ feedstock and make it travel with a velocity of 1200 m/s towards the substrate. The high kinetic energy of the feedstock conveyed by the gas stream assures the top-coating with dense microstructure and strong adhesion at the interface, as shown in Fig. 1.28a. The detonation gun thermal spray also allows to prepare the TBCs with vertical cracks to the substrate, also known as dense vertically cracked (DVC) TBCs (Fig. 1.28b). The vertical cracks play the same role as the pores and splat boundaries in the APS TBCs and the disconnected columnar grains in the EBPVD TBCs. The cracks can reduce the thermal conductivity of the coat and provide the strain tolerance at high temperatures to avoid delamination of the coat and spallation failure. Since the DVC TBCs prepared by the detonation gun thermal spray has higher density and stronger adhesive strength than the others, it exhibits better Vickers hardness, as shown in Fig. 1.29. The hardness for the DVC TBC at room temperature is ~ 12 GPa comparable to that for the fully dense YSZ (10-14 GPa) and much higher than the other TBCs such as EBPVD TBC (2 GPa), APS TBC (3 GPa), and suspension plasma sprayed TBC (4 GPa).

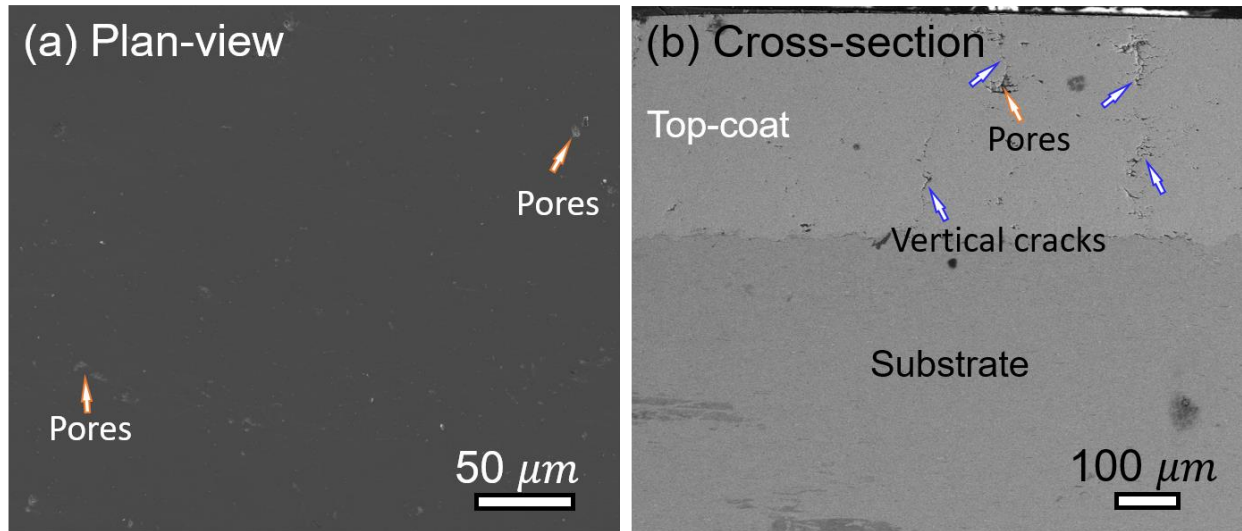


Figure 1.28. SEM images of DVC TBC prepared by detonation gun thermal spray from (a) plan-view and (b) cross-sectional view showing dense microstructure and vertical cracks.

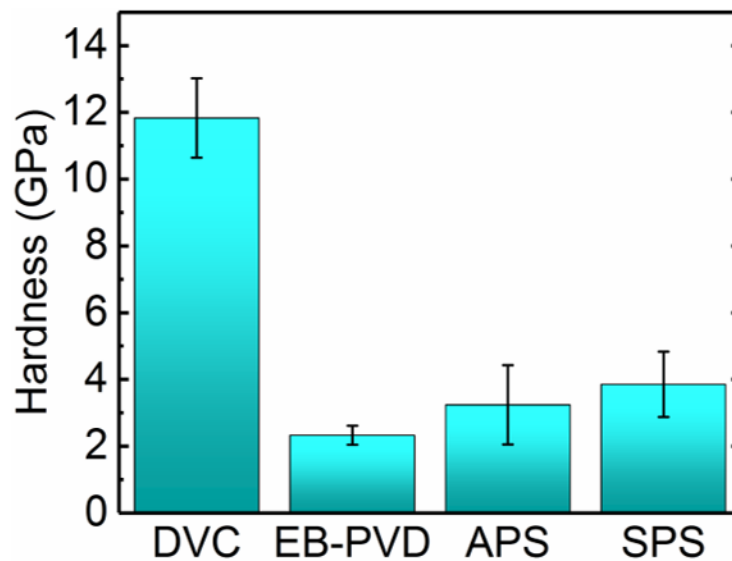


Figure 1.29. A plot of Vickers hardness for TBCs prepared by detonation gun thermal spray, EBPVD, APS, and suspension plasma spray.

1.7. Motivation and Objective

The motivation and objective of this thesis is to investigate micromechanical behavior and deformation mechanisms of ZrO_2 stabilized by the most common dopants (Y_2O_3 and MgO) and prepared by several techniques that include conventional firing, flash sintering, spark plasma sintering, air plasma spray, and detonation gun thermal spray. ZrO_2 is chosen to study the effects of processing techniques on the micromechanical properties because it has been widely used for

many applications that require a variety of processing methods. Furthermore, ZrO_2 is one of the most widely used structural ceramics due to its superb strength and fracture toughness that comes from several toughening mechanisms such as the martensitic transformation, ferroelastic domain switching, microcracking, and crack deflection. Processing parameters to consolidate ZrO_2 were decided in such a way that near theoretical density with ultrafine grains can be achieved. Micropillars fabricated on such samples have numerous grains so that they can somewhat represent the mechanical properties at mesoscale. *In-situ* microcompression tests were employed to study deformation mechanisms of ZrO_2 as a function of temperature, strain rate, and pillar diameters. The conclusions of each study were derived from extensive X-ray diffraction (XRD), SEM, energy-dispersive X-ray spectroscopy (EDS), EBSD, and TEM works on as-prepared and compressed samples.

CHAPTER 2. EXPERIMENTAL

2.1. Processing techniques

2.1.1. Powder preparation

ZrO₂ powders used in this thesis were purchased from Tosoh Corporation. Pure ZrO₂ (TZ-0, 40nm) and 3YSZ (TZ-3Y-E, 40 nm) were prepared by precipitation method from precursors, ZrOCl₂·8H₂O and YCl₃·6H₂O as a stabilizer. The co-precipitates were then dried, calcinated, milled, and spray dried to obtain non-stabilized and partially stabilized ultrafine granules. The chemical composition of pure ZrO₂ and 3YSZ is shown in Table 2.1.

Table 2.1. Chemical composition of non-stabilized ZrO₂ and 3YSZ from Torso Corp.

Chemicals	Pure ZrO ₂	3YSZ
Y ₂ O ₃ (mol%)	0	3
Y ₂ O ₃ (wt%)	0	5.2 ± 0.5
HfO ₂ (wt%)	< 5.0	< 5.0
Al ₂ O ₃ (wt%)	≅0.1	0.1 ~ 0.4
SiO ₂ (wt%)	≅ 0.02	≅ 0.02
Fe ₂ O ₃ (wt%)	≅ 0.01	≅ 0.01
Na ₂ O (wt%)	≅ 0.04	≅ 0.04

XRD data was collected from the 3YSZ raw powder used in this thesis to ensure the stability of the tetragonal phase and chemical composition. Fig. 2.1. shows XRD patterns from Tosoh TZ-3Y-E without heat treatment and typical tetragonal ZrO₂ indexed by PDF#83-0113. Tosoh TZ-3Y-E contains a small fraction of monoclinic ZrO₂ confirmed by XRD peaks at 28.17° and 31.47°, but a majority of the peaks come from tetragonal ZrO₂. The highest intensity of Tosoh TZ-3Y-E is found at 30.19° for the (101) plane of tetragonal ZrO₂, which is comparable to 30.204° for the same plane from PDF#83-0113. The minor difference (0.014°) in the two theta values indicates that the tetragonality of Tosoh TZ-3Y-E is comparable to that of 3YSZ indexed by PDF#83-0113, and thus the Y₂O₃ concentration of Tosoh TZ-3Y-E appears to be very close to 3 mol%.

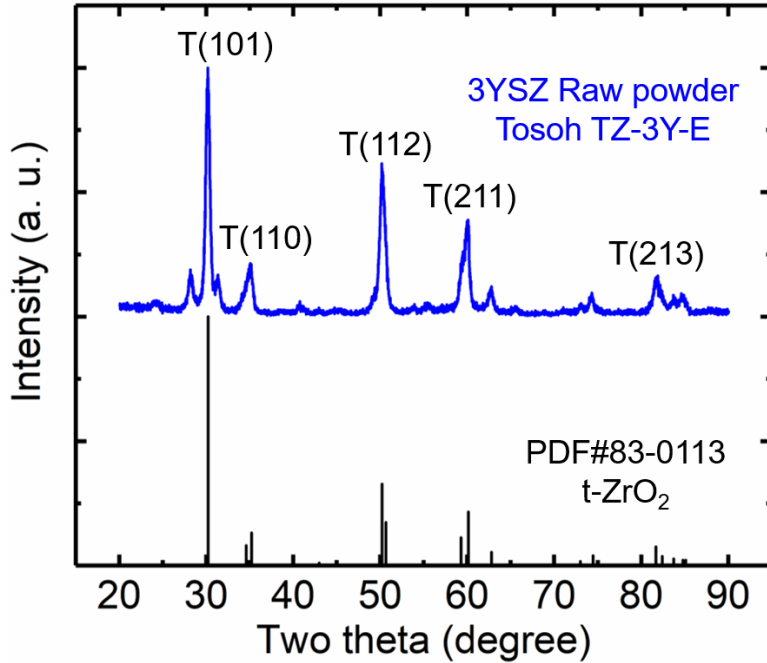


Figure 2.1. XRD patterns from 3YSZ raw powder (Tosoh TZ-3Y-E) and typical tetragonal ZrO_2 indexed by PDF#83-0113.

In a case where ZrO_2 needs to be stabilized by other stabilizers such as MgO , non-stabilized ZrO_2 was ball-milled in an aqueous media (methanol) with a stabilizer at a desired ratio in a vertical high energy planetary ball mill (VPMC-4, MSE Supplies, Fig. 2.2a) equipped with a chiller (Fig. 2.1b) to maintain a milling temperature at $\sim 0^\circ\text{C}$. The homogeneously mixed powders were then dried on a hot plate, calcinated, and dry-milled to remove agglomerates.



Figure 2.2. (a) Vertical high energy planetary ball mill and (b) chiller used in this thesis.

2.1.2. Flash sintering

Flash sintering experiments were carried out in a dilatometer (DIL801 Horizontal Dilatometer, TA Instruments). Pt electrodes are inserted in the dilatometer and connected to a direct current power supply (DLM 300-2, 300V, 2A, Sorensen). The Pt electrodes sandwich a green body sample, as shown in Fig. 2.3 to apply electric field. The temperature of the furnace can range from room temperature to 1500°C with a maximum heating rate of 25 °C/min. The assembly of the electrodes and the green body are pushed by an Al₂O₃ rod with a pressure of 10 kPa to maintain a rigid contact. During the flash experiments, furnace temperature and displacement of the sample are recorded by the dilatometer, and the power supply keeps track of the electric field, current density, and power density. Once the preset limit of the current density is reached, a programmed feedback loop in the power supply switches voltage control to current control mode and holds the preset current density for a desired holding time. To make a green body pellet, a raw power (0.3-0.4 g) was put in a stainless steel die with a diameter of 6 mm and uniaxially cold-pressed. The height of the green body sample was measured to preset the value of an electric field. The density of a green body ranges from 45 to 60% of a theoretical density in general.

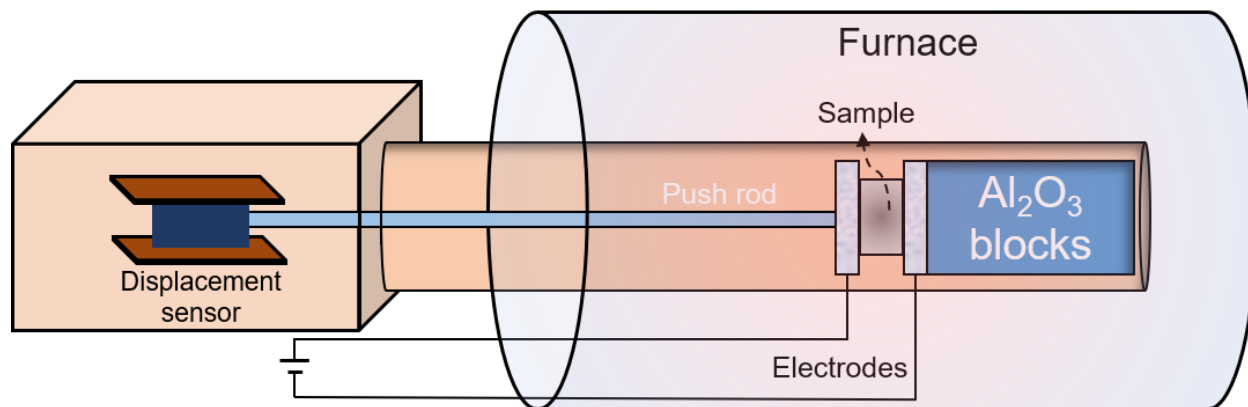


Figure 2.3. A schematic representation of an experimental setup for flash sintering.

2.1.3. Spark plasma sintering

A SPS system (SPS10, Thermal Technology, Fig. 2.4) is employed to produce dense ceramic pellets in this thesis. A graphite die with an inner diameter of 10 mm is filled with a raw powder (0.7 ~ 0.8 g) and wrapped by a graphite felt to prevent thermal emission during the sintering process. The sample temperature was monitored by a k-type thermocouple inserted through a hole of a graphite punch when the maximum temperature $\leq 1000^{\circ}\text{C}$, or a pyrometer aiming at a hole of the graphite die when the temperature $\geq 1000^{\circ}\text{C}$. The chamber is maintained at a low vacuum of $\leq 1 \times 10^{-2}$ torr and an external pressure from a hydraulic pressing system on top of the chamber can range 10 to 120 MPa. During the process, the software can record sample temperature, applied pressure, chamber pressure, voltage, current, ram displacement, and ram temperatures.

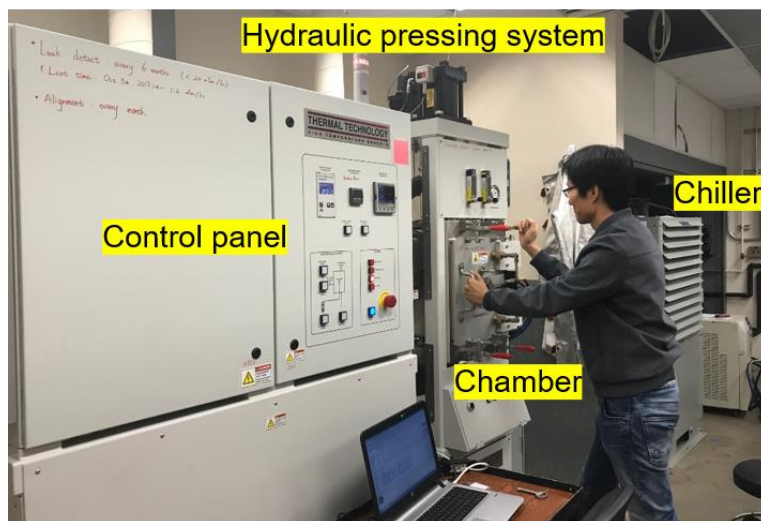


Figure 2.4. SPS system in Purdue University

2.1.4. Air plasma spray and detonation gun thermal spray

YSZ TBCs investigated in this thesis were provided by Praxair Surface Technologies. To deposit APS TBCs, a mixture of Ar and H₂ gas was introduced in a chamber to generate the plasma with a high enthalpy of the plasma plume. The addition of H₂ gas enables to melt YSZ feedstock that has a melting temperature of ~ 2700°C. 50 g/min YSZ feedstock was loaded into the plasma plume and, the plasma pushed the completely melted feedstock towards the metal substrate. The spray parameters were such that they could create a high density of desirable defects in the topcoat of the APS TBC applications such as microcracks, pores, and splat boundaries.

To deposit the DVC TBCs, a detonation gun (Super D-GunTM, Praxair Surface Technologies) was utilized. A mixture of the YSZ feedstock, oxygen, acetylene, and propylene with a spark at an appropriate time can create the combustion in an elongated chamber that can convey the high kinetic energy to the partially melted YSZ. A nitrogen sweep gas is introduced to clean the chamber after the detonation, and a mixture of the feedstock and reactive gases are reloaded for the next deposition. The feedstock with a high momentum can travel towards the metal substrate at a velocity of 1200 m/s, and thus dense TBCs with vertical cracks and strong bonding strength at an interface of the topcoat and bond-coat can be made.

2.2. Microstructure Characterization

2.2.1. Scanning electron microscope

SEM utilizes a focused electron beam landing on a surface of a sample to create an image. The interaction between the emitted electron beam and atoms of the sample surface can produce several signals that include secondary electrons, backscattered electrons, transmitted electrons, X-rays, and specimen current. The low energy secondary electrons ejected from the sample surface by inelastic scattering interaction can be collected by an Everhart-Thornley detector (ETD) [145]. The secondary electron image features well-defined topography attributed to the brightness difference between an edge and a flat surface of the sample. On the other hand, the high energy backscattered electrons from the electron beam are reflected by elastic scattering interaction with the sample surface [145]. Depending on the atomic number of the sample, the intensity of the backscattering electron varies. The heavier atoms can backscatter the electrons more strongly, thereby exhibiting brighter contrast than the lighter atoms. The backscattered electrons can also create EBSD image

that resolves crystallographic orientation and crystal structure of the sample. The X-rays originated from the interaction between the electron beams and the sample can be detected by EDS and provides chemical information.

Focused ion beam (FIB) utilizes a liquid metal ion source such as Ga. Once the Ga source is heated, it flows to the edge of W needle, where a high electric field is applied to form a Taylor cone. The radius of the cone is a few nanometers so that it can facilitate the use of FIB in a precise manner for nanostructure construction. In this thesis, FEI Quanta 3D FEG Dual Beam SEM/FIB (Fig. 2.5) was extensively used to fabricate TEM samples, micro, and nanopillars. Gas injection system with a primary source of Pt and Omniprobe micromanipulator system in the SEM were utilized to make TEM specimens for deformed pillars and samples difficult to prepare into a TEM lamella by manual polishing.

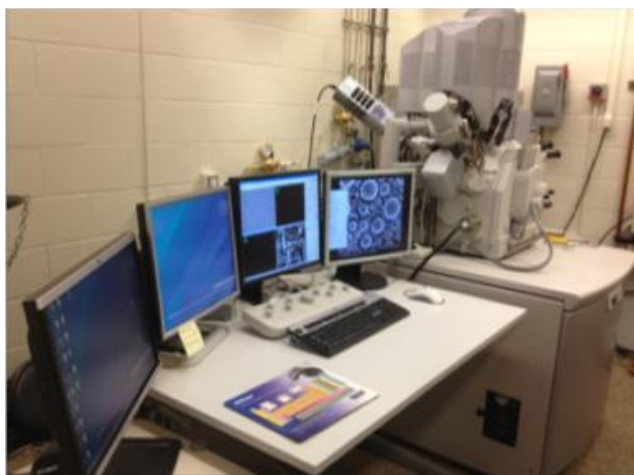


Figure 2.5. FEI Quanta 3D FEG Dual Beam SEM/FIB in Purdue University.

2.2.2. Transmission electron microscope

TEM can create an image of a sample by a beam of electrons transmitted through or diffracted by a specimen. The specimen thickness should be less than 100 nm to permit the electrons to traverse. TEM characterizes the microstructure of materials at the atomistic scale due to the small wavelength of electrons, and thus nanoscale defects in ceramics such as point defects, dislocations, stacking faults, secondary phase, and twin boundaries can be resolved in TEM [146]. This instrument has several different operating modes involving bright-field, dark-field, electron diffraction, scanning TEM, precession electron diffraction, and a combination of these. In this

thesis, An FEI Talos 200X TEM/STEM (Fig. 2.6) with ChemiSTEM technology (X-FEG and SuperX EDS with four silicon drift detectors) was employed at electron accelerating voltage of 200 kV. Bright-field and dark-field modes are utilized to observe general microstructure (grain size and grain morphology), and defects like dislocations, twin boundaries, and stacking faults. Phase analysis and texture study were conducted by selected area electron diffraction mode. Scanning TEM and EDS were used for chemical characterization such as atomic distribution, chemical segregation, and precipitate identification.

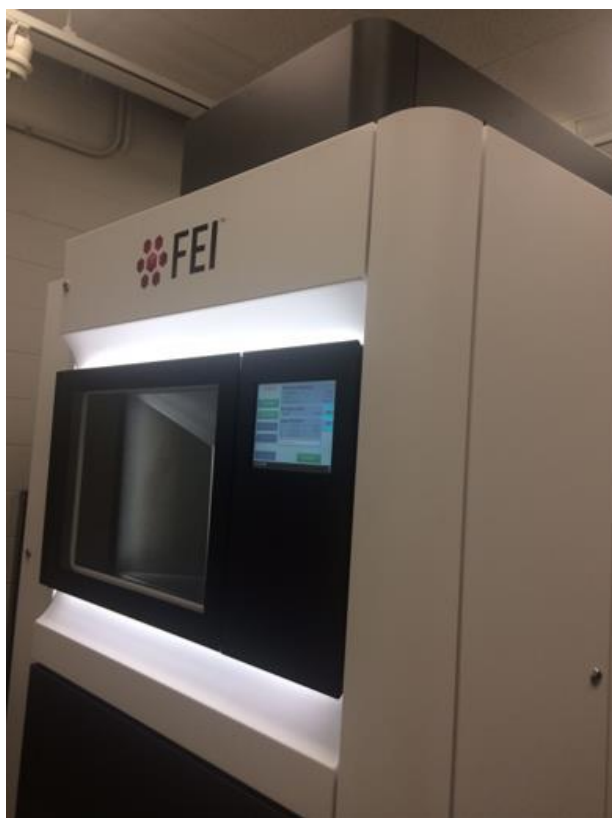


Figure 2.6. FEI Talos 200X TEM/STEM in Purdue University.

2.3. Micromechanical properties

2.3.1. *In-situ* micropillar compression

Micropillars with an aspect ratio of 2-3 were fabricated by FIB and compressed by a Hysitron PI 88×R PicoIndenter inside SEM (FEI Quanta 3D FEG) as shown in Fig. 2.7a. The microcompression system contains a piezoelectric actuator on the capacitive transducer that collects force-displacement data. The sample stage enables to meticulously adjust the position of

the micropillars in five directions (x, y, z, tilt, and rotation). Diamond or W flat punch tips with a diameter of 5, 10, and 20 μm designed for high-temperature compression experiments were used for the micromechanical testing at various temperatures (25-670°C). Before compressing each pillar, an average drift rate and noise level were measured in the preloading session for 45 s to precisely collect the load and displacement data. For high-temperature tests (Fig. 2.7b), the flat punch designed for high temperatures was attached to a probe heater, and a V-shaped Mo clamped a sample to a ceramic stage heater. The probe and stage heaters were simultaneously heated at a rate of 10-25 °C/min and isothermally preserved at a desired temperature for 30 min before conducting a compression test to eliminate the thermal and mechanical drifts. When the measured drift rate is within 0-0.5 nm/s and the noise level is less than 8 μN , the compression tests were carried out.

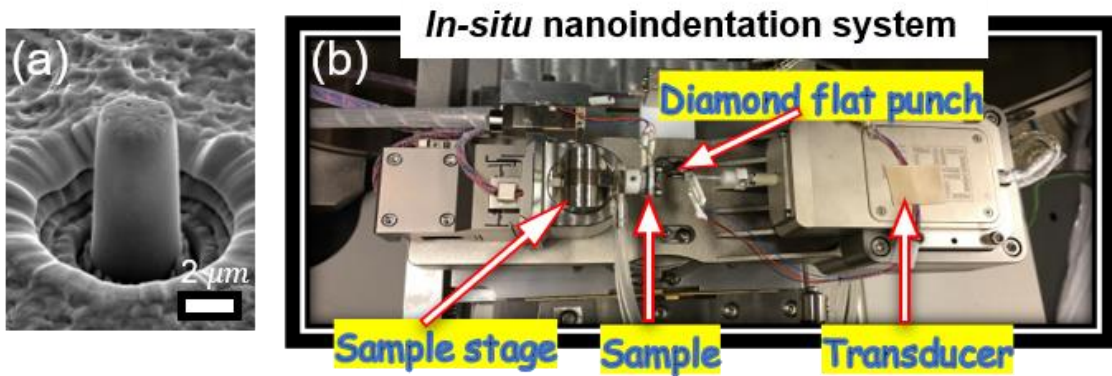


Figure 2.7. Micropillar and *In-situ* nanoindentation system used in this study.

2.3.2. Vickers hardness

Vickers hardness test utilizes a pyramidal diamond indenter to measure a hardness of a material. To define the hardness known as Vickers Pyramid Number (HV) that can be converted to a unit of pascal, a length of the diagonal marked by the diamond indenter and an applied force need to be identified. HV can be given as [147],

$$HV = \frac{1.8544F}{d^2} \left[\frac{\text{kgf}}{\text{mm}^2} \right] \quad (2.1)$$

where F is the force in kg·f, and d is the diagonal length in mm. Then, HV can be converted to a unit of GPa using a conversion factor of 0.0098. In this thesis, a microhardness tester (LECO Corporation, LM 247AT) equipped with a Vickers tip and optical microscope was employed for

Vickers hardness measurements. Numerous indents were made on samples with a load ranging from 50 to 1000 g·f. Lengths of diagonal indent were measured under an SEM to calculate the microindentation hardness precisely.

CHAPTER 3. HIGH TEMPERATURE DEFORMABILITY OF DUCTILE FLASH SINTERED CERAMICS BY IN-SITU COMPRESSION

The following chapter contains content reproduced with permission from “Jaehun Cho, Qiang Li, Han Wang, Zhe Fan, Jin Li, Sichuang Xue, Suryanarayana Karra, Haiyan Wang, Troy B. Holland, Amiya K. Mukherjee, R. Edwin García and Xinghang Zhang. “High temperature deformability of ductile flash sintered ceramics by in-situ compression.” *Nature Communications* 9:2063 (2018): 1-9.” Copyright 2018 Springer Nature

3.1. Overview

Flash sintering has attracted significant attentions lately as its remarkably rapid densification process at low sintering furnace temperature leads to the retention of fine grains and enhanced dielectric properties. However, high temperature mechanical behaviors of flash-sintered ceramics remain poorly understood. Here, we present high temperature (up to 600°C) *in-situ* compression studies on flash sintered yttria-stabilized zirconia (YSZ). Below 400°C, the YSZ exhibits high ultimate compressive strength exceeding 3.5 GPa and high inelastic strain (~ 8%) due primarily to phase transformation toughening. At higher temperatures, crack nucleation and propagation are significantly retarded, and prominent plasticity arises mainly from dislocation activity. The high dislocation density induced in flash-sintered ceramics may have general implications for improving the plasticity of sintered ceramic materials.

3.2. Introduction

Ceramic materials have a variety of high temperature applications, such as thermal barrier coatings for high-thrust engines and turbines [12]. One promising candidate for thermal barrier coatings is yttria-stabilized zirconia (YSZ). YSZ offers one of the lowest thermal conductivities, ~ 2.3 W/mK at ~ 1000°C [148]. Monolithic zirconia has monoclinic phase [space group $P2_1/c$] at room temperature. However, the tetragonal phase [space group $P4_2/nmc$] of zirconia can be stabilized by doping zirconia with Y_2O_3 , CeO_2 , and MgO [2,3]. The discovery of martensitic phase transformation (from tetragonal to monoclinic phase) in ZrO_2 has led to significant investigations on its deformability. The volume expansion (~ 4%) during martensitic phase transformations near the crack tips induced by an external stress can introduce compressive stress that can in turn retard crack propagation [9,10]. Therefore, YSZ provides new opportunities for various applications,

including reliable thermal and environmental barrier coatings, solid oxide fuel cells, and shape memory devices, just to name a few [12–14].

A majority of ceramic materials possess high strength but low toughness at low temperature due to the lack of dislocation enabled deformability [8]. Certain nanostructured ceramics have shown high strength, wear resistance and/or fracture toughness at elevated temperatures [149–151]. However, conventional sintering typically requires very high temperature and long sintering time and thus leads to significant grain coarsening [152]. Recently, it has been discovered that YSZ can be fully densified within a few seconds at a temperature much lower than conventional sintering temperature by a novel sintering technique named flash sintering [58]. The ultra-fast sintering technique enables the retention of nanograins and enhanced dielectric properties [153]. Flash sintering occurs by applying a ramp heating process at a constant heating rate under moderate electrical fields [63,71,72,75,154–158]. Once the temperature is above the onset of the flash temperature, under applied electrical field, a densification process takes place within a few seconds as evidenced by a sudden increase of electrical conductivity, accompanied with drastic increase in mass density [80].

Prior studies on the mechanical behaviors of YSZ showed superelasticity and shape memory effect at room temperature [40,41,43,45,46]. However, our understanding of the mechanical behaviors of small scale YSZ specimens at elevated temperatures remains limited. Recently, Korte and Clegg showed that microcompression tests on small specimens can be carried out at an elevated temperature ($\sim 500^\circ\text{C}$) by heating the sample stage and indenter tip without a significant mechanical and thermal drift ($\sim 1 \text{ nm/s}$) [49,50]. High-temperature micropillar compression technique enables the study on the temperature dependent deformation mechanisms for brittle materials at elevated temperatures. Furthermore, the deformability of flash-sintered ceramics is largely unknown despite an intriguing microstructure including the generation of a large number of charged defects during the flash sintering process [80].

Here, we report *in-situ* micropillar compression studies on the deformability of a flash sintered 3 mol % yttria stabilized zirconia (3YSZ) at elevated temperatures (up to 600°C). The flash sintered 3YSZ contains abundant dislocations. The mechanical behaviors of the flash-sintered 3YSZ are highlighted by increased plasticity, and temperature dependent transition of deformation mechanism.

3.3. Experimental

3.3.1. Flash sintering

Flash sintering was performed on a custom-modified thermomechanical testing system (SETSYS Evolution, SETARAM Instrumentation). Specimens with a diameter of 5 mm and a thickness of 2 mm prepared by using commercially available 3YSZ (TZ-3Y-E, Tosoh corp., 40 nm particle size) were sandwiched between two platinum electrodes. An alumina rod was utilized to apply minimum pressure (a few kPa) to ensure rigid contact between the electrodes and sample. A DC power of various voltage was applied to achieve electric field of 1.5, 15, and 150 V/cm with a constant heating rate of 25°C/min (maximum temperature was set to 1300°C). The experiment was performed in the presence of air. After the onset of flash, the system was switched from the voltage control mode to a current control mode. The experiment was terminated right after switching to current control mode to prohibit grain growth. The linear shrinkage of the samples was measured by a dilatometer.

3.3.2. TEM sample preparation

Plan-view TEM samples of flash sintered 3YSZ were prepared through the conventional approach, which includes manual grinding, polishing, dimpling and final polishing in an ion milling system (PIPS II, Gatan). Low energy ion polishing (2 kV) was used to minimize ion milling-induced damage. An FEI Talos 200X TEM/STEM with ChemiSTEM technology (X-FEG and SuperX EDS with four silicon drift detectors) operated at 200 kV was used in this study for microstructure characterization and energy-dispersive X-ray spectroscopy (EDS) chemical mapping.

3.3.3. Microcompression test

Before preparing micropillars, as-sintered YSZ was polished with SiC sandpapers, ~ 1 μm diamond papers, and ~ 20 nm colloidal silica to minimize the roughness of the surface. Then micropillars of flash sintered 3YSZ with ~3 μm in diameter and a diameter-to-height aspect ratio of 1:3-1:2 were prepared using focused ion beam (FEI quanta 3D FEG) and a series of concentric annular milling and polishing with progressively de-escalated currents were adopted to reduce tapering angle. Micropillars were fabricated in a dense area judged by SEM in the central region of the specimen to avoid inhomogeneous microstructure that often appears near the sample edge.

Micropillar compression experiments have been performed using a Hysitron PI 87×R PicoIndenter equipped with a piezoelectric actuator on the capacitive transducer that enables the collection of force-displacement data inside a scanning electron microscope (FEI quanta 3D FEG). Moreover, a 20 μm diamond flat punch tip designed for high temperature compression experiments was used to conduct *in-situ* compression experiments and the geometric variation of micropillars was synchronized to evolving force-displacement curve. For high temperature *in-situ* compression setups, the flat punch was fastened to probe heater and the specimens were clamped by a V-shaped molybdenum to a ceramic heating stage. The temperature on two heating terminals were simultaneously ramped up at a rate of 10 °C/min and isothermally preserved for 30 min before implementing every single compression experiment to eliminate the thermal-driven drifts on both probe and stage sides. An average drift rate of 0.2-0.5 nm/s was estimated in preloading process for 45 s and the estimated force noise level is less than 8 μN prior to compression. An overestimation of specimen displacement during the compression test induced by a displacement associated with the measuring instrument (machine compliance) was systematically measured during *in-situ* SEM studies and corrected.

3.3.4. Finite element analysis

The microstructure shown in Fig. 3.1a with three different grain orientations was subjected to a compression of −200MPa in the in-plane vertical direction, while the bottom boundary was fixed, and the out-of-plane state of stress was set to plane strain conditions. Material properties are summarized in Table 3.1. Assigned Euler angle orientations are, for the bottom grain, $(\alpha, \beta, \gamma) = (0,0,0)$, for the top-right grain, $(\alpha, \beta, \gamma) = (0, 45, 0)$ and for the top-left grain, $(\alpha, \beta, \gamma) = (45, 45, 0)$. Euler angles operations are: first rotate angle b degrees about the z-axis, then rotate a degrees about the y-axis, and finally rotate g degrees about new z-axis. The mechanical equilibrium state of the polycrystalline was solved using OOF2 [159], an open source implementation of the finite element method. The relative numerical tolerance was set to 1×10^{-10} . The simulation used 40 GB of RAM and a wall time of approximately 4 h.

Table 3.1. Elastic properties of tetragonal zirconia [15]

C_{11} (GPa)	C_{12} (GPa)	C_{13} (GPa)	C_{33} (GPa)	C_{44} (GPa)	C_{66} (GPa)
395	26	105	326	42	56

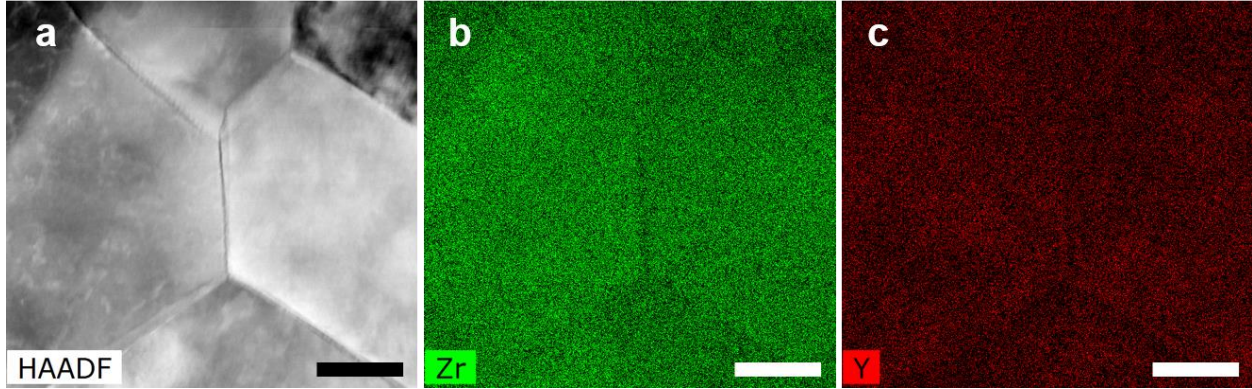


Figure 3.1. STEM micrograph. **a** A STEM micrograph of the flash-sintered 3YSZ showing several triple junctions among grains. Scale bar, 60 nm. **b-c** The EDS mapping of zirconium and yttrium. Note that zirconium and yttrium are nearly uniformly distributed throughout the grains. The grain boundaries appear to have slight deficiency in zirconium. Scale bar, 60 nm.

3.4. Results

3.4.1. Microstructural characterization

3YSZ (TZ-3Y-E, Tosh corp., 40 nm) was heated in a thermomechanical analyzer with platinum electrodes at a constant heating rate of 25°C/min under an electrical field of 150 V/cm. The ultrafast densification process occurred at a furnace temperature of 1150-1200°C in a few seconds (Fig. 3.2), which is significantly lower compared to conventional sintering temperature of ~ 1900°C to sinter 3YSZ in just a few seconds [160]. The applied heat and electrical field were removed right after the onset of flash sintering to prevent grain growth. Even though the densification process of 3YSZ occurred at relatively low temperature, X-ray diffraction pattern shows a dominant tetragonal phase without evident monoclinic and cubic phases (Fig. 3.3). To evaluate the residual stress that may be formed during flash sintering, X-ray peak broadening in Fig. 3.3 was systematically investigated by the Williamson-Hall analysis. The Williamson-Hall equation for the stress calculation can be written as [161],

$$\beta_{hkl} \cos\theta = \frac{K\lambda}{D} + 4\sin\theta\sigma/E_{hkl} \quad (3.1)$$

where β_{hkl} is the peak broadening at half the maximum intensity in the unit of radians, K is the shape factor, λ is the X-ray wavelength, D is the mean size of crystalline, σ is the residual stress, and E_{hkl} is the elastic modulus along $[hkl]$ direction. The elastic moduli along $[hkl]$ direction for a tetragonal structure is given as [162],

$$\frac{1}{E_{hkl}} = S_{11}(\alpha^4 + \beta^4) + (2S_{13} + S_{44})(\alpha^2\gamma^2 + \beta^2\gamma^2) + S_{33}\gamma^4 + (2S_{12} + S_{66})\alpha^2\beta^2 \quad (3.2)$$

where S_{ij} are the elastic compliance constants, and α, β , and γ are the directional cosines of the $[hkl]$ direction and the X, Y, and Z axis. The elastic compliance constants for tetragonal ZrO₂ are shown in Table 3.2.

Table 3.2. The elastic compliance constants for tetragonal ZrO₂ [163].

Compliance	Values
S ₁₁	0.0038473
S ₁₂	-0.0021833
S ₁₃	-0.000402
S ₃₃	0.0029956
S ₄₄	0.0193874
S ₆₆	0.0054999

With the elastic moduli along $[hkl]$ direction obtained using Eq. 3.2 and Table 3.2, $\beta_{hkl}\cos\theta$ can be plotted as a function of $4\sin\theta/E_{hkl}$ and the slope of the line regression line is the residual stress residing in the flash-sintered 3YSZ as shown in Fig. 3.4. The residual stress was determined to be 229.5 MPa. Energy dispersive spectroscopy reveals that zirconium and yttrium are uniformly distributed throughout the grains, and zirconium is slightly deficient along grain boundaries (Fig. 3.1). Fig. 3.5a shows a scanning electron microscopy (SEM) image of an unpolished flash-sintered 3YSZ. An average grain size of 870 nm was determined by a systematic grain intercept method (Fig. 3.6) [164]. However, bright-field transmission electron microscopy (TEM) micrograph reveals the existence of subgrains as shown in Fig. 3.5b. The average subgrain size is 159 nm. The flash-sintered 3YSZ was densified to 98% of theoretical density (determined by numerous micrographs) with nanopores indicated by red arrows in Fig. 3.5b. Black arrows in Fig. 3.5b indicate internal defects in grains generated during the flash sintering process. Deformation twinning which is frequently observed in bulk tetragonal zirconia [165] was rarely observed in this study, which may be due to the ultrafine grain sizes.

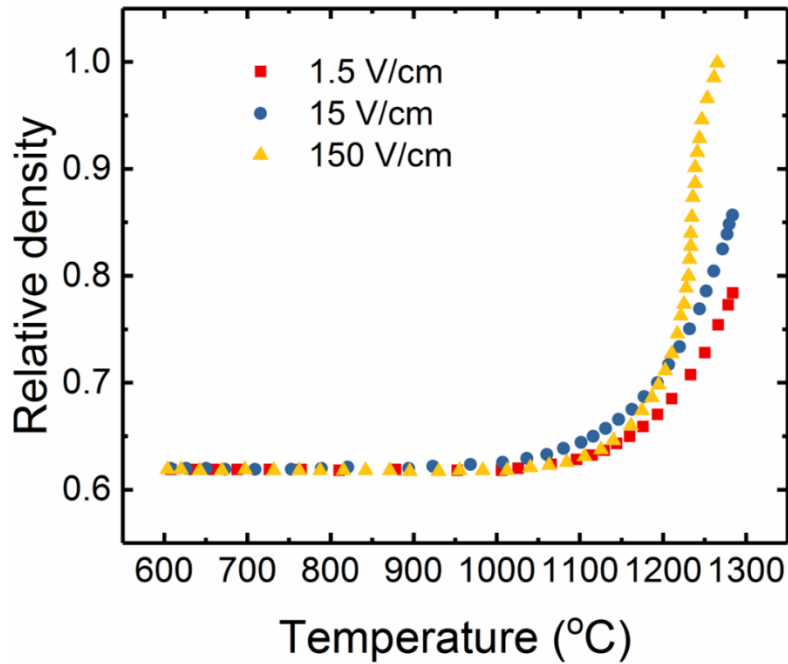


Figure 3.2. Relative density comparing to theoretical value as a function ramping temperature during flash sintering. 3YSZ was sintered at a constant heating rate of 25°C/min under an electrical field of 1.5, 15, and 150 V/cm. Flash sintering under an electric field of 150 V/cm took place at 1,150-1,200°C in a few seconds.

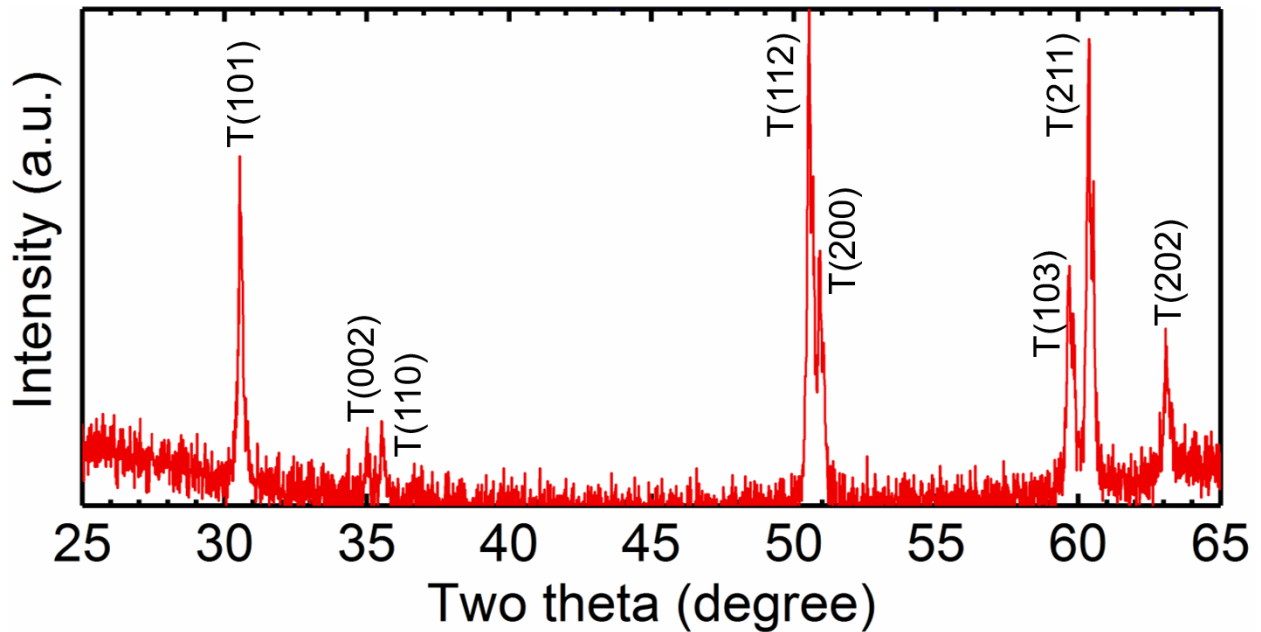


Figure 3.3. XRD patterns of flash sintered 3YSZ at an electrical field of 150 V/cm, showing dominant metastable tetragonal phase and crystallographic plane indices.

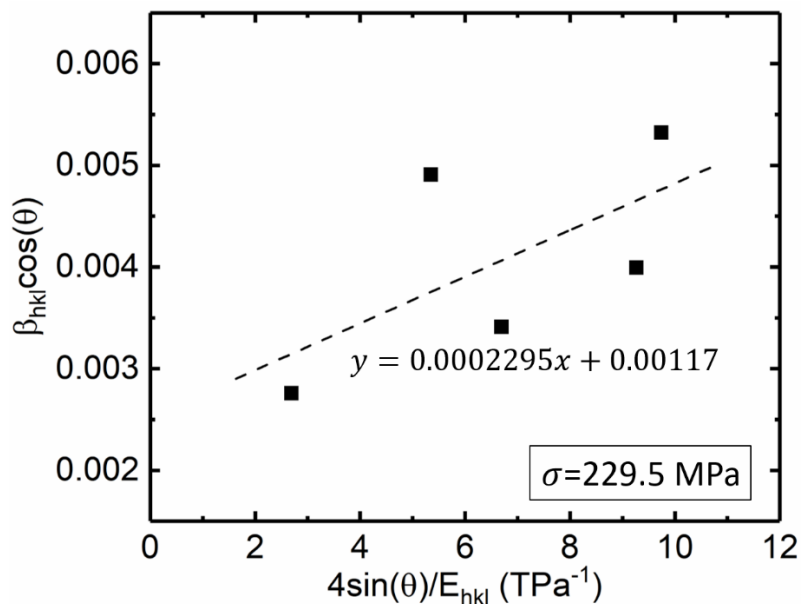


Figure 3.4. The determination of the residual stress using the Williamson-Hall analysis.

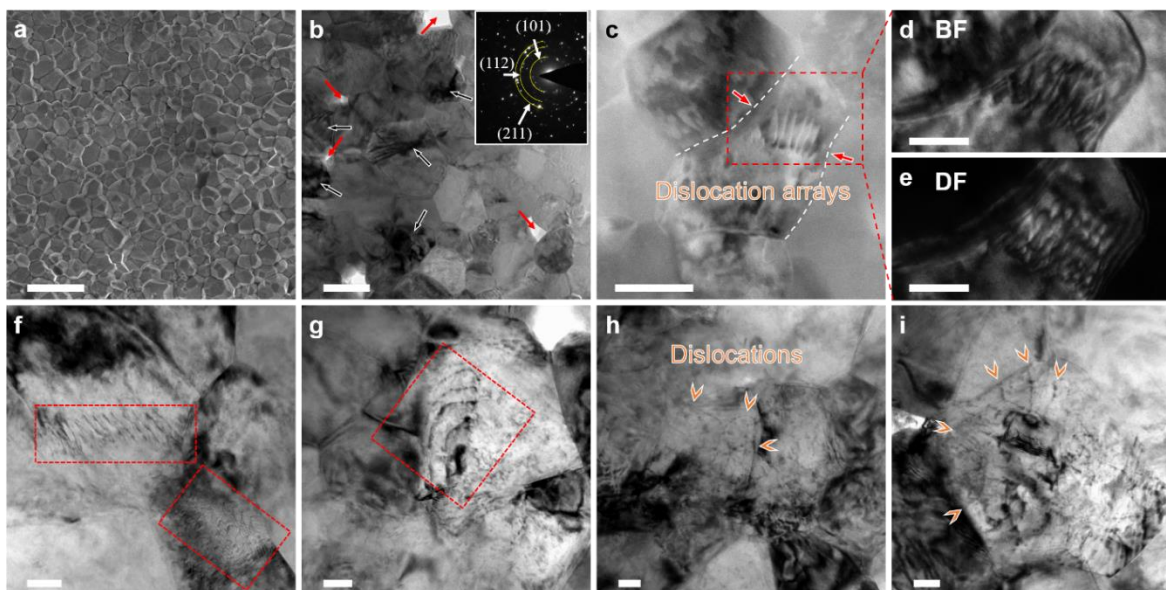


Figure 3.5. Microstructure of flash-sintered 3YSZ. **a** SEM images of the unpolished flash-sintered 3 YSZ. The average particle size is $\sim 1 \mu\text{m}$. Scale bar, $3 \mu\text{m}$. **b** Bright-field TEM micrograph showing subgrains with grain boundaries and defects generated during flash sintering (labeled by black arrows) and nanopores ($\sim 1.4\%$) (indicated by red arrows). The inserted SAD pattern shows diffraction rings. Scale bar, 200 nm . **c** A STEM micrograph showing a dislocation array inside a grain in the flash sintered 3YSZ. The dislocation array was generated in a bottleneck region of the grain as indicated by red arrows. Scale bar, 100 nm . **d-e** Bright-field (BF) and dark-field (DF) TEM micrographs showing the dislocation array in the boxed region in **c**. Scale bar, 50 nm . **f-i** Numerous BF TEM images of the flash sintered 3YSZ showing the existence of dislocations and dislocation arrays in grains. Scale bar, 50 nm .

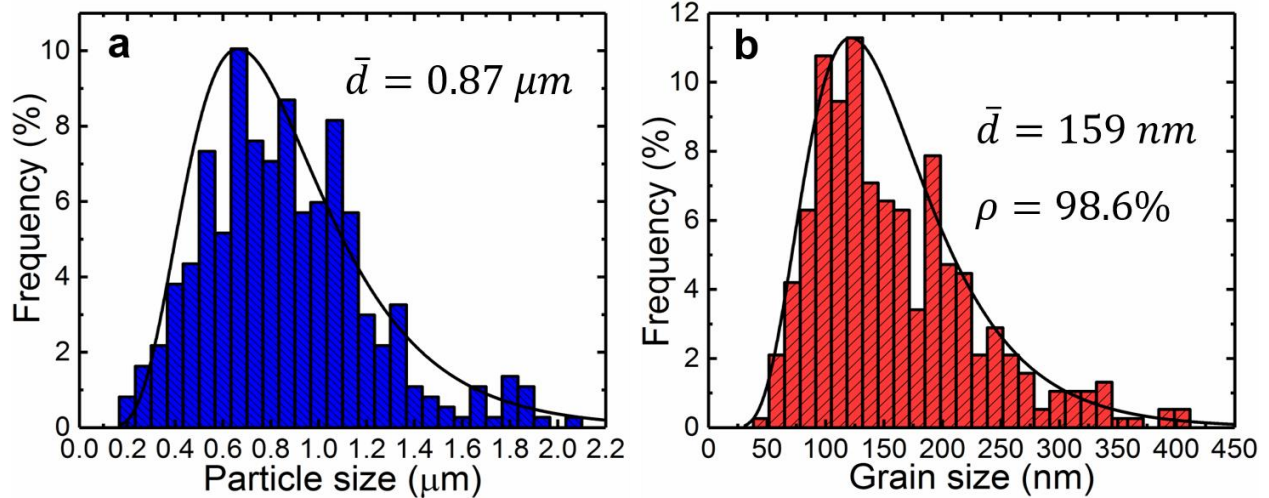


Figure 3.6. Grain size distribution. **a** Agglomerated particle size distribution and **b** subgrain size distribution of flash- sintered 3YSZ calculated by systematic grain intercept method. The average grain size and subgrain size are $0.87 \mu\text{m}$ and 159 nm , respectively. The density of flash-sintered ceramic is $\sim 98\%$.

3.4.2. Preexisting dislocations

Many of the defects in the grains are identified to be high-density dislocation networks (Fig. 3.7). Furthermore, scanning TEM (STEM), bright-field and dark-field TEM micrographs in Fig. 3.5c, d and e show an array of dislocations inside a grain. Also, the dislocation arrays were observed frequently in the flash-sintered 3YSZ as can be seen in bright-field TEM micrographs in Fig. 3.5f-i and Fig. 3.8. Meanwhile, 3YSZ synthesized at lower electric fields (1.5 V/cm and 15 V/cm) and at the same heating rate (25°C/min) was also prepared to study the effect of electric field on the dislocation generation. The relative density of 78 and 85% was achieved for the 1.5 and 15 V/cm specimens, respectively (Fig. 3.2). The grain intercept method [164] reveals average grain sizes of 59 ± 7 and $57 \pm 9 \text{ nm}$ for 3YSZ sintered under 1.5 and 15 V/cm , respectively. The TEM studies reveal little dislocations or dislocation arrays in these specimens (Fig. 3.9).

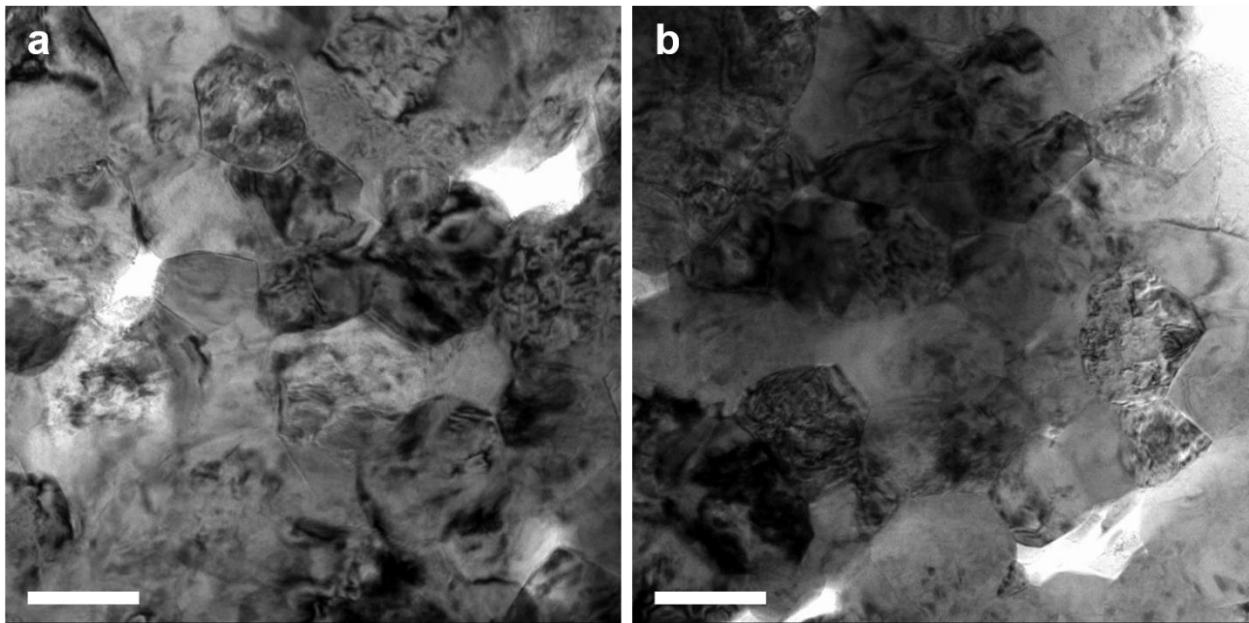


Figure 3.7. Bright-field TEM images of flash-sintered 3YSZ under an electric field of 150 V/cm indicating the existence of grains with significant internal defects. Many of these internal defects appear to be high-density dislocation networks. Scale bar, 200 nm.

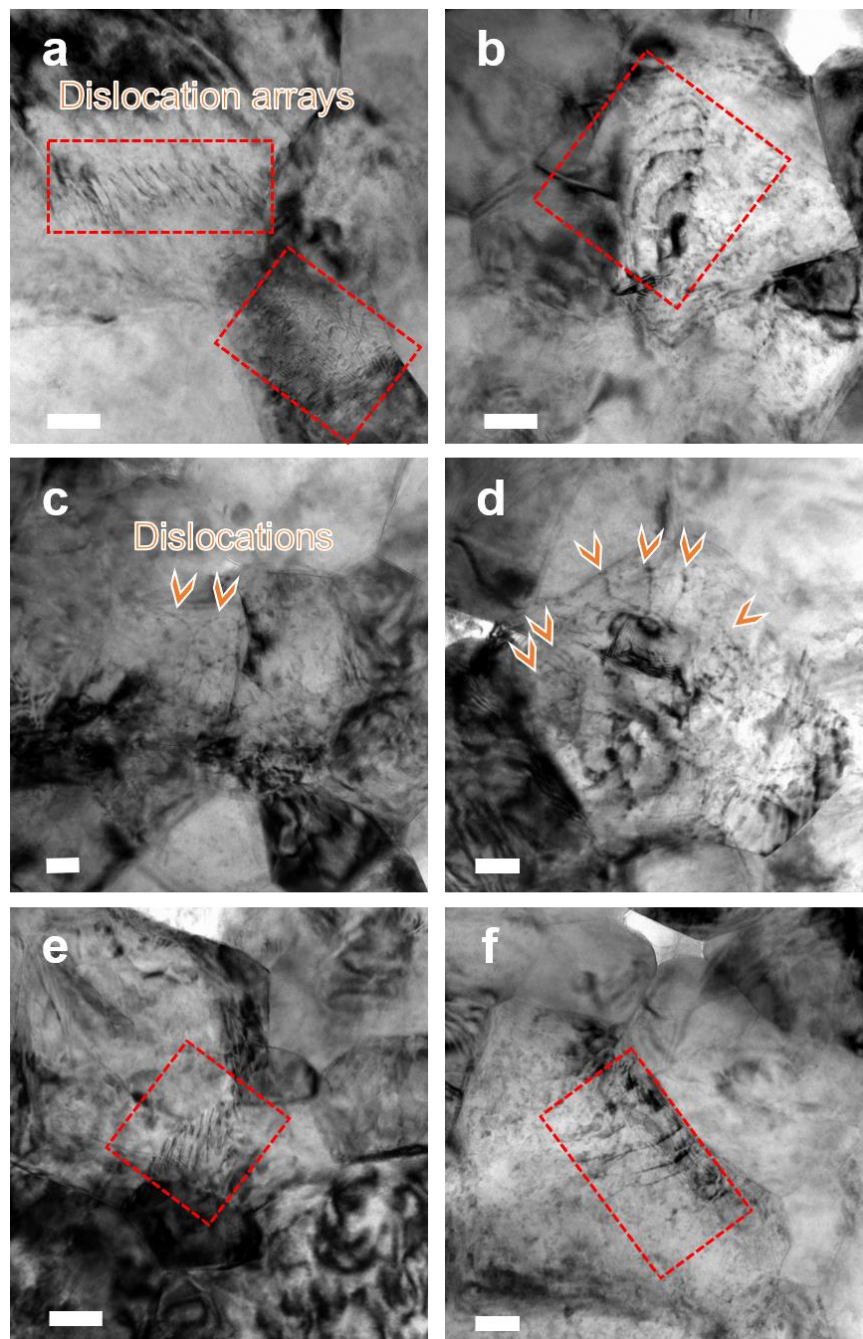


Figure 3.8. Bright-field TEM micrographs. **a-f** Bright-field TEM images of the flash sintered 3YSZ showing the existence of dislocations and dislocation arrays in grains. Dislocation arrays were frequently observed near triple junctions. Dislocations may arise from the large stress concentration near triple junctions induced during flash-sintering of 3YSZ. Scale bar, 50 nm.

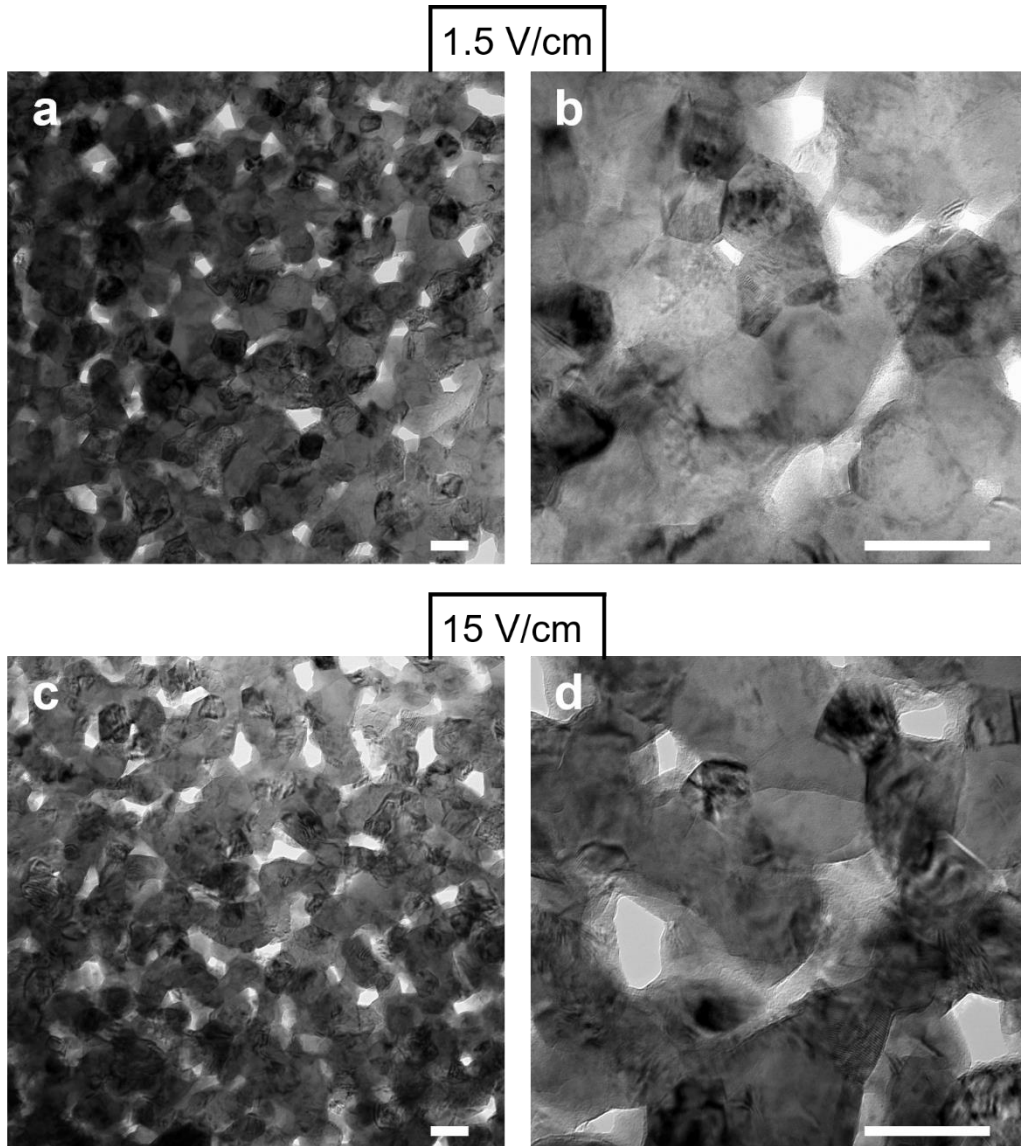


Figure 3.9. Bright field TEM images of 3YSZ processed under 1.5 V/cm and 15 V/cm showing nanograins. **a-b** 3YSZ sintered under 1.5 V/cm. Scale bar, 100 nm. **c-d** 3YSZ sintered under 15 V/cm. Scale bar, 100 nm. Dislocations and dislocation arrays rarely exist inside the grains unlike 3YSZ sintered under 150 V/cm.

3.4.3. *In-situ* microcompression tests

Micropillars with 3 μm in diameter and 6 μm in height were fabricated using the focused ion beam (FIB) technique on the flash-sintered 3YSZ. Taking into consideration the average subgrain size of the specimen, ~ 160 nm, each pillar contains more than 5,000 subgrains. Thus, the mechanical behaviors of the micropillars are a good representation of a large number of grains. Uniaxial *in-situ* microcompression tests on the micropillars were carried out from room

temperature to 600°C at a constant strain rate of $5 \times 10^{-3} \text{ s}^{-1}$ inside an SEM microscope with partial unloading at strain of 0.5 and 1%, to evaluate the apparent elastic modulus at each test temperature. Fig. 3.10 shows snapshots of SEM images taken during the *in-situ* compression tests of micropillars at different strain levels at room temperature and 400°C. Micropillars compressed at room temperature sustained a strain up to 8% without crack formation, and then experienced brittle catastrophic fracture at a strain of ~ 9%. For micropillars tested at 400°C, cracks nucleated at smaller strain, ~ 4%, and a greater crack density was observed comparing to the specimens tested at room temperature. Meanwhile, cracks propagated downward gradually along the axial (loading) direction, but no catastrophic failure was observed. Fig. 3.10i shows that the maximum flow stress exceeds 3.5 GPa in specimens tested at room temperature; whereas the peak stress reaches 2 GPa for specimens tested at 400°C at a true strain of 4%, and the stress decreases thereafter.

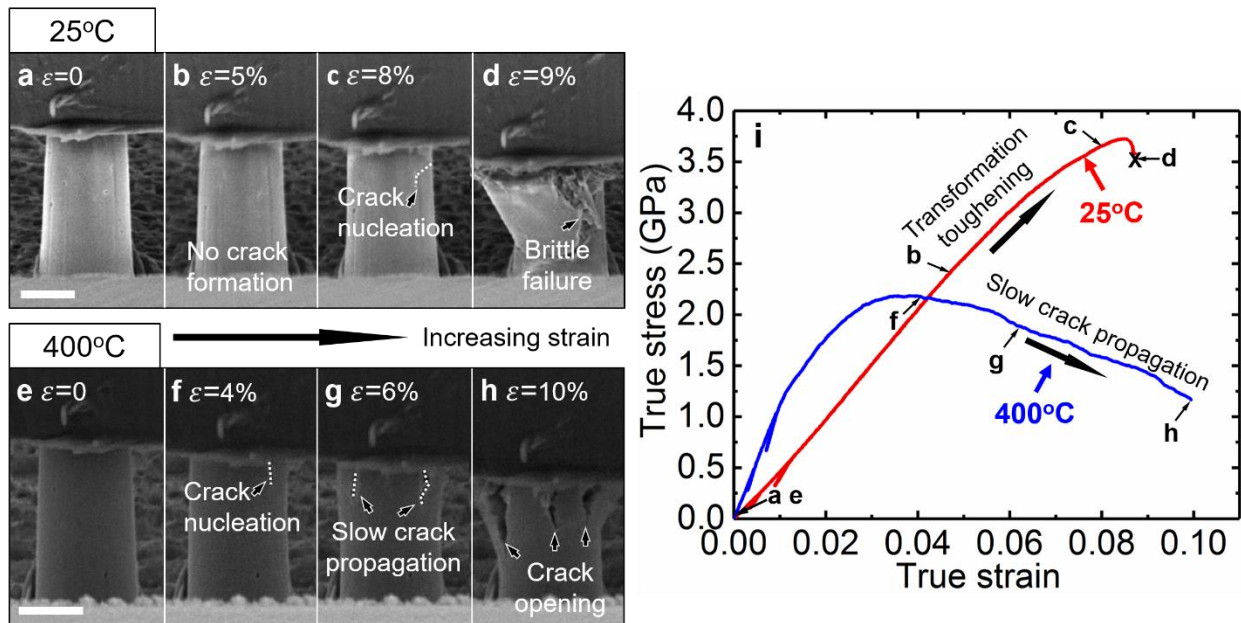


Figure 3.10. Uniaxial *in situ* microcompression tests on the flash sintered 3YSZ at room temperature and 400°C at a constant strain rate of $5 \times 10^{-3} \text{ s}^{-1}$. **a-d** SEM images during *in situ* compression test of micropillars at different strain levels at 25°C. No crack can be detected until a true strain of 8%. At the strain of 9%, the pillar experienced brittle catastrophic fracture. Scale bar, 2 μm . **e-h** For micropillars tested at 400°C, cracks nucleated at smaller strain, ~ 4%. Crack density increased with compressive strain. However, cracks propagated downward gradually and slowly without catastrophic failure. Scale bar, 2 μm . **i** The corresponding true stress-strain curve shows that the flow stress exceeds 3.5 GPa for pillars tested at 25°C. In comparison, the pillar tested at 400°C has a flow stress of 2 GPa and higher elastic modulus.

3.4.4. Temperature dependence of deformation mechanisms

Fig. 3.11a-j compare SEM images of flash sintered 3YSZ micropillars before and after microcompression tests at various temperatures. It shows that 400°C is a fiducial temperature at which fracture mechanisms change drastically. At 25 and 200°C, the micropillars, though they sustained a large strain, fractured in a brittle (catastrophic) manner. On the other hand, when tested between 400 to 600°C, multiple cracks initiated and propagated from the top surface down into the pillars, leading to the formation of cauliflower morphologies at the top of the pillars (Fig. 3.11f, h, and j). As the test temperature rose, a prominent decrease of crack density and propagation was observed, implying that a new deformation mechanism began to govern the inelastic behavior of the pillars at 400°C and beyond. Fig. 3.11k compares corresponding stress-strain curves of pillars tested at different temperatures with black arrows, indicating the ultimate compressive strength (UCS) of the pillars. Five true stress-true strain curves were obtained for reproducibility tests at each temperature (shown in Fig. 3.12). The UCS of the flash-sintered 3YSZ decreases monotonically with increasing test temperature as shown in Fig. 3.12l. However, elastic modulus (measured from a series of partial unloading experiments) first increases with test temperature up to 400°C and decreases thereafter. The critical strain for the nucleation of cracks decreases with increasing test temperature, reaches a minimum at 400°C, and then increases to ~ 7.5% at 600°C. Meanwhile, 3YSZ was also sintered without electric field at a constant heating rate of 25°C/min to 1300°C and exhibited a failure stress of 2 GPa and a failure strain of 4%.

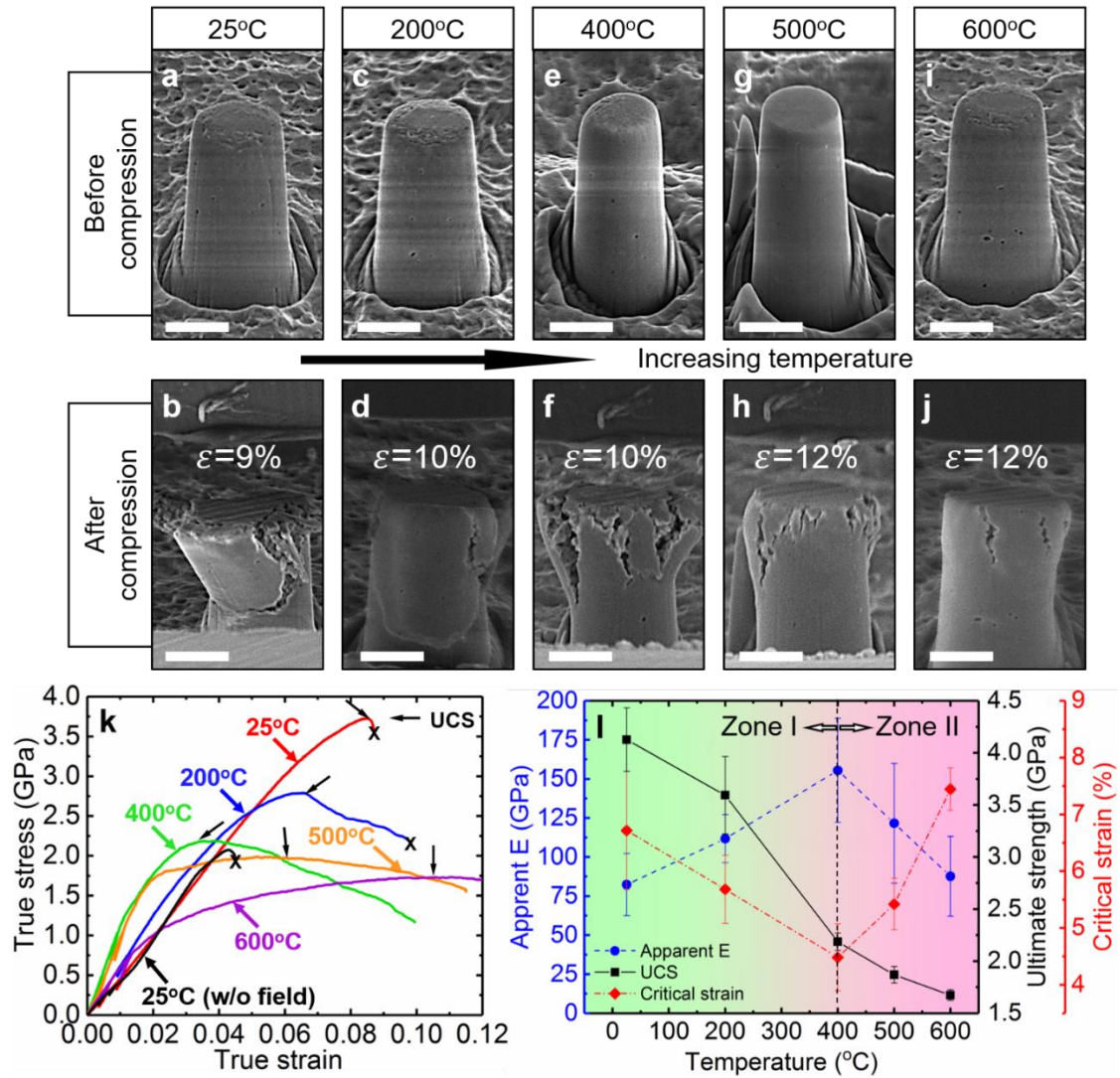


Figure 3.11. SEM images of the flash sintered 3YSZ micropillars before and after compression tests from 25°C to 600°C and corresponding mechanical properties. **a-d** When tested at 200°C and below, the pillar fractures in a brittle manner (into 2 major sections) at very large true strain. Scale bar, 2 μm . **e-j** When tested at 400-600°C, multiple cracks formed and propagated slowly into the pillars, leading to formation of the cauliflower type of pillar tops. At 600°C, crack density and propagation distance were substantially reduced. Scale bar, 2 μm . **k** Corresponding true stress-strain curves of pillars tested at different temperatures. Black arrows indicate the ultimate compressive strength (UCS) of the pillars. Partial unloading at 0.5 and 1% strains were performed to investigate the apparent elastic moduli of pillars tested at different temperatures. A stress-strain curve for 3YSZ sintered without the electrical field is shown as reference. **l** Ultimate compressive strength (UCS) decreases monotonically with increasing test temperature. The elastic modulus increases with test temperature up to 400°C and decreases thereafter. Meanwhile, the critical strain at which the first crack nucleation takes place decreases with temperature to a minimum of 4.5% strain at 400°C and increases thereafter to 7.5% when tested at 600°C. 400°C is the onset temperature where a different inelastic deformation mechanism begins to operate. Zone 1 represents phase transformation toughening from room temperature to 400°C. Zone 2 corresponds to dislocation creep dominant plasticity above 400°C.

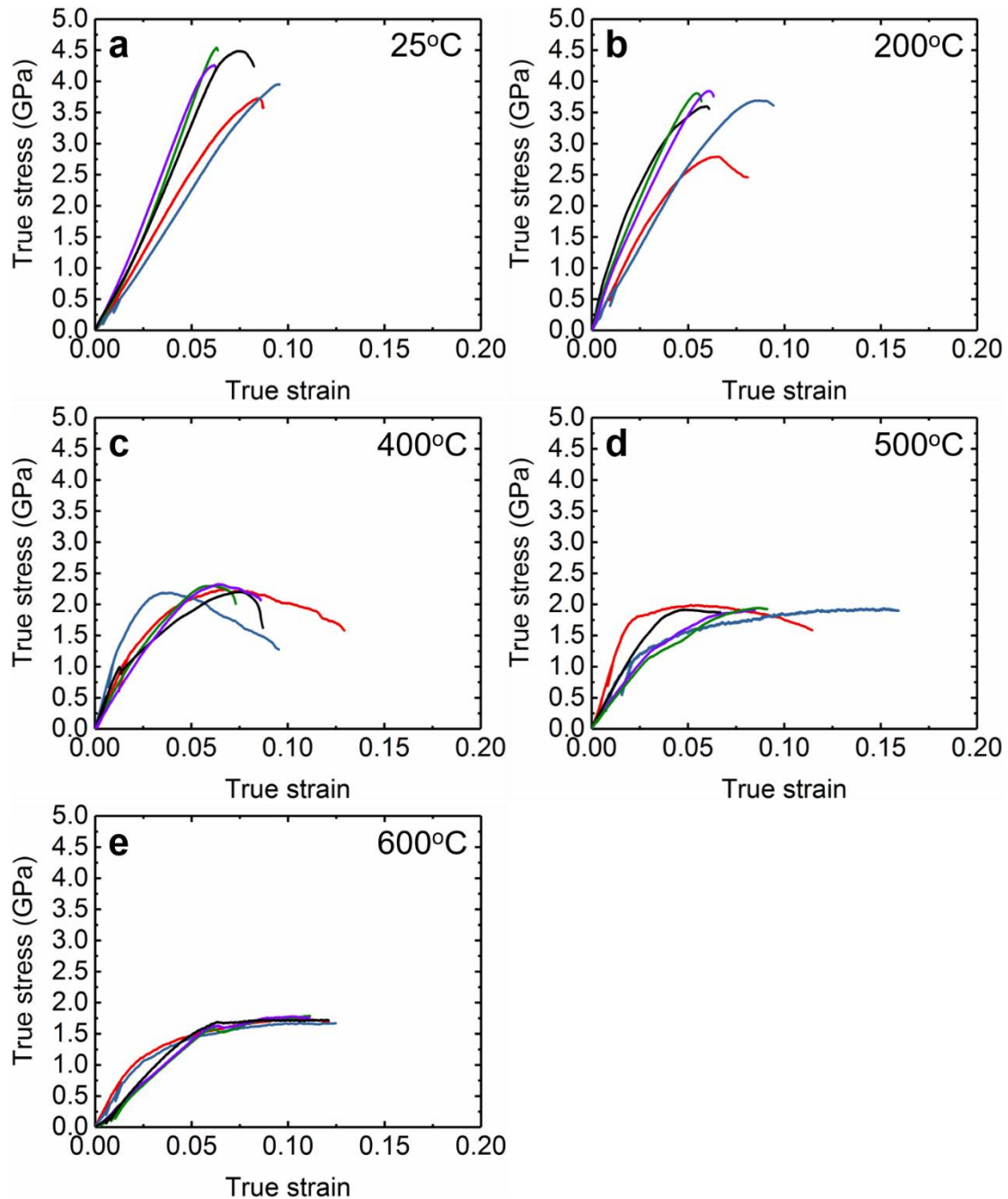


Figure 3.12. Repeatability of true stress-strain curves for 3 YSZ tested at **a** 25°C, **b** 200°C, **c** 400°C, **d** 500°C, and **e** 600°C. Five microcompression tests were carried out to check repeatability of the tests. Flow stresses in most studies show good agreement. Unloading studies at 0.5 and 1% strain were carried out to measure the apparent elastic moduli at each temperature.

3.4.5. Martensitic transformations

Meanwhile, we carried out TEM experiments on the YSZ pillars tested after microcompression tests at room temperature. Fig. 3.13a-b show the SEM micrographs of the pillar before and after compression test at room temperature. The pillar fractured at a flow stress of ~ 4 GPa and a strain of $\sim 6\%$ (Fig. 3.13c). Bright-field XTEM image of the fractured pillar clearly shows the fracture surface and embedded ultrafine grains (Fig. 3.13d-f). Numerous grains in vicinity of the fracture surface were examined carefully. The diffraction pattern of grain 1 (Fig. 3.13g) was observed along the $[\bar{1}01]$ zone axis and indexed to be a monoclinic phase (JCPDS#37-1484). The interplanar spacing of the (111) plane is measured to be 0.279 nm, consistent with the theoretical value of 0.284 nm. Grains 2 and 3 were examined along respective zone axis of $[1\bar{3}2]$ and $[\bar{1}12]$ and indexed to be monoclinic zirconia phase. These studies show that the tetragonal-to-monoclinic phase transition indeed takes place during the compression tests.

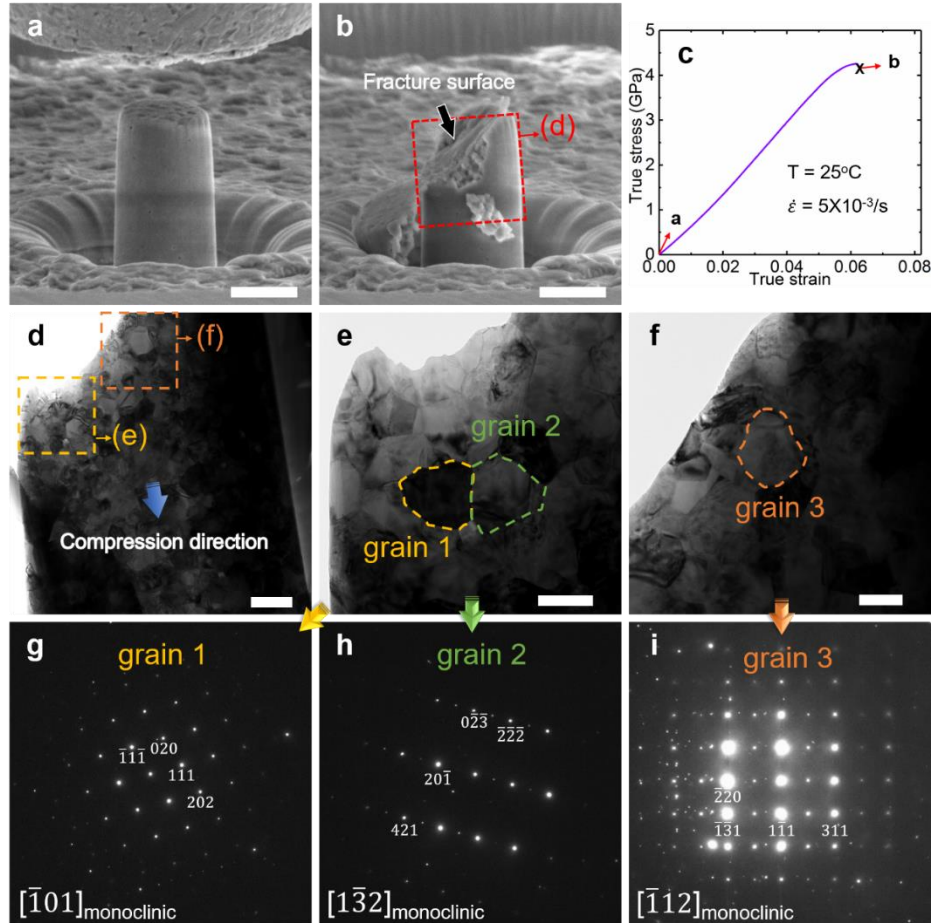


Figure 3.13. TEM analyses of a 3 YSZ pillar tested at room temperature. a-b The SEM image of the pillar before and after compression test at room temperature. Scale bar, 2 μm . c The corresponding stress-strain curve showing a flow stress of 4 GPa and a fracture strain of $\sim 6\%$. d Bright-field XTEM image of the fractured pillar. Scale bar, 500 nm. e-f Bright-field XTEM images of the pillar showing ultrafine grains near fracture surface. Grains 1-3 were chosen to identify phase transformation. Scale bar, 200 nm. g-i Selected area electron diffraction (SAED) patterns showing that grains 1-3 have monoclinic zirconia phase examined along respective zone axis of $[\bar{1}01]_{\text{monoclinic}}$, $[1\bar{3}2]_{\text{monoclinic}}$, and $[\bar{1}12]_{\text{monoclinic}}$.

3.4.6. Cyclic loading tests

30 cyclic loading and partial unloading tests were carried out at a strain rate of $5 \times 10^{-3} \text{ s}^{-1}$ at room temperature and 400°C as shown in Fig. 3.14. Holding segments prior to unloading for one second (during which displacement remains constant) were added. First, 30 cyclic loadings (with increasing strain in each cycle) up to a strain of 4% were conducted with partial unloading to half of the maximum applied strain in each cycle in order to maintain a solid contact between the diamond tip and pillar. No crack was observed for the specimens tested at room temperature during

the cyclic tests, and the pillar exhibited a significant amount of recoverable strain during unloading (Fig. 3.14b). After cyclic tests, a monotonic compression test (highlighted by a red curve in Fig. 3.14e) was conducted on the same micropillar up to a strain of 7%. The pillar exhibited 6% recoverable and 1% irrecoverable strain without crack (Fig. 3.14c). The same pillar then experienced a catastrophic failure in a succeeding monotonic compression test (Fig. 3.14d) at a strain of 8% shown by a green curve in Fig. 3.14e. In comparison, YSZ subjected to cyclic loading tests at 400°C (Fig. 3.14i) showed much less recoverable strain than that tested at room temperature. Also, small cracks formed (as shown in Fig. 3.14g) at a strain of 4% during the cyclic loading test. The subsequent monotonic microcompression test on the same pillar highlighted as a red curve in Fig. 3.14i shows that the pillar exhibited a UCS of 2 GPa, and a residual strength of 1.5 GPa at a strain of 9%, and multiple cracks formed after compression tests (Fig. 3.14h).

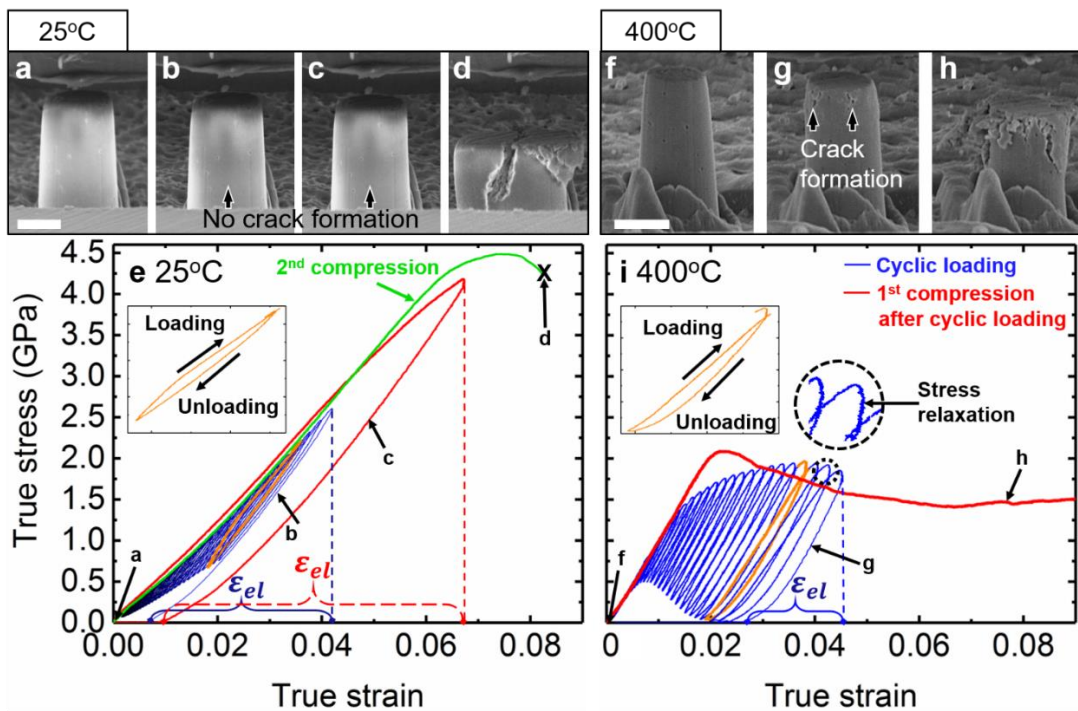


Figure 3.14. Cyclic loading and following monotonic compression tests at a strain rate of $5 \times 10^{-3} \text{ s}^{-1}$ at 25°C and 400°C and the corresponding stress-strain curves. **a** and **f** SEM images of micropillars before cyclic loading tests. Scale bar, 2 μm . **b** and **g** SEM micrographs of micropillars after 30 cyclic loading tests. The cyclic stress-strain curves are shown as blue curves. **c** and **h** After the first monotonic compression tests highlighted in red curves. **d** After the second monotonic compression test highlighted in green. The 27th loading-unloading curves at each temperature shown in orange color and enlarged in the inserted stress-strain curves clearly show the hysteresis loops. The upper portion of a loading-unloading curve is enlarged in a circle to illustrate the stress relaxation for 1 second of holding at 400°C.

3.4.7. Finite element method analysis on stress field distribution for dislocations

The effects of an externally applied or self-induced stress field, on polycrystalline YSZ was determined by solving the mechanical equilibrium equation:

$$\nabla \cdot \vec{\sigma} = \vec{0} \quad (3.3)$$

where the elastic stress, $\vec{\sigma}$, is linearly proportional to the elastic strain, $\vec{\epsilon}$, as specified by Hooke's law, $\sigma_{ij} = C_{ijkl}\epsilon_{kl}$. The resultant state of stress distribution in a polycrystal imposes a Peach-Köhler force on any existing dislocations, $\vec{F} = (\vec{b} \cdot \vec{\sigma}) \times \vec{\xi}$, which in turn induces dislocation motion, i.e., $\vec{v} = M\vec{F}$ [166]. For YSZ, nine crystallographically possible elemental dislocation configurations were numerically explored through finite element method (FEM) analysis [159]. Overall, calculations demonstrate that shear stresses concentrate at grain corners and boundaries and enable the nucleation and propagation of dislocations into the grains, thus promoting plastic deformation and leading to the pile-up of defects at the core of the abutting grains. An example of these calculations is shown in Fig. 3.15 for an arbitrary crystallographic orientation of grains assigned to the microstructure of Fig. 3.1a. For $\vec{b} = 3.16[\bar{1}11] \text{ \AA}$ and $\vec{\xi} = [110]$ [167], line defects are favored to move away from the grain boundary into the grain. At the grain boundary, Fig. 3.16c shows outward pointing forces on both sides of the grain boundary, pulling dislocations into the grain(s), while enabling metastable dislocation configurations at the grain boundary. Similarly, Fig. 3.16d shows that grain corners act as a dislocation source, greatly contributing to the plastic deformation of the surrounding grains. In some cases, the extent of the forces exerted on the dislocations only spans a few nanometers and, in other cases, the same grain boundary can act as a dislocation sink on one side of the interface and as a source on the other. Finally, in some cases, dislocations are entirely unaffected by the grain boundary, but the grain corner always remains active (Fig. 3.16). These effects are more pronounced for large angle misorientations, and stresses above the yield point.

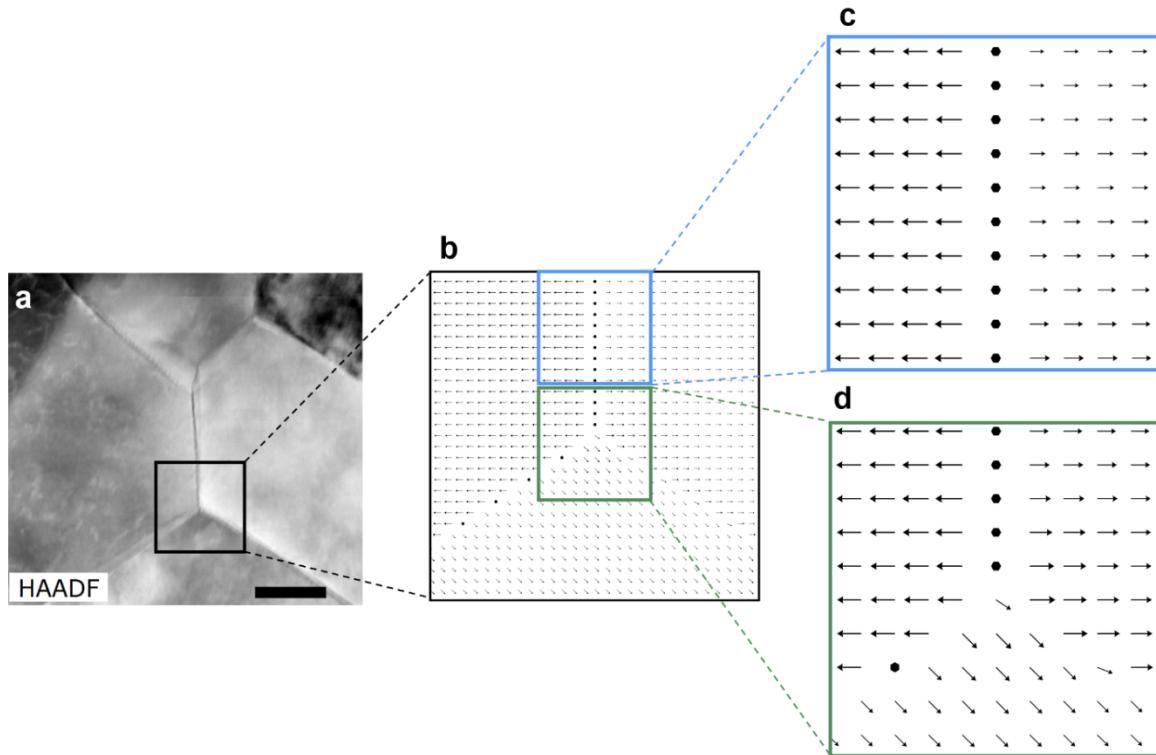


Figure 3.15. Peach-Köhler force distribution in the vicinity of grain boundaries. **a** Original microstructure. Scale bar, 60 nm. **b** Zoom-in region around a selected grain corner highlighted in the black-box region. Assigned Euler angle orientations are, for the bottom grain $(\alpha, \beta, \gamma) = (0, 0, 0)$, for the top-right grain, $(\alpha, \beta, \gamma) = (0, 45, 0)$ and for the top-left grain, $(\alpha, \beta, \gamma) = (45, 45, 0)$. For the BCT system, $\vec{b} = 3.16[\bar{1}11]$ Å and dislocation line, $\vec{\xi} = [110]$, **c-d** The Peach-Köhler forces for a polycrystal subjected to a -200MPa in-plane vertical compression for plane strain conditions at selected locations. The maximum magnitude of the force per unit length on the test dislocations is $|\mathbf{F}|=0.059$ N/m. For this particular Burgers vector and line direction, the resultant force field favors dislocations to pile up in the abutting grains, making grain boundaries and corners sources and sinks of dislocations.

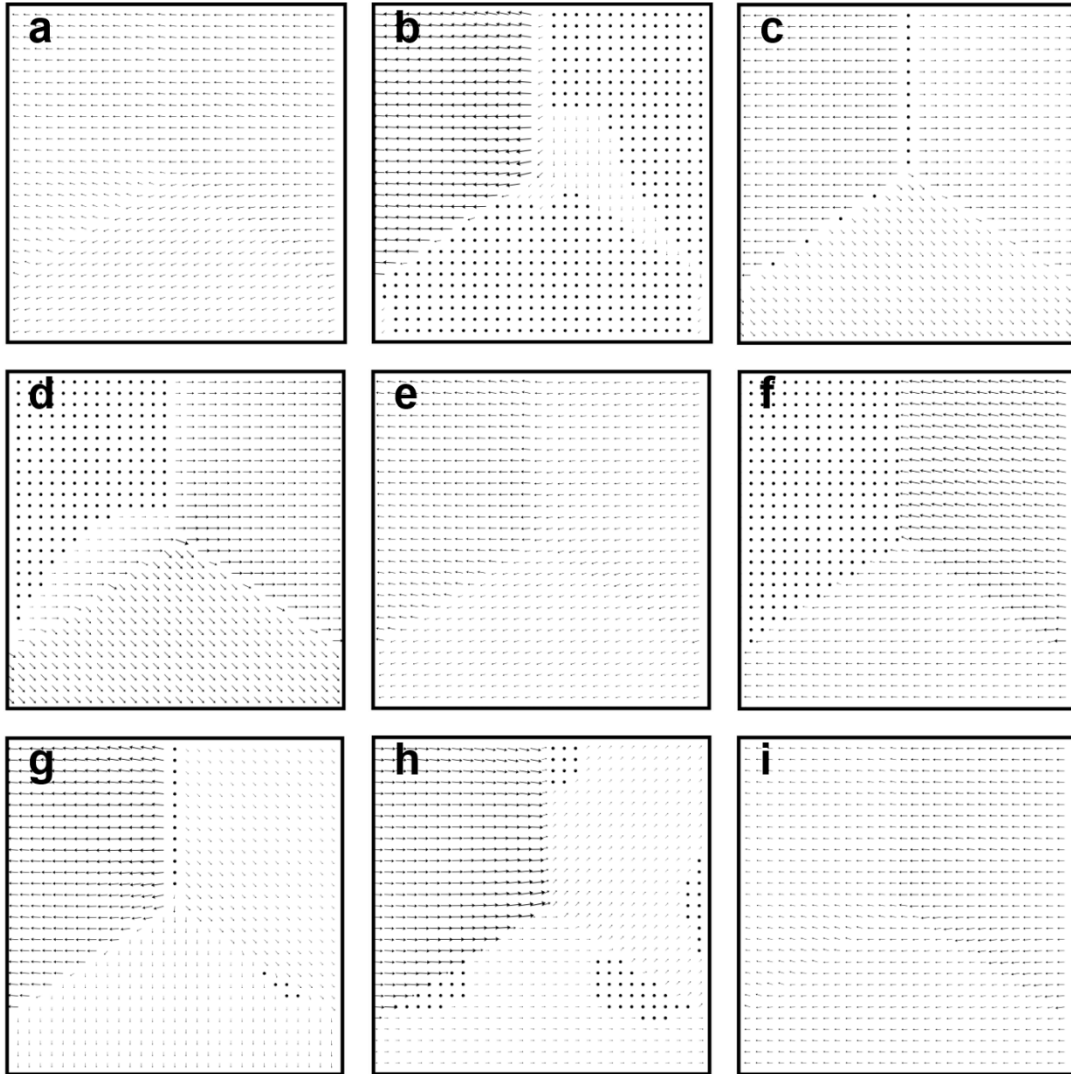


Figure 3.16. Summary of Peach-Köhler forces for microstructure shown in Fig. 3.14a. Each inset shows a different test dislocation line: a $\vec{b} = 3.16[111]$ Å and $\vec{\zeta} = [111]$, b $\vec{b} = 3.16[111]$ Å and $\vec{\zeta} = [1\bar{1}0]$, c $\vec{b} = 3.16[\bar{1}11]$ Å and $\vec{\zeta} = [110]$, d $\vec{b} = 3.16[111]$ Å and $\vec{\zeta} = [110]$, e $\vec{b} = 3.16[111]$ Å and $\vec{\zeta} = [101]$, f $\vec{b} = 3.16[111]$ Å and $\vec{\zeta} = [011]$, g $\vec{b} = 3.16[111]$ Å and $\vec{\zeta} = [100]$, h $\vec{b} = 3.16[111]$ Å and $\vec{\zeta} = [010]$, and i $\vec{b} = 3.16[111]$ Å and $\vec{\zeta} = [001]$. In all cases, grain corners and boundaries become sources or sinks for dislocations.

3.5. Discussion

In general dislocations are rare in ceramics as the strong covalent and ionic bonding greatly discourage the formation of dislocations in ceramics. However, TEM studies show ample evidence for the formation of high-density dislocations in flash sintered 3YSZ. Also, dislocation arrays are frequently observed near triple junctions. It is likely that a large stress concentration (gradient)

develops near triple junctions during the rapid grain growth process. Significant mass (atomic) transport occurs during the flash sintering process to fill in the voids between grains/particles during a very short sintering time (several seconds). The high rate (4-5 orders of magnitude faster than conventional sintering) of mass transport and flow near triple junctions may lead to substantial plastic deformation (enabled by high-density dislocation arrays as shown in Fig. 3.5c) during flash sintering [80]. This assertion coincides with TEM studies of 3YSZ sintered under 1.5 and 15 V/cm, which display insignificant grain growth and little dislocations. Rapid grain growth and large electric field may play a significant role in producing dislocations and their arrays by generating the internal stress during flash sintering. The electric field of 1.5 and 15 V/cm for flash-sintering 3YSZ is insufficient to induce dislocations. Interestingly, intragranular dislocations and dislocation entanglement in 3YSZ have been observed at ultra-high temperature, 1400°C during tensile creep tests at 50 MPa [168]. In the current study, the generation of intragranular dislocations, their arrays and entanglement near triple junctions may strongly depend on stress and high strain rate plastic flow during flash sintering. The shear stresses allowing dislocation pile-up in 3YSZ range from 350 to 1260 MPa based on the lattice dislocation pile-up model [169]:

$$\tau = \frac{Gb}{2L}N \quad (3.4)$$

where G is the shear modulus, b is the Burgers vector, N is the number of intragranular dislocations in the pile-up within a grain, and L is the length of dislocation pile-ups. From TEM measurement on dislocation separation distances in the pile-ups, ~ 20 nm, in flash sintered 3YSZ, the shear stress during flash sintering is estimated to be ~ 1230 MPa (by taking $G = 65$ GPa and b for $\langle 110 \rangle$ type lattice dislocation = 3.6×10^{-10} m), which is within the range that can form dislocation arrays in 3YSZ at elevated temperatures during flash sintering. The dislocation density in many grains reaches as high as $2 - 3 \times 10^{12}$ m⁻², comparing to the typical density of $\sim 10^8$ - 10^{10} m⁻² in a majority of ceramics. These high-density dislocations play a vital role on the deformability of the flash-sintered 3YSZ tested at elevated temperatures. It is well known that dislocation glide is unlikely to take place in bulk ceramic material at room temperature unless applying a confinement pressure via hydrostatic or gaseous medium [49]. However, at microscales, plastic deformation of certain ceramics by glide of dislocations has been observed [170,171]. Camposilvan et al. investigated the plasticity of conventionally sintered YSZ at small scales at room temperature and speculated that dislocation activity along with transformation induced-plasticity at a higher stress level (without showing direct evidence of dislocations) may be a possible inelastic deformation

mechanism for YSZ [43]. Our finite element method analysis on stress distribution for dislocations in polycrystalline YSZ further supports this assertion and shows that shear stress concentration near grain boundaries and triple junctions induces the nucleation and migration of dislocations, thereby enhancing plastic deformation of YSZ (Fig. 3.15 and 16).

A strain of ~8% for stabilized zirconia owing to martensitic transformation-induced plasticity has been previously reported [14,41,43,45,46]. However, micropillars exhibiting such a large strain were often limited to single and oligocrystalline structures to minimize internal mismatch stresses during martensitic transformation. The micropillars of the flash-sintered 3YSZ consist of subgrains, ~ 160 nm in diameter, much smaller than the diameter of the micropillars (3 μm). Thus, the large ~8% inelastic flow may arise from not only transformation induced plasticity but also dislocation activity especially at higher stress level.

For micropillars tested at 400°C, cracks nucleated at smaller strain, ~ 4%, due to the lack of martensitic transformation toughening. At elevated temperatures, the metastable tetragonal phase begins to thermally transform into stable tetragonal and cubic phase, degrading the deformability of the flash sintered 3YSZ by transformation toughening. However, at 400°C, cracks initiated from the top surface of the micropillar, propagate downward gradually and slowly without catastrophic failure unlike the brittle catastrophic fracture of micropillars tested at room temperature. The prominent variation of fracture morphology of the deformed pillars implies that a new inelastic deformation mechanism supersedes martensitic transformation toughening as temperature rises. In the conventionally sintered bulk YSZ system, it is known that the 700 to 800°C temperature range favors other mechanisms (grain boundary sliding, ferroelastic domain switching and/or dislocation activity) as a substitute to martensitic transformation [39]. However, the flash sintered YSZ contains nanograins, oxygen vacancies and abundant preexisting dislocations, which may result in the early activation of other inelastic deformation mechanisms at 400°C [83,153]. It is worth mentioning that the critical strain for the pillars compressed at 200°C is still high (~6%). Catastrophic failure of pillars was also observed for specimens tested at 200°C, and transformation toughening-induced plasticity remains the dominant inelastic deformation mechanism of the flash-sintered 3YSZ.

At an even greater test temperature, the martensitic phase transformation toughening is gradually replaced by the activation of a new inelastic deformation mechanism. Basically, the critical strain at which the first crack occurs decreases with increasing test temperature and reaches

a minimum at $\sim 400^\circ\text{C}$ as can be seen in Fig. 3.11i. The earlier occurrence of cracks at an elevated temperature (at lower critical strain than that at room temperature) implies a lack of transformation toughening. The critical strain for the onset of crack propagation increases when the test temperature is $> 400^\circ\text{C}$. Furthermore, in contrast to the crack triggered catastrophic failure in low temperature specimens (25 and 200°C), cracks in high temperature specimens ($\geq 400^\circ\text{C}$) propagate slowly and are more uniformly distributed in the top portion of the deformed pillar, leading to the dilated cauliflower morphology. The slow crack propagation speed indicates enhanced compressive ductility at elevated temperature. As phase transformation toughening is less likely to operate at high temperatures, the enhanced plasticity of YSZ may arise from deformation mechanisms, such as dislocation creep and/or grain boundary sliding. The high-density dislocations in flash sintered specimens suggest that dislocation power creep type of mechanism is highly likely. Meanwhile the small grains retained in the flash sintered specimens may promote grain boundary sliding as a favorable deformation mechanism. Therefore, 400°C is the brittle-to-ductile transition temperature for flash sintered YSZ, a much lower value than the one reported for conventionally sintered or single crystal YSZ systems ($\sim 800^\circ\text{C}$) [52].

The apparent elastic moduli of tested YSZ are lower than the theoretical values (210 GPa) at all test temperatures. It is well known that the underestimation of elastic modulus in the microcompression tests can be attributed to taper angle of the pillars, misalignment between the tips and pillars, and stress concentration on the top surface of the pillars [43]. Taking the underestimation into consideration, it is still surprising that the apparent elastic modulus of the flash sintered 3YSZ increases with temperature and reaches a maximum at 400°C (Fig. 3.11i). This is because: a) the dominant phase of 3YSZ at room temperature is metastable tetragonal phase of zirconia and the elastic modulus of tetragonal phase is known to be lower than that of monoclinic and cubic phase [167,172]. When temperature increases, an increasing portion of tetragonal zirconia undergoes transformation to stable tetragonal and cubic phase, which may lead to the slight increase of the apparent elastic modulus⁴⁶ [15]. b) Ceramic materials retaining superelasticity usually exhibit lower elastic modulus due to the strain burst. It follows that the larger elastic modulus observed at elevated temperatures is an indication of suppression of the martensitic phase transformation due to thermodynamically reinforced stability of tetragonal phase [17,18]. The total free energy change for martensitic transformation per unit volume (ΔU_0) can be expressed as [17],

$$\Delta U_0 = \Delta U_c + \Delta U_e + \Delta U_s - \Delta U_l \quad (3.5)$$

where ΔU_c is the chemical free energy change, ΔU_e the elastic energy change associated with volume expansion of tetragonal zirconia constraint by matrix, ΔU_s the interface energy change (negligible), and ΔU_l the change in free energy associated with an external applied stress. This mechanical term should be larger than the first three terms on the right-hand side for martensitic transformation to occur. When the chemical free energy term ($\Delta S_m(M_s - T)$) and additional free energy change ($\Delta S_m(M_s - T_o)$) due to the presence of dopant are taken into account [18], the total free energy change as a function temperature is given,

$$\Delta U_o = \Delta S_m(M_s - T) - \Delta U_l \quad (3.6)$$

where ΔS_m is entropy change associated with martensitic transformation and M_s is the martensitic start temperature. When $M_s = T$, spontaneous martensitic transformation takes place without the external stress. As test temperature increases, the chemical energy change also increases (note that entropy term is negative value), thereby requiring larger mechanical term to overcome free energy barrier for martensitic transformation to occur.

The higher temperature ($T > 400^\circ\text{C}$) weakens the interatomic bonds and thus reduces the elastic modulus, and high-density flash sintered dislocations significantly contribute to the plasticity of 3YSZ as manifested by the increasing critical strain to nearly 7.5% before the observation of cracks at 600°C . In summary, elastic modulus, critical strain and fracture behavior of flash-sintered 3YSZ at each test temperature indicate that 400°C is the temperature beyond which inelastic deformation mechanism of the flash-sintered YSZ changes prominently. Therefore, Zone 1 in Fig. 3.11i corresponds to transformation toughening dominated region below 400°C ; whereas Zone 2 is associated to dislocation activity and presumably grain boundary sliding dominant region above 400°C .

An indirect way to confirm martensitic transformation is to check the existence of reverse transformation. As shown in Fig. 3.14a-e, a significant amount of recoverable strain was observed during partial unloading owing to reverse transformation at room temperature. Furthermore, hysteresis loops appear as strain increases. The area of the hysteresis loop tends to increase as stress and strain both increase. The appearance of hysteresis loops may be attributed to reverse transformation and reopening of closed pores in the flash-sintered 3YSZ [51]. The pillar after the cyclic loading test experiences 1% plastic strain, but still does not exhibit cracks as can be seen in Fig. 3.14b. It is worth mentioning that the stress-strain curves show stronger linearity as the cyclic compression tests are conducted on the same pillar. The stress-strain curve for the second

monotonic test shows the highest linearity compared to the cyclic loading and the first monotonic compression test. This implies that martensitic transformation begins to concede as consecutive compression tests are carried out on the same pillar because part of the transformed monoclinic phase does not revert to tetragonal as the load on the pillar is removed [173]. Cyclic loading tests at 400°C show significantly less recoverable strain than the room temperature tests due primarily to the lack of transformation toughening, but the hysteresis loop remains visible presumably due to reopening of the microcracks and pores. An increase of crack density and slow crack propagation seem to prevent the pillars from undergoing brittle fractures and the pillar achieves a residual strength of 1.5 GPa. Furthermore, stress relaxation measured during the holding segment (1 s for cycles) is observed at both room temperature and 400°C (Fig. 3.17). Room temperature test exhibits the same amount of stress relaxation during holding regardless of the overall strain. The formation of new microcracks and strain energy reduction in the pillar may result in the stress relaxation at room temperature [174]. On the other hand, a significant increase of stress relaxation (the absolute value of stress reduction) is observed at 400°C and the stress relaxation increases as the pillar undergoes plastic flow. Stress relaxation at high temperature is normally due to high temperature and stress induced-sintering and closure of pores [174]. However, this mechanism is less likely at the low temperature (400°C). Thus, stress relaxation taking place at 400°C may be mainly contributed by a thermally activated inelastic process such as the effect of grain boundary sliding, and/or diffusional creep of dislocations generated during the ultrafast sintering process. Another possible explanation is transient dislocation movement during the holding segment triggered by dislocation gliding, which is more likely to happen at elevated temperatures [43]. Thus, the observation of stress relaxation may indicate that the dislocation activity contributes to deformability of flash-sintered 3YSZ together with grain boundary sliding and/or diffusion induced-inelastic mechanism above 400°C. The proposed relaxation mechanisms are all thermally activated phenomenon and time is an important variable. To better understand the inelastic mechanism activated at elevated temperature, systematic strain rate jump microcompression tests are needed in future studies.

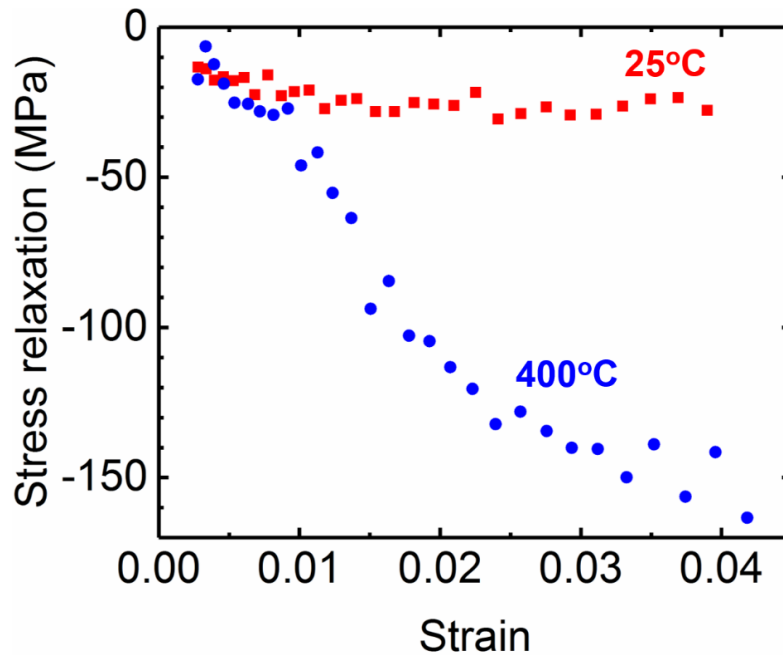


Figure 3.17. Stress relaxation as a function strain at room temperature and 400°C during one second holding segment of cyclic loading and unloading tests.

3.6. Conclusions

In conclusion, the first *in-situ* study on mechanical behavior of flash sintered YSZ was performed inside SEM at elevated temperatures up to 600°C. At room temperature YSZ micropillars sustain giant strain (~8%) comparing with its bulk counterpart (~2%) due to the stress-induced martensitic transformation toughening. However, the pillars fracture catastrophically after the nucleation of cracks. In comparison, a brittle-to-ductile transition of fracture mode is observed at 400°C in flash sintered YSZ, much lower than the ~800°C reported in conventional bulk YSZ. The enhanced plasticity at elevated temperatures is due to the transition from phase transformation toughening to dislocation creep, as the dominant inelastic deformation mechanism due to the existence of high density of dislocations in flash sintered YSZ and/or to early initiation of grain boundary sliding owing to nanosized grains. This study provides the first evidence on superior mechanical properties of flash sintered ceramics, and *in-situ* nanomechanical testing technique at elevated temperatures and provide an important way to fundamentally understand the densification and mechanical properties of ceramics.

CHAPTER 4. STUDY OF DEFORMATION MECHANISMS IN FLASH-SINTERED YTTRIA-STABILIZED ZIRCONIA BY IN-SITU MICROMECHANICAL TESTING AT ELEVATED TEMPERATURES

The following chapter contains content reproduced with permission from “J. Cho, J. Li, H. Wang, Q. Li, Z. Fan, A. Mukherjee, W. Rheinheimer, H. Wang, X. Zhang. “Study of deformation mechanisms in flash-sintered yttria-stabilized zirconia by in-situ micromechanical testing at elevated temperatures.”, *Materials Research Letters*, 7 (2019): 194-202.” Copyright 2019 Taylor & Francis Group

4.1. Overview

Flash sintering has received wide attention lately due to its ultrafast densification process at low sintering temperature. However, the deformability of flash-sintered ceramics remains poorly understood. Yttria-stabilized zirconia (YSZ) was processed by flash sintering to study deformation mechanism. Transmission electron microscopy studies show that the flash-sintered YSZ contains ultrafine grains and dislocations. Strain rate jump tests at elevated temperature by *in-situ* microcompression test indicate the existence of a large threshold stress. The activation energy of deformation is ~145 kJ/mol, similar to the activation energy for oxygen vacancy migration. The deformation mechanisms of the flash-sintered YSZ at elevated temperatures are discussed.

4.2. Introduction

Field-assisted sintering technique (FAST) is of great industrial importance and widely applied due to a significant energy saving by lowering sintering temperature and time [175]. Flash sintering, one of the FASTs, is a newly developed technique that permits the dramatic reduction of sintering time and temperature and permits substantial currents to flow through specimens [58]. During flash sintering, an ultrafast densification process occurs by applying an electrical field at a constant heating rate. When the furnace temperature is higher than the onset (flash) point, which is dependent upon the magnitude of applied electric field and the material's conductivity, an instantaneous densification process takes place within a few seconds [80]. Many ceramic systems, such as yttria-stabilized zirconia (YSZ), titania, zinc oxide, and ceria have been successfully prepared by flash-sintering [59,63,158,176], and the number of flash-sintered ceramic systems increases rapidly. Among these systems, YSZ is one of the most widely explored ceramics in the

field of flash sintering, as YSZ has a variety of important industrial applications, such as thermal barrier coatings, dental implants, oxygen sensors, and solid oxide fuel cells [7,12,177,178].

Mechanical behavior of YSZ has been intensively investigated. Among these there are several studies on microscale mechanical testing, which mostly highlight superior superelasticity and shape memory effect at room temperature owing to martensitic transformation [14,41–43,45,46,179]. However, our understanding on deformation mechanisms of microscale YSZ at elevated temperatures remains limited. In addition, ceramics processed by flash sintering technique is known to have intriguing microstructures containing a considerable number of charged defects and ultrafine grain sizes [80,83]. Our previous *in-situ* study shows that the flash-sintered YSZ has a high density of preexisting dislocations induced by flash sintering and has a transition of deformation mechanisms at 400°C [180]. Here, we report further studies on underlying deformation mechanism of the flash-sintered 3 mol % yttria doped zirconia (3YSZ) at elevated temperature (above 400°C). We utilize *in-situ* microcompression jump tests to avoid complicated data analyses associated with nanoindentation [181]. These tests reveal the existence of a large threshold stress for activation of dislocation creep. Furthermore, the activation energy for creep is measured from *in-situ* compression tests and provides important insight on defect dominated deformation mechanisms in flash-sintered ceramics.

4.3. Experimental procedures

The experiment was conducted in a customized thermomechanical analyzer (SETSYS Evolution, SET ARAM Instrumentation). Disk-shaped 3YSZ specimens with a diameter of ~ 5 mm and a thickness of ~ 2 mm (using TZ-3Y-E powders, from Tosoh corp., with 40 nm grain size, please see Table 4.1 for purity information.) were sandwiched between two Pt electrodes. An alumina rod pushed the electrodes with a few kPa pressure to insure a rigid contact between the sample and electrodes. A compact specimen dimension was intentionally used to minimize density and grain size fluctuations throughout the sample. An electrical field of 150 V/cm was applied to the specimen with a constant heating rate of 25 °C/min until the sample undergoes a rapid densification at a furnace temperature of 1150°C. Right after the onset of flash, the applied heat and electrical field were removed right away to prohibit grain growth.

Table 4.1. Compositions of chemicals in 3YSZ (Provided by Tosoh corp.)

Chemicals	Content (%)
Y ₂ O ₃ (mol%)	3
Y ₂ O ₃ (wt%)	5.2 ± 0.5
HfO ₂ (wt %)	< 5.0
Al ₂ O ₃ (wt %)	0.1 ~ 0.4
SiO ₂ (wt %)	≦ 0.02
Fe ₂ O ₃ (wt %)	≦ 0.01
Na ₂ O (wt %)	≦ 0.04

Transmission electron microscopy (TEM) studies were performed on the as-sintered 3YSZ. Sequential grinding, polishing, dimpling and ion milling (PIPS II, Gatan) were employed to manually prepare TEM specimens of the flash-sintered 3YSZ. TEM experiment were performed on an FEI Talos 200X transmission electron microscope operated at 200 kV.

To investigate the microscale mechanical behavior of flash-sintered 3YSZ, micropillars with ~ 3 μm in diameter and ~ 8 μm in height were fabricated by focused ion beam (FIB) technique in an FEI 3D FEG scanning electron microscope. Prior to the fabrication of micropillars, the specimen was polished by SiC sandpapers, ~ 1 μm diamond papers, and ~ 20nm colloidal silica. The pillars were prepared on a dense area (judged by SEM studies) in the center of the sample to avoid inhomogeneous microstructure. The pillars from this region contain only a few nanovoids as can be seen in Fig. 4.1. The specimen was mounted on a ceramic stage heater in a Hysitron PI 88×R nanoindentation system. A 5 μm diameter diamond flat punch tip equipped on a piezoelectric transducer for collection of force and displacement was used to compress the micropillars. The diamond flat punch and specimen were heated to desired temperature (450, 550, and 650 °C) at the same ramping rate of 20 °C/min. The microcompression tests were conducted when thermal equilibrium is achieved to minimize mechanical and thermal drifts. Thermal drift rate, less than 1.1 nm/s, was measured prior to each compression tests for 40 s. True displacement data compensating the displacement offset were acquired by the nanoindentation system.

4.4. Results

TEM micrograph (Figure 4.1(a)) shows ultrafine grain size in the flash-sintered 3YSZ. A systematic linear intercept method reveals the average grain size (more than 200 grains) of 159±70

nm with a large variation, and the flash-sintered 3YSZ has a 98% density determined by many micrographs. TEM studies also show a significant amount of preexisting dislocations (Figure 4.1(b)). Strain rate jump tests were carried out on numerous micropillars at different temperatures (450, 550, and 650 °C) to study the underlying deformation mechanisms. A strain rate of $5 \times 10^{-4} \text{ s}^{-1}$ was applied in the elastic region ($\sim 2\%$) of the stress-strain curve, and strain rates of $3 \times 10^{-3} \text{ s}^{-1}$, $1 \times 10^{-2} \text{ s}^{-1}$, $5 \times 10^{-2} \text{ s}^{-1}$, and $3 \times 10^{-1} \text{ s}^{-1}$ were applied in the plastic deformation region to obtain flow stresses at each temperature. Figure 4.1 (c-e) shows SEM snapshots of the tested pillars at various strains at each temperature. Cracks propagated downwards from top surface, but no catastrophic failure was observed after tests at elevated temperatures. Figure 4.2 (a-c) shows multiple stress-strain curves of strain rate jump tests at three temperatures. The stress-strain behavior shows good reproducibility taking into consideration the porous nature of ceramic materials. As test temperature increases, the flow stresses tend to decrease, and crack density and propagation speed reduce significantly. The flow stresses for each strain rate were obtained at a strain of 6%, which is the half of the maximum compression strain (12%). Such a strain value permits the least extrapolation for stress analysis at each strain rate. Also, every stress-strain curve collected at three temperatures shows the obvious stress plateau above 4 to 5% strain, indicating that the strain from which the flow stresses is collected should be larger than 5% strain.

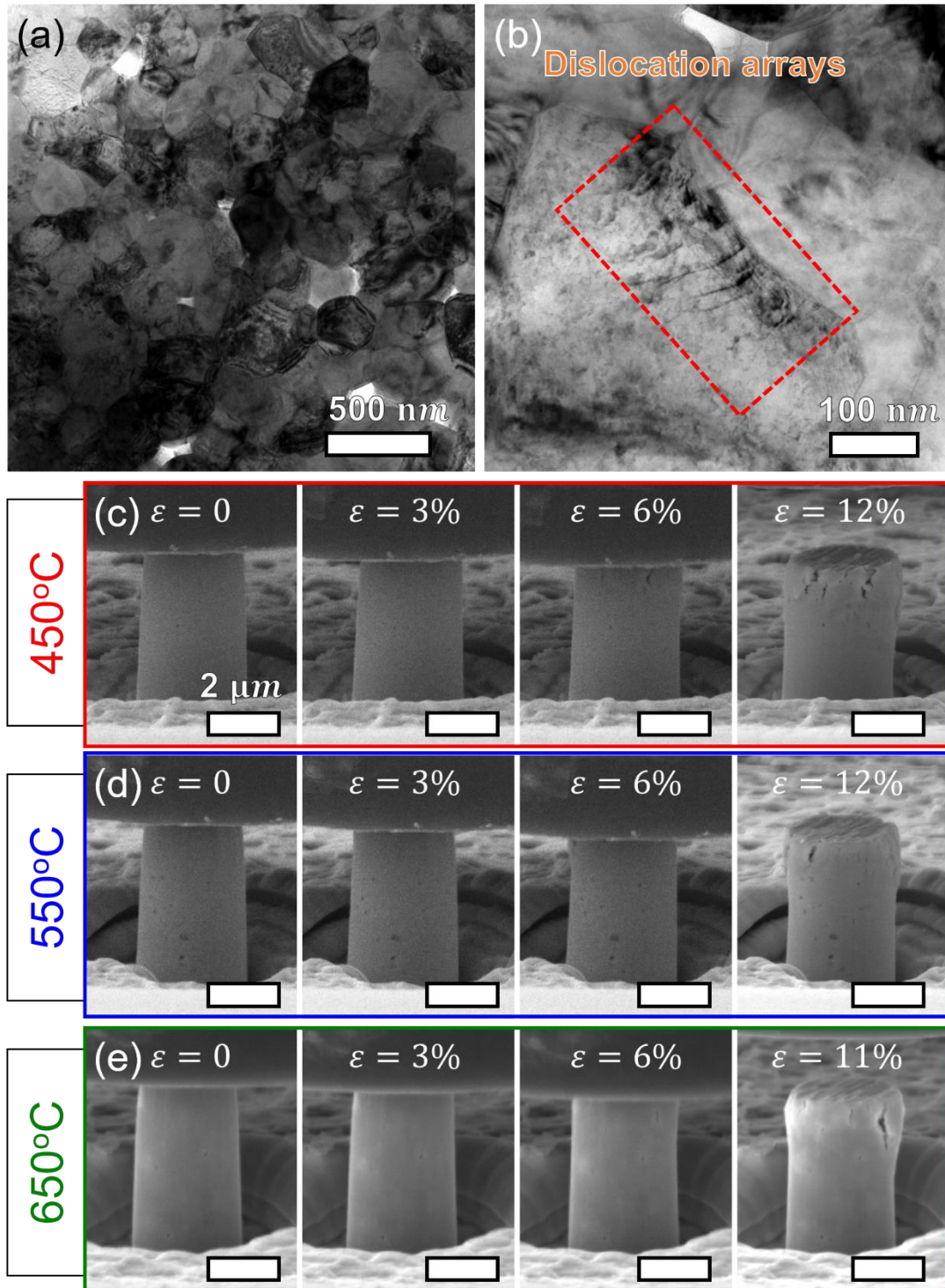


Figure 4.1. Microstructure and strain rate jump tests on the flash sintered 3YSZ. (a-b) Bright field TEM micrographs of the flash sintered 3YSZ showing (a) ultrafine grains and (b) an array of preexisting dislocations. (c-e) SEM snapshots of the pillars tested at 450, 550, and 650°C at 0, 3%, 6%, and final strains (11-12%). Several cracks propagated from the top surface of the pillar. Crack length and density reduce as test temperature rises.

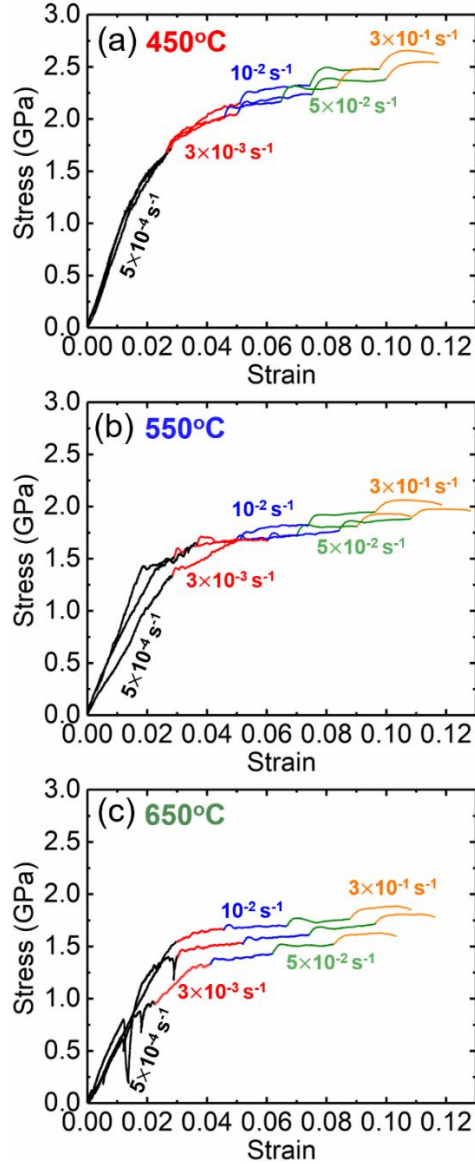


Figure 4.2. Stress-strain curves for strain rate jump tests on the flash sintered 3YSZ at 450, 550, and 650°C. Stress-strain curves for three strain rate jump tests at (a) 450°C, (b) 550°C, and (c) 650°C. Strain rate of $5 \times 10^{-4} \text{ s}^{-1}$ was employed in the elastic region. Strain rates of $3 \times 10^{-3} \text{ s}^{-1}$, $1 \times 10^{-2} \text{ s}^{-1}$, $5 \times 10^{-2} \text{ s}^{-1}$, and $3 \times 10^{-1} \text{ s}^{-1}$ were utilized in the plastic region to obtain flow stresses at each temperature. The flow stresses increase with increasing strain rate and decreasing temperature.

The flow stresses at various temperatures and strain rates were extracted and plotted as a function of strain rate after taking natural logarithm (Figure 4.3 (a)). Strain rate sensitivity (m) at a fixed temperature and strain can be calculated by

$$m = \left(\frac{\partial \ln \sigma}{\partial \ln \dot{\epsilon}} \right)_{\epsilon, T} \quad (4.1),$$

where σ is an applied stress and $\dot{\epsilon}$ is strain rate [182]. m values obtained from the slope of the fitting line in Figure 4.3 (a) at 450, 550, and 650 °C are 0.043 ± 0.022 , 0.034 ± 0.011 , and 0.030 ± 0.030 , respectively. The deformation mechanism of materials at elevated temperature follows an Arrhenius-type relation under the assumption that the deformation is dominated by a single process [183] and can be expressed by

$$\dot{\epsilon} = A_o \sigma^n \exp\left(-\frac{Q}{RT}\right) \quad (4.2),$$

where A_o is the pre-exponential constant, n is the stress exponent, and Q is activation energy of the dominant deformation mechanism. When we assume the constant stress exponent and applied stress, Equation (4.2) can be rewritten as,

$$\dot{\epsilon} = A_1 \exp\left(-\frac{Q}{RT}\right) \quad (4.3)$$

where A_1 is a constant, which includes the applied stress term [184]. The assumption of the constant stress exponent for the power law means that there is no transition in deformation mechanisms within the test temperatures which agrees well with our previous study [180]. When the applied stress is fixed at 2,000 MPa, the corresponding strain rates can be obtained at each temperature by drawing a horizontal line in Figure 4.3 (a). By plotting $\ln \dot{\epsilon}$ vs. $1000/T$, the activation energy can be calculated from the slope (Figure 4.3 (b)). The activation energy so calculated is 347 ± 151 kJ/mol. Plotting $\ln\left(\dot{\epsilon} \exp\left(\frac{Q}{RT}\right)\right)$ vs. $\ln \sigma$ with a substitution of the activation energy of 347 kJ/mol into Equation (4.1) yields an unusually large stress exponent of ~ 30 (Figure 4.3 (c)). The unphysically high stress exponent obtained using this method implies that threshold stress must be taken into account for exploring the underlying deformation mechanism. The threshold stress, σ_o , can be graphically determined by plotting $\dot{\epsilon}^{1/n}$ vs. σ at each temperature and is used to correct the stress in Equation (4.2) as follows:

$$\dot{\epsilon} = A_o (\sigma - \sigma_o)^n \exp\left(-\frac{Q}{RT}\right) \quad (4.4)$$

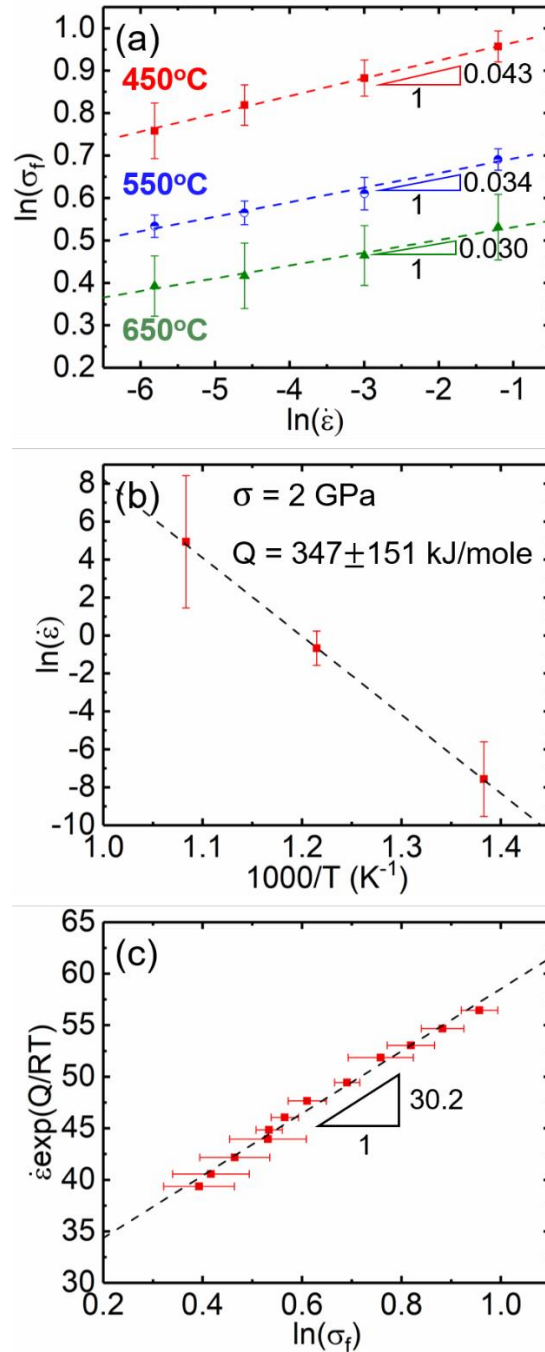


Figure 4.3. Data processing from strain rate jump tests on the flash sintered 3YSZ at 450, 550, and 650°C before considering the presence of the threshold stresses. (a) Effect of strain rates on flow stress at each temperature. Note that the natural logarithm of both strain rate and flow stress is taken and plotted. The slopes represent strain rate sensitivity (m). (b) Temperature dependence of strain rate at a flow stress of 2 GPa. The activation energy for the underlying deformation mechanism turns out to be 347 ± 151 kJ/mole. (c) Flow stress versus the normalized strain rate. The slope indicates the stress exponent (n). The abnormally high stress exponent (30.2) implies the existence of the threshold stress.

The threshold stress is determined from the intercept between the linear regression of extrapolated data points and the stress axis (when $\dot{\epsilon} = 0$) as demonstrated in Figure 4.4. To determine the threshold stress, the stress exponent must be known. The most common deformation mechanisms of YSZ system are diffusional creep ($n=1$), grain boundary sliding ($n=2$) and dislocation creep ($n=7$) [185,186]. Figure 4.4 (a-c) shows $\dot{\epsilon}^{1/n}$ vs. σ plot when we assume that the dominant deformation mechanism is diffusional creep, or grain boundary sliding, or dislocation creep, respectively. When the stress exponent is assumed to be 1, the fitting of data points significantly deviates from the linear regression dotted lines, indicating that $n = 1$ is an unlikely scenario. Similarly, the assumption of $n = 2$ also leads to noticeable deviation from the linear regression line. When $n = 7$ is assumed, the linear regression lines exhibit best fits for data points at all three test temperatures, indicating that the same deformation mechanism takes place during this temperature range, which justifies the assumption of a constant stress exponent in Equation (4.3). Therefore, the threshold stresses at each temperature were obtained from the linear extrapolation of the experimental data using $n = 7$. The data was replotted in Figure 4.5 after taking the effective stress ($\sigma - \sigma_o$) into account. Plotting $\ln(\sigma - \sigma_o)$ vs. $\ln\dot{\epsilon}$ in Figure 4.5 (a) shows corrected strain rate sensitivities of 0.155 ± 0.085 , 0.142 ± 0.050 , and 0.154 ± 0.151 at 450, 550, and 650°C, respectively. The corrected activation energy of 145 ± 74 kJ/mole was obtained at a constant flow stress of 500 MPa by plotting $\ln\dot{\epsilon}$ vs. $1000/T$. The strain rate sensitivities become much greater and the activation energy significantly decrease after the correction of the flow stress. The determination of the threshold stresses with an imposed stress exponent of 7 naturally returns a self-consistent stress exponent of 6.7 as demonstrated in Figure 4.5 (c).

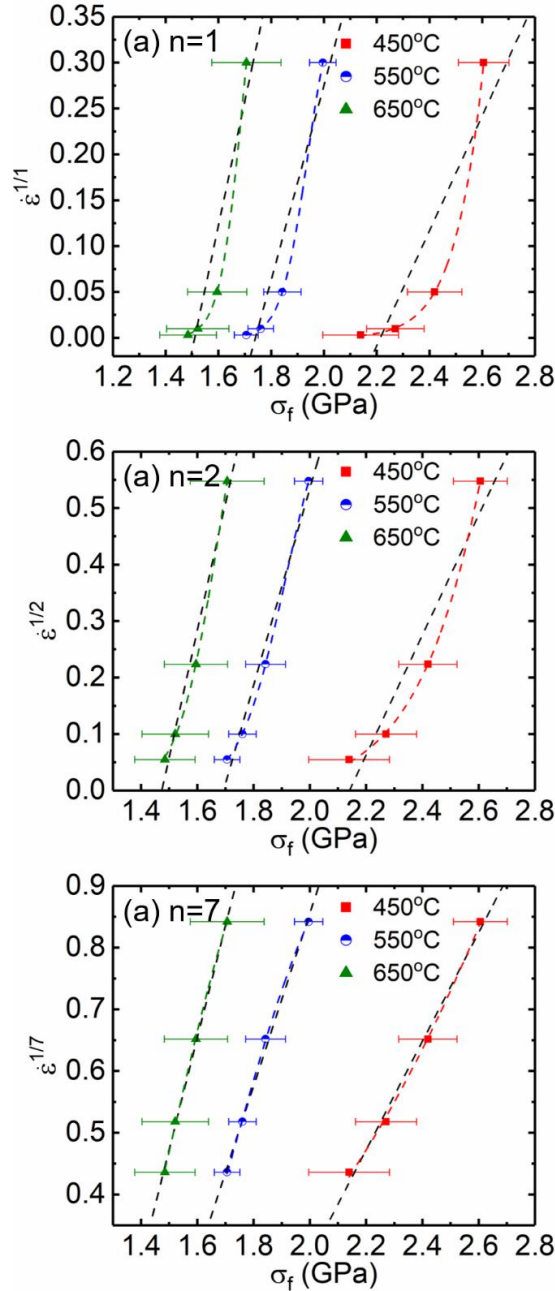


Figure 4.4. The determination of the threshold stress for the flash sintered 3YSZ at 450, 550, and 650°C. (a) The determination of the threshold stress with a stress exponent of 1. The actual data points are significantly deviated from the linear regression lines as indicated by the curved dash lines. (b) The determination of the threshold stress with a stress exponent of 2. The actual data shows better linear fit than those with a stress exponent of 1, but still deviates from the linear regression lines by exhibiting positive upward curvature. (c) The determination of the threshold stress with a stress exponent of 7. The linear regression lines match well with the actual data. The extrapolation of the linear line to zero strain rate describes the threshold stress.

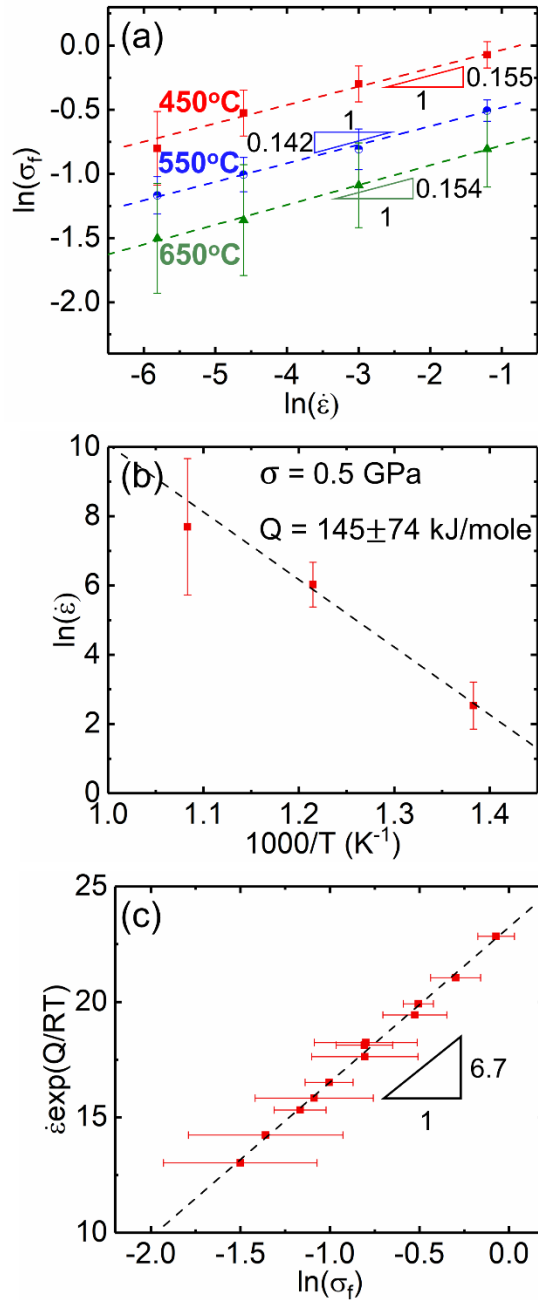


Figure 4.5. Corrected data processing from strain rate jump tests on the flash sintered 3YSZ at 450, 550, and 650°C in consideration of the presence of the threshold stress. (a) The corrected flow stress as a function of strain rates at each temperature. The strain rate sensitivities after the correction increase to 0.15. (b) Temperature dependence of strain rate at a flow stress of 500 MPa. The activation energy is estimated to be 145 ± 74 kJ/mole. (c) The corrected flow stress versus the normalized strain rate. The data correction with an imposed stress exponent of 7 returns the stress exponent of 6.7.

4.5. Discussion

A majority of ceramic materials have little dislocations, unless deformed at high temperatures. Prior studies on flash-sintered 3YSZ show that arrays of dislocations are retained frequently. Some dislocations exist near the triple junctions where the sintering stress is concentrated during the flash sintering process [180]. This noticeable presence of high-density dislocations in the flash-sintered 3YSZ is surprising. It has been shown that flash sintering can induce significant amount of point defects in ceramics [83]. We anticipate that substantial mass transport during flash sintering results in considerable plastic flow, which is accommodated by generation and migration of a high-density of dislocations [80]. We also hypothesize that during flash sintering, the transient high current densities through specimens along with locally very high temperatures due to Joule heating promote sintering and introduce a significant number of defects, such as Frenkel defects [58], dislocations, and stacking faults. The formation or nucleation of these defects facilitate the plastic deformation of flash sintered YSZ via a defect (dislocation) dominated plasticity. The activity of dislocations may not play a significant role in the deformability of 3YSZ at room temperature as the glide of dislocations is often hindered by the strong covalent and ionic bonding. However, the nucleation and activity of dislocations in bulk 3YSZ were often observed after mechanical tests at high temperatures ($> 800^{\circ}\text{C}$) [168,187]. In the current study, abundant intragranular dislocations and entanglement were already generated during the high strain rate mass flow during fast densification in the flash-sintering process. Furthermore, the plastic deformation of ceramics by dislocation glide in micromechanical tests has been observed previously because the miniaturization of specimen decreases strain gradients and the population of intrinsic flaws [49,170,171]. Therefore, it may be possible that the numerous preexisting dislocations contribute to the deformability of the flash-sintered 3YSZ at the intermediate test temperatures in the current study. One may speculate that the high concentration of defects (dislocations and point defects) may be unstable and tends to decrease significantly at high temperatures. However, in the present *in-situ* experiments, the test temperatures are relatively low, ranging from 450 to 650°C, which are equivalent to 0.27 - 0.31 T_m . At these temperatures, the mobility (i.e. diffusion coefficients) of cationic point defects is negligible. As such, a defect equilibration involving a diffusion of cationic defects is less likely to occur for kinetic reasons. Also, the intermediate temperature is insufficient for recovery of dislocations in ceramics.

Initial plots of the experimental data from the strain rate jump tests, following Equation (4.1), yield the stress exponent of 30, too high to physically describe the appropriate deformation mechanisms. Such an abnormally large n value has been reported before, and the introduction of threshold stress as shown in Equation (4.4) returns a more appropriate n value and activation energy [188–190]. Following a similar methodology, the linear regression of the data using a n value of 7 provides the best linear fit as evidenced in Figure 4.4 (c). Furthermore, the usage of a modified creep equation returns a self-consistent n value of 6.7, indicating the methodology applied here is appropriate. An n value of 7 corresponds to dislocation glide dominated creep mechanism. Thus, the current study suggest that the dislocation activity may be the dominant deformation mechanism in the flash-sintered 3YSZ between 450°C and 650°C. This temperature range is lower than the onset of dislocation controlled creep in conventional YSZ which typically is higher than 800°C.

Table 4.2. Flow stress, yield strength and threshold stress at each temperature and strain rate.

Temperature (°C)	Strain rate (s ⁻¹)	Flow stress (GPa)	Yield strength (GPa)	Threshold stress (GPa)
450	0.003	2.14±0.14	1.32±0.25	1.67±0.05
	0.01	2.27±0.11		
	0.05	2.42±0.10		
	0.3	2.61±0.10		
550	0.003	1.71±0.05	1.19±0.10	1.39±0.02
	0.01	1.76±0.05		
	0.05	1.84±0.07		
	0.3	2.00±0.05		
650	0.003	1.48±0.11	1.07±0.13	1.24±0.11
	0.01	1.52±0.12		
	0.05	1.60±0.11		
	0.3	1.71±0.13		

The threshold stresses obtained from the intercept of the linear extrapolation with the stress axis are 1.67, 1.39, and 1.24 GPa for tests at 450, 550, and 650°C, respectively. The threshold stress of ~ 1.7 GPa is abnormally large to be explained by using the conventional concept of grain-boundary dislocations and surface tensions. As such, the introduction of friction stress can help understand the large threshold stresses determined here. It is known that materials with high Peierls stress tend to have large errors in activation energies and stress exponents when calculated using

conventional creep equations [191]. Therefore, the introduction of σ_o , referred to as internal stress or friction stress, in the creep equations is necessary to obtain appropriate values [192]. Given that YSZ is a ceramic material, its high Peierls stress, σ_o is > 1.0 GPa, in this study is not very surprising. Kamimura *et al.* (2018) suggested Equation (4.5) yielding Peierls stress (τ_p) for 3YSZ via Peierls-Nabarro model of the planar core dislocation [193].

$$\tau_p = \mu k \frac{b}{\delta} \exp\left(-k\pi \frac{h}{\delta}\right) \text{ and } k = \frac{1}{2\pi} \left(\frac{\sin^2\theta}{1-\nu} + \cos^2\theta\right) \quad (4.5),$$

where μ is the shear modulus, k is an preexponential factor, b is the Burgers vector, δ is the lattice periodicity, h is the spacing of the glide plane, and ν is the Poisson's ratio. Their equation yields the maximum value of 6.4 GPa for 3YSZ at 450°C, higher than the threshold stress obtained in this study. Baufeld *et al.* derived Peierls stress of 4.5 GPa for fully stabilized zirconia (doped with 11 mol% Y_2O_3) at 600°C using experimental data [194]. Dominguez-Rodriguez *et al.* determined the friction stress of 2.4 GPa for 9.4 mol% YSZ at $<570^\circ\text{C}$ [195]. We believe that the segregated oxygen vacancies at the dislocation core reduces the Peierls (friction) stress considerably by decreasing the strength of interatomic bonds.

The threshold stresses observed in metallic materials are typically measured at high temperature, where sometimes superplasticity has been observed in, e.g. Al alloys [190]. Furthermore, the threshold stress appears to decrease at higher test temperature. In this study, higher test temperature may weaken the strong covalent and ionic bonding of 3YSZ, such that the threshold stress decreases as temperature increases. Furthermore, the calculated threshold stresses are comparable to the yield strength of specimens at each temperature as shown in Table 1. As such, we hypothesize that the large threshold stress in this study is (1) the stress necessary to activate the migration of dislocations or (2) the stress necessary to overcome the friction caused by the point defects segregated along the dislocation cores. In general, the yield strength of polycrystalline ceramic materials indicates the stress necessary for microcracking, phase transformation, or dislocation movement [196]. It was reported that dislocation dominated plastic flow is favorable at the low homologous temperature and high external stress [197]. The highest test temperature in this *in-situ* study is equivalent to $0.31T_m$ and the applied external stress is higher than 1 GPa. On the other hand, the high threshold stress may also be related to segregation of charged point defects along the dislocation cores, exerting a pinning effect that can be explained by interpretation of the activation energy shown in the next paragraph.

The activation energy for the rate controlling mechanism is ~ 145 kJ/mol after taking the presence of threshold stress into consideration. Such a value is significantly less than the activation energy for grain boundary diffusion and lattice diffusion of cations, but comparable to the activation energy for oxygen and oxygen vacancy migration ($96.5 \sim 220$ kJ/mol) in YSZ (See Table 4.3) [71,198–201]. As will be discussed in the following, it seems likely that this low activation energy is a consequence of point defect segregation to the dislocations and their pinning and dragging impact due to diffusion. When assumed that the migration of dislocations is governed by thermal activation required to overcome local obstacles (point defects in our hypothesis) and/or friction stress, we can estimate the activation energy of dislocation movement by adopting the classical dislocation theory. Impurity segregation to dislocations is a well-known phenomenon in the metallic materials and is known to be analogous to grain boundary segregation [202–204]. Such segregation can pin dislocations and hinder their motion. However, if these segregates have a suitable diffusion coefficient, they might be dragged along with migrating dislocations, causing a solute drag effect [205–208] again analogue to solute drag on grain boundary motion [209]. The same concept applies to ceramic materials, although segregation is also related to electrostatics as defects now involve charges [210–213]. As such, dislocation lines can have a charge causing additional driving force for their segregation. Around the dislocation line, complementary charge accumulates to compensate the charge of the dislocations, analogous to space charges at grain boundaries [210,213]. As mobile segregates (point defects) cause a solute drag for dislocations, the diffusion of point defects would be the rate limiting step for dislocation movement. In the case of YSZ, segregations of Y and O to the grain boundaries have been reported [214]. In the present in situ experiments up to 650°C , cationic defects are largely immobile in YSZ. However, oxygen (and oxygen vacancy) diffusion in YSZ is known to be have very high diffusion coefficients [215]. As such, it is likely that the migration of dislocations in YSZ involves the diffusion of segregated oxygen or oxygen vacancies. The agreement of the measured activation energy of dislocation migration (145 kJ/mole) with oxygen or oxygen vacancy diffusion ($96.5 - 220$ kJ/mole) supports this hypothesis.

Table 4.3. Activation energy of grain boundary and lattice diffusion for Zr, Y, O, and oxygen vacancy (V_o).

	Grain boundary diffusion (kJ/mole)	Lattice diffusion (kJ/mole)
Cations (Zr, Y)	370 [216]	460 - 650 [217–219]
O	188 [201]	220 [201]
V_o	-	96.5 - 164 [71,198–200]

We can also adopt the classical dislocation theory to estimate the activation energy of dislocation movement. If the migration of dislocations is governed by thermal activation required to overcome local obstacles (point defects in our hypothesis) and/or friction stress, the deformation rate can be written as,

$$\dot{\epsilon} = \dot{\epsilon}_o \exp\left(-\frac{\Delta G}{kT}\right) \quad (4.6),$$

where $\dot{\epsilon}_o$ is a preexponential factor and ΔG is the change in Gibbs free energy [220]. The newly defined strain rate sensitivity with a unit of pressure is given by,

$$I = \frac{\Delta\sigma}{\Delta \ln \dot{\epsilon}} \quad (4.7),$$

where I is the strain rate sensitivity and σ is the applied stress. The calculated strain rate sensitivity values are 107, 64, 53 MPa for 450, 550, 650°C experiments, respectively. The activation volume of dislocation movement can be experimentally determined by,

$$V = \frac{kT}{mI} \quad (4.8),$$

where m is the Schmid factor for the primary slip system. The Schmid factor of 0.47 for the (001)[1 $\bar{1}$ 0] primary slip system is employed in this analysis. By taking Burgers vector for <110> type lattice dislocation = $3.6 \times 10^{-10} m$, the respective activation volumes of $4.2b^3$, $8.1b^3$, and $10.9b^3$ at 450, 550, and 650°C are determined. The activation enthalpy can be written as

$$\Delta H = -kT^2 \left(\frac{\Delta\sigma}{\Delta T}\right)_{\dot{\epsilon}}/I. \quad (4.9)$$

So the calculated values are given as $\Delta H(450^\circ\text{C}) = 2.24 \text{ eV}$, $\Delta H(550^\circ\text{C})=2.28 \text{ eV}$, and $\Delta H(650^\circ\text{C})=3.44 \text{ eV}$. Lastly, the Gibbs free energy of activation in Equation (4.6) can be calculated by [221]

$$\Delta G = \frac{\Delta H + T \frac{d\mu}{dT} \frac{m\sigma}{\mu} V}{1 - \frac{T}{\mu} \frac{d\mu}{dT}}. \quad (4.10)$$

The shear modulus (μ) at the test temperatures is calculated from the elastic modulus of 3YSZ reported by Shimada et al. (1984) using the following equation [222].

$$\mu = \frac{E}{2(1+\nu)} \quad (4.11)$$

where E is the elastic modulus and ν is the Poisson's ratio, ~ 0.31 for 3YSZ [135]. The Gibbs free energy values are calculated to be: $\Delta G(450^\circ\text{C}) = 1.93$ eV, $\Delta G(550^\circ\text{C}) = 1.87$ eV, and $\Delta G(650^\circ\text{C}) = 2.82$ eV. The calculated Gibbs free energy based on the classical dislocation theory lies in the reasonable ranges (180 ~ 272 kJ/mol), in good agreement with the activation energy obtained from the power law creep, 145 kJ/mol derived from our jump tests. What is more, these free energy values are consistent with the model of thermally activated migration of dislocations in the literature [194]

4.6. Conclusions

In summary, 3YSZ was processed by the flash sintering technique under an electric field of 150 V/cm. *In-situ* microcompression tests on the flash sintered 3YSZ was performed at 450 ~ 650°C to study the underlying deformation mechanism. Strain rate jump tests lead to a stress exponent of ~ 7 , and threshold stresses comparable to the yield strengths. The calculated activation energy of 145 kJ/mol is comparable to the activation energy for oxygen vacancy migration. This study suggests that the abundant defects induced during flash sintering (oxygen vacancies, and dislocation) lead to improved plasticity, and the deformation mechanism may be dislocation glide and climb assisted by oxygen vacancy migration over the temperature range of 450 - 650°C for the flash-sintered 3YSZ. This study sheds lights on the mechanical behavior of an important class of ceramic materials that have widespread industrial applications.

CHAPTER 5. IN-SITU HIGH TEMPERATURE MICROMECHANICAL TESTING OF ULTRAFINE GRAINED YTTRIA-STABILIZED ZIRCONIA PROCESSED BY SPARK PLASMA SINTERING

The following chapter contains content reproduced with permission from “J. Cho, J. Li, Q. Li, J. Ding, H. Wang, S. Xue, T. Holland, A. Mukherjee, H. Wang, X. Zhang. “In-situ high temperature micromechanical testing of ultrafine grained yttria-stabilized zirconia processed by spark plasma sintering.”, *Acta Materialia*, 155 (2018): 128-137.” Copyright 2018 Elsevier B. V.

5.1. Overview

Yttria-stabilized zirconia (YSZ) exhibits both enhanced strength and fracture toughness attributed to transformation-induced plasticity. Recent studies show that miniaturization of YSZ to the microscale enhances the effectiveness of stress-induced phase transformation by reducing mismatch stress among incommensurate grains. However, the fundamental understandings on the high temperature micromechanical behaviors of ultrafine grained YSZ remain limited. Here, we report on the high temperature (up to 670°C) *in-situ* micromechanical testing of spark plasma sintered YSZ. The mechanical behaviors of YSZ tested below 400°C are highlighted by large inelastic strain (~ 7%) due primarily to phase transformation toughening. Beyond 400°C, martensitic transformation toughening is gradually superseded by grain boundary sliding triggered by ultrafine grains. The micropillars tested at 670°C exhibit significantly enhanced plastic flow, arising mainly from dislocation activity along with grain boundary sliding.

5.2. Introduction

Zirconia (ZrO_2) has monoclinic phase at room temperature, and undergoes tetragonal-to-monoclinic phase transformation at ~950°C upon cooling, which results in ~4% volume expansion [1]. The large volume change in zirconia induced by phase transformation may cause catastrophic failures of components during thermal cycling. The phase transformation can be suppressed by doping zirconia with oxides such as Y_2O_3 , CeO_2 , CaO and MgO [2–4]. As a result of doping, metastable tetragonal or cubic phase of zirconia is stabilized at room temperature. Metastable phases have the same structure as that in pure zirconia, but it contains dopant cations and oxygen vacancies to maintain the charge neutrality [5]. It is known that the presence of oxygen vacancies

permits the cation and anion relaxations, and thus stabilizes the metastable phases at room temperature [6]. Among numerous possible dopants, yttria (Y_2O_3) is attractive in that 3 mol % yttria is sufficient to fully stabilize tetragonal zirconia [23].

Although strength and fracture toughness are often mutually exclusive for most structural materials [8], yttria stabilized zirconia (YSZ) exhibits both enhanced strength and fracture toughness owing to the tetragonal-to-monoclinic martensitic transformation occurring near crack tips [9–11]. A compressive strain field generated by the volume expansion due to martensitic transformation near the crack tip retards the crack propagation, thereby increasing the fracture toughness [11]. Zirconia with enhanced fracture toughness has been used for various applications including thermal barrier coatings, oxygen sensors, fuel cells, and shape memory devices [12–14]. It has been shown that miniaturization of stabilized zirconia to microscale permits the stress induced transformation at a low stress without fracture [14]. For instance, while bulk stabilized-zirconia exhibits a failure strain of 3% upon compression [39], microscale stabilized-zirconia sustains 8% of compressive strain without fracture, and demonstrates superelasticity and shape memory effect attributed to the significantly enhanced martensitic transformation and less population of intrinsic microcracks [40–43,45–47,180]. These studies suggest a new paradigm for ceramic materials to be used in microelectromechanical system, sensing, and actuation applications [48,223,224].

Most of the recent micromechanical testing studies on zirconia focus primarily on maximization of the effectiveness of martensitic transformation by increasing grain size and decreasing the specimen size. A smaller number of grains in stabilized zirconia alleviates mismatch stress among grains during martensitic transformation, such that transformation induced toughening can be triggered at low stress without fracture [14]. However, it is known that YSZ with large grains suffers from significant mechanical degradation at elevated temperature and is vulnerable to chemical and thermal ageing [23]. Therefore, it is necessary to evaluate the micromechanical behavior of ultrafine grained YSZ at elevated temperature. In this study, we used spark plasma sintering to fabricate ultra-fine grained YSZ, and *in-situ* microcompression tests were carried out from 25 to 670°C inside a scanning electron microscope. Temperature dependent fracture behaviors and transitions of the underlying deformation mechanisms are discussed.

5.3. Materials and methods

Commercially available 3 mol% yttria stabilized zirconia (3YSZ) powder (TZ-3Y-E, Tosoh corp., ~ 40 nm) was sintered by the spark plasma sintering (SPS) technique. The powder was put in a graphite die and hot pressed up to 10 kN during the sintering experiments. The pulsed direct current was applied through the graphite die and the sintering temperature rose to 1026°C at a ramping rate of 100°C/min. The temporal Joule heating generated inside the graphite die permitted the achievement of a relative density of 94% (measured by Archimedes' density method in distilled water) at a furnace temperature lower than conventional sintering temperature for YSZ (~1500°C). The rapid densification process, within a few minutes, during SPS facilitates the retention of fine grains. Prior to conducting micromechanical testing, spark plasma sintered 3YSZ was characterized by X-ray diffraction (PANalytical Empyrean), scanning electron microscopy (SEM) (using an FEI quanta 3D FEG scanning electron microscope) and transmission electron microscopy (TEM) (on an FEI Talos 200X TEM/STEM microscope with a super EDX detector). TEM specimens of the as-sintered 3YSZ were prepared by manual grinding, polishing, dimpling and low energy (2 kV) ion milling (PIPS II, Gatan) to reduce ion milling induced damage. The TEM microscope operated at 200 kV was used to examine the microstructure of specimens. SEM (FEI Nova Nano SEM) was also employed to examine the microstructure of specimens after microcompression tests.

Micropillars with ~3 μm in diameter and ~8 μm in height were fabricated by means of focused ion beam (using the FEI quanta 3D FEG SEM microscope). Most pillars have an aspect ratio of 1:2.6 and a tapering angle of less than 2°. Before fabricating micropillars on the specimen, a series of polishing was conducted using SiC sandpapers, ~ 1 μm diamond papers, and ~ 20 nm colloidal silica to minimize the roughness of the surface. The polished specimen was mounted on a specimen stub for SEM and coated with platinum at 40 mA for 60 s to enhance the electric conductivity. The stub was tilted at 52° in an SEM chamber to make the ion beam perpendicular to the specimen base. A large crater was made using high ion beam current (30 nA) at an ion beam voltage of 30 kV. Thereafter, micropillars with ~3 μm in diameter and ~8 μm in height were prepared by a series of decelerated currents to reduce tapering angle and smoothen the pillar surface. Meanwhile, careful astigmatism and focus corrections at each step were conducted to sharpen the ion beam. The pillars were prepared near the center of the specimen in order to avoid

inhomogeneous microstructure near the edge, which may be generated by frictional force between the powders and graphite die.

A nanoindentation system (Hysitron PI 88×R) was employed for micromechanical testing on the fabricated micropillars inside the FEI quanta 3D FEG SEM microscope. A 5 μm diamond flat punch tip designed specifically for high temperature tests was mounted on a piezoelectric transducer that collects force-displacement data. The specimen was inserted between a V-shaped Mo clamp and a ceramic heating stage and tightly fixed to minimize the machine compliance. The machine compliance was systematically measured prior to the actual test.

The nanoindentation system was tilted at 15° in the SEM chamber for better visualization of the pillar morphology during the compression test. The diamond flat punch and the sample were heated simultaneously by the probe heater and the ceramic heating stage, respectively, to identical desired temperature at a ramping rate of $20^\circ\text{C}/\text{min}$. Once the desired temperature was reached, the specimen was kept at such a temperature for 30 min prior to conducting the microcompression experiment to acquire thermal equilibrium and minimize thermal drifts. Thermal drifts are of concerns when conducting microcompression tests at elevated temperatures. Thermal drift rates were measured during preloading steps over 40 s of every compression test. Thermal drifts do not vary noticeably with increasing test temperature as can be seen in Fig. 5.1. Drift rates at each temperature calculated from the slopes of each curve are less than 0.7 nm/s. The individual compression test lasts ~ 50 s with a strain rate of $5 \times 10^{-3} \text{ s}^{-1}$, and thus the actual displacement offset is less than 40 nm, which is equivalent to a strain of 0.005 for pillars with 8 μm in height. After the acquisition of the drift rate at each experiment, the nanoindentation system compensates displacement drift based on the calculated drift rates and yields the calibrated displacement data.

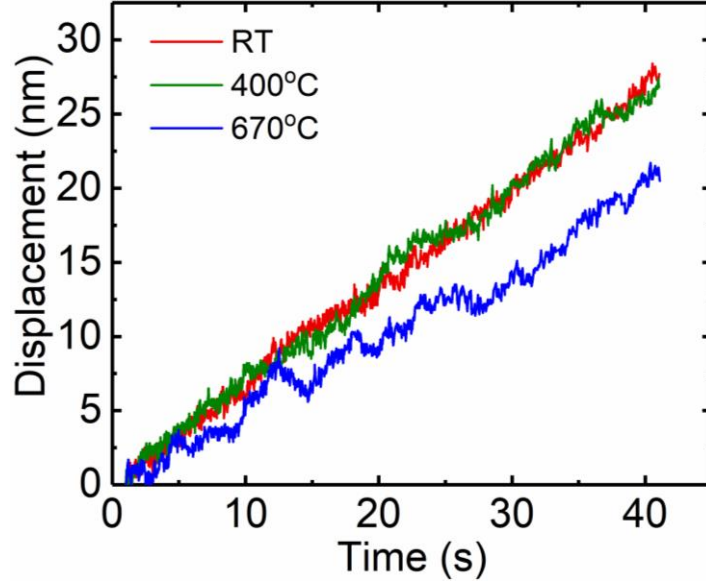


Figure 5.1. Displacement vs. time curves at RT, 400, and 670°C. The slopes of curves (drift rate) are less than 0.7 nm/s in every case.

Machine compliance needs to be measured particularly at high forces prior to compression test because it may affect total displacement significantly. There are three factors affecting the machine compliance: transducer, indenter probe, and sample mounting. To minimize compliance from sample mounting method, we avoid using a soft material to glue a sample on a stage. Instead we mount the sample underneath V-shaped Mo fixture tightly such that machine compliance coming from sample mounting method is minimized. In order to calculate machine compliance from transducer and indenter probe, an array of indents using a Berkovich tip was collected on the standard fused quartz at high loads (more than 5,000 μN). The total compliance, C_{total} (inverse of stiffness) is given as,

$$C_{\text{total}} = C_m + \frac{\sqrt{\pi}}{2} \times \frac{\sqrt{H}}{E_r} \times \frac{1}{\sqrt{P_{\text{max}}}} \quad (5.1)$$

where C_m is machine compliance, H is the hardness of standard fused quartz, E_r is the reduced modulus, and P_{max} is the maximum load. By plotting C_{total} vs. $\frac{1}{\sqrt{P_{\text{max}}}}$, machine compliance can be obtained from the Y-axis intercept, which is about 3.0 nm/mN. High temperature compression test system is equipped with a cooling system to make sure that only the diamond tip and specimens are heated during tests. Also, diamond has much higher elastic modulus and melting temperature than the specimens. Therefore, a machine compliance change between room temperature and high temperature is negligible.

5.4. Results

Prior to *in-situ* compression test, the microstructure of spark plasma sintered 3YSZ was investigated in detail. XRD study (Fig. 5.2) confirms the polycrystalline nature of the specimen, and the dominant phase is the metastable tetragonal zirconia, capable of transforming into monoclinic phase under stresses. Using the XRD data in Fig. 5.2, X-ray peak broadening was measured at half the maximum intensity to evaluate the lattice strain in the spark plasma sintered 3YSZ. the Williamson-Hall method was introduced to estimate the residual stress [161]:

$$\beta_{hkl}\cos\theta = \frac{K\lambda}{D} + 4\sin\theta\sigma/E_{hkl} \quad (5.2)$$

where β_{hkl} is the peak broadening at half the maximum intensity in the unit of radians, K is the shape factor, λ is the X-ray wavelength, D is the mean size of crystalline, σ is the residual stress, and E_{hkl} is the elastic modulus along $[hkl]$ direction. The elastic moduli along $[hkl]$ direction for a tetragonal structure can be calculated using Eq. 3.2 and Table 3.2. The residual stress, σ , then can be obtained by plotting $\beta_{hkl}\cos\theta$ versus $4\sin\theta/E_{hkl}$. Fig. 5.3 shows the plot of $\beta_{hkl}\cos\theta$ versus $4\sin\theta/E_{hkl}$ with a linear regression line, the slope of which is the residual stress determined to be 359.4 MPa. Fig. 5.4 (a) shows an SEM micrograph of agglomerated grains of as-sintered 3YSZ. Despite lower sintering temperature and shorter sintering time compared to conventional sintering, the structures were well densified (~94%) and retained ultrafine grain size. The TEM micrograph in Fig. 5.4 (b) shows ultra-fine grains with a few nanopores. The inserted selected area diffraction (SAD) pattern shows no preferred crystallographic orientation, consistent with XRD result. High resolution TEM micrograph in Fig. 5.4 (c) reveals a triple junction among three sintered grains and the grain boundaries contain no amorphous phase. It has been shown that amorphous phase along grain boundaries may reduce the cohesive grain boundary strength during large strain deformation at elevated temperatures [44]. Grain size was measured by the intercept method by using numerous TEM images, and the average grain size is ~ 175 nm as shown in the statistical distribution of grain size in Fig. 5.4 (d).

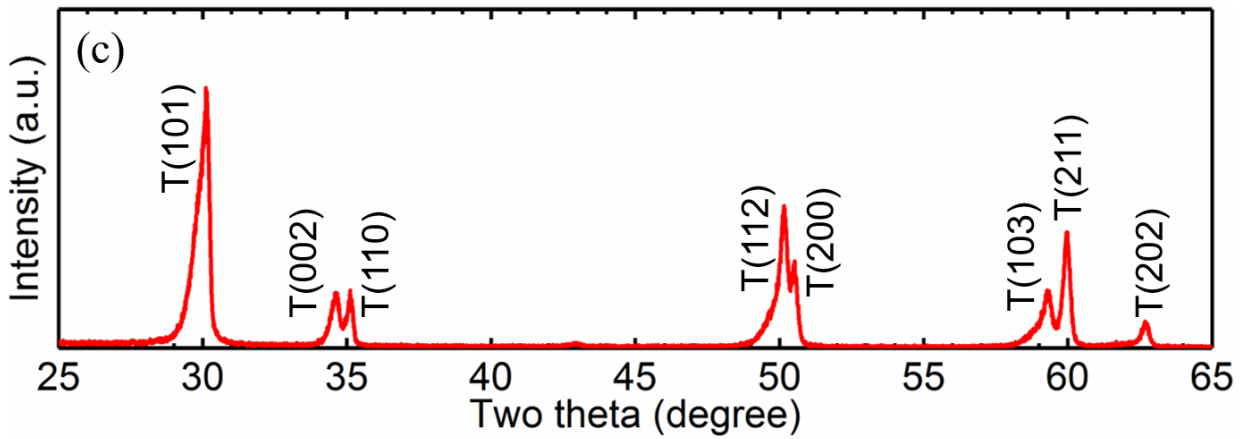


Figure 5.2. XRD patterns of spark plasma sintered 3YSZ with crystallographic plane indices. It is shown that metastable tetragonal zirconia is a dominant phase without evident cubic and monoclinic zirconia phase.

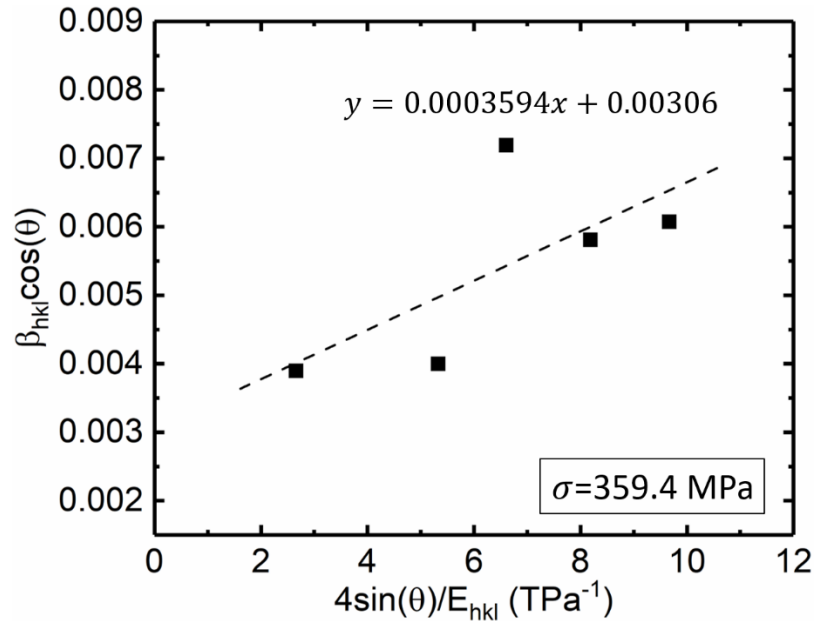


Figure 5.3. The determination of the residual stress in SPS YSZ using the Williamson-Hall analysis.

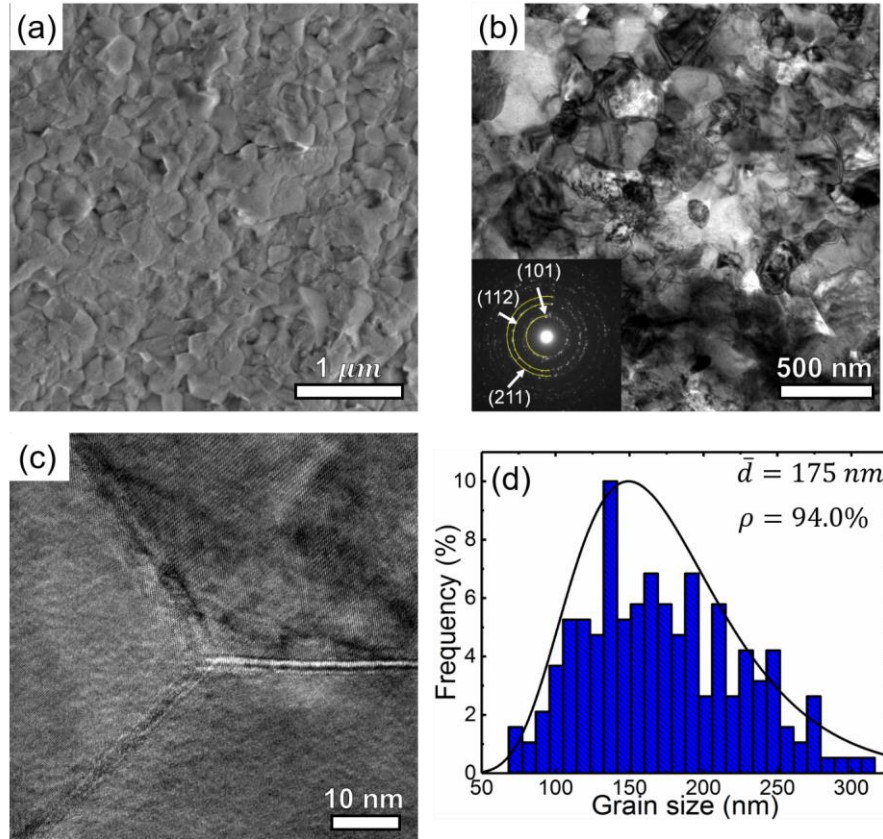


Figure 5.4. Microstructure of SPS 3YSZ and grain size analysis. (a) An SEM image of a typical unpolished region showing agglomerated grains. (b) A bright-field TEM micrograph showing ultrafine grains, and the inserted SAD pattern shows continuous rings of the tetragonal phase. (c) A high-resolution TEM image showing a clear triple junction without glassy phase along the grain boundaries. (d) Grain size distribution determined by the intercept method showing the average grain size of ~ 175 nm.

To evaluate the mechanical behavior of the spark plasma sintered 3YSZ, we first carried out *in-situ* microcompression tests at room temperature and at a strain rate of 5×10^{-3} /s inside an SEM microscope. Partial unloading segments within an elastic region (at a displacement of 60 and 120 nm) were applied to determine the apparent elastic modulus. Three compression tests were conducted to check the repeatability of the experiments. Thereafter, the test temperature rose to 200, 400, 600, and 670°C and the tests were carried out at the same strain rate.

The evolutions of pillar morphology during *in situ* tests at three representative temperatures (25, 400, and 670°C) are compared in Fig. 5.5 (a-c). The corresponding true stress-strain curves are compared in Fig. 5.5 (d). The pillar tested at 25°C deformed elastically up to $\sim 5\%$ of strain without any crack. The nucleation of crack is observed (Fig. 5.5 (a₃)) at 6% of strain and a flow

stress of ~ 4.5 GPa, followed by prominent fracture accompanied by shear offsets. For the pillar tested at 400°C , cracks nucleated at 6% (corresponding to a peak stress of 2.2 GPa) propagated slowly downward. At a failure strain of 9%, multiple cracks were observed accompanied by outward buckling of the top portion of the pillar. On the other hand, the pillar compressed at 670°C exhibit no evident cracks up to a surprisingly large strain of 30%. After reaching a yield strength of ~ 1.4 GPa, a long plateau was observed in the true stress-strain curve (Fig. 5.5 (d)).

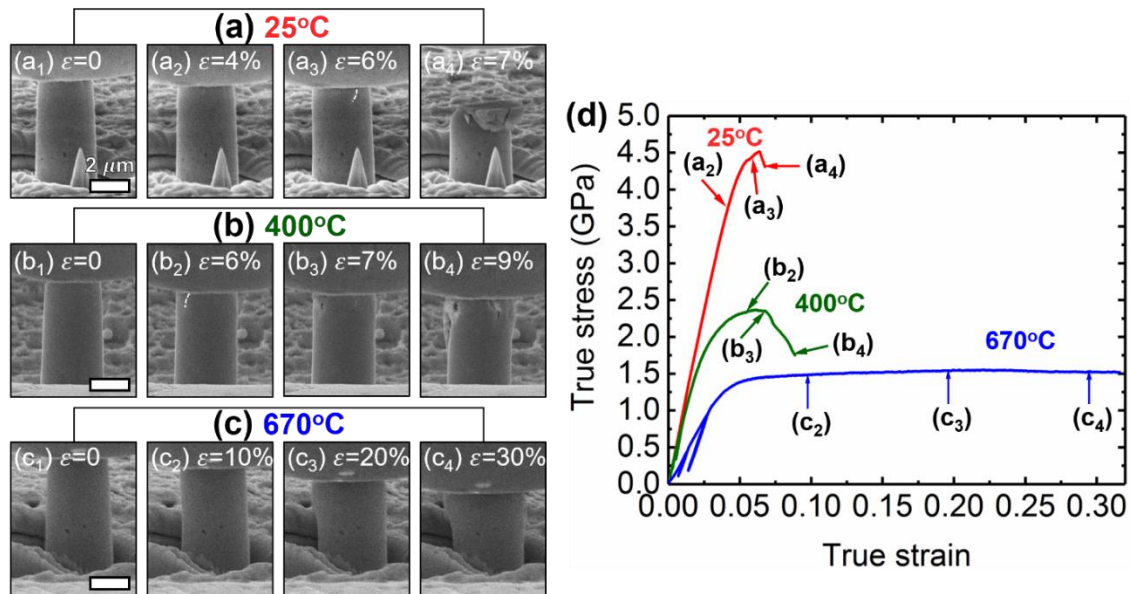


Figure 5.5. Comparison of morphology evolution and stress-strain behaviors of micropillars during *in-situ* compression tests at 25, 400, and 670°C . (a₁-a₄) At 25°C , cracks were nucleated at a strain of 6%, and the pillar fractured in a brittle manner right after the crack nucleation. (b₁-b₄) The micropillars tested at 400°C show crack formation at a strain of 5~6%. However, cracks propagated downward slowly into the pillar without brittle failure. (c₁-c₄) When compressed at 670°C , the pillars deformed gradually and uniformly in the top portion of the pillars with little cracks. (d) The true stress-strain curve collected at 25°C deviates from its linearity at a strain of 4%, corresponding to a stress level of ~ 4 GPa. The yield strength and flow stress both decrease for pillars tested at elevated temperatures. The pillars tested at 670°C reached a constant flow stress of ~ 1.5 GPa until a strain of 30% without softening. Partial unloading was performed in all tests to obtain a reliable measurement of modulus. The white dash lines in the SEM micrographs indicate cracks.

SEM micrographs in Fig. 5.6 compare the morphology of the micropillars before and after the *in-situ* compression tests at various temperatures. Pillars tested at 200°C or below exhibited catastrophic failure (shear offsets) at a strain of 4-7% (Fig. 5.6 a-b). When tested above 400°C , pillars showed no shear failure (Fig. 5.6 c-e); instead, several cracks formed near the top of the

pillars slowly propagated downward into the pillars and the crack propagation speed decreases at higher test temperatures. The pillars tested at 670°C dilated significantly near the top without evidence of shear bands (Fig. 5.6 (e)). Fig. 5.7 (a-e) show numerous stress-strain curves at each test temperature and the results show in general good reproducibility when taking typical porous nature of ceramic materials into account. In Fig. 5.7 (f) compares the representative true stress-strain curves at various test temperatures. When $T \leq 400^\circ\text{C}$, pillars reached a maximum flow stress, which decreased drastically thereafter. When $T \geq 600^\circ\text{C}$, the flow stress reached a plateau of ~ 1.4 GPa.

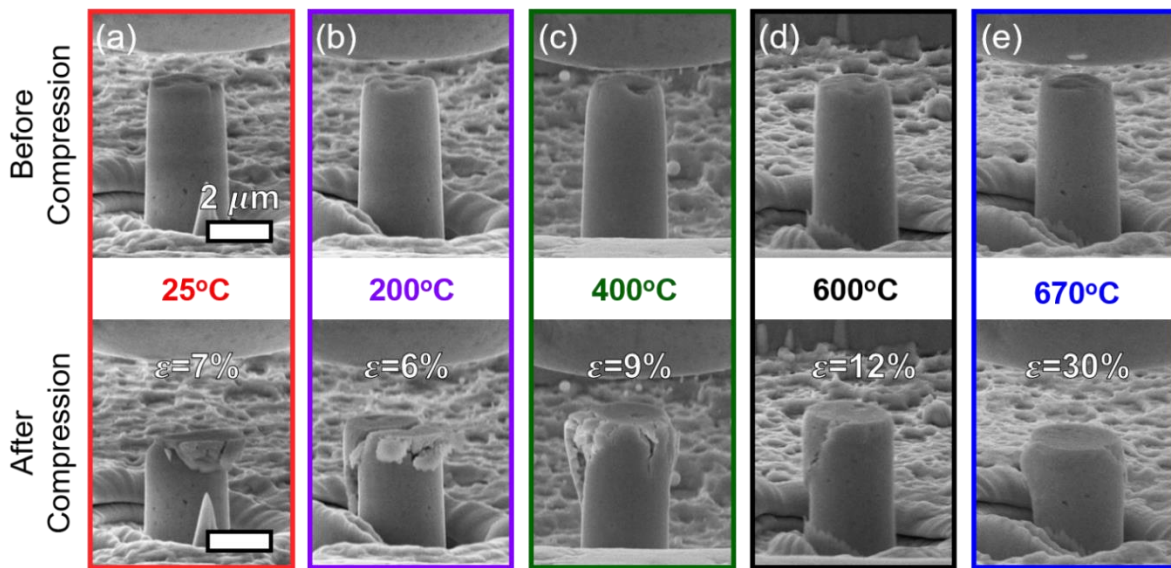


Figure 5.6. SEM images of micropillars before and after microcompression tests at elevated temperatures up to 670°C. (a-b) When tests were conducted below 200°C, the micropillars exhibit brittle fracture at a strain of 4-7%. (c-d) Transitions of deformation mechanisms were observed in pillars tested at 400 and 600°C. Several cracks nucleated from the top of the pillars and propagated slowly downward into the pillars. (e) The pillars tested at 670°C showed significantly enhanced plastic flow ability. The deformation was mainly accommodated by the top half of the pillar, and the crack propagation speed was greatly reduced.

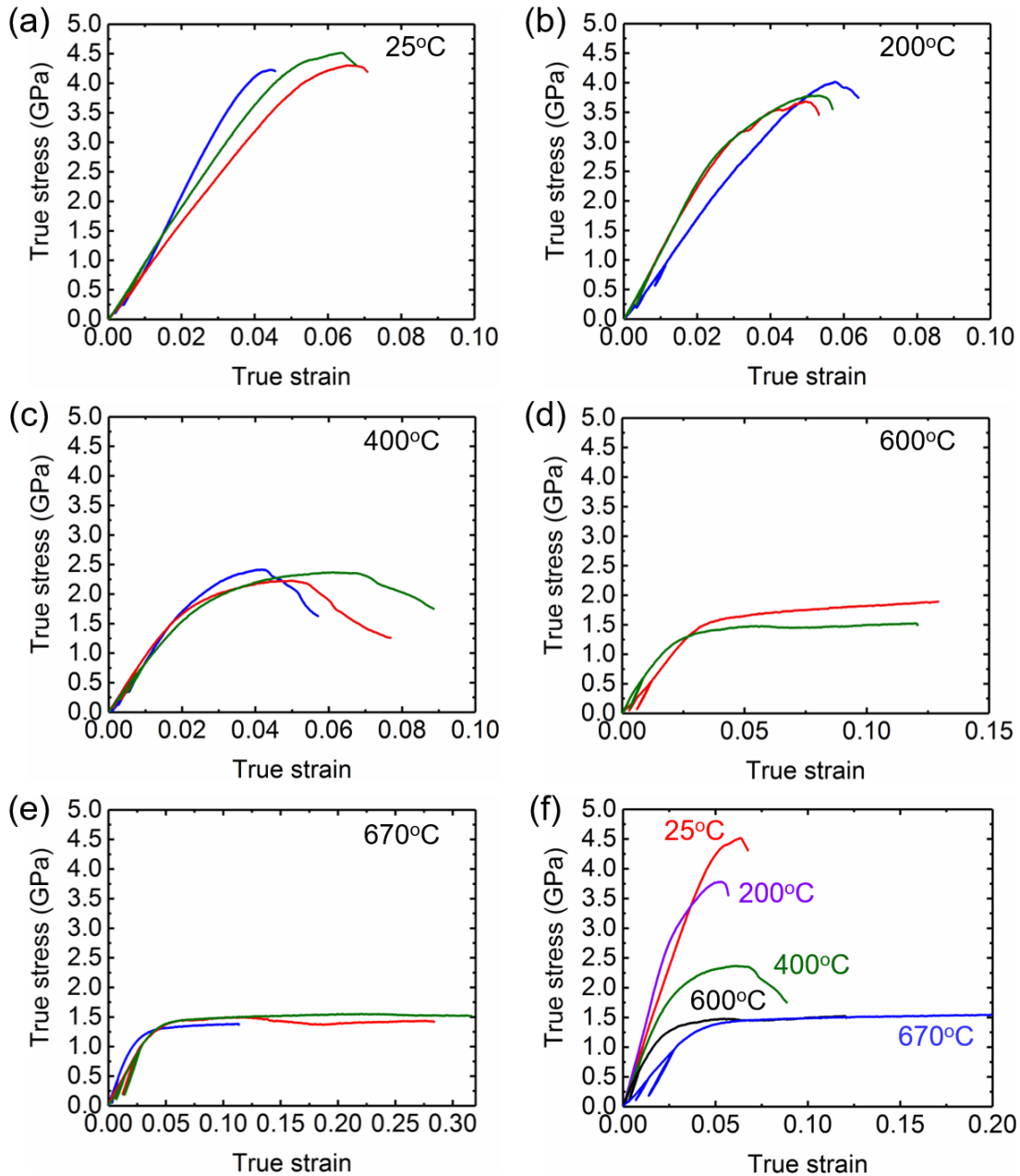


Figure 5.7. Stress-strain curves for SPS 3YSZ micropillars tested *in-situ* at different temperatures at a strain rate of 5×10^{-3} /s. Numerous tests were carried out to check the reproducibility of the experimental results at (a) 25°C, (b) 200°C, (c) 400°C, (d), 600°C, and (e) 670°C. (f) Comparison of stress-strain curves at different temperatures. Partial unloading at displacement of 60 and 120 nm was conducted to measure the apparent elastic modulus of SPS 3YSZ at different temperatures.

The fracture surfaces of micropillars after the compression tests at 25, 400, and 670°C were examined by SEM microscope equipped with a through-the-lens detector for high-resolution imaging. Fig. 5.8 (a) and (b) show the top-down and side view (20°) of the pillar fractured at 25°C

in a brittle manner. The fracture surface appears relatively smooth, and individual grains cannot be clearly resolved, indicating transgranular fracture. Numerous shear bands (indicated by black arrows in Fig. 5.8 (b)) are observed on the fracture surface. Moreover, surface rumpling (wavy lines on the surface of pillars) is shown in the region (labeled in white box) adjacent to the fracture surface. On the other hand, when tested at 400°C, the fracture surface reveals grain boundaries clearly, indicating the occurrence of intergranular fracture. In the case of pillars tested 670°C, no prominent fracture surface can be resolved. Small cracks were distributed on the top half of the pillars along the grain boundaries.

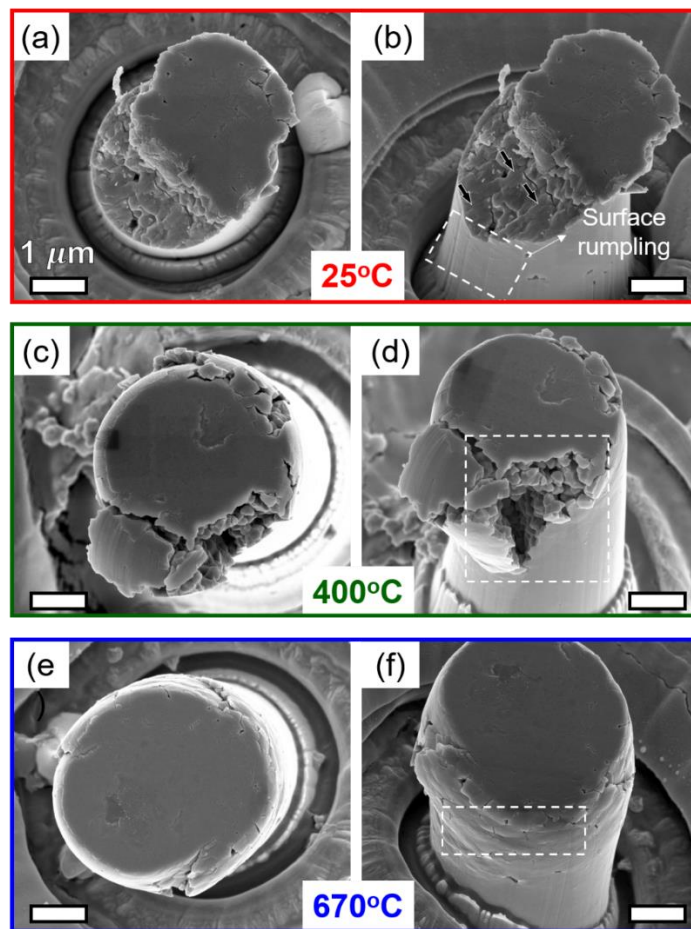


Figure 5.8. Top (left panel) and side (right panel) views of pillars tested at 25, 400, and 670°C. (a-b) For the pillars tested at 25°C, transgranular fracture with several shear bands (black arrows) was observed. Surface rumpling in the boxed region was observed due to martensitic phase transformation. (c-d) When tested at 400°C, fracture surface reveals individual equiaxed grains highlighted in the white box. (e-f) Little fracture was detected for the pillars tested at 670°C. After compression to a true strain of 30%, surface roughening in the boxed region can be seen as shown in the box.

The YSZ pillars deformed at room temperature and 400°C were examined in TEM to evaluate the dominant deformation mechanisms. As shown in Fig. 5.9 (a-d), for the pillar fractured at room temperature, several grains near the fracture surface were examined along respective zone axis of $[\bar{1}00]$, $[1\bar{1}2]$, and $[\bar{1}01]$, and best indexed as a monoclinic zirconia. Fig. 5.9 (e-h) show bright-field XTEM images of top, middle, and bottom sections of the pillar compressed at 400°C. Top and middle portions of the pillar (where applied stress is concentrated) exhibit a high density of local grain separations (gaps) as indicated by red arrows. In comparison, the bottom portion of the deformed pillar has little sign of gaps along grain boundaries, implying that the plastic deformation was accommodated primarily by the top and middle section of the pillars. Fig. 5.10 shows cross sections of the pillars tested at 400 and 670°C imaged by focused ion beam. At 400°C, cracks appear to propagate intergranularly, and most grains remain equiaxed (Fig. 5.10 (a)). Several large cavities (indicate by red arrows) were observed. In comparison, for the pillar tested at 670°C (up to a true strain of 30%), no significant crack was observed (Fig. 5.10 (b)). Numerous elongated grains (indicated by blue arrows) perpendicular to the compression direction as well as a high density of small cavities in the top of the deformed pillars are clearly resolved.

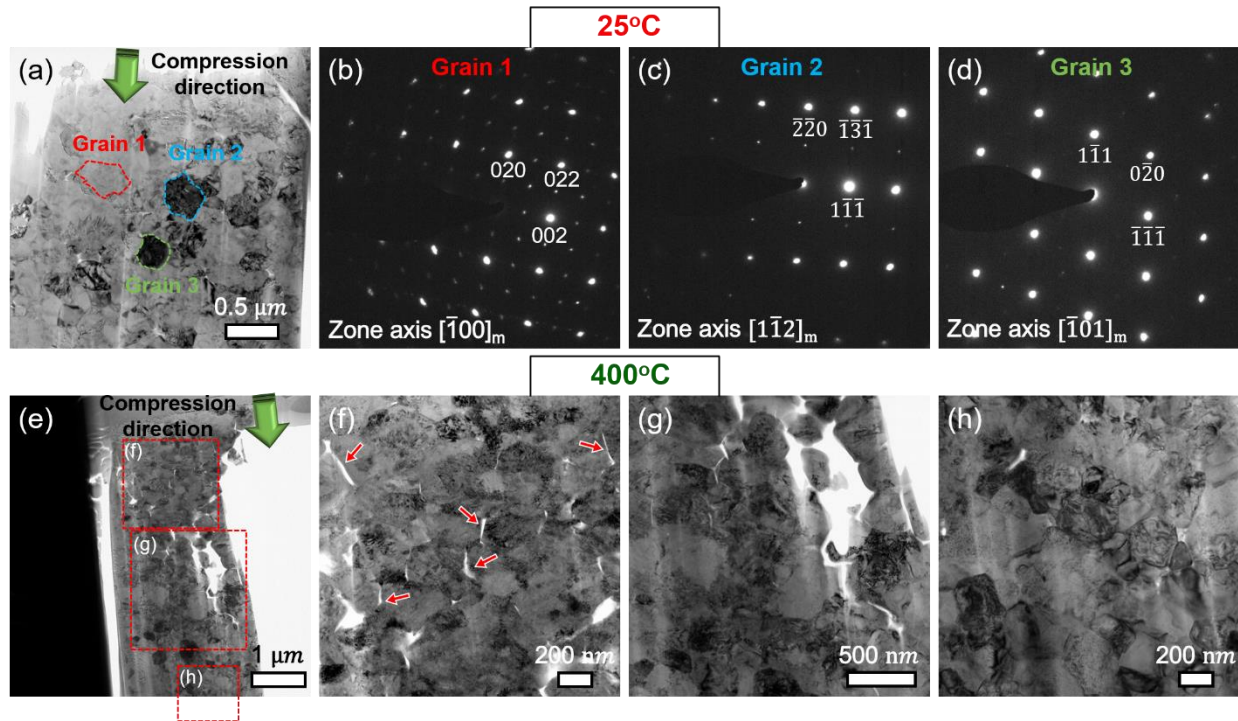


Figure 5.9. TEM analyses of the 3YSZ pillars tested at room temperature and 400°C. (a) Bright-field XTEM image of the deformed pillar at room temperature. Grains 1-3 were chosen to identify the phase transformation. (b-d) Selected area electron diffraction (SAED) patterns showing that grains 1-3 have monoclinic zirconia phase examined along respective zone axis of $[\bar{1}00]_m$, $[1\bar{1}2]_m$, and $[\bar{1}01]_m$. (e) Bright-field XTEM image of the deformed pillar at 400°C. (f) Top portion of the deformed pillar showing gaps along grain boundaries induced by grain boundary sliding (indicated by red arrows). (g) Intergranular fracture in the middle section of the deformed pillar. (h) The bottom portion of the deformed pillar shows no grain boundary gaps.

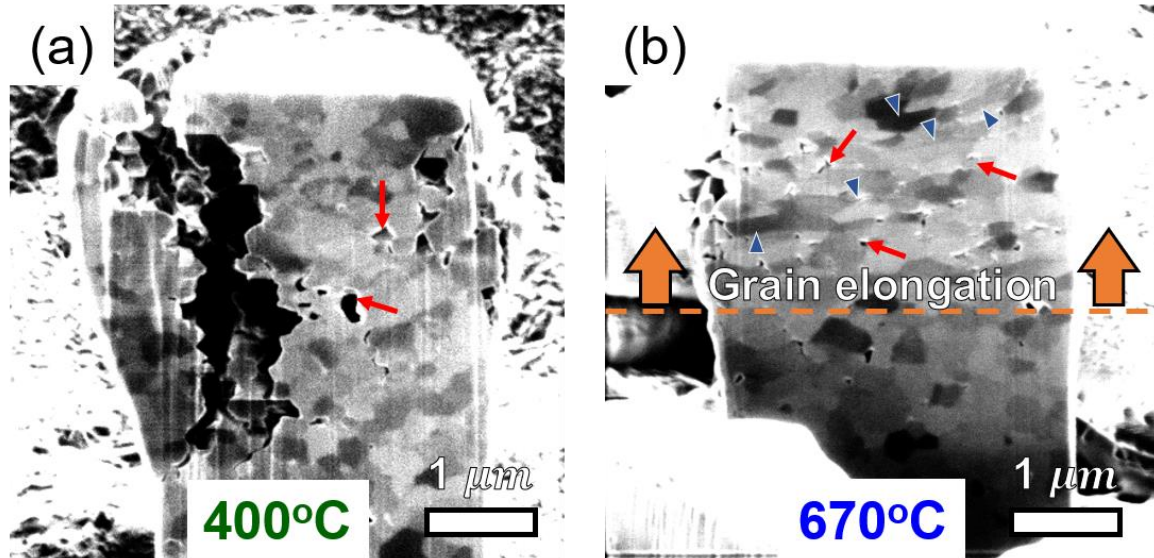


Figure 5.10. Cross section FIB ion microscopy images of the compressed pillars. (a) The cross-sectional view of the pillar tested at 400°C at a strain of 9% shows crack propagation path and cavities generated along the grain boundaries due to mechanical test. (b) For the pillar tested 670°C, no obvious crack was observed. Elongated grains with numerous nanoscale cavities indicated by blue and red arrows, respectively in the top half of the pillar were resolved.

The cross section of the pillar tested at 670°C was also examined by TEM (Fig. 5.11 and 12). Numerous deformed grains exhibit arrays of dislocations as demonstrated in a typical example in Fig. 5.11 (b). Interplanar spacing of the (002) plane in this grain (Fig. 5.11 (c)) is calculated to be 0.257 nm, which coincides with the reported reference spacing of 0.259 nm for bulk materials. The SAD pattern in Fig. 5.11 (b) reveals the tetragonal zirconia phase examined along the $[\bar{1}00]$ zone axis. Filtered high resolution TEM image in Fig. 5.11 (d) from high resolution TEM in Fig. 5.11 (b) shows abundant dislocations. Monoclinic phase was also detected as can be seen in SAD for a large area of the deformed pillar in the indexed Fig. 5.12 (a). Fig. 5.12 (b) shows the deformed grain (into monoclinic phase) containing martensite lath and stacking faults. The SAD pattern of the center grain in Fig. 5.12 (b) shows clear monoclinic phase (Fig. 5.12 (c)). High-resolution TEM micrograph (Fig. 5.12 (d)) shows the presence of high-density stacking faults in the deformed grains.

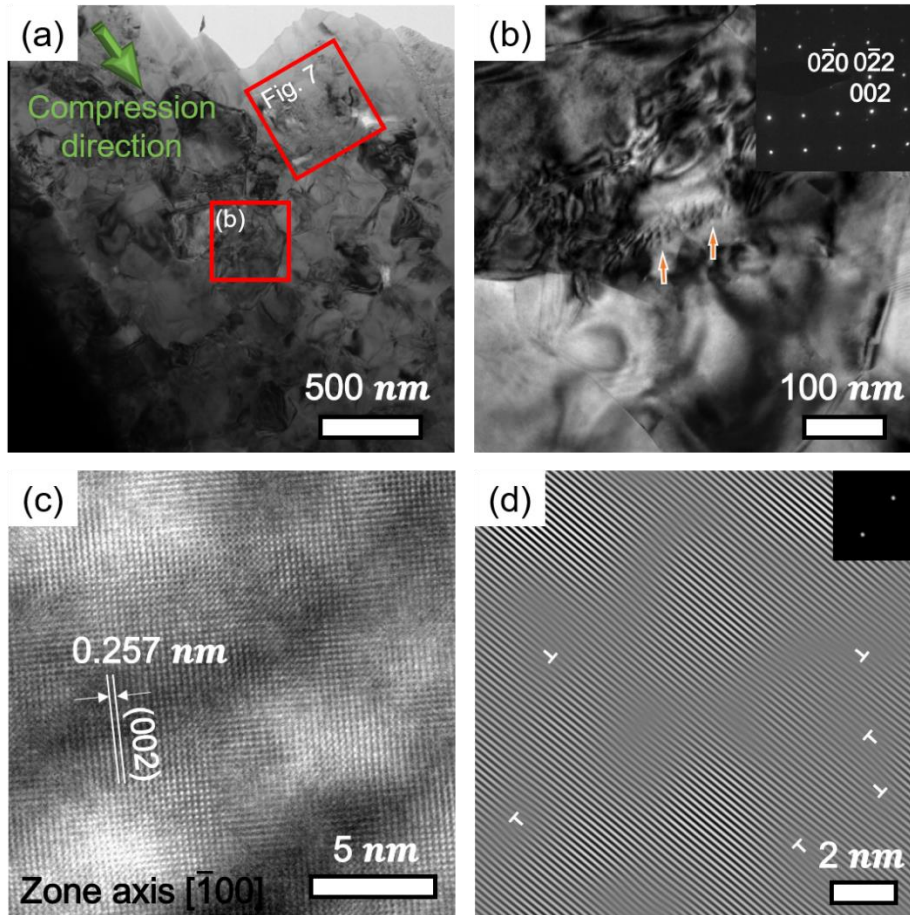


Figure 5.11. TEM images of the pillar after compression test at 670°C. (a) BF TEM images of the deformed pillar showing the location of the grains in Fig. (b) and Fig 5.12. (b) Arrays of dislocations within grains were verified (marked by orange arrows). (c) High resolution TEM image of the grain retaining arrays of dislocations with selected area diffraction pattern of the grain examined along $[\bar{1}00]$ zone axis. (d) FFT processed high resolution TEM image shows the presence of abundant dislocations along $(0\bar{2}2)$ plane.

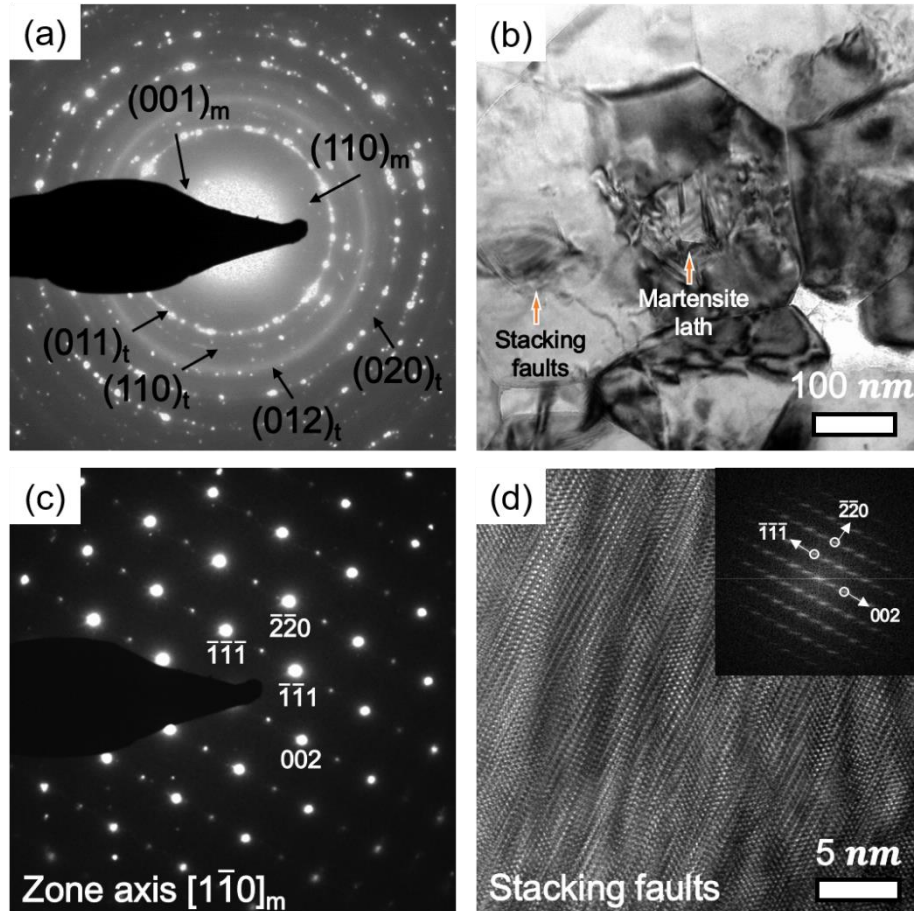


Figure 5.12. TEM images of the compressed pillar at 670°C showing the deformation induced monoclinic zirconia. (a) SAD pattern with continuous rings indicates dominant tetragonal phase with monolithic diffraction spots arising from a few grains that underwent martensitic transformations. (b) Bright-field TEM image of a grain with monoclinic phase shows martensite lath and stacking faults. (c) SAD pattern of the grain with monoclinic phase. (d) High resolution TEM image and the inserted FFT confirms the presence of stacking faults.

5.5. Discussions

5.5.1. Transformation induced toughening

The pillars tested at room temperature retain surface rumpling adjacent to fracture surface presumably due to the volume expansion induced by martensitic phase transformation. It has been reported that the amount of yttria in zirconia and grain size play a pivotal role in triggering martensitic transformation [17–20,225,226]. Specifically, the presence of low yttria content (~ 3 mol%) enhances transformability from tetragonal to monoclinic phase by increasing tetragonality [20]. Meanwhile large grain sizes result in high internal residual stresses and thus ease the martensitic transformations at low applied stresses. The internal residual stress is known to be

proportional to the grain size and the local mismatch stress, which is generated by anisotropic thermal expansion coefficients ($\alpha_a \neq \alpha_c$) of the tetragonal phase along a and c axis [17]. The critical grain size of polycrystalline 3YSZ below which the tetragonal phase becomes stable is reported to be $\sim 1 \mu\text{m}$ [227]. Therefore, it appears that the ultrafine 3YSZ grains in this study (with an average grain size of $\sim 175 \text{ nm}$) are fully stabilized as evidenced by the XRD pattern (Fig. 5.2). Triggering martensitic transformation requires higher external stress when the YSZ has smaller grain sizes. The deviation of the stress-strain curves from a linear behavior is often considered as the onset of martensitic transformation [39,43]. The true stress-strain curves collected at 25°C lose their linearity at a stress level of $\sim 4 \text{ GPa}$, higher than the reported value ($\sim 3 \text{ GPa}$) for 3YSZ with an average grain size of 320 nm [228]. The difference in critical stress may be attributed to higher stability of the tetragonal phase induced by the smaller grains in the current study. A large failure strain of 6-7% for pillars tested at room temperature arises from transformation toughening, in agreement with previous research regarding the microcompression tests on polycrystalline YSZ [19, 36]. When the pillar consists of a few grains, a failure strain of 8% can be achieved [14, 21]. It is known that a smaller number of grains generate less internal mismatch stresses among incommensurate neighboring grains, thereby eliminating crack formation during martensitic transformation. Furthermore, miniaturized YSZ can also exhibit higher failure strain than that for bulk counterpart ($\sim 3\%$) due to small specimen size, which leads to less population of intrinsic flaws and enhanced stress relaxation induced by a high surface-area-to-volume ratio [14].

To justify this assertion, micropillars with diameters of 1.5 and $0.7 \mu\text{m}$ were tested to study the effect of pillar size on plasticity at room temperature. Fig. 5.13 shows the stress-strain behaviors for micropillars with a diameter of 3 , 1.5 and $0.7 \mu\text{m}$, respectively. For the $3 \mu\text{m}$ diameter pillars, catastrophic failure took place mostly at a strain of $\sim 7\%$ and at a stress of $\sim 4\text{-}4.5 \text{ GPa}$. On the other hand, the $1.5 \mu\text{m}$ diameter pillars showed a fracture strain of 8-10% after the pillars reached to an ultimate compressive strength of $\sim 4.5\text{-}5.8 \text{ GPa}$. $0.7 \mu\text{m}$ pillars showed a peak stress of $\sim 6 \text{ GPa}$ and prominent plasticity, up to $\sim 15\%$ strain without significant fracture. These studies demonstrate that there is indeed a pillar size effect on plasticity when pillar diameter is comparable to grain size. As the micropillars in our study with dimensions of $3 \mu\text{m}$ in diameter and $8 \mu\text{m}$ in height have nearly 7,000 grains, the mechanical behavior derived from this study may be comparable to bulk counterpart (which also contains a large number of grains). In addition, it cannot be ruled out that dislocation glide may contribute to the large inelastic flow together with

martensitic transformation toughening, especially at high stresses, because the field-assisted sintering technique is a non-equilibrium process that may generate a significant amount of defects [83,180].

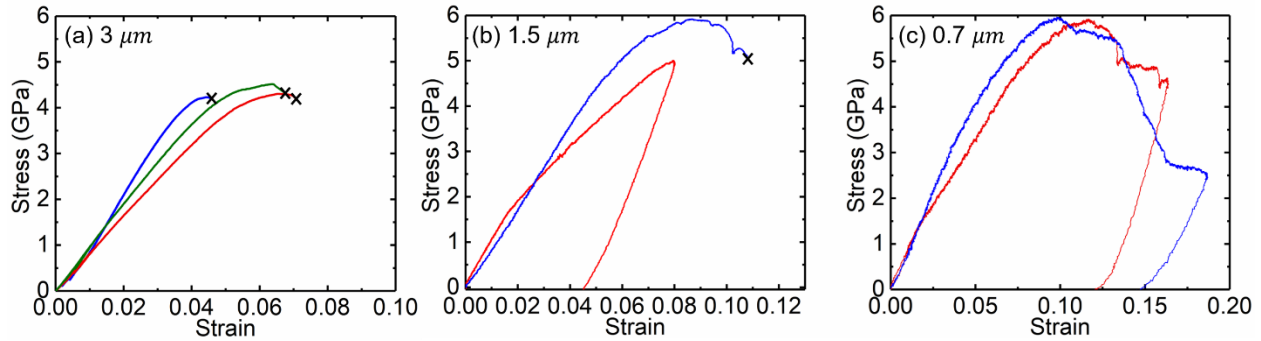


Figure 5.13. Stress-strain curves for the micropillars with a diameter of (a) 3 μm (b) 1.5 μm and (c) 0.7 μm . As the diameter of micropillars increases, fracture strain and peak stresses increase. Fracture events are indicated by X-shaped cross.

We have also performed a series of cyclic loading tests to verify the existence of hysteresis loops in the stress-strain curve caused by martensitic phase transformations. Fig. 5.14 shows stress-strain curve of 20 loading-unloading cycles at a strain rate of $5 \times 10^{-3} \text{ s}^{-1}$ at room temperature. 5th, 11th, and 19th loading and unloading curves are highlighted in red to show the hysteresis loops due to martensitic transformation. The area inside the loop increases with stress, implying that more grains with tetragonal phase experiences martensitic transformation as the applied stress increases. Meanwhile, the TEM experiments on the YSZ pillars after microcompression tests at room temperature directly confirm the formation of monoclinic phase (due to tetragonal-to-monoclinic martensitic phase transformations) as demonstrated in Fig. 5.9. The interplanar spacing of the (020) and (002) planes of the grain 1 in Fig. 5.9 (a) are measured to be 0.259 and 0.254 nm, consistent with the theoretical values of 0.261 and 0.254 nm, respectively. Grains 2 and 3 were examined along respective zone axis of $[1\bar{1}2]$ and $[\bar{1}01]$ and indexed to be monoclinic zirconia phase as well.

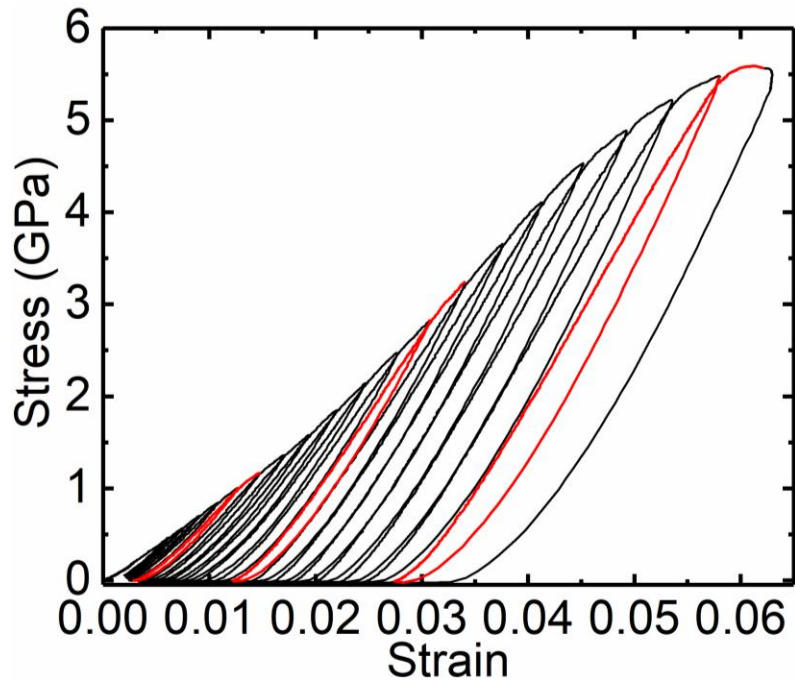


Figure 5.14. Cyclic loading tests at a strain rate of $5 \times 10^{-3} \text{ s}^{-1}$ at room temperature. 5th, 11th, and 19th loading and unloading curves are highlighted in red to show hysteresis loops.

Micropillars with a high aspect ratio of 1:5 were also compressed at room temperature to examine the effectiveness of martensitic transformation (see Fig. 5.15). The pillar was bent without fracture upon loading and the deviatoric strain was partially recovered upon unloading. The presence of the partial recovery implies that room temperature is between the austenite start and finish temperature. Therefore, some portion of monoclinic phase induced by external stress undergoes reverse transformation and contributes to the shape recovery [57].

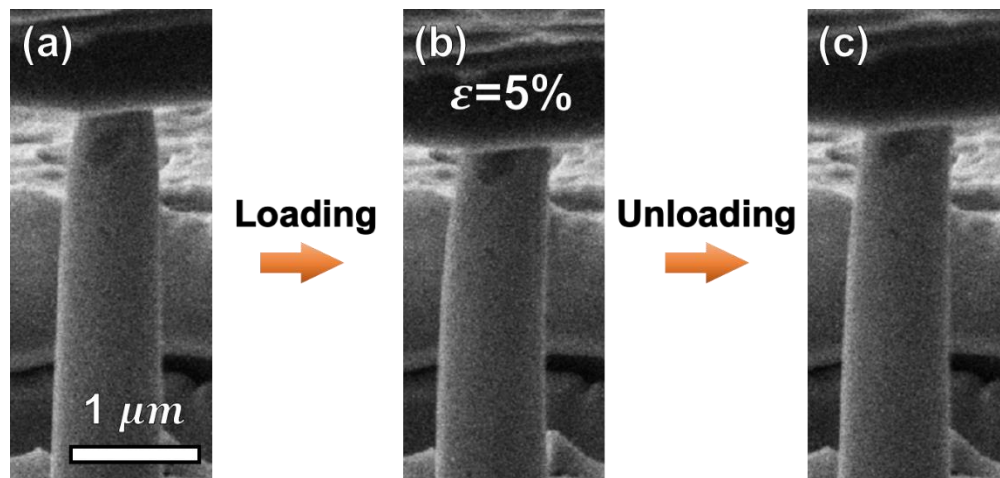


Figure 5.15. Microcompression test on a pillar with high aspect ratio at room temperature. (a) Before the compression test. (b) The pillar experienced a strain of 5% and bent without any crack owing to martensitic transformation, which prevents crack propagation upon loading. (c) After elimination of loading, the deviatoric strain was partially recovered due to reverse martensitic transformation (monoclinic to tetragonal zirconia). Partial shape recovery implies that the test temperature is between austenite start and finish temperature.

5.5.2. Evolution of deformation mechanisms at 400°C

The apparent elastic modulus of the 3YSZ specimens measured using unloading curves (at displacements of 60 and 120 nm) increases with increasing test temperature up to 200°C and decreases thereafter as shown in Fig. 5.16 (a). It was reported that elastic modulus of transformable YSZ is lower than the theoretical value (~210 GPa) due to strain burst induced by martensitic transformation [9,14]. As temperature increases, the stabilization of transformable tetragonal phase requires higher external stresses to activate martensitic transformation, leading to greater measured elastic modulus. However, it is also likely that the increase in elastic modulus is associated with pillar tapering angle or misalignment. In the process of fabricating the micropillars, we used a series of concentric annular milling and polishing with progressively de-escalated currents to minimize tapering angle of the pillar, such that the pillars we tested retains tapering angles less than 2°. To address the alignment issue between the pillars and the tip, we took full advantage of *in-situ* experiment to minimize visible alignment issues by tilting and rotating the sample stage under SEM prior to conducting the compression tests.

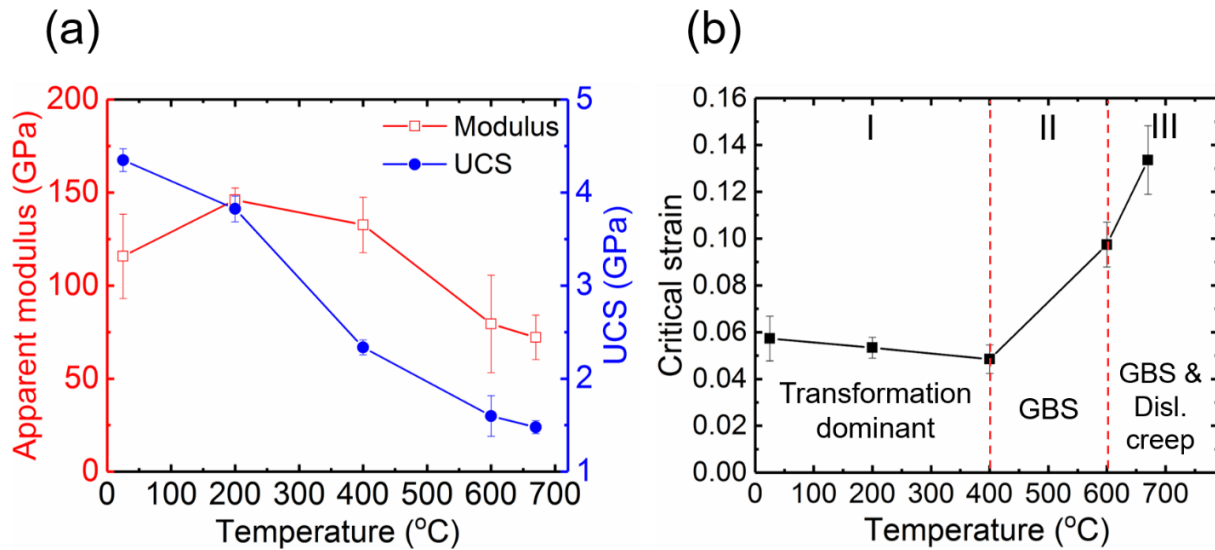


Figure 5.16. Mechanical properties of SPS 3YSZ as a function of test temperatures. (a) The apparent elastic modulus (red curve) increases with increasing temperature up to 200°C and decreases thereafter. The ultimate compressive strength (UCS) decreases monotonically with the increasing test temperature. (b) The critical strain at which the first crack occurs for the onset of crack nucleation decreases slightly with test temperature up to 400°C, due to the gradual suppression of martensitic transformation. Beyond 400°C, the critical strain increases monotonically with test temperature and the dominant deformation mechanism changes.

The pillars tested at 200°C fractured in a brittle manner, but it showed both transgranular and intergranular cracks on the fracture surface (Fig. 5.17). It is likely that transformation toughening gradually diminishes, and a new inelastic deformation mechanism is triggered as temperature increases. The intergranular crack propagation among ultrafine grains indicates that the grain boundary sliding mechanism may begin to operate from 200°C. For the pillars tested at 400°C, the decrease of elastic modulus may be due to a weaker interatomic bonding at elevated temperature [172,229,230]. The pillars tested at 400°C exhibited predominantly intergranular cracking, indicating that external stress exceeds the cohesive grain boundary strength before reaching a critical stress for martensitic transformation. It was shown that the degree of intergranular fracture increases under the aggressive test environment (elevated temperature and large applied stress) and with the presence of solute segregation along grain boundaries [231]. Energy-dispersive X-ray spectroscopy in TEM studies revealed yttrium segregation along the grain boundary (Fig. 5.18). Although the grain boundaries have no detectable amorphous phase, which promotes the grain boundary sliding at elevated temperatures [44], yttrium segregation along the grain boundaries may contribute to the transition of deformation mechanisms at 400°C. Therefore,

both environmental factor (elevated temperature) and microstructures (ultrafine grains and yttrium segregation) may result in the evolution of deformation mechanisms at 400°C.

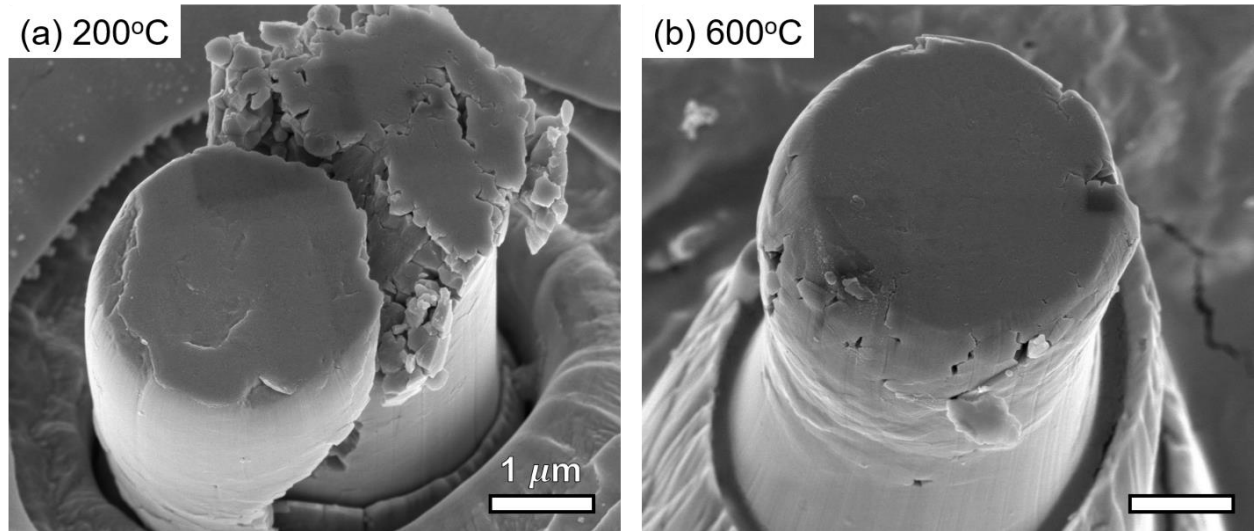


Figure 5.17. SEM images of compressed pillars at 200 and 600°C. (a) Pillars tested at 200°C fractured catastrophically. Fracture arises mainly from transgranular cracking, but intergranular cracking was also observed. (b) For pillars tested at 600°C, no significant fracture was appreciable. It appears that the strain was accommodated by change in internal structure based on the observation of elongated grains.

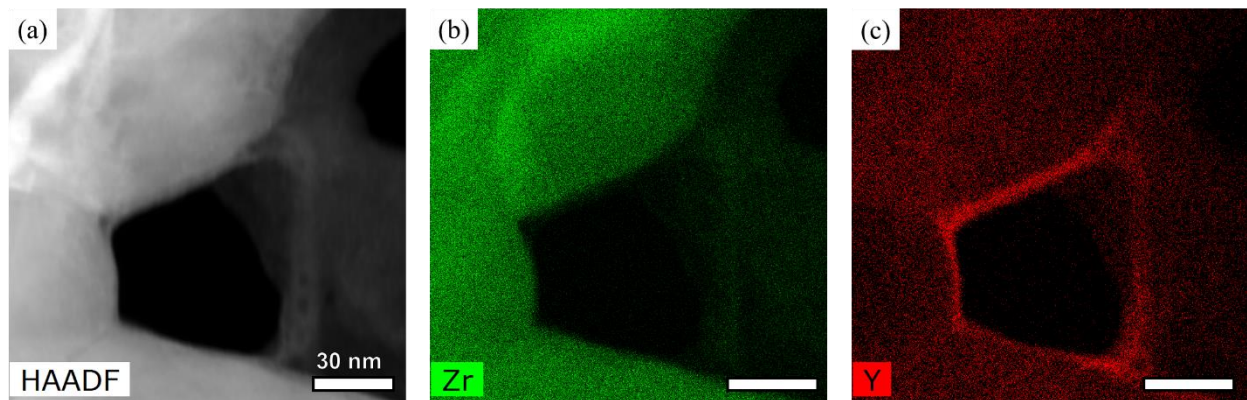


Figure 5.18. Energy dispersive X-ray spectroscopy images. (a) Scanning TEM image of 3YSZ showing clear grains and pore. (b) EDS mapping of zirconium. (c) EDS mapping of yttrium showing yttrium segregation along the grain boundaries which may promote grain boundary sliding as temperature increases.

Critical strain at which the first crack nucleates was measured and plotted as a function of temperature in Fig. 5.16 (b). The critical strain gradually decreases with the test temperature up to

400°C and increases rapidly thereafter. The decrease of critical strain may imply the gradual replacement of transformation-induced plasticity by other inelastic deformation mechanism. For the pillars tested at 200°C, a measured critical strain (~5.5%) comparable to that for room temperature tests and the presence of intergranular cracks suggest that transformation toughening is still operative, but the cohesive grain boundary strength decreases to a level similar to the critical stress for martensitic transformation. At 400°C, although the martensitic phase transformation is largely suppressed during compression tests, the measured critical strain is ~5%, still higher than that for the coarse-grained bulk counterpart (~3%), indicating the presence of inelastic deformation, such as the grain boundary sliding mechanism. SEM studies of the deformed pillars show the presence of cavitation and a majority of grains remain equiaxed, in support of the grain boundary sliding mechanism. Also, the TEM study of the compressed pillar at 400°C strengthens this assertion by showing the local grain separations (gaps) induced by grain boundary sliding (as indicated by red arrows in Fig. 5.9 (f)). The large plastic deformation was mainly accommodated by grain boundary sliding mechanism. However, at the test temperature of 400°C (equivalent to $0.23T_m$), there was insufficient diffusional flows to accommodate the local grain separations and cavitation.

It was reported, for the conventionally sintered bulk YSZ, that the temperature of 700 to 800°C is a fiducial temperature beyond which other deformation mechanisms such as dislocation glide, grain boundary sliding, and ferroelastic domain switching supersede martensitic transformation [39]. However, ultrafine grain size and preexisting defects in YSZ processed by the field-assisted sintering technique may activate other deformation mechanisms such as grain boundary sliding at relatively lower temperature than the defect free bulk counterpart [153].

5.5.3. The evolution of deformation mechanism at 670°C

The pillars tested at 670°C deformed plastically till a large strain of 30% without softening. It appears that the large strain generated during compression test at 670°C is accommodated by internal microstructure change and grain boundary sliding especially in the top portion of the pillars as can be seen in Fig. 5.5 (c). Also, the cross-section SEM micrograph (Fig. 5.10 (b)) supports that the significant plastic deformation was manifested by elongated grains. Based on the classical theory of superplasticity, diffusional flow through lattice or grain boundary accounts for superplastic flow at low stresses, and dislocation creep mechanism operates at higher stress levels

[232]. Ashby *et al.* described deformation mechanism for polycrystalline materials by introducing both grain boundary sliding and diffusional accommodation [197]. In this model, grain boundary sliding with diffusional flow accommodation at low stress levels exhibits insignificant grain elongation, but dislocation glide and climb dominant flow is often manifested by extensive elongation of grains. Taking the low homologous temperature (670°C is equivalent to $0.31T_m$) and high external stress into account, dislocation creep dominated plastic flow appears to be the dominant deformation mechanism at this temperature. The absence of cavity formation in the vicinity of top surface of the pillar suggests that the cavitation generated by grain boundary sliding was fully accommodated by dislocations, which were activated by stress concentration at the top portion of the pillar. On the other hand, higher density of cavitation in the middle portion of the deformed pillar indicates a lack of the dislocation-induced accommodation. In addition, the long plateau for the pillar tested at 670°C in the true stress-strain curve (Fig. 5.5 (d)) is often observed in superplastic deformation of YSZ above 1300°C [233]. Furthermore, high-density dislocations were observed in grains (Fig. 5.11 (b)) after compression tests. The pillars tested at 600°C experienced a similar type of dislocation creep dominated plastic flow (Fig. 5.17 (b)). It is known that ceramics materials are in general brittle due to the lack of dislocation dominated plasticity. The current study shows, however, dislocation accommodated plasticity in YSZ at relatively low-test temperatures.

Superplasticity is readily observed in numerous metallic materials tested at high temperatures above $0.67T_m$ [190,234,235], but is limited to YSZ, Al_2O_3 , Si_3N_4 and their composites in case of ceramics [44,236–238]. YSZ is a typical oxide material exhibiting superplastic deformation because yttrium segregation along grain boundaries limits grain growth and enables to achieve ultra-fine grains [239] as demonstrated in this study. However, ultra-high temperatures (above 1300°C) and low strain rates (below 10^{-4} s^{-1}) are often necessary to observe superplastic behavior of tetragonal zirconia [240–242]. It was reported that zirconia composite (zirconia, spinel, and alumina) can exhibit superplastic deformation at a high strain rate up to 1 s^{-1} , but at an ultra-high temperature (1650°C) [243]. On the other hand, Yoshida *et al.* (2018) demonstrated superplastic behavior of 3YSZ at low furnace temperature (800°C) and at high strain rate ($2 \times 10^{-3} \text{ s}^{-1}$) with the assistance of a strong electric field (190 V/cm) during deformation, but the actual temperature of the sample might be higher than the furnace temperature due to Joule heating [244]. These prior studies suggest that superplastic behavior of ceramic materials occurs in an aggressive

environment such as ultra-high temperatures or large electric fields. Our study shows, however, that 30% plastic deformation of 3YSZ is achievable at significantly low temperature (670°C) without applying a strong electric field. Additionally, we anticipate that scaling the pillar dimensions down to micron or submicron ranges may also contribute to plastic deformation, as the increasing surface area-to-volume ratio may facilitate stress relaxation by free surfaces. To better understand the superplastic behavior of 3YSZ at microscale, further systematic investigations are needed.

Interestingly, some regions containing monoclinic zirconia phase were occasionally observed after microcompression tests at 670°C as shown in Fig. 5.12. Significant deviatoric strain may be present to activate martensitic transformation at such a high temperature [245]. Although tetragonal zirconia was thermodynamically stabilized at 670°C, sporadic martensitic phase transformation was still triggered, presumably due to the application of large compressive strain (~30%). However, the contribution of martensitic transformation to the plastic flow at 670°C is insignificant as extensive SAD patterns show the dominant tetragonal phases in the deformed pillars (Fig. 5.12 (a)). Stacking faults were frequently observed in monoclinic grains as shown in Fig. 5.12 (b) and (d). Stacking faults may be generated to accommodate the significant shear strain induced by martensitic transformation (~16%) and/or prevent grains from local microcracking.

The enhanced deformability of the pillars at 670°C might partially be attributed to the impact of SPS processing. Nanostructured ceramics processed by SPS usually retain nanovoids. 3YSZ in our study also contains nanovoids. Hence the large plastic deformation at high temperatures may be partially attributed to the closure of nanovoids upon compression. Also, it is known that the field-assisted sintering technique increases vacancy concentrations due to its non-equilibrium processing nature [83]. Interaction between nanovoids and a high concentration of vacancies may be enhanced by increasing vacancy diffusivity at elevated temperatures, and thus contribute partially to the enhancement of the plastic deformation.

5.6. Conclusions

In-situ high temperature (up to 670°C) microcompression tests of the spark plasma sintered 3YSZ were performed inside a scanning electron microscope. The deformation mechanism at room temperature is dominated by martensitic transformation and the pillars sustained a strain of ~6% before fracture. At elevated temperature, ~ 400°C, martensitic transformation induced

toughening is gradually superseded by grain boundary sliding. At 600°C or greater, significant dislocation creep dominated deformation accompanied by grain elongation operates and pillars accommodate large compressive strain without fracture.

CHAPTER 6. COMPARISON OF TEMPERATURE DEPENDENT DEFORMATION MECHANISMS OF 8YSZ THERMAL BARRIER COATINGS PREPARED BY AIR-PLASMA-SPRAY AND D-GUN THERMAL SPRAY: AN IN SITU STUDY

The following chapter contains content reproduced with permission from “J. Cho, J. Li, J. Lopez, W. Jarosinski, M. Gentleman, Z. Shang, S. Xue, H. Wang, X. Zhang. “Comparison of temperature dependent deformation mechanisms of 8YSZ thermal barrier coatings prepared by air-plasma-spray and D-gun thermal spray: an in situ study.”, *Journal of the European Ceramic Society*, 39 (2019): 3120-3128.” Copyright 2019 Elsevier B. V.

6.1. Overview

8 weight percent yttria stabilized zirconia (8YSZ) has gained widespread use in thermal barrier coatings (TBCs) for the hot sections of aero and power generation turbines due to its superb thermal and mechanical properties. In this study, *in situ* microcompression tests were conducted to evaluate the mechanical performance of 8YSZ coatings with dense vertically cracked (DVC) microstructures produced by detonation gun thermal spray to those deposited by air plasma spray (APS). At room temperature, the APS coatings showed high variability in fracture strength resulting from cracks and pores in the coating. DVC coatings, conversely, exhibited fracture strengths ranging from 3.9 to 6.6 GPa and less variability in fracture strength attributed to the relatively dense and less defective microstructure. At 500°C, both coatings showed better consistency of fracture strength and enhanced deformability owing to deformable pores, ferroelastic domain switching, and dislocation activities.

6.2. Introduction

Thermal barrier coatings (TBCs) are widely used in gas turbine engines for thermal insulation of superalloy structural components. Their use results in reduced energy consumption and extended service duration of gas-turbine components by minimizing the thermal exposure and stresses on those components at increased operation temperatures [12,142,246–250]. In particular, yttria stabilized zirconia (YSZ) has become the industry standard due to its low thermal conductivity, high coefficient of thermal expansion (CTE) that matches well with the metallic substrate, and high temperature phase stability with the thermally grown aluminum oxide scale

formed at the bondcoat/TBC interface [12,31–34]. Some compositions of YSZ exhibit high strength and fracture toughness concurrently, which are usually mutually exclusive but necessary for resistance of the coatings to foreign object damage (FOD) and erosion [8,251]. The use of 8YSZ in TBC applications is based to some extent on the work of Stecura (NASA reports 1980's) that showed an increase in furnace cyclic fatigue life for this composition [252–254]. The increase in coating performance is due to 1) the presence of the metastable t' phase produced by the rapid cooling of this composition on deposition which suppresses the equilibrium tetragonal-to-monoclinic phase transformation, and 2) the ability of t' structure to ferroelastically toughen the material.[15,248,252,255] As a result of the ferroelastic toughening mechanism, 8YSZ exhibits a fracture toughness of $\sim 3 \text{ MPa}\cdot\sqrt{m}$, more than twice the toughness of non-ferroelastically toughened 20 wt.% YSZ ($\sim 1.2 \text{ MPa}\cdot\sqrt{m}$) with the cubic crystal structure [26,28,256–258]. Subsequently, the mechanical properties and impact and erosion performance of YSZ TBCs are highly dependent on their compositions and deposition techniques.

Deposition techniques including air plasma spray (APS), electron-beam physical vapor deposition (EB-PVD), high velocity oxygen fuel (HVOF) thermal spray, and detonation gun (D-gun) thermal spray have been commonly adopted to deposit 8YSZ for thermal barrier applications. In most of these applications, the goal of the process is to develop coatings with defects such as pores and splat boundaries to decrease the overall thermal conductivity of the coating and reduce microstructural features that increase the strain compliance of the rigid ceramic on higher CTE metallic substrate. In APS TBCs, considerable porosity (15 to 25%) and cracks parallel to the substrate in the form of splat boundaries are intentionally introduced into the coating to reduce thermal conductivity and enhance the strain tolerance to achieve these goals [141]. In the case of coatings produced by EB-PVD, the coatings exhibit columnar grains with abundant nanoscale porosity and vertical gaps between columns to achieve these goals [259–262]. In the case of the HVOF process, coatings are deposited by high velocity particle impacts that result in dense, and often vertically cracked structures with outstanding adhesion and excellent strain compliance [141]. Finally, in the case of D-gun thermal spray, extremely high velocities of feedstock lead to significantly improved bond strength and density [263].

It is important to understand the thermomechanical behavior of YSZ coatings as they are susceptible to FOD and erosions during high temperature operation. It has been reported that the erosion resistance of the coatings appears to be closely related to their fracture toughness

[251,256,264,265]. Therefore, many attempts have been made to tailor the chemistry of coatings for enhancing the fracture toughness of YSZ. A fracture toughness of $\sim 17 \text{ MPa}\cdot\sqrt{m}$ was achieved in nanocrystalline YSZ with grain size of $\sim 90 \text{ nm}$ and Y_2O_3 concentration of 1 mol % [20]. A small amount of the stabilizer in nanocrystalline YSZ maximizes tetragonality to the point just before spontaneous phase transformation, thereby enhancing the transformation toughening. Adding a small number of dopants in the YSZ matrix can also increase the fracture toughness. For example, the addition of Ta_2O_5 in YSZ matrix leads to distorted tetragonal lattice and thus enhances the transformability of YSZ to monoclinic phase [19,24]. On the other hand, the substitution of Ti^{4+} for Zr^{4+} in 7 wt.% YSZ (7YSZ) matrix with a dominant t' zirconia can increase the fracture toughness by two folds as the improved tetragonality provides more efficient ferroelastic toughening [26,30]. Wang *et al.* reported the hardness (8 GPa) and fracture toughness ($2 - 2.3 \text{ MPa}\cdot\sqrt{m}$) for APS TBCs with a segmented structure [266]. On the other hand, it was also shown that nanostructured EBPVD TBCs with 8 mol.% Y_2O_3 exhibits an abnormally high hardness of 21.7 GPa [267].

In this study, 8YSZ (8 wt.%) coatings were deposited at Praxair Surface Technologies (Indianapolis, IN) using commercially relevant APS and detonation gun thermal spray processes. These processes resulted in porous APS coatings and dense vertically cracked (DVC) coatings. These coatings were then subjected to *in situ* microcompression testing at room temperature and 500°C to better understand the temperature dependent mechanical properties of these coatings. Of particular interest was the influence of microstructures and test temperatures on the deformation mechanisms of coatings.

6.3. Experimental Procedures

6.3.1. TBC depositions

Atmospheric plasma sprayed 8YSZ coatings were fabricated using Praxair Surface Technologies' proprietary plasma spray device. Argon was used as the primary gas to create the plasma and hydrogen was added as a secondary gas. The introduction of diatomic gas (hydrogen) increases the enthalpy of the plasma plume which is necessary to deposit materials with high melting temperatures. The YSZ powder was fed radially into the plasma plume at 50 grams/minute and during this process, the molten particles of YSZ were accelerated from the spray device

towards the substrate by the momentum imparted to them by the plasma gases. Each individual molten particle depositing on the substrate is referred to as a splat. Coating formation is governed by the successive deposition of splats. Spray parameters were chosen to deposit a typical lamellar coating structure with microstructural defects such as splat boundaries, interconnected and globular porosity as well as microcracks. This would be categorized as a typical low density/porous APS TBC.

The DVC coatings were deposited by a detonation gun (Super D-Gun™, Praxair Surface Technologies). This process involves a series of detonations created by mixing the raw 8YSZ powder and fuels (oxygen, acetylene, and propylene) into an elongated chamber and adding a spark at an appropriate time. The detonation is followed by a nitrogen sweep gas to clean the chamber before it is reloaded and fired again (8 to 16 times per second). The powder enters the chamber prior to detonation as the material needs to acquire appropriate momentum and kinetic energy before impact to enhance the density and bond strength between the deposition layer and the substrate.

6.3.2. Microstructure characterizations

Phases of the TBCs were examined by X-ray diffraction (XRD) technique on a PANalytical Empyrean X'pert PRO MRD diffractometer with a $2 \times$ Ge (220) hybrid monochromator to select $\text{Cu K}\alpha_1$. As-deposited TBCs were polished with a 600, 800, and 1200 grit SiC sandpapers followed by 15, 6, 3, and 1 μm diamond papers on a tripod fixture. The polished surfaces of TBCs were further treated using ~ 20 nm colloidal silica for scanning electron microscopy (SEM) studies by using an FEI Quanta 650 FEG SEM microscope. As-deposited specimens for transmission electron microscopy (TEM) studies were prepared by manual polishing followed by Ar ion milling (PIPS II, Gatan). TEM experiments were carried out on an FEI Talos 200X analytical microscope operated at 200 kV. After micromechanical testing, an FEI Teneo VS SEM microscope equipped with a through the lens detector was employed to examine the microstructure of deformed pillars. With respect to post-compression analysis of the deformed pillars, gas injection system and Omniprobe micromanipulator system were utilized to make TEM specimens from the deformed pillars.

6.3.3. Micropillar fabrications

Before fabricating the micropillars on the two coatings, the coatings were well polished by fine diamond papers such that continuous and smooth surfaces were obtained. An FEI quanta 3D FEG dual beam SEM/FIB microscope was utilized to fabricate micropillars 1.5 μm in diameter and 3.3 μm in height within the coatings with the apparent loading direction for compression parallel to the surface of the coatings. The aspect ratio of the pillars was ~ 2.2 . The pillars were fabricated in the following steps. Diamond-polished TBC samples were coated with platinum at 40 mA for 60 s in a sputter coater (Cressington 208HR) to minimize the electron charging effect during SEM operation by enhancing the electric conductivity after being mounted on a specimen holder with a carbon tape. Then, the sample holder was tilted by 52° to align with the Ga^+ ion beam and the eucentric height was adjusted accordingly. The pillars were made using series of decelerated currents (65 to 0.1 nA) at a 30 kV ion beam voltage to smoothen pillar surface and minimize tapering angle (less than 2°).

6.3.4. *In situ* microcompression tests

In situ microcompression tests on the micropillars of APS and DVC coatings were carried out using a nanoindentation system (Hysitron PI 88 \times R) equipped with a 20 μm in diameter diamond flat punch tip. The diamond flat punch with the diameter of 20 μm can cover and compress the entire surface of the pillar top so that stress field is uniformly distributed throughout the pillar. The TBCs were mounted on a ceramic heating stage and tightly fixed with a V-shaped Mo clamp. After installing the nanoindentation system with the specimens inside the FEI quanta 3D FEG SEM, 15° tilt was made to better display the pillars during the compression tests. The positions of the pillar and the tip were carefully aligned using a stage controller prior to conducting the tests. In the case of high temperature experiments, the tip and the sample were simultaneously heated to the set temperature (500°C) with a ramp rate of $20^\circ\text{C}/\text{min}$. The system was held at 500°C for 30 min to acquire thermal equilibrium thereby minimizing thermal and mechanical drifts before conducting the compression tests. The drift rate was measured to be less than 1.0 nm/s and displacement offset was compensated accordingly.

6.4. Results

XRD spectra in Figure 6.1 show that both the APS and DVC TBCs exhibited the metastable tetragonal prime (t') phase. A zoom-in view in Figure 6.1(b) shows two peaks from (004) and (400) t' phase over the two-theta range of 72° to 76° . These peaks clearly differentiate the t' phase from the equilibrium tetragonal (t) and cubic (C) phases. Prior to conducting *in situ* micromechanical testing, the microstructures of APS and DVC TBCs were investigated by TEM. Bright-field TEM micrographs of APS and DVC coatings in Figure 6.2 reveal ultra-fine grains and preexisting intergranular cracks in both films. Grain intercept method [164] analysis showed that the average grain size of APS coating was 323 ± 111 nm, with a large variation of grain size. The average grain size for the DVC coating was 169 ± 45 nm.

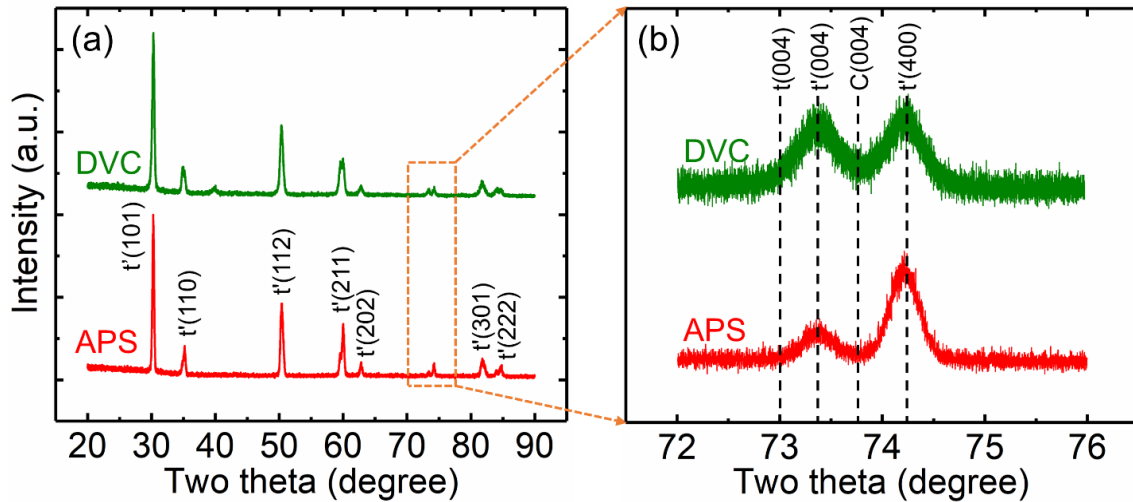


Figure 6.1. XRD patterns of APS and DVC 7 YSZ coatings. (a) The dominant phase is tetragonal prime (t') zirconia for both TBCs, which is not transformable to monoclinic phase upon compression owing to higher yttria concentration (8 wt%) and high rate deposition. (b) A magnified view of XRD patterns in the range of 72 to 76° clearly distinguish the t' phase from tetragonal (t) and cubic (C) zirconia.

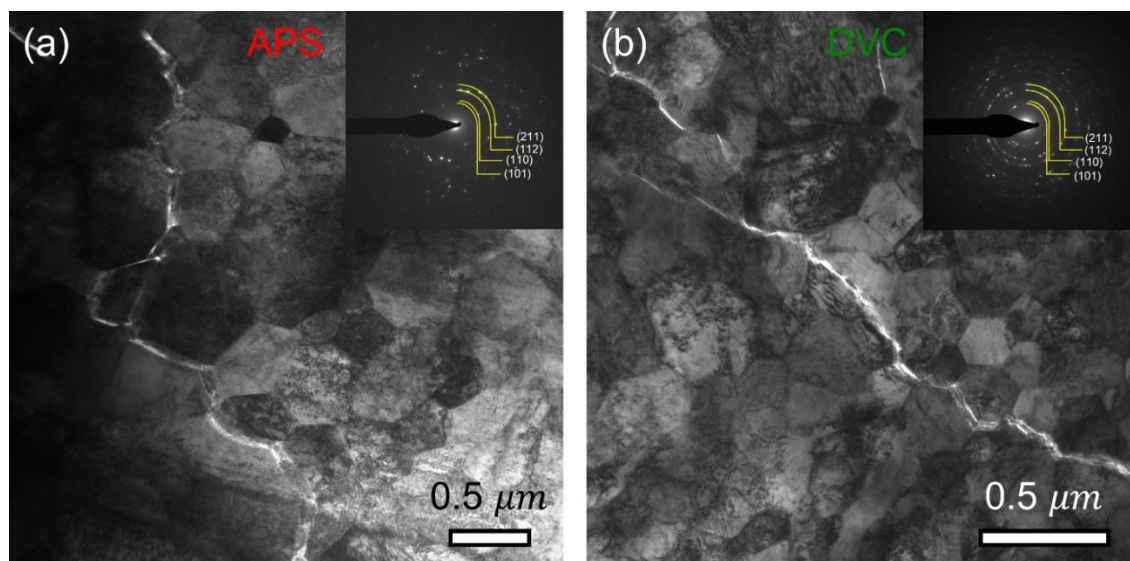


Figure 6.2. TEM images of APS and DVC YSZs showing grain sizes and preexisting cracks with inserted selected area diffractions. (a) Bright-field TEM image of APS TBC with preexisting cracks. Grain intercept method reveals an average grain size of 323 ± 111 nm. (b) TEM micrograph of DVC YSZ with clearly resolved intergranular cracks. The average grain size is 169 ± 45 nm.

Figure 6.3 shows SEM images of typical morphologies of the two coatings from top-down and cross-section views. APS TBC exhibits a mixture of dense matrix and pores. For DVC TBC, some vertical cracks and pores were occasionally observed. The micropillars fabricated by FIB of both coatings were first compressed at room temperature. Figure 6.4 shows the pillar morphology evolution during the *in situ* compression tests at different strain levels. The APS 8YSZ micropillar in Figure 6.4(a) experienced no crack nucleation after a strain of 6% was applied; but following the formation of a small crack at 7.5% strain, the pillar underwent catastrophic failure as identified by the sudden stress drop in Figure 6.4(c). In contrast, the micropillar of DVC YSZ in Figure 6.4(b) showed crack nucleation at a strain of 6%. These cracks, however, were slow to propagate into the pillar and did not initiate immediate catastrophic failure as evidenced in the corresponding stress-strain curve in Figure 6.4(c).

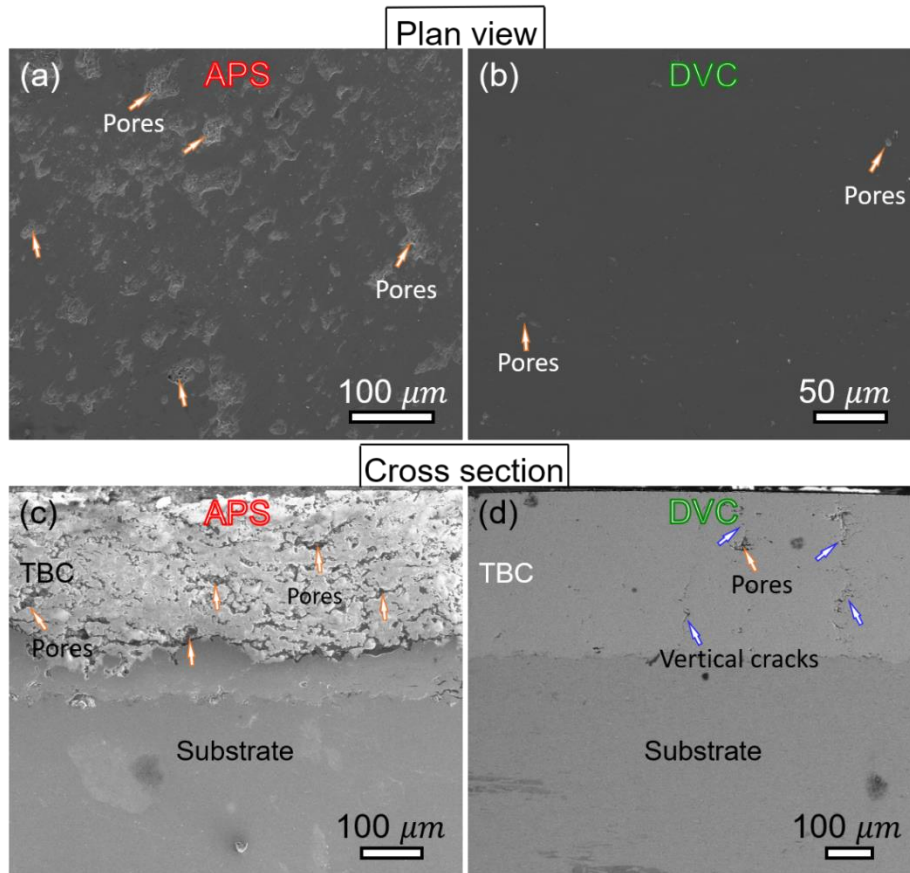


Figure 6.3. (a-b) Plan-view SEM images of APS and DVC TBCs after polishing. (c-d) Cross-section SEM images of APS and DVC TBCs after polishing.

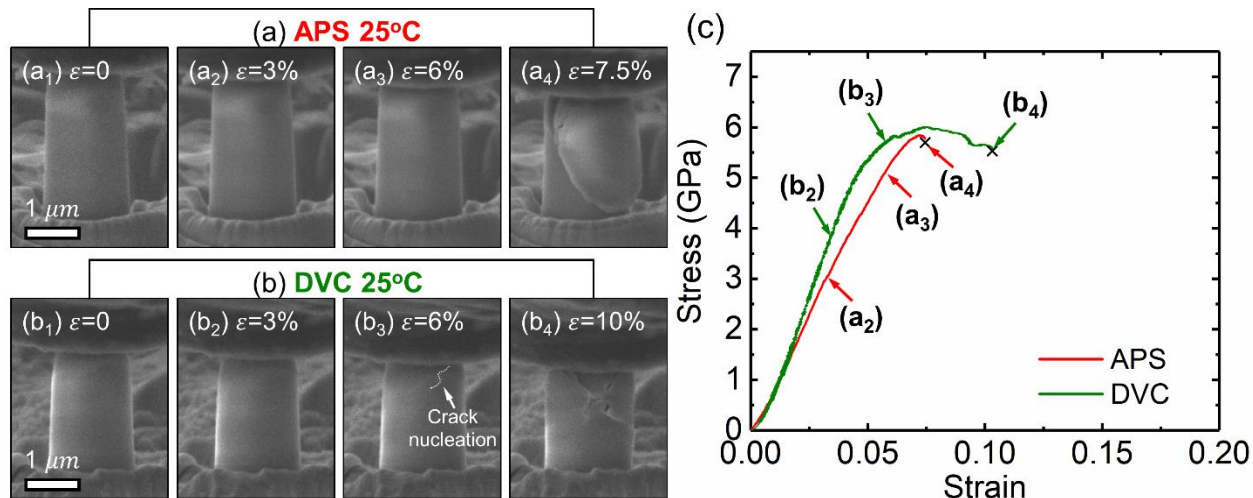


Figure 6.4. SEM snapshots of micropillars ($\sim 1.5 \mu\text{m}$ in diameter and $\sim 3.3 \mu\text{m}$ in height) during *in-situ* compression tests at room temperature at a constant strain rate of $5 \times 10^{-3} \text{ s}^{-1}$ showing typical morphology evolutions at different strain levels. (a₁-a₄) For the micropillars of APS TBC, no cracks were observed at a strain of 6%, but the pillar fractured into two major pieces right after the crack nucleation at a strain of 7.5%. (b₁-b₄) The DVC YSZ micropillars exhibit crack nucleation at a strain of 6%. However, cracks slowly propagated downward into the pillar rather than showing a catastrophic failure. (c) The stress-strain curve for APS YSZ exhibits a sudden load drop after reaching an ultimate compressive strength of 5.8 GPa. On the other hand, the stress-strain curve for DVC YSZ shows an ultimate compressive strength of 6 GPa at a strain of 7.5% followed by gradual softening to a strain of 10%. See Supplementary Videos 1 and 2 for greater details.

In situ compression experiments were also conducted at 500°C. The micropillar of APS TBC sustained a large plastic deformation ($\sim 23\%$) and exhibited significant dilation of the pillar top with insignificant formation of cracks as shown in SEM micrographs in Figure 6.5(a). This observation coincides with the stress-strain curve in Figure 6.5(c), where no prominent stress drop is observed. For the micropillar of DVC TBC, on the other hand, prominent cracks were initiated at the pillar top at a strain of 7%, accompanied by a stress drop in the stress-strain curve as shown in Figure 6.5(c). The shear offset was slowly developed along the crack pathway, but no catastrophic failure was observed until a strain of 23%. The DVC pillars reached somewhat higher flow stress than the APS 8YSZ pillars. Figure 6.6 shows SEM images of the deformed pillars at 500°C. Pillars fabricated by APS exhibited fewer cracking events at elevated temperature than those tested at room temperature. Also, after a large strain, 23%, the APS pillar showed substantial dilation of the upper half portion with the presence of high-density deformation bands. In contrast, the DVC pillar tested at 500°C showed prominent cracks propagating vertically into the pillars.

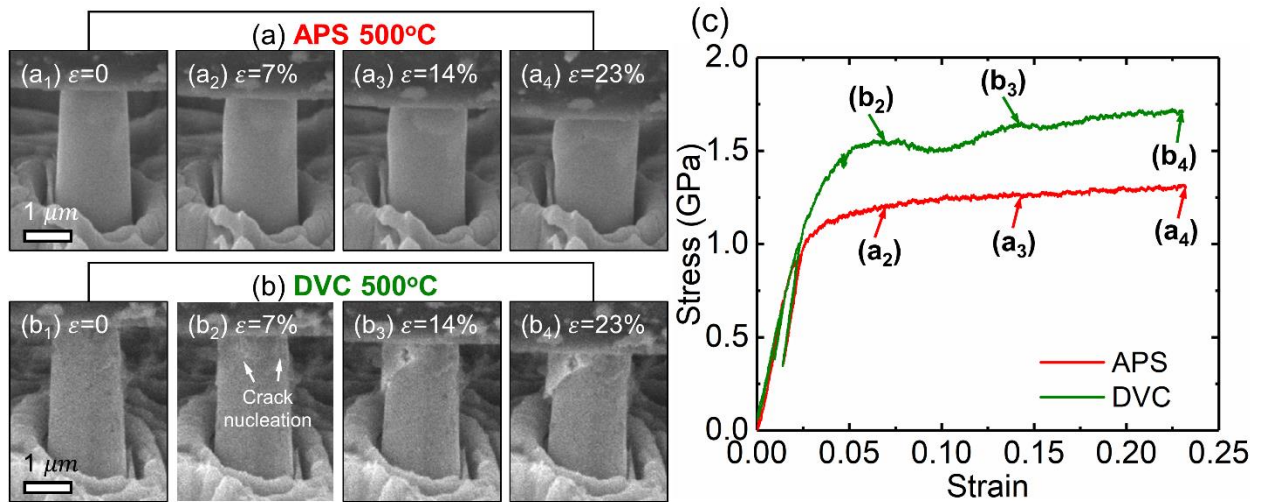


Figure 6.5. Typical morphology evolutions of APS and DVC YSZ micropillars during *in-situ* compression tests at 500°C. (a₁-a₄) For the APS micropillar, a few prominent cracks were generated at a strain of 14%. The large plastic strain was accommodated mainly by the dilation of the top section of the pillar. (b₁-b₄) For the DVC micropillar, cracks were nucleated at an early stage (7% strain), but gradually and slowly propagated into the pillar such that no catastrophic failure was observed. (d) The corresponding stress-strain curves show the flow stresses for APS and DVC TBCs are ~ 1.2 and ~ 1.6 GPa, respectively. The stress-strain curve for DVC TBC exhibits local load drops induced by cracks during the compression test. See Supplementary Videos 3 and 4 for greater details.

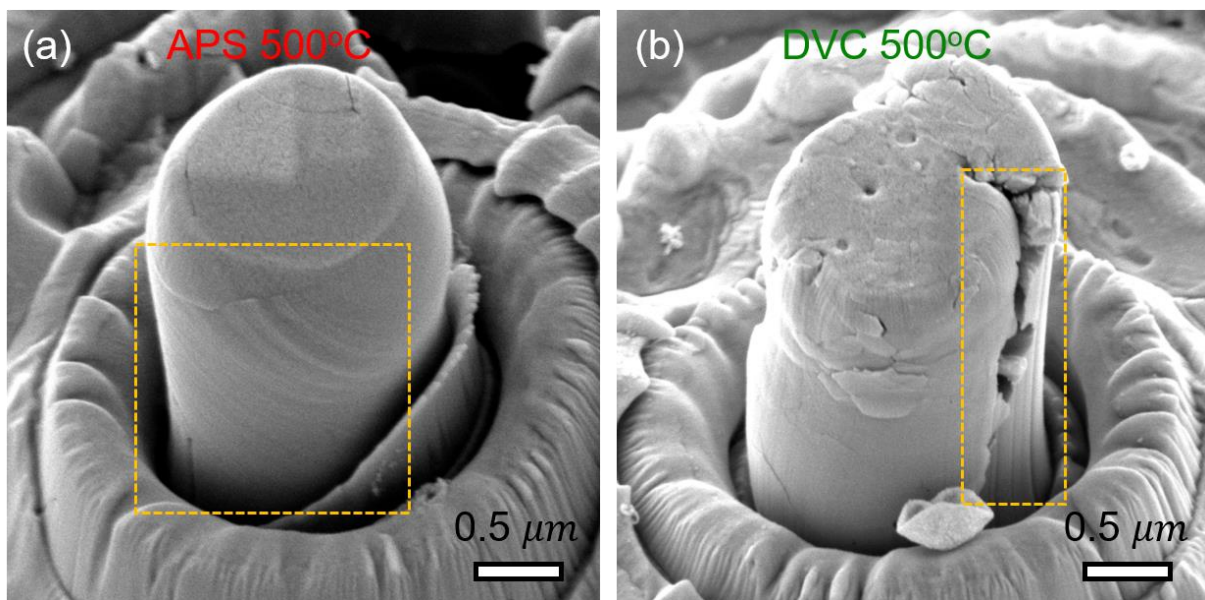


Figure 6.6. SEM images of the pillars compressed at 500°C showing typical deformation-induced morphology changes. (a) APS pillar compressed to a strain of 23% contains a few small cracks in the prominently dilated pillar top. The orange box revealed a high-density of deformation bands. (b) For the DVC pillar compressed to a strain of 23%, large cracks highlighted in the orange box propagated vertically into the pillar, which did not show significant pillar top dilation.

To examine the deformations in a greater detail, the pillars tested at room temperature and 500°C were analyzed by TEM. The APS pillar fractured at room temperature contains a relatively small number of defects within grains as shown in Figure 6.7. A few dislocations were observed under weak beam dark field condition. On the other hand, for the DVC pillar fractured at room temperature, a high density of stacking faults was frequently observed in deformed specimens (Figure 6.8). Selected area diffraction (SAD) studies for both pillars along $\langle 111 \rangle$ zone axis reveal that the intensity of two $\{112\}$ diffraction spots are much brighter than that of the third $\{112\}$ diffraction dot. The dark-field TEM micrographs using three $\{112\}$ diffraction spots show that the relative incidence of two sets of tetragonal variants were larger than that of the third tetragonal variant, indicating the occurrence of ferroelastic domain switching.

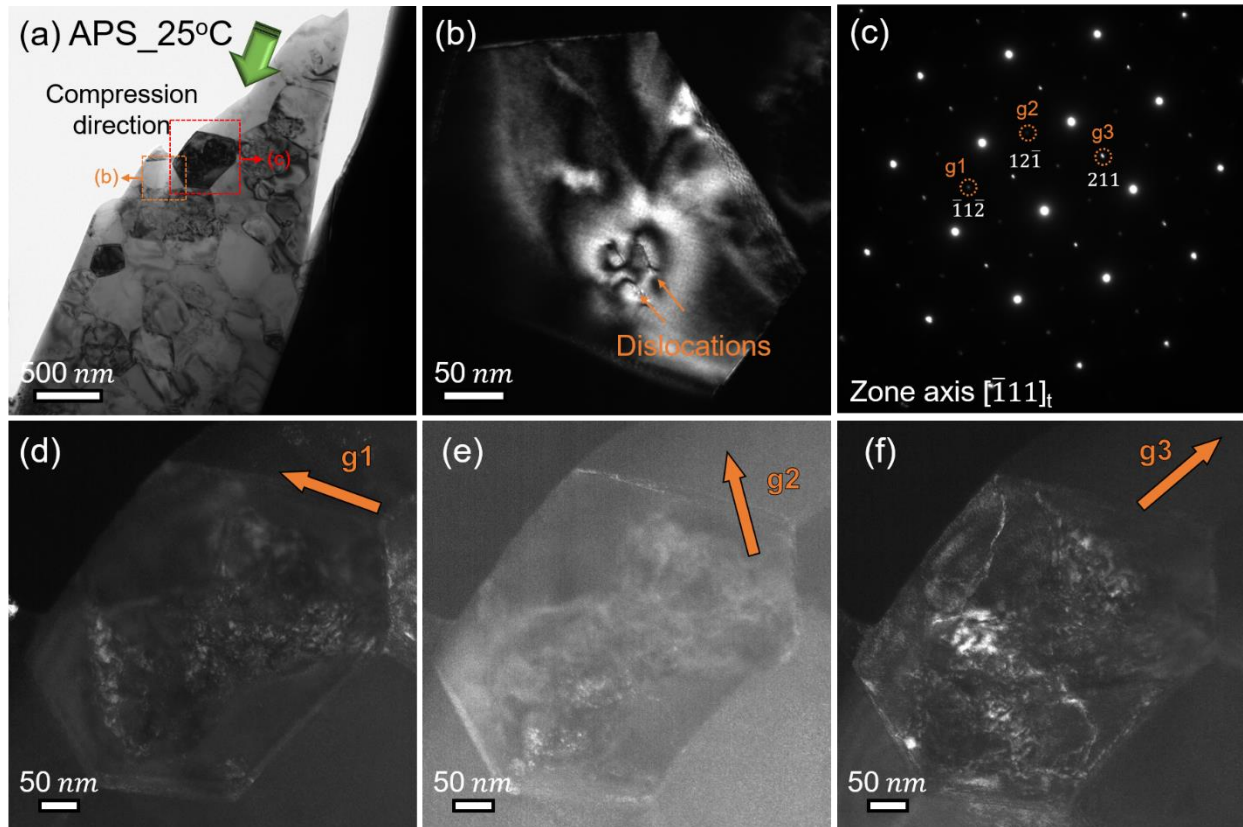


Figure 6.7. TEM analyses of the APS TBC pillar compressed at room temperature. (a) Bright-field XTEM image of the fractured pillar. (b) A grain of the fractured pillar showing dislocations and dislocation strain field obtained by two beam condition diffraction. (c) SAD pattern of a grain in examined along $[\bar{1}11]_t$ zone axis. Three $\{112\}$ tetragonal variants were chosen to investigate the relative incidence of each tetragonal variant. (d-f) Dark-field TEM images of the pillar top showing three tetragonal variants $(\bar{1}1\bar{2})$, $(12\bar{1})$, and (211) .

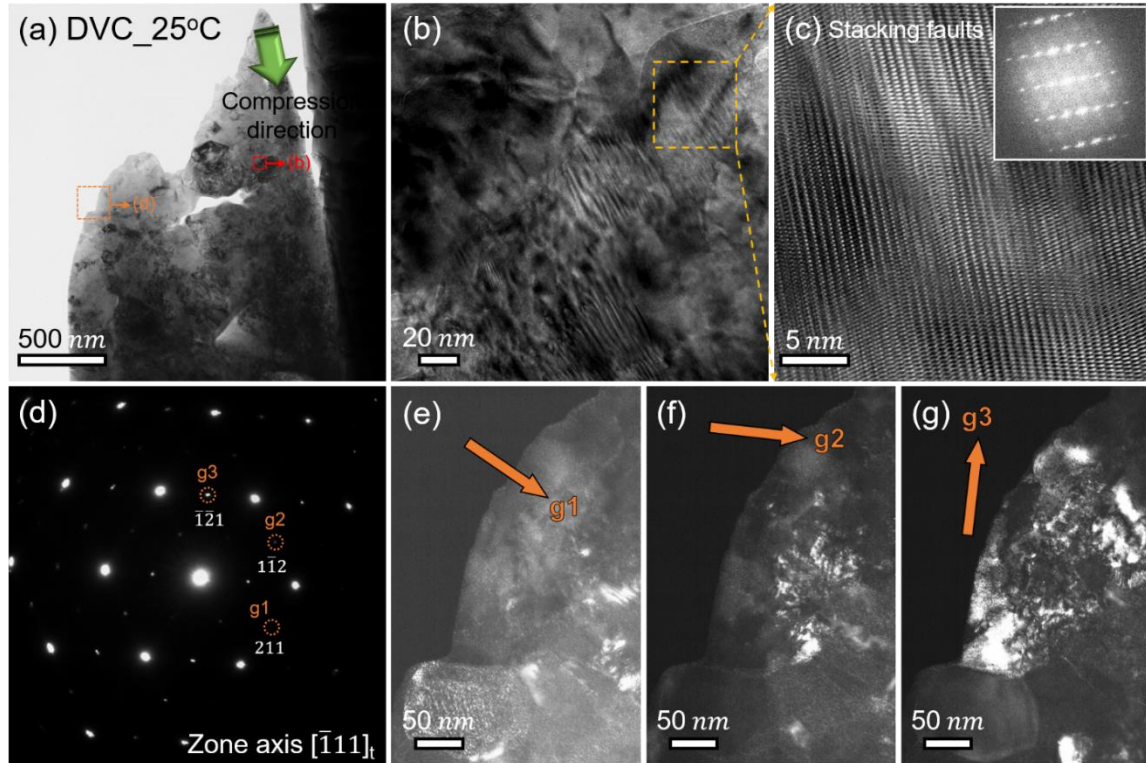


Figure 6.8. TEM analyses of the DVC TBC pillar compressed at room temperature. (a) Bright-field XTEM image of the fractured DVC pillar. (b) A region of the fractured pillar containing a high density of stacking faults. (c) High resolution TEM images and the inserted FFT confirming the occurrence of stacking faults. (d) SAD pattern of the grain in Figure 6.8(b) observed along $[\bar{1}11]_t$ zone axis. (e-g) Dark-field TEM images of the pillar top showing relative incidence of three tetragonal variants.

Figure 6.9 and 6.10 show the cross-sectional TEM images of the deformed APS and DVC TBC pillars at 500°C, containing a high density of stress-induced defects in the upper half of the deformed pillars. The APS pillar had a high density of dislocation tangles in the severely deformed area (Figure 6.9b). In the case of the DVC pillar, stacking faults was observed near the fractured regions of the deformed (Figure 6.10). SAD studies were carried out for both deformed pillars in the vicinity of the pillar top along $\langle 111 \rangle$ zone axis. Figures 6.9(d-f) and Figure 6.10(e-g) show dark-field TEM images using three $\{112\}$ diffraction dots. The TEM micrographs showed that in both deformed APS and DVC YSZ pillars two sets of tetragonal variants associated with ferroelastic domains were abundant while the third tetragonal variant diminished after deformation. On the other hand, the SAD studies on the APS and DVC pillars compressed at 25 and 500°C reveal that there is no stress-induced phase transformation (PDF#48-0224) as shown in Figure 6.11.

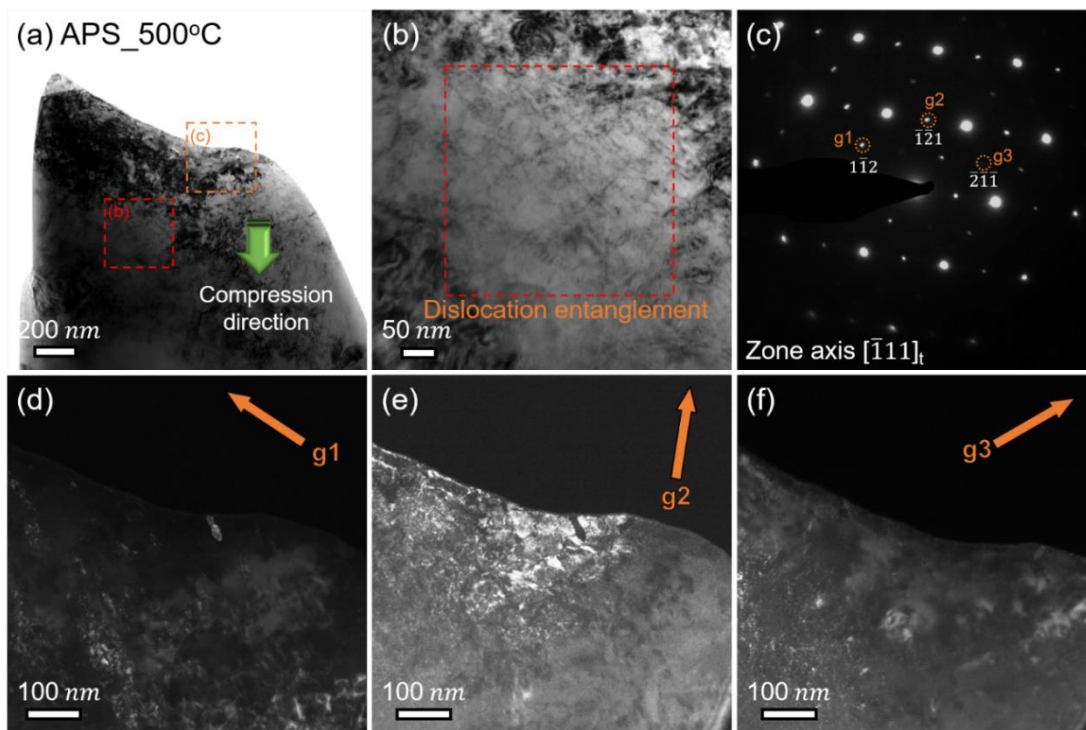


Figure 6.9. TEM analyses of the APS TBC pillar compressed at 500°C. (a) Bright-field XTEM image of the upper half of the deformed pillar. (b) A region of the deformed pillar showing a high density of dislocations. (c) SAD pattern examined along $[\bar{1}11]_t$ zone axis. Three $\{112\}$ tetragonal twin variants were chosen to investigate the appearance of each tetragonal variant. (d-e) Dark-field TEM images of the pillar top showing two tetragonal variants ($1\bar{1}2$) and ($\bar{1}\bar{2}1$). (f) The third tetragonal variant ($\bar{2}\bar{1}\bar{1}$) is largely absent.

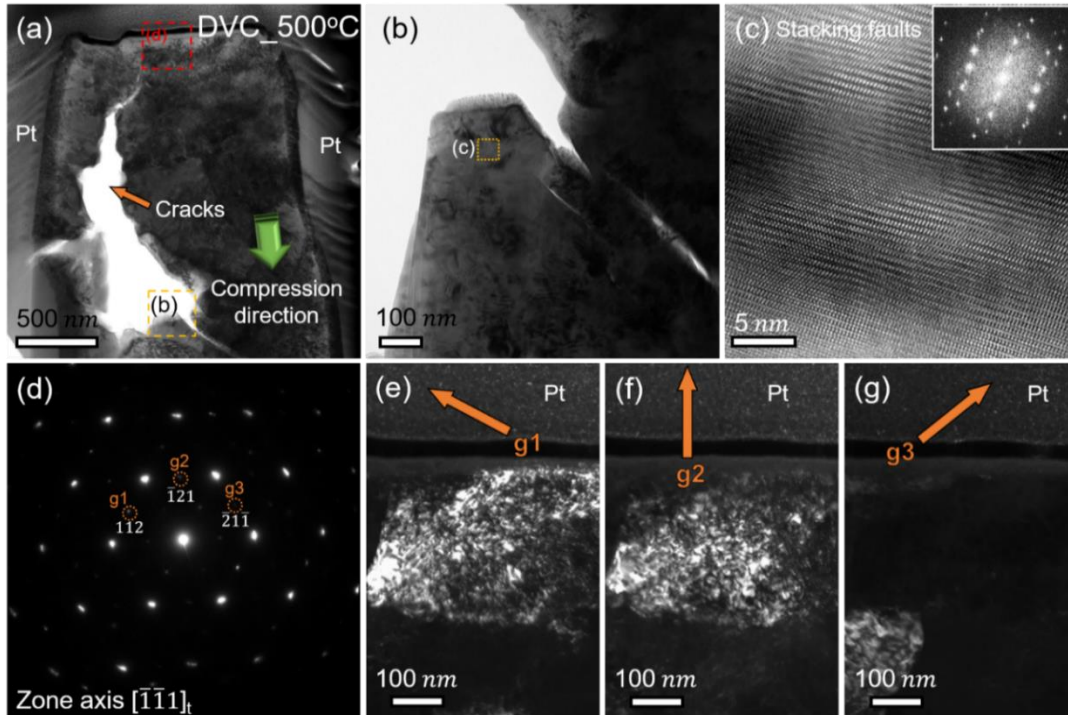


Figure 6.10. TEM analyses of the DVC TBC pillar deformed at 500°C. (a) Bright-field XTEM image showing overall structure of the deformed pillar containing cracks. (b) Fractured region of the deformed pillar containing a high-density of stacking faults. (c) High resolution TEM of stacking faults with inserted FFT. (d) SAD pattern showing $\{112\}$ planes examined along the $[\bar{1}\bar{1}\bar{1}]$ zone axis. Three $\{112\}$ tetragonal variants were selected to conduct dark-field TEM experiments. (e-g) Dark-field TEM images of the pillar top showing the absence of one tetragonal variant in the deformed pillar top attributed to ferroelastic domain switching to the other two tetragonal variants (e and f).

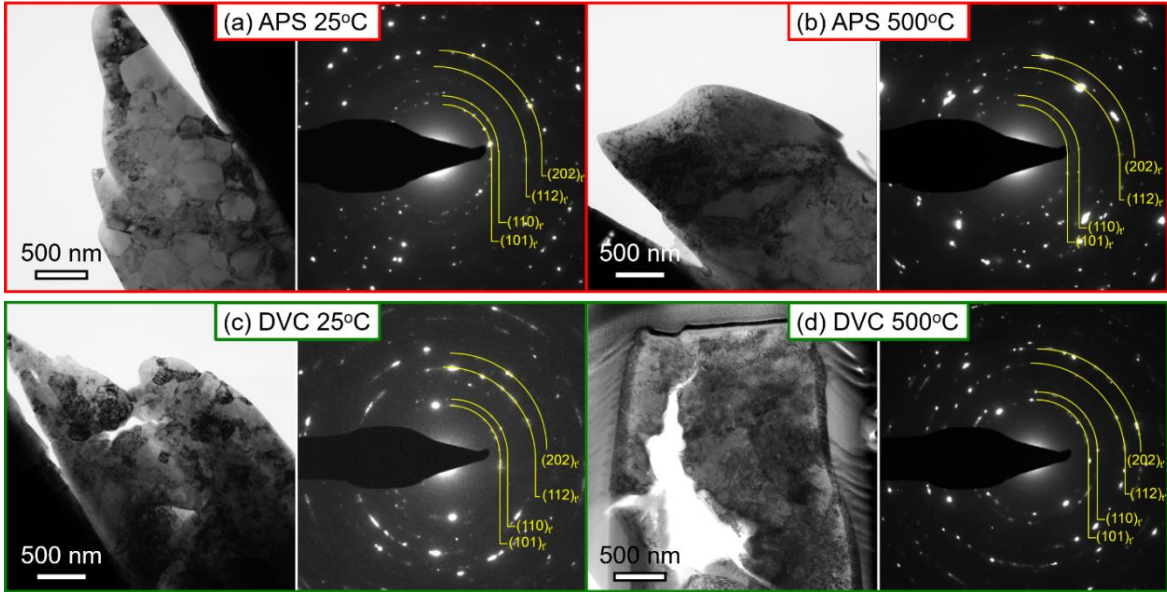


Figure 6.11. SAD patterns on the APS and DVC pillars tested at 25 and 500°C. No cubic and monoclinic phases were observed.

Figure 12 shows numerous stress-strain curves of APS and DVC YSZ pillars tested at room temperature and 500°C at a constant strain rate of 5×10^{-3} /s. The APS YSZ micropillars exhibited a large variation of fracture strengths (0.6 ~ 6.6 GPa) when compressed at room temperature. Most of the pillars show little plasticity after yielding, indicating catastrophic brittle fracture. On the other hand, the DVC YSZ pillars show less dispersed fracture strengths ranging from 3.9 to 6.6 GPa when tested at room temperature. Most DVC YSZ pillars reached a few percent of strain beyond ultimate compressive strength before the onset of a significant cracking event. When tested at 500°C, however, both systems exhibited significantly reduced variation in fracture strength when compared to the measurements at room temperature. At 500°C, the fracture strengths of the APS coatings varied from 1.0 to 1.3 GPa, while the DVC YSZ pillars ranged over 1.3 ~ 1.8 GPa.

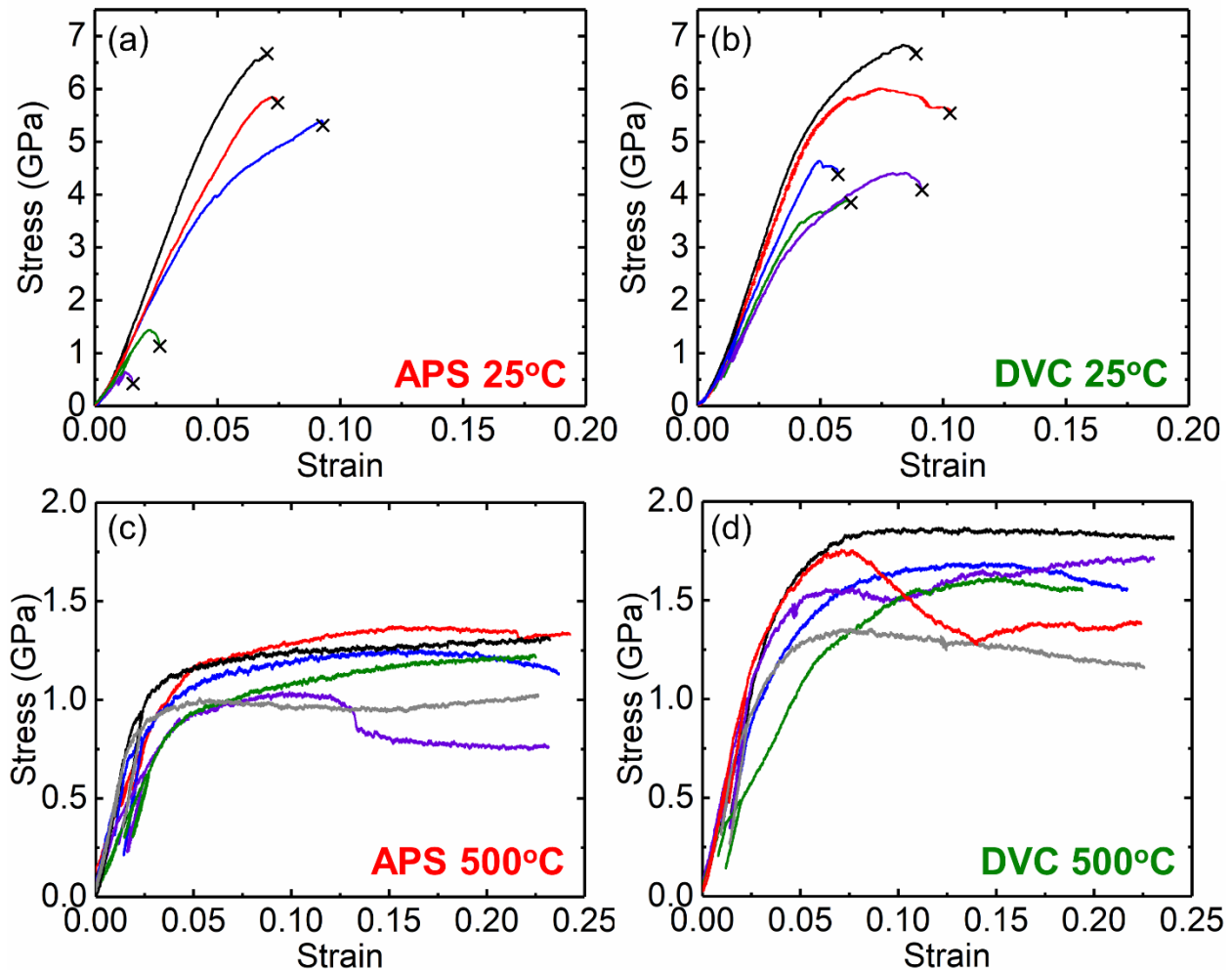


Figure 6.12. Numerous stress-strain curves for the numerous APS and DVC micropillars tested at room temperature and 500°C at a strain rate of $5 \times 10^{-3} \text{ s}^{-1}$. The X-shaped mark represents the fracture strain. (a) The APS micropillars compressed at room temperature show scattered fracture strengths (0.6 ~ 6.6 GPa) resulting from preexisting cracks and pores. (b) For the DVC pillars tested at room temperature, fracture strengths are less dispersed, ranging from 3.9 to 6.6 GPa. (c) For the APS TBC pillars tested at 500°C, the variation of fracture strengths decreases significantly, and the average fracture strength is ~ 1.2 GPa. (d) The DVC TBC pillars tested at 500°C also shows less variable fracture strengths (1.3 ~ 1.8 GPa) compared to that at room temperature with an average fracture strength of 1.6 GPa.

6.5. Discussion

6.5.1. Pillar fabrication and microstructure difference in APS and DVC coatings

As most TBC coatings have pores, it is challenging to test the mechanical behavior of these coatings via micropillar compression tests. As the micropillar dimensions are merely several microns, it is important to avoid the regions with large catastrophic pores or cracks while preparing

the pillars. Testing the mechanical behavior of TBC coatings with the large pores and cracks will introduce significant errors and uncertainty. Hence, we used the regions with acceptable porosity to fabricate pillars so that the intrinsic mechanical properties of the materials prepared by the two different techniques can be probed. However, fabrication of pillars on locally dense surface area does not necessarily mean that the entire pillar structure is free from pores and cracks, simply because there are some pores and cracks right underneath the continuous surfaces as shown in Figure 6.13. Hence, the mechanical behavior has a natural Weibull type of distribution despite the usage of micromechanical testing technique. There are natural differences in pore and crack sizes between the two types of coatings. In general cracks and pores in APS pillars are larger than those in the DVC pillars. The pillars retain the preexisting cracks and pores in such a way that their intrinsic microstructures are reflected in the pillars tested in this study. This microstructure difference results in obvious difference in mechanical behaviors between the two types of coatings.

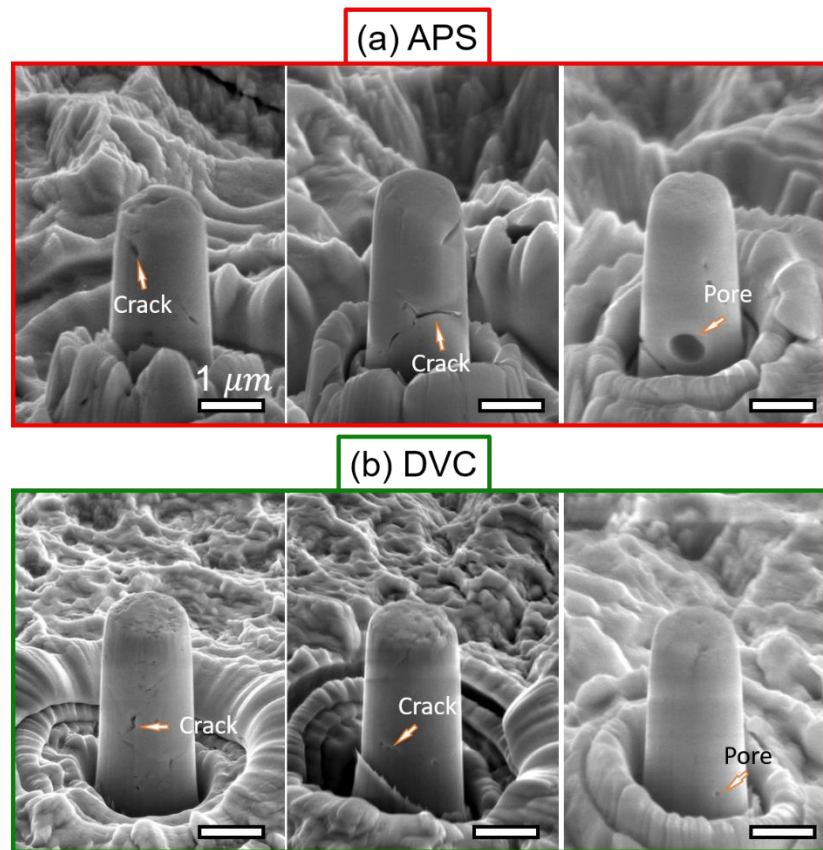


Figure 6.13. SEM images of (a) APS and (b) DVC pillars showing preexisting pores and cracks. In general, pore and crack sizes of APS TBC pillars are larger than those of DVC TBC pillars.

XRD studies clearly show that both the APS and DVC TBCs retain the metastable tetragonal prime (t') phase. High rate depositions and lower tetragonality resulting from high dopant concentrations than equilibrium t phase yield this metastable phase that inhibits phase transformation to monoclinic zirconia when externally compressed. Meanwhile, the large grain size difference between the two types of coatings may arise from different deposition methods. The velocity of feedstock at the exit of the chamber for D-gun thermal spray reaches supersonic values (~ 900 m/s). Moreover, the temperature of combustion flame for D-gun spray is relatively low ($\sim 3,900^\circ\text{C}$), resulting in partial melting of feedstock in the stream, and provides shorter time for grain growth after deposition, leading to small average grain size of ~ 169 nm for DVC coatings [141,263]. Whereas, APS technique completely melts the powder using ultrahigh temperature of combustion flame ($\sim 25,000^\circ\text{C}$) and introduces much lower particle velocity (~ 300 m/s), and consequently leads to larger average grain size, ~ 323 nm. The grain size difference may account for the higher flow stress of the DVC coating than the APS coating based on the Hall-Petch relation that shows smaller grain sizes lead to higher mechanical strength of materials [268,269].

6.5.2. Room temperature deformability of APS and DVC pillars

During room temperature testing, the stress-strain curves for both APS and DVC pillars deviated from linearity, indicating the onset of plastic yielding, before reaching maximum stress. In general, the yielding of polycrystalline ceramic materials is often attributed to phase transformation, dislocation activity, or microcracking [196]. In the current study, the dominant phase of both types of TBCs was t' zirconia as evidenced by the XRD studies. Again, it is known that this metastable phase suppresses transformation to the monoclinic phase upon compression as evidenced by Figure 6.12. Additionally, a majority of ceramic materials exhibit little to no dislocation activity at low temperatures as a result of the hampering of dislocation nucleation and motion by strong ionic and covalent bonds. For the YSZ system, dislocation-accommodated deformations have been observed at temperatures higher than 800°C [39,185,186,197]. Therefore, the formation of stress-induced microcracks in the vicinity of preexisting cracks and pores may be a main contributor to the non-elastic deformation observed in both coatings studied here. The high density of pre-existing pores and cracks in the APS coatings lead to microcrack formation at lower stresses than those observed in DVC coatings and hence result in less nonlinear strain as shown in the stress-strain curves.

Given that both APS and DVC TBCs have a significant number of processing-induced cracks and pores, their compressive fracture strains are surprisingly high and such a phenomenon can be interpreted from the following perspectives. First, we examine the influence of specimen sizes on measured non-elastic strain. It was reported that the miniaturization of YSZ specimens results in large fracture strains, reaching $\sim 8\%$, which is considerably greater than those observed in the bulk ($\sim 3\%$) [14,39,43,45,179,180,270]. Comparing to bulk specimens, the microscale specimens often have less probability of containing fatal (large) intrinsic flaws, and an increased surface area to volume ratio facilitates stress relaxation, thereby increasing fracture strain significantly [14,49,50]. Second, because the tetragonal-to-monoclinic phase transformation was suppressed by the presence of the metastable t' phase here, the large fracture strain observed in Figure 6.5 requires the operation of other toughening mechanism, which is most likely ferroelastic domain switching.

In general, the observation of mechanically induced twinning is a direct evidence of ferroelastic domain switching in zirconia [271,272]. The forbidden $\{112\}$ diffractions along the $\langle 111 \rangle$ zone axis emerge due to the existence of three twin variants in the tetragonal zirconia system [28,56,271]. Accordingly, three $\{112\}$ tetragonal twin variants were chosen for both coatings to investigate occurrence of each tetragonal variant after deformation. As evidenced by SAD studies and dark-field TEM images in Figure 6.7 and 6.8, two tetragonal variants are abundant, whereas the third one is largely absent, as a consequence of ferroelastic switching upon loading.

Third, the large inelastic strain in deformed coatings may also arise from defects, such as dislocations and stacking faults. The fractured APS pillars show some evidences of dislocation activities which somewhat contribute to non-elastic deformation. On the other hand, the fractured DVC pillars clearly show a high density of stacking faults. The formation of stacking faults can accommodate the plastic deformation and hamper grains from local microcracking, thereby contributing to the high fracture strains.

6.5.3. Comparison of mechanical behavior of APS vs. DVC 8YSZ at elevated temperatures

Conducting micromechanical testing at the actual operation temperature of the turbine engine blade ($\sim 1300^\circ\text{C}$) is extremely challenging. The state-of-the art high temperature *in situ* microcompression tool cannot reach such a high temperature. Alternatively, the test temperature

of 500°C was carefully chosen as an intermediate temperature given that homologous temperature of the test condition ($0.26T_m$) is a half of that of the actual operating condition ($0.52T_m$). It is recognized that the mechanical responses of the two coatings at 500°C cannot represent the actual operation conditions, but these test results provide insight for understanding the deformation mechanisms of the two types of TBCs at elevated temperatures.

The APS and DVC coatings deformed at 500°C show two sets of abundant tetragonal variants and a third diminishing variant (Figure 6.9 and 6.10). Among the three variants, the diminishing tetragonal variant has its c-axis most closely aligned with the direction of compressive load, which indicates that the other two abundant tetragonal variants grow at the expense of the third variant as a result of stress-induced ferroelastic switching. It has been reported that ferroelastic domain switching remains active in YSZ up to 1000°C [39,56,179]. Therefore, the large plastic deformations observed for both coatings at room temperature and 500°C may have a significant contribution from the ferroelastic domain switching process.

In addition to the evidence of ferroelastic domain switching, there was also some evidence of high temperature dislocation activity seen in the deformed APS pillars. The density of dislocations in the pillars tested at 500°C was considerably higher than those fractured at room temperature. This difference in defect density may also contribute to the large plastic strain observed in the APS coatings tested at elevated temperatures. While dislocation activity is rarely observed at intermediate temperatures in bulk ceramic materials, the non-equilibrium structures may result from the plasma spray process that facilitates rapid mass transport and thereby introducing dislocations during deposition of such coatings. Further investigation on the formation mechanisms of dislocations in as-deposited coatings is necessary to support this hypothesis. The large plastic strain of APS TBC may also be attributed to the closure of preexisting cracks and micropores during deformation. When deformed under compression at elevated temperatures, these preexisting small pores and cracks may no longer play a significant role in triggering the brittle failure but may deform to accommodate plastic strain. The decrease in variability of fracture strength for the APS TBC at room temperature and 500°C supports this assertion and suggests that the pores and microcracks are no longer the primary drivers for coating failure, but possibly accommodate strain instead. On the other hand, the DVC coating has less dislocation activity and much less preexisting cracks and pores to accommodate strain during compression at elevated temperatures (500°C), and consequently forms large cracks.

6.6. Conclusions

The mechanical behaviors APS and DVC 8YSZ coatings parallel to the substrates were investigated by *in situ* microcompression tests at room temperature and 500°C. At room temperature, the high density of pre-existing cracks and pores in APS TBC caused a large dispersion of fracture strength (0.6 ~ 6.6 GPa). DVC coatings exhibits less dispersed fracture strength (3.9 to 6.6 GPa) resulting from the relatively dense structure. At 500°C, however, APS TBCs exhibited significantly enhanced deformability arising from deformable pores, ferroelastic domain switching, and dislocation activities. In comparison, at the same test temperature, the DVC coating with lower porosity and minimal dislocation activity exhibited relatively brittle behavior, even in the presence of ferroelastic domain switching. Both APS and DVC coating pillars showed considerably enhanced reliability of fracture behaviors at elevated temperature.

CHAPTER 7. MICROMECHANICAL PROPERTIES OF MAGNESIA-PARTIALLY STABILIZED ZIRCONIA (MG-PSZ) PREPARED BY SPARK PLASMA SINTERING

7.1. Overview

Magnesia partially stabilized zirconia (Mg-PSZ) was prepared by spark plasma sintering (SPS) with subeutectoid aging to finetune its mechanical properties. With the rapid heating and cooling rate capability of SPS, Mg-PSZ with much smaller grain size and higher residual stress than conventionally sintered Mg-PSZ can be produced. After 4 hr aging a significant phase decomposition of cubic phase into tetragonal, orthorhombic, and monoclinic zirconia occurs, which provides, in turn, a peak toughness owing to the tetragonal-to-monoclinic transformation toughening. SPSed Mg-PSZ underwent significant destabilization after 8 hr aging attributed to the presence of high internal stress and a high volume of grain boundaries.

7.2. Introduction

Monolithic zirconia (ZrO_2) has compelling mechanical, chemical, physical, and thermal properties, but it was of less industrial importance due to an occurrence of catastrophic fracture induced by phase transformation upon heating and cooling [1,12]. The high-temperature phase of tetragonal zirconia (t) transforms into monoclinic zirconia (m) at $\sim 950^\circ C$ upon cooling, which causes $\sim 4\%$ volume expansion and a shear strain of 0.16 [1]. This large volume change induced by the phase transformation can cause disastrous failure in its service as industrial components. However, it was found that the phase transformation can be suppressed by doping lower valance oxides such as Y_2O_3 , CeO_2 , CaO , and MgO [2–4]. As a result, tetragonal or cubic zirconia namely, stabilized-zirconia can be obtained at room temperature, which results in the drastic improvement of its industrial applicability. The mechanical strength and fracture toughness of stabilized zirconia can be considerably enhanced through the tetragonal-to-monoclinic transformation occurring at crack-tips, which can ultimately retard crack propagation [9–11]. Also, its mechanical properties turn out tunable by adjusting a degree of stabilization (depending strongly on the heat-treatment, dopant type, and dopant concentration) and processing techniques [20,180,270,273]. Therefore, stabilized zirconia has become one of the most used ceramics as a reliable structural material.

Among many possible dopants in zirconia system, magnesia (MgO) is known as the most interesting dopant in that it can provide quite complicated microstructures and unique mechanical properties, highly depending on its thermal treatment [1]. 9 ~ 10 mol % magnesia with balanced zirconia is the most commonly used composition in the industry to obtain magnesia partially stabilized zirconia (Mg-PSZ). Mg-PSZ has a lenticular shape of dispersed t-phase precipitates in a cubic (c) zirconia matrix. This unique combination can allow retention in Mg-PSZ of both high strength and enhanced fracture toughness [1]. A cubic solid solution of 9 ~ 10 mol% magnesia with balanced zirconia can be acquired at sintering temperature of $\geq 1700^{\circ}\text{C}$ and nanosized t-ZrO₂ precipitates are formed upon subsequent furnace cooling. Since martensitic start temperature is below room temperature, further heat-treatments are required to increase the size and density of t-ZrO₂ precipitates through eutectoid aging ($\text{c-ZrO}_2 \rightarrow \text{t-ZrO}_2 + \text{MgO}$, $1240^{\circ}\text{C} - 1400^{\circ}\text{C}$) or subeutectoid aging ($\text{c-ZrO}_2 \rightarrow \text{t-ZrO}_2 + \text{MgO} \rightarrow \text{m-ZrO}_2 + \text{MgO}$, $<1240^{\circ}\text{C}$) [21]. The eutectoid aging of the c-ZrO₂ solid solution can provide diffusion-controlled t-precipitate coarsening and nucleation, but it is a sluggish process due to the low driving force [22]. Therefore, for a commercial reason, the subeutectoid aging is commonly chosen for the thermal treatment, despite the formation of m-ZrO₂ at an expense of t-ZrO₂, and yet it produces one of the toughest ceramics. For example, when aged at 1100°C for 8 hrs, the phase content of t-ZrO₂ increased to 47% at an expense of c-ZrO₂ (10%), which results in the contribution from transformation toughening to fracture toughness (ΔK_T) of $7.53 \text{ MPa}\cdot\text{m}^{1/2}$, with an insignificant hardness loss (10 GPa) [274].

Spark plasma sintering (SPS) is an electric current assisted consolidation technique where high pulsed direct currents passing through a graphite die can generate resistance heat, thereby allowing achievement of the theoretical density of a specimen. This technique offers the high heating and cooling rate together with pressure, which enables rapid densification and drastic grain size reduction [179]. In this study, we demonstrate the one-step preparation of Mg-PSZ using SPS with two different maximum temperatures (1700°C and 1850°C), and subsequent subeutectoid aging at 1100°C for various aging times. The microstructure evolution of SPSed Mg-PSZ is investigated and its effect on micromechanical properties is discussed.

7.3. Materials and methods

Commercially available non-stabilized zirconia powder (TZ-0, Tosoh corp., ~ 40 nm) and magnesia (US Research Nanomaterials, Inc., ~ 20 nm) were ball-milled with zirconia balls at 80

rpm in methanol media for 24 hrs to obtain a homogeneous mixture (9.7 mol% MgO with balanced zirconia). Then, the mixed slurry was dried at 80°C for 3 hrs. The dried mixture was put in a tube furnace and heated at 500°C for 5 hrs to burn out the residual polymers and moistures. The homogeneously mixed powder was sintered by SPS furnace (SPS-10, Thermal Technologies LLC). The mixture was loaded in a 10 mm graphite die and placed in a chamber. The maximum temperatures were set to 1700°C and 1850°C at a heating rate of 500°C/min and held at the temperatures for 5 mins in a low vacuum atmosphere (10^{-3} torr). The sintering temperature was measured by a pyrometer aiming at a hole in the middle of the graphite die. Meanwhile, a pressure of 50 MPa was applied during the sintering experiments. After 5 mins of holding time at the maximum temperatures, the specimens were cooled down to 1100°C for the subeutectoid aging at a cooling rate of 500°C/min and held for 0, 0.5, 2, 4, and 8 hrs. The specimens were immediately cooled down to room temperature at the cooling rate of 500°C/min after the heat treatment at 1100°C.

Prior to conducting microstructure analyses and microindentation experiments, SPSed specimens were characterized by X-ray diffraction (XRD, PANalytical Empyrean). Then, scanning electron microscopy (SEM, FEI Quanta 3D FEG scanning electron microscope) and transmission electron microscopy (TEM, FEI TALOS F200X TEM/STEM with ChemiSTEM technology, X-FEG, and SuperX EDS) at 200 kV were utilized to carry out microstructural and chemical analyses. TEM specimens of the specimens were prepared by mechanical grinding, polishing, dimpling, and subsequent low energy (2 kV) ion milling in a precision ion milling equipment (PIPS II, Gatan) to reduce ion milling induced damage and obtain thin area observable in TEM.

The density of the specimens was measured by the Archimedes method. Prior to conducting mechanical testing, the specimens were polished by a series of SiC sandpapers, diamond pastes ($\sim 1 \mu\text{m}$), and colloidal silica ($\sim 20 \text{ nm}$). A microhardness tester (LECO Corporation, LM 247AT) equipped with a Vickers tip was employed for microhardness measurements of the polished samples. More than 20 indents were made on each sample with a load of 1 kg.f. The central region of the samples was indented to minimize the effect of inhomogeneous microstructure resulted from the frictional force between the powders and graphite die. The lengths of diagonal indents and cracks were measured under an SEM to calculate the microindentation hardness and fracture toughness.

7.4. Results

The density was measured to be $\geq 95\%$ by Archimedes' principle in distilled water for all the SPSed Mg-PSZ with maximum temperatures of 1700°C and 1850°C, and subsequently aged for 0.5, 2, 4, and 8 hrs. Despite the short holding time (5 mins) at the maximum temperature, the hot-pressing (50 MPa) helps the specimens to achieve nearly full density. Figs. 7.1a and b show XRD patterns of Mg-PSZ with different aging times. As-sintered specimens without subeutectoid aging (highlighted in black) show the nature of fully stabilized zirconia, exclusively consisting of cubic phase represented by red diamond shapes. Also, little t-ZrO₂ peaks were detected for 30 min aged specimens (highlighted in blue). After 2 hr subeutectoid aging (highlighted in red) for both samples, the peaks from t-ZrO₂ precipitates (blue squares) begin showing up. In addition, m-ZrO₂ (half-solid green circle) shows up for Mg-PSZ sintered at 1700°C (1700Mg-PSZ) after 2hr aging, while the specimen sintered at 1850°C (1850Mg-PSZ) retains no apparent m-phase yet. After 4 hr aging (highlighted in green), many peaks from m-ZrO₂ emerge for both specimens. After 8 hr aging (highlighted in orange), m-ZrO₂ becomes the dominant phase at an expense of c- and t-phases for 1700Mg-PSZ, while 1850Mg-PSZ still remains partly stabilized. Fig. 7.1c shows the phase stability ratio of two samples as a function of aging time calculated on the basis of the intensity of XRD peaks. The stability ratio is given as [275],

$$\text{Stability ratio} = \frac{\text{Intensity of } 29.92^\circ}{\text{Intensity of } 28.06^\circ + \text{Intensity of } 31.24^\circ + \text{Intensity of } 29.92^\circ} \quad (7.1)$$

where 29.92° represents c- and/or t-ZrO₂, while 28.06°, and 31.24° come from m-ZrO₂. The stability ratio of two specimens comparably decreases until aged for 2 hrs. Thereafter, the stability ratio of 1700Mg-PSZ decreases more rapidly than that of 1850Mg-PSZ and becomes non-stabilized zirconia after 8 hr aging. Figs. 7.1d-f show an SEM micrograph of 1700Mg-PSZ with inverse pole figure and kernel average misorientation (KAM) map obtained by electron backscatter diffraction (EBSD). The grain intercept method reveals an average grain size of $13.4 \pm 6.0 \mu\text{m}$. KAM map shows the existence of significant residual stress within both grain interiors and grain boundaries. On the other hand, 1850Mg-PSZ shows a larger grain size of $54.9 \pm 20.7 \mu\text{m}$ as shown in Fig. 7.1g and h. Also, the intensity of the residual stress for 1850Mg-PSZ was less than that for 1700Mg-PSZ and the residual stress is more prevalent along grain boundaries than within grain interiors. To quantify the residual stress, the XRD $\sin^2(\Psi)$ method was introduced. The residual stress can be calculation by [276],

$$\frac{\partial d_{\phi,\Psi}}{\partial \sin^2\Psi} = \left(\frac{1+\nu}{E}\right)_{hkl}\sigma d_o \quad (2)$$

where ϕ is the in-plane rotation, Ψ is the tilt angle to the surface normal, ν is the Poisson ratio, E is the elastic modulus, σ is the residual stress, and d_o is the interplanar spacing without the residual stress. Fig. 7.2 shows interplanar spacing of the (311) plane as a function of $\sin^2(\Psi)$. $\frac{\partial d_{\phi,\Psi}}{\partial \sin^2\Psi}$ and d_o in Eq. (2) can be obtained from the slope and intercept of the linear regression lines in Fig. 7.2. The XRD $\sin^2(\Psi)$ method yields the tensile residual stress of 472 and 226 MPa for 1700Mg-PSZ and 1850Mg-PSZ without subeutectoid aging, respectively.

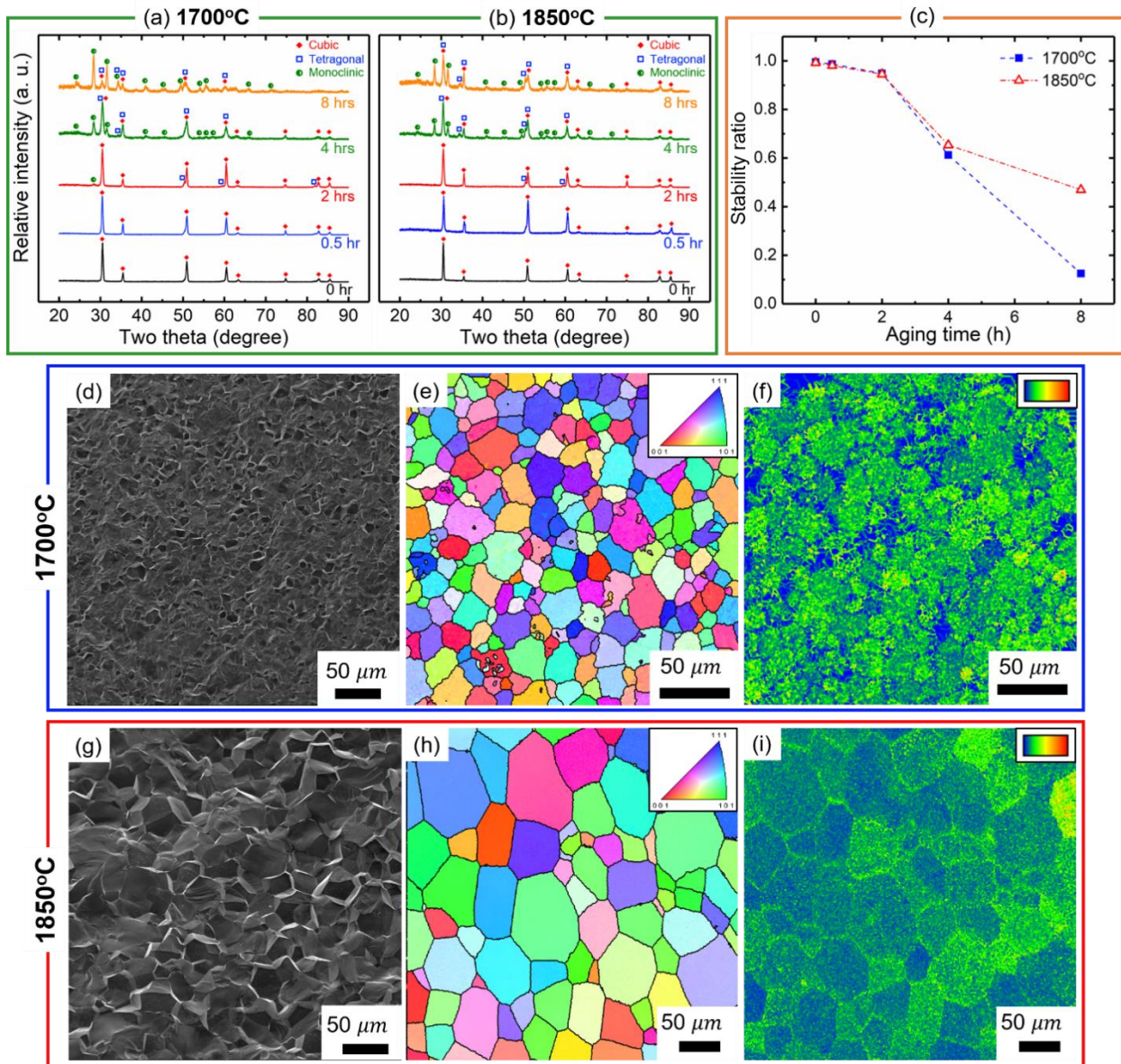


Figure 7.1. XRD patterns and microstructure analyses of Mg-PSZ processed by spark plasma sintering at 1700°C and 1850°C. (a-b) XRD patterns of Mg-PSZ sintered at 1700°C and 1850°C, and subsequently heat-treated at 1100°C for different aging times (0, 0.5, 2, 4, and 8 hrs). For both samples, t-phase starts showing up after 2 hr aging and m-phase emerges after 4 hr aging. (c) Phase stability ratio of two samples as a function of aging time. A ratio of c- and t-phases to m-phase in the sample sintered at 1700°C decreases significantly after 8hr aging. (d-f) SEM micrograph, inverse pole figure and KAM map of Mg-PSZ sintered at 1700°C. The average grain size is 7 μm and significant residual stress is observed within grain interiors. (g-i) SEM micrograph, inverse pole figure and KAM map of Mg-PSZ sintered at 1850°C. The average grain size is determined to be 30 μm and residual stress is predominant along grain boundaries.

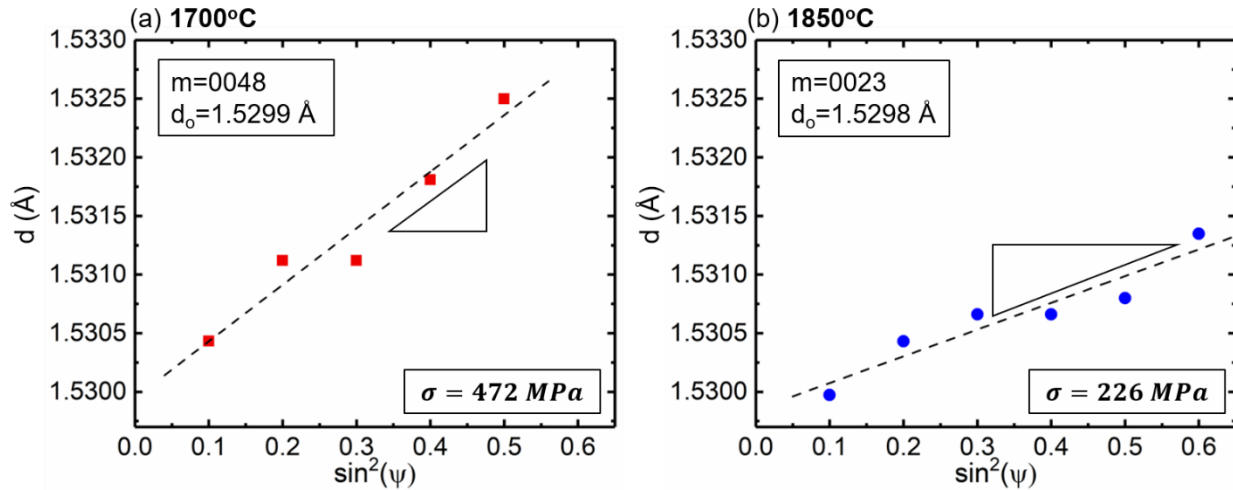


Figure 7.2. Determination of the residual stress in as-sintered Mg-PSZ at (a) 1700 and (b) 1850°C. Plots of d spacing of the (311) plane versus $\sin^2(\Psi)$ yields the tensile residual stress of 472 MPa and 226 MPa for 1700Mg-PSZ and 1850Mg-PSZ, respectively. m is the slope of the linear regression line and d_0 is the unstressed d spacing of the (311) plane.

Figs. 7.3a-b show TEM micrographs of 1700Mg-PSZ without subeutectoid aging, revealing the presence of low density of nano-precipitates. The inserted selected area electron diffraction (SAD) in Fig. 7.2a confirms that the dominant phase of the as-sintered specimen is c-ZrO₂. High-resolution TEM (HRTEM) images in Figs. 7.3c and d show the presence of nano t- and m-ZrO₂ precipitates, undetectable from XRD. Scanning TEM and energy dispersive X-ray spectroscopy (EDS) map for Zr, O, and Mg elements reveal the homogenous distribution of each element throughout the specimen (Figs. 7.3Se-h).

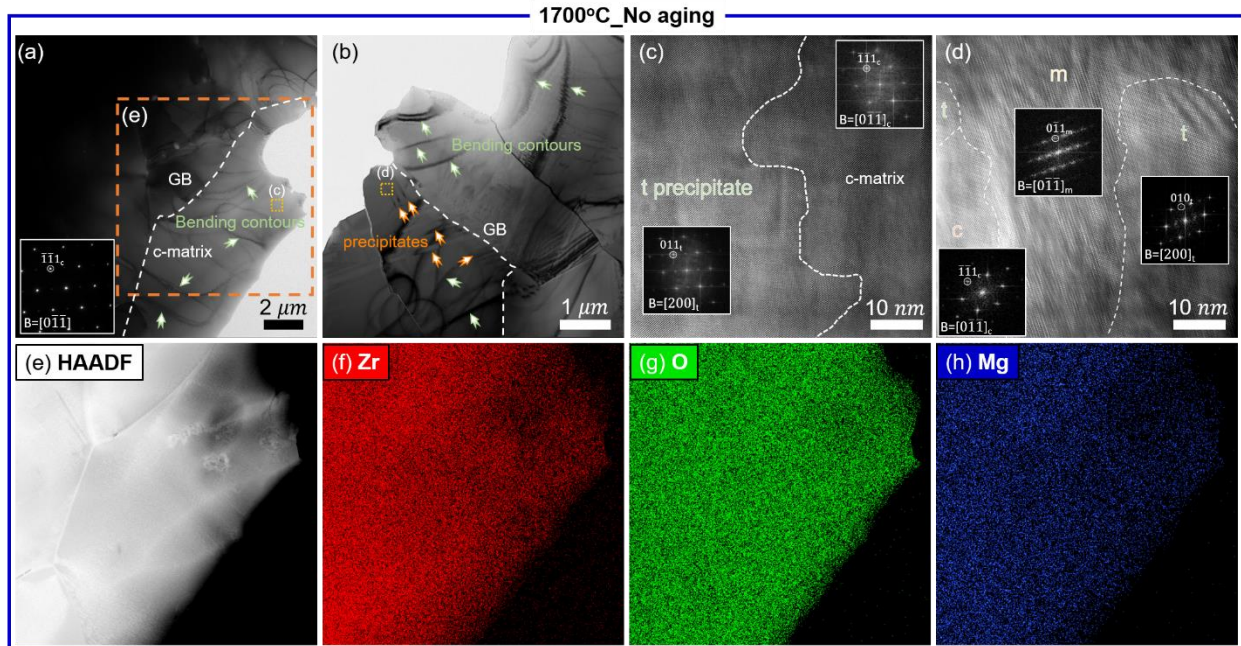


Figure 7.3. TEM micrographs of as-sintered Mg-PSZ at 1700°C. (a-b) Bright-field TEM micrographs of as-sintered Mg-PSZ showing clear c-matrix with low density of precipitates and bend contours. (c-d) HRTEM micrographs showing the existence of t- and m-precipitates. (e-h) HAADF image and EDS map of as-sintered Mg-PSZ showing uniform distribution of Mg throughout the specimen.

On the other hand, after 2 hr aging, the 1700Mg-PSZ shows the lenticular-shaped precipitates with significant contrast difference indicated by orange arrows in Figs. 7.3a-b. The precipitates are identified as t- and m-ZrO₂ embedded in c-matrix as shown in an HRTEM micrograph in Figs. 7.3c. Scanning TEM and EDS map of 2 hr aged Mg-PSZ show homogeneous distribution of Zr and O, and Mg deficiency in the precipitates (Fig. 7.4d-g). After 1700Mg-PSZ was aged for 4 hrs, a density of nano precipitates (indicated by orange arrows in Fig. 7.5a) increased significantly and twin-related m-ZrO₂ precipitates along a grain boundary were observed. Fig. 7.6 also shows additional TEM micrographs of twin-related monoclinic variants nucleated from grain boundaries. Fig. 7.5b shows an HRTEM micrograph of m-variants and the twin-relation was confirmed by an inserted FFT. Nanoprecipitates after 4 hr aging were identified as a mixture of orthorhombic (o), t- and m-ZrO₂ as shown in Fig. 7.5c-d. Scanning TEM image and EDS map in the same region reveal the obvious enrichment of Zr and deficiency of Mg in m-variants and nano precipitates.

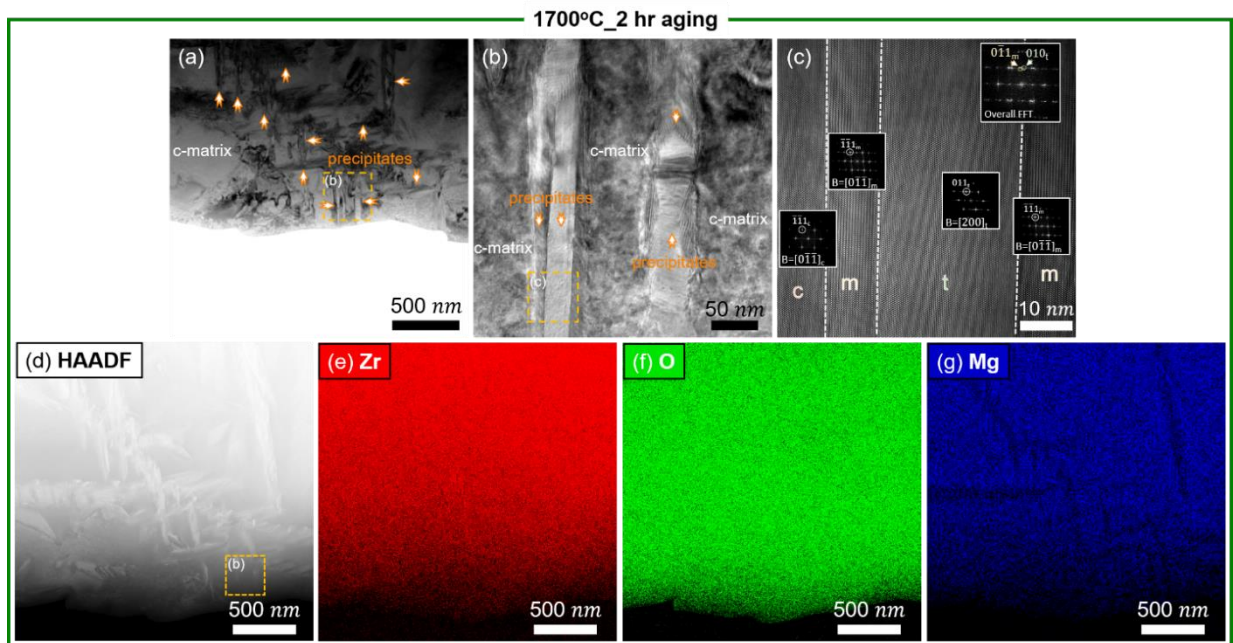


Figure 7.4. TEM micrographs of Mg-PSZ sintered at 1700°C followed by 2 hr aging. (a) Low-magnification bright-field TEM image showing the presence of lenticular precipitate indicated by orange arrows. (b) Bright-field TEM micrograph of precipitates from an inserted box in Fig. (a), showing two precipitates embedded in c-matrix. (c) HRTEM micrograph from the precipitate of Fig. (b), showing the presence of t- and m-phases, confirmed by the inserted FFTs. (d-g) High-angle annular dark field (HAADF) image and EDS map of 2 hr aged Mg-PSZ showing Mg deficiency in precipitates.

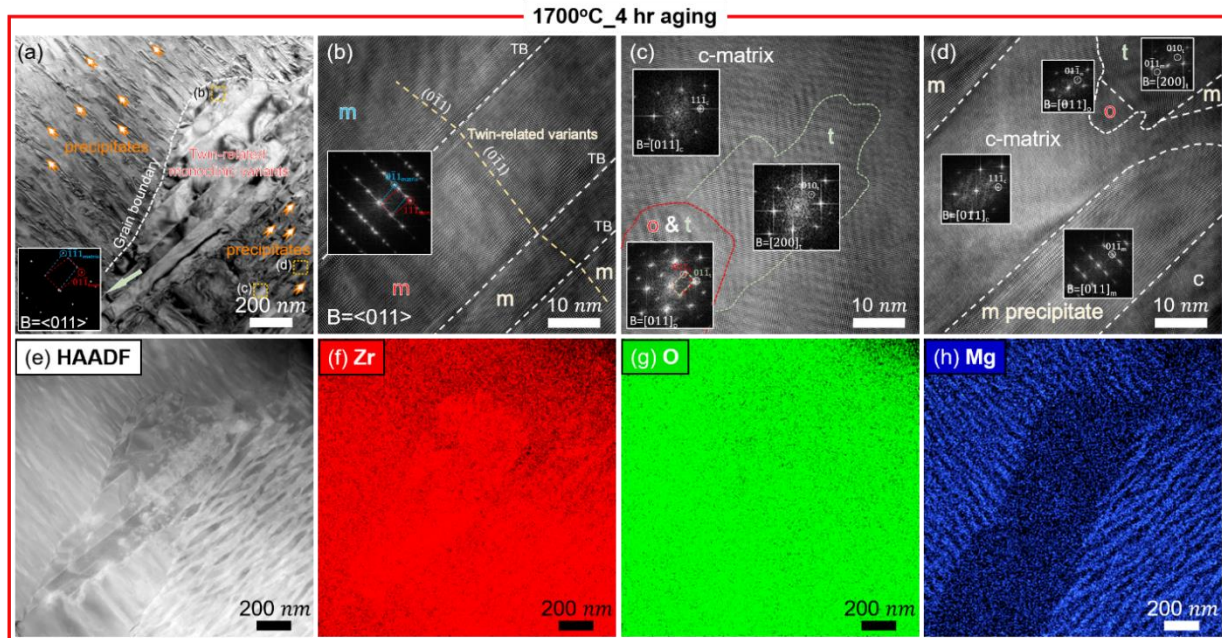


Figure 7.5. TEM micrographs of Mg-PSZ sintered at 1700°C followed by 4 hr aging. (a) Low-magnification bright-field TEM image showing the presence of lenticular precipitate (indicated by orange arrows) and monoclinic variants. (b) HRTEM micrograph of monoclinic variants showing twin-relation as evidenced by an inserted FFT. (c) HRTEM micrograph of c-matrix site showing the presence of t- and o-phases, confirmed by inserted FFTs. (d) HRTEM image of the lenticular precipitate, consisting mainly of m-phases confirmed by the inserted FFTs. (e-h) HAADF image and EDS map showing the enrichment of Zr and deficiency of Mg in precipitates.

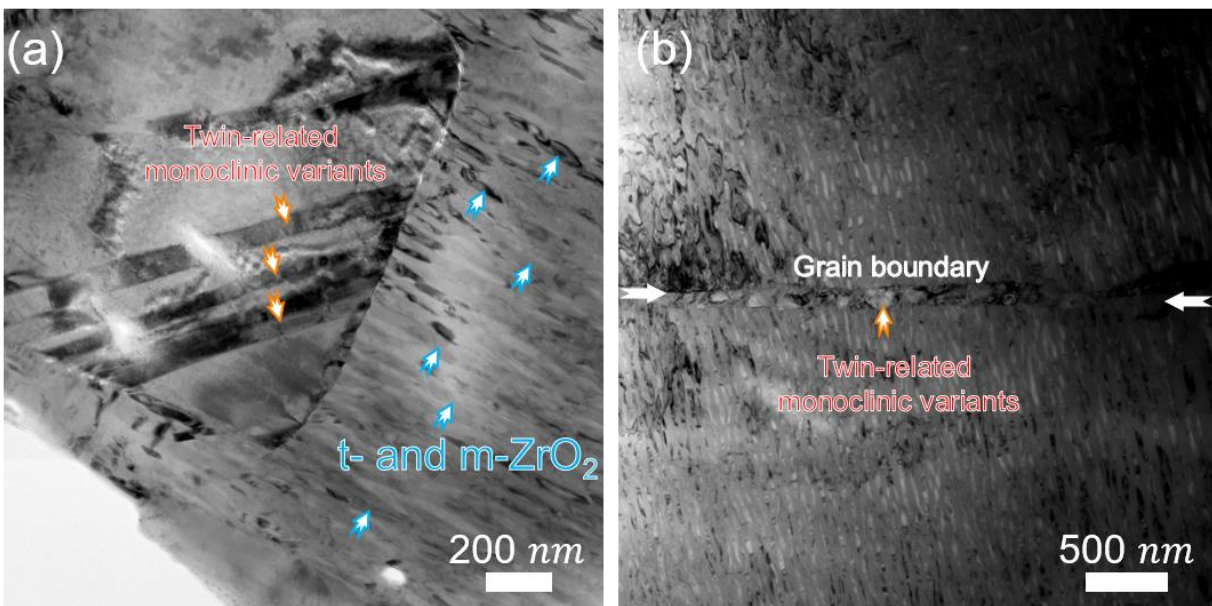


Figure 7.6. TEM micrographs of Mg-PSZ sintered at 1700°C and subsequently aged for 4 hrs. (a-b) Bright-field TEM micrographs showing the presence of twin-related monoclinic variants along grain boundaries.

Figs. 7.7a-b show the Vickers hardness and fracture toughness as a function of aging time for 1700Mg-PSZ and 1850Mg-PSZ, respectively. The Vickers hardness was calculated by the following equation,

$$HV = \frac{1.8544F}{d^2} [kg \cdot f/mm^2] \quad (7.2)$$

where HV is the Vickers hardness, F force in kg·f and d diagonal length in mm. Then, HV was converted to a unit of GPa using a conversion factor of 0.0098. The Vickers indentation toughness was determined by the equation suggested by Lankford [277],

$$K_{Ic} = 0.0782 \cdot (HV \cdot a^{\frac{1}{2}}) \cdot \left(\frac{E}{HV}\right)^{2/5} \cdot \left(\frac{c}{a}\right)^{-1.56} \quad (7.3)$$

where K_{Ic} is the fracture toughness, HV the Vickers hardness, a the diagonal half-length, E the elastic modulus (210 GPa), and c the crack length from a corner of the indent. The hardness of as-sintered Mg-PSZ at 1700°C is 13.5 GPa and decreases monotonically to 8.0 GPa after 8 hr aging. Meanwhile, the indentation toughness increases from 4.4 to 8.6 MPa·m^{1/2} after 4 hr aging and decreases to 5.7 MPa·m^{1/2} after 8 hr aging thereafter. For 1850Mg-PSZ, the as-sintered specimen shows a hardness of 12.5 GPa and it decreases monotonically to 9.2 GPa after 8hr aging. The fracture toughness reaches the maximum value when aged for 4 hrs (8.2 MPa·m^{1/2}) and decreases thereafter to 5.8 MPa·m^{1/2} after 8 hr aging.

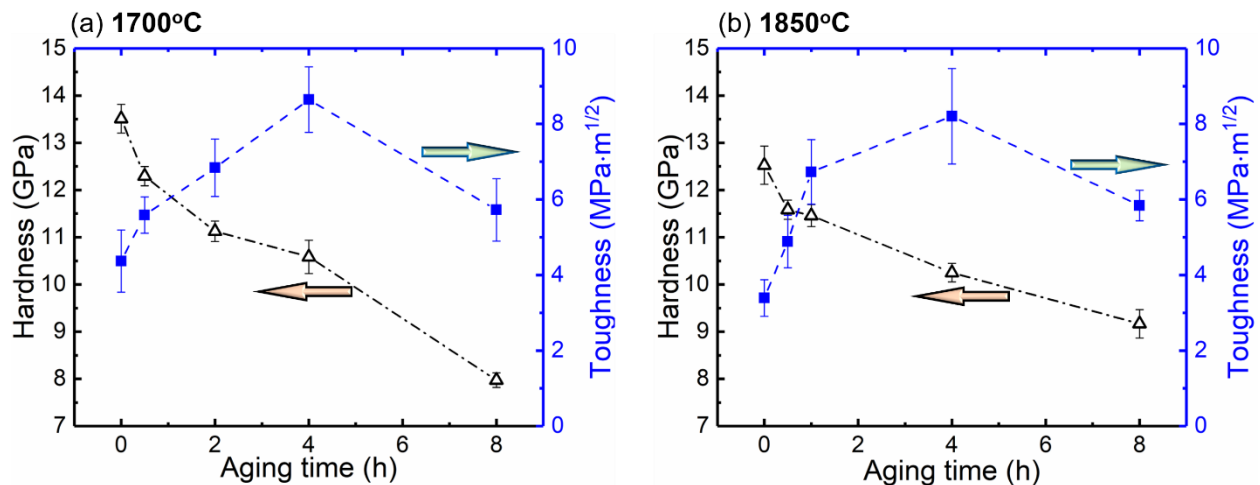


Figure 7.7. Microindentation hardness and fracture toughness as a function of aging time for Mg-PSZ prepared by spark plasma sintering at (a) 1700 and (b) 1850°C. Hardness of Mg-PSZ decreases monotonically with increasing aging time for both specimens. Fracture toughness reaches to the highest value when aged for 4 hrs and decreases thereafter.

7.5. Discussion

The maximum temperatures of 1700°C and 1850°C were chosen to compare the effect of grain size on the microstructure evolution and the consequent mechanical properties of Mg-PSZ. When Mg-PSZ is prepared conventionally that utilizes low heating and cooling rate (40 ~ 500 °C/h), and long holding time (2 ~ 4 hrs), it naturally yields a large grain size of 50 ~ 100 μm , comparable to the grain size of 1850Mg-PSZ in this study [21,274,278,279]. Meanwhile, the Vickers hardness of the as-sintered specimen at 1700°C is 13.5 GPa, higher than that of 12.5 GPa for the as-sintered specimen at 1850°C. The apparent microstructural difference between two specimens are the grain size confirmed by EBSD, which may yield the higher hardness for 1700Mg-PSZ than for 1850Mg-PSZ [268,269,280]. The grain size reduction for 1700Mg-PSZ comes mainly from the lower maximum temperature and the high heating rate (500 °C/min) enabling to minimize the exposure of grains to an intermediate temperature region where significant grain coarsening occurs. Since SPS is a non-equilibrium processing technique with high cooling rate capability, it can also generate a high degree of internal residual stress which is confirmed by EBSD and the XRD $\sin^2(\Psi)$ method. The higher residual stress for 1700Mg-PSZ than for 1850Mg-PSZ may be attributed to the shorter processing time that in turn reduces the time to equilibrate the residual stress.

Two specimens exhibit the obvious difference in the phase stability in that the 1700Mg-PSZ loses its c- and t-ZrO₂ more rapidly than 1850Mg-PSZ after 4 hrs of subeutectoid aging. It appears that internal stress within grain interiors and grain boundaries is built up as the temperature of SPSed Mg-PSZ decreases during the rapid cooling process, and this internal stress in t-ZrO₂ tends to facilitate phase transformation to m-ZrO₂ [17,281]. The less residual stress for 1850Mg-PSZ (as shown in Fig. 7.1i) may be attributed to longer sintering time to release and equilibrate the accumulated stress by grain coarsening. The drastic loss of phase stability directly impacts its mechanical properties. For example, the hardness of both specimens decreases as c-ZrO₂ is decomposed to t- and m-ZrO₂. Also, both specimens exhibit the maximum toughness after 4 hr aging due to the high density of t-ZrO₂, in drastic contrast to conventionally sintered Mg-PSZ which shows the peak toughness after 8 hr subeutectoid aging at 1100°C [274]. SPSed Mg-PSZ exhibits early phase decomposition (confirmed by FFTs and EDS maps) presumably due to the presence of the residual stress induced by non-equilibrium process and a high volume of grain boundaries owing to small grain size, which is classical nucleation sites for m-ZrO₂ [282]. This assertion is supported by the fact that twin-related m-ZrO₂ precipitates in this study are also

commonly found near grain boundaries as shown in Fig. 7.5a and Fig. 7.6. Meanwhile, o-ZrO₂ precipitates are occasionally found in 4 hr aged Mg-ZrO₂ and it is known to be transformed from t-ZrO₂ [283,284]. The o-ZrO₂ precipitates are not easily transformable under mechanical loading such that a large quantity of o-ZrO₂ may result in a decrease of fracture toughness [285,286]. On the other hand, the other unique precipitate, δ (Mg₂Zr₅O₁₂), formed during subeutectoid aging is responsible for increasing the metastability of t-ZrO₂, and thus enhance the fracture toughness of Mg-PSZ [274,282]. However, no δ phase was observed in this study.

7.6. Conclusions

In summary, 9.7 mol% Mg-PSZ was prepared by spark plasma sintering at 1700°C and 1850°C with subsequent subeutectoid aging at 1100°C. Due to the high heating and cooling rate of SPS, Mg-PSZ retained small grain size (13.4 μm) and high residual stress, which altered its mechanical properties. A significant phase decomposition of c-ZrO₂ into t-, o-, and m-ZrO₂ for both specimens occurred after 4 hr aging where the peak toughness with minor hardness loss was observed. After 8 hrs of subeutectoid aging, 1700Mg-PSZ underwent more destabilization than 1850Mg-PSZ. The early phase decomposition of c-ZrO₂ for 1700Mg-PSZ is attributed to the presence of high internal stress and a large volume fraction of grain boundaries, which can be nucleation sites for the m-ZrO₂.

CHAPTER 8. CONCLUSIONS AND FUTURE WORK

8.1. Conclusions

ZrO₂ stabilized by Y₂O₃ and MgO was prepared by conventional firing, flash sintering, spark plasma sintering, air plasma spray, and detonation gun thermal spray, and their mechanical properties were investigated at microscale by employing the microcompression tests. The major findings are summarized as follows:

(1) 3YSZ with a transformable tetragonal phase was successfully prepared by flash sintering under an electric field of 150V/cm. The flash-sintered 3YSZ retains a high density of dislocations that may be induced by substantial mass transport induced plastic flow during flash sintering. *In-situ* study on the flash sintered 3YSZ was performed at 25-650°C. At room temperature, the micropillars show a high fracture strain (~8%) due to the stress-induced martensitic transformation toughening but fracture catastrophically after that. A brittle-to-ductile transition of fracture mode is observed at 400°C in the flash sintered 3YSZ due to the transition from the phase transformation toughening to dislocation activity and grain boundary sliding. The preexisting dislocations in the flash sintered YSZ cause an inelastic deformation at 400°C together with early initiation of grain boundary sliding owing to nanosized grains. Strain rate jump tests confirmed the deformation mechanisms at 450, 550, and 650°C, where a stress exponent of ~ 7 and activation energy of 145 kJ/mol are obtained. The activation energy of 145 kJ/mol is comparable to the activation energy for oxygen vacancy migration. This study suggests that the abundant dislocations and oxygen vacancies induced during flash sintering lead to the early initiation of dislocation glide and climb assisted by oxygen vacancy migration.

(2) 3YSZ was successfully prepared by spark plasma sintering at ~ 1026°C. *In-situ* microcompression tests of the spark plasma sintered 3YSZ were performed at 25 to 670°C, and the microstructure of deformed pillars was investigated by TEM. The deformation mechanism at room temperature is dominated by martensitic transformation, and the pillars exhibit brittle failure at a strain of ~7%. At 400°C, the transformation toughening mechanism is gradually superseded by the other inelastic deformation mechanism, grain boundary sliding. At 600°C or greater, grain elongation with local grain separation was observed after compression, indicating that grain boundary sliding with dislocation creep accommodation is activated.

(3) 8 wt% YSZ TBCs prepared by air plasma spray and detonation gun thermal spray were investigated by *in-situ* microcompression tests at two temperatures, room temperature and 500°C. At room temperature, the high density of pre-existing cracks and pores in air plasma sprayed TBCs result in scattered fracture strength, but it shows much consistent stress-strain behavior at 500°C. Thermal sprayed TBCs exhibit less dispersed fracture strength at room temperature owing to the dense structure. At 500°C, it shows strength degradation, but better deformability. Ferroelastic domain switching toughening is observed in both coatings regardless of the test temperatures. Meanwhile, dislocation activity was observed at 500°C for the air plasma sprayed TBCs and improved deformability significantly. For the thermal sprayed TBCs, no dislocation activity is observed.

(4) 9.7 mol% MgO doped ZrO₂ (Mg-PSZ) was prepared by spark plasma sintering at 1700°C and 1850°C with subsequent subeutectoid aging at 1100°C. Owing to the high heating and cooling rate of the process (500°C/min), Mg-PSZ retains relatively smaller grain size (13.4 μm) and high residual stress than conventionally sintered Mg-PSZ (~100 μm), which in turn yield high hardness. A significant phase decomposition of the cubic phase into tetragonal, orthorhombic, and monoclinic ZrO₂ is observed after 4 hr subeutectoid aging. After 8 hrs of subeutectoid aging, 1700Mg-PSZ underwent more rapid phase decomposition than 1850Mg-PSZ due to the presence of high residual stress and high volume of grain boundaries. The highest fracture toughness can be achieved after 4hrs of subeutectoid aging for both samples without significant hardness loss.

8.2. Comparison of deformation mechanisms for FS 3YSZ and SPS 3YSZ

Flash sintering and spark plasma sintering of 3YSZ yield comparable microstructural characteristics such as grain size (159 nm for FS YSZ vs. 175 nm for SPS YSZ), final mass density, residual stress, and dominant phase (tetragonal ZrO₂). Both specimens retain a significant amount of the residual stress presumably due to rapid heating and cooling rates. Their dominant deformation mechanisms are slightly different depending on test temperatures. For example, dislocation activity for FS 3YSZ was triggered beyond the test temperature of 400°C, whereas the SPS 3YSZ requires 600°C to activate dislocations. The fact that dislocation activity for FS 3YSZ can be triggered at a much lower temperature may be attributed to the existence of abundant defects. A high density of the pre-existing defects such as oxygen vacancies and dislocations induced during flash sintering can remove the need for defect nucleation, and thus facilitates plastic

deformation of FS 3YSZ at lower test temperatures. On the other hand, the as-sintered SPS 3YSZ exhibits less dislocations, and thus a higher test temperature (600°C) is necessary to nucleate dislocations. The onset temperature (600°C) for dislocation activities of SPS 3YSZ is still lower than 800°C necessary for conventionally sintered 3YSZ [39]. Several factors may have contributed to the improved plasticity in SPS 3YSZ. First, dislocations were also observed in SPS YSZ and thus facilitate the nucleation and migration of dislocations during deformation. Second, the grain size of SPS YSZ is typically much smaller than conventional 3YSZ, and hence grain boundaries may facilitate deformation at reduced test temperatures. Third, the micropillars have a large surface-to-volume ratio and may facilitate the dislocation nucleation and stress relaxation.

Another difference in deformation mechanisms between FS and SPS 3YSZ is the presence of grain boundary sliding for SPS 3YSZ beyond 400°C. To activate grain boundary sliding, grain boundary cohesive strength should be weakened so that grain boundaries can become the preferential crack-pathway (intergranular fracture) upon mechanical loading. Intergranular fracture may occur due to the strain homogenization of materials, nanovoid nucleation and coalescence along grain boundaries, and segregation of solutes and impurities [287]. STEM EDS reveals that SPS 3YSZ retains a high degree of Y segregation along grain boundaries as shown in Fig. 5.18, and it may facilitate grain boundary sliding at elevated temperatures. Y in stabilized ZrO₂ can produce extrinsic point defects and a corresponding space charge. A large amount of Y segregation along grain boundaries can increase the degree of the non-stoichiometry at the interface and produce even higher density of point defects than the lattice [236]. The higher density of oxygen vacancies along grain boundaries may form nanovoids at elevated temperatures that can weaken the grain boundary cohesive strength, and thus result in intergranular fracture upon a mechanical loading. Also, different Y/Zr ratio between grain boundaries and lattices means that the tetragonality of YSZ along grain boundaries and in lattices is different. This difference develops a mismatch stress at the interface due to anisotropy in thermal expansion coefficient ($\alpha_a \neq \alpha_c$) at elevated temperatures. The mismatch stress at the interface may result in the reduction of grain boundary cohesive strength and ease grain boundary sliding. Interestingly, no high level of Y segregation was observed in FS 3YSZ as shown in Fig. 3.1. This observation may be attributed to the short processing time of FS 3YSZ at maximum sintering temperature. Note that as soon as the flash event happens, the power supply was turned off to minimize grain growth. The application of electric field was stopped right after the onset of flash, which significantly

reduces a time for Y cation to migrate towards grain boundaries. The presence of grain boundary sliding for SPS 3YSZ may contribute to higher critical strain than FS 3YSZ above 400°C as shown in Fig. 8.1. Besides, the dislocation activity was observed together with grain boundary sliding for SPS 3YSZ above 600°C, which further facilitate the plastic deformation of SPS 3YSZ.

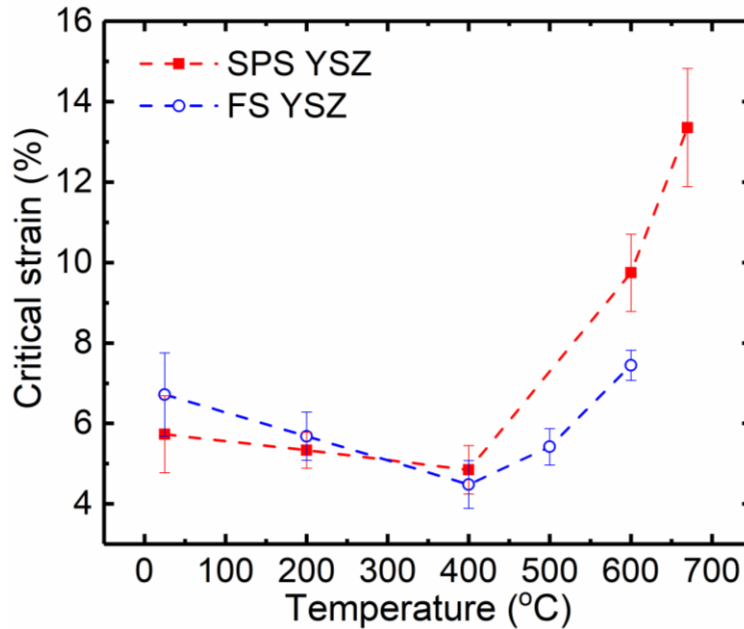


Figure 8.1. Critical strain versus test temperature for FS and SPS 3YSZ.

8.3. Future work

It was shown in this thesis that processing techniques can considerably alter the mechanical properties of ZrO_2 . Applying an electric field during the sintering process can introduce many defects such as vacancies, dislocations, and stacking faults, which, in turn, impact the materials' properties. Flash sintering, which applies intermediate-to-large electric field to ceramics, can be an important processing technique to produce materials with tunable mechanical, optical, and electrical properties. Some ceramic systems have been successfully processed by flash sintering (ZrO_2 , ZnO, TiO_2 , CeO_2 , $SrTiO_3$, $BiFeO_3$, $MgTiO_3$, Al_2O_3 , and composite materials) [59–68], and thus future work is to investigate the mechanical behavior of flash-sintered ceramics other than ZrO_2 . Among many demonstrated ceramics, preliminary investigation for the mechanical behavior of flash-sintered ZnO is shown in this chapter.

8.3.1. Mechanical behavior of flash sintered ZnO

8.3.1.1. Flash sintering of ZnO

Flash sintering of ZnO has been demonstrated in previous studies and does not require high temperatures or a large electric field. For example, Schmerbauch *et al.* flash-sintered ZnO with a relative density of ~ 95% under an AC electric field of ~ 160 V/cm at a furnace temperature of ~ 650°C [288]. Zhang *et al.* investigated the effect of the atmosphere in flash sintering behavior of ZnO and achieved ~ 97% relative density at a furnace temperature of ~ 120°C in the presence of Ar with 5 mol% H₂ [154]. The increase in conductivity in the reducing environment is believed to be responsible for the significantly reduced onset temperature of flash [154]. Bicer *et al.* observed rapid densification of ZnO with a relative density of ~ 99% at a furnace temperature of 588 ~ 834°C under an electric field of 50 V/mm during their *in-situ* energy dispersive X-ray diffraction study [289]. Recently, Phuah *et al.* flash-sintered ZnO under a DC electric field of 60 and 120 V/cm to study the effect of an abrupt increase in current on its microstructure by using a transmission electron microscope [290]. They observed greater grain size in the flash-sintered ZnO with a controlled current ramp while stacking faults were observed in both samples, presumably due to the formation of point defects during the flash event [290].

For the preliminary study in this thesis, ZnO nanoparticles (Sigma Aldrich, MO) with particle sizes < 100 nm were used to prepare cylindrical green bodies in a stainless-steel die under a uniaxial pressure of 150 MPa. The green body pellets (with a diameter of 6 mm, a height of 3 mm, and a green density of 55 ~ 60%) were inserted between parallel Pt electrodes. A pressure of 10 kPa was applied by an alumina rod to maintain good electrical contact between the green body and electrodes. An electric field of 60 V/cm was applied to the ZnO green body after the furnace temperature reached 700°C. After applying the electric field for 20 s, the rapid non-linear rise in the current and power-spike were observed, as seen in Fig. 8.2a and b. The abrupt linear shrinkage to 16% occurred at the onset of flash. Then, the FS ZnO was cooled down at a cooling rate of 25 °C/min after applying a current density of 10 A/cm² for 60 s. The density of the as-sintered ZnO was measured to be 95% by the Archimedes method. For comparison, the ZnO green body was heated at a rate of 10 °C/min and held at 1100°C for 60 s without an applied electric field (Fig. 8.3a). The density of the conventionally sintered (CS) ZnO was calculated to be 94% by the Archimedes method. XRD study of FS ZnO shows the dominant phase of wurtzite (Fig. 8.2c) and similarly for the CS ZnO (Fig. 8.3b). SEM and TEM images of the FS ZnO on the positive side

show very little porosity between the grains. The grain intercept method reveals that the average grain size on the positive side of the FS ZnO is $1.3 \pm 0.3 \mu\text{m}$. On the other hand, Fig. 8.3c and d show SEM and TEM micrographs of the CS ZnO with an average grain size of $1.7 \pm 0.6 \mu\text{m}$. The grain morphology of the FS ZnO on the negative side was also shown in Fig. 8.4a and b for the comparison. The average grain size of the FS ZnO on the negative side is $1.2 \pm 0.2 \mu\text{m}$. Interestingly, stacking faults were observed in the FS ZnO, as shown in the bright-field (BF) TEM micrograph in Fig. 8.4c and d, while no stacking fault was observed in the CS ZnO. The inverse pole figure and GND map analyzed by ASTAR in Fig. 8.2f and g show no obvious texture formation after sintering and initial GND density of $1.2 \times 10^{12} \text{m}^{-2}$ on the positive side. Meanwhile, ASTAR study on the CS ZnO reveals GND density of CS ZnO to be $1.10 \times 10^{12} \text{m}^{-2}$ (Fig. 8.3g).

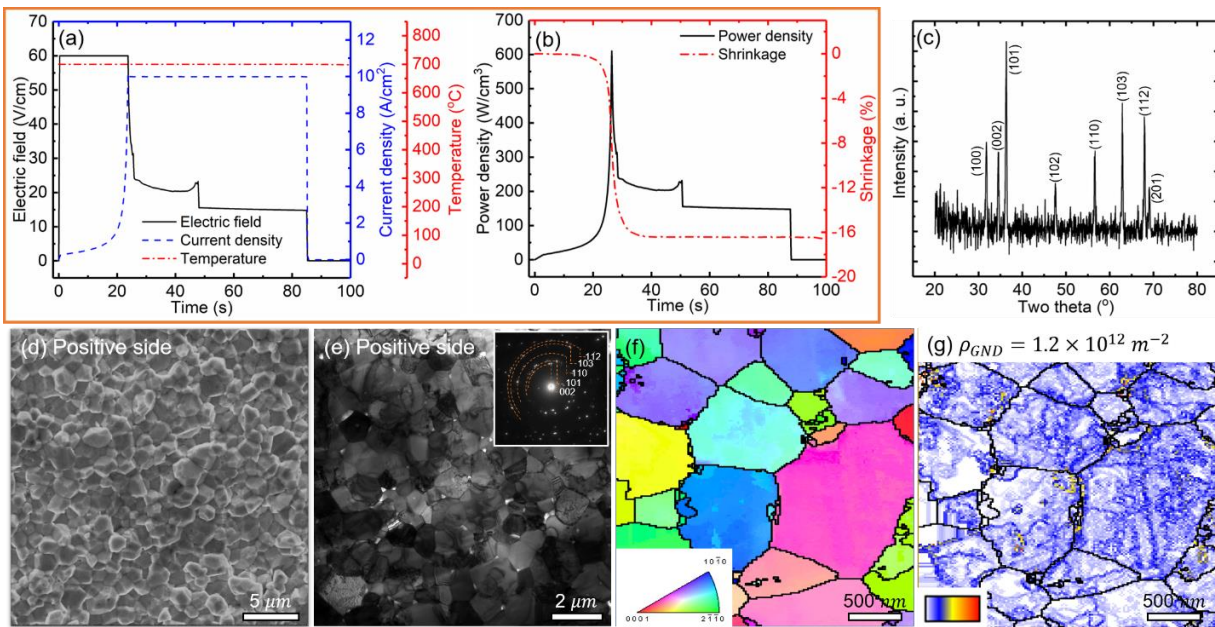


Figure 8.2. Flash sintering conditions and microstructure of the flash-sintered ZnO. (a) An electric field of 60 V/cm was applied to the ZnO green body under the isothermal condition (700°C). After the onset of flash sintering, a current density of 10 A/cm^2 was applied for 60 s. (b) The power-spike and abrupt linear shrinkage were observed at the onset of flash sintering. (c) The XRD pattern of the sintered ZnO reveals a typical wurtzite crystal structure. (d) SEM micrograph of the as-sintered ZnO from the positive side showing the typical granular morphology. (e) TEM micrograph showing grains with an average grain size of $1.3 \mu\text{m}$, and nanovoids at the grain boundaries. (f) Inverse pole figure crystal orientation map shows the polycrystalline nature of the sintered ZnO with high angle grain boundaries. (g) Geometrically necessary dislocation (GND) map shows the average GND density of the flash-sintered ZnO at the positive side is $1.2 \times 10^{12} \text{m}^{-2}$.

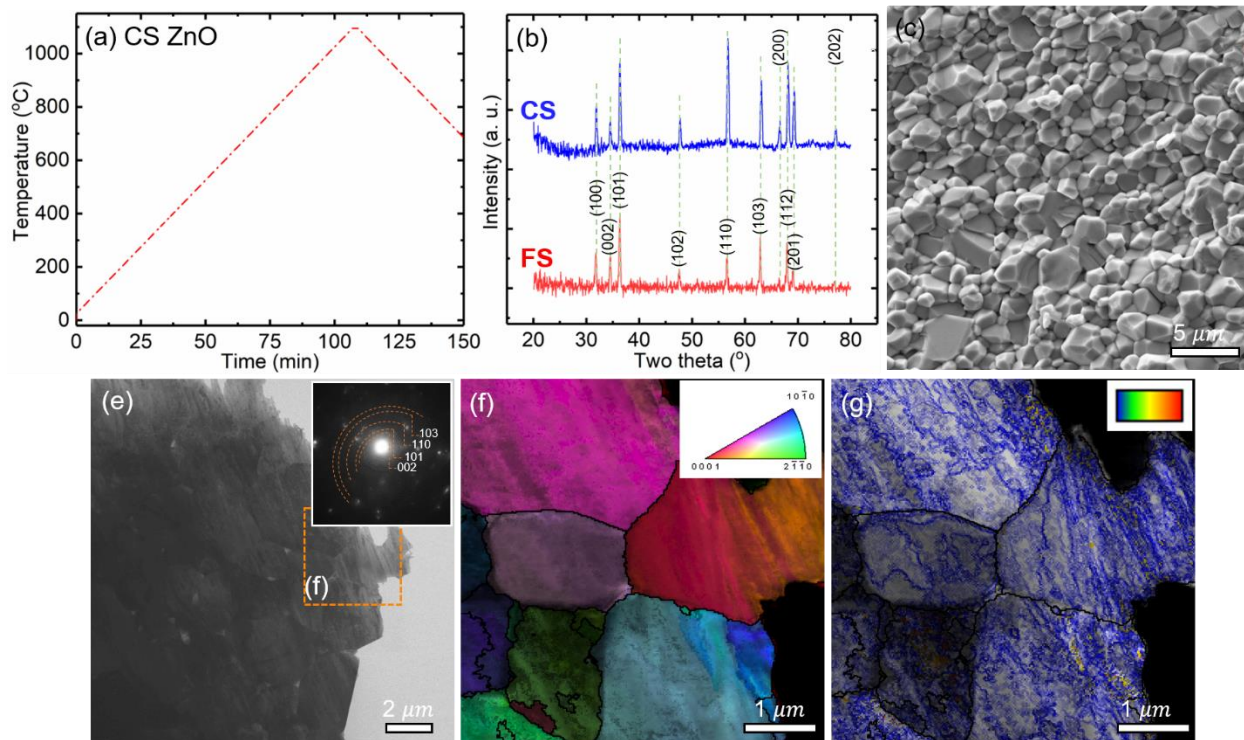


Figure 8.3. Sintering parameter and microstructure of the conventionally sintered ZnO. (a) Green body ZnO was heated at a heating rate of 10 °C/min and held at 1100°C for 1 min. (b) XRD pattern of the CS ZnO shows no considerable difference in texture and peak position when compared to the FS ZnO. (c-d) SEM and bright-field TEM micrographs of the CS ZnO show a larger grain size ($\sim 2 \mu\text{m}$) than the FS ZnO. (f-g) Inverse pole figure and GND map of CS ZnO showing average GND density of $1.10 \times 10^{12} \text{ m}^{-2}$.

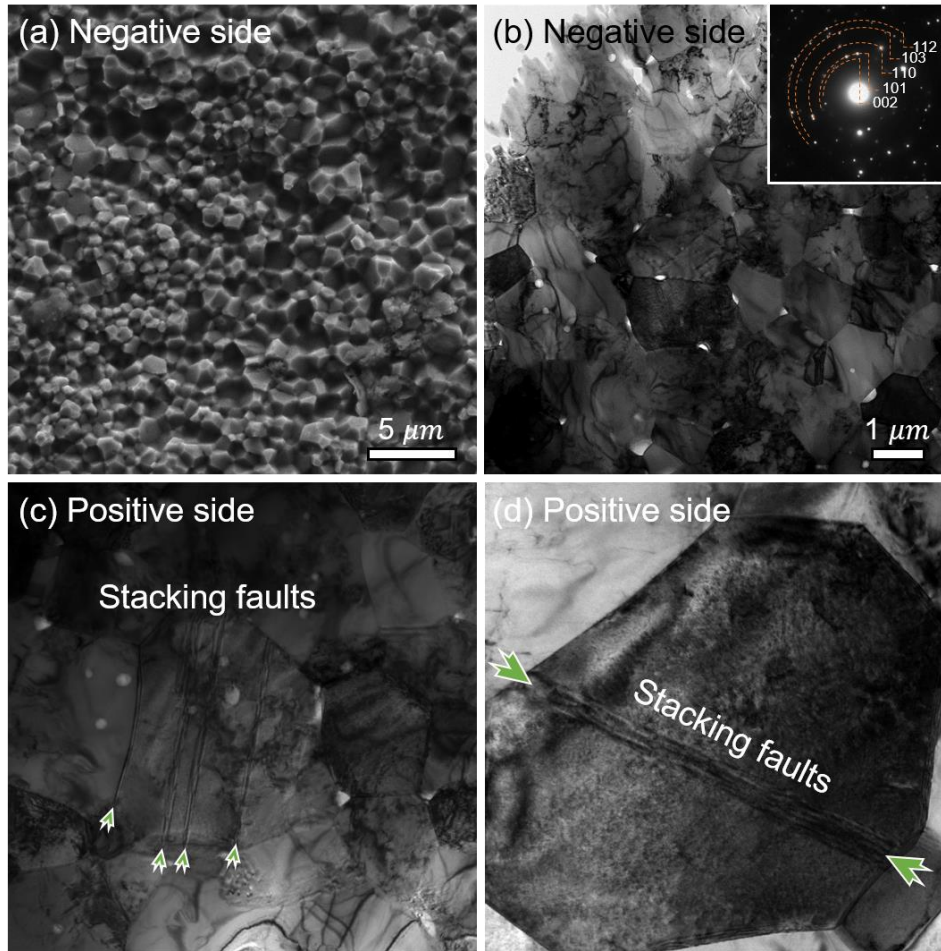


Figure 8.4. Microstructure of the FS ZnO at the negative and positive sides. (a) SEM image of the FS ZnO at the negative side. (b) BF TEM image of as-sintered ZnO grains at the negative side. (c-d) TEM micrographs of the FS ZnO at the positive side show stacking faults and grain size similar to the negative side.

8.3.1.2. Mechanical testing

Prior studies on mechanical properties of ZnO have focused primarily on one-dimensional nanostructures, such as nanorods, nanotubes, and nanowires, due to their potential to be building blocks of nanoelectronics or nanogenerators with high piezoelectric constants. Several theoretical and experimental studies have suggested that there exists a strong size effect in the elastic modulus, fracture strength and fracture strain along [0001] direction of ZnO nanostructures [291]. The elastic modulus of ZnO nanowires tends to be higher than that of the bulk counterpart (140 GPa) [292]. Several micromechanical testing coupled with atomic force microscopy (AFM), scanning electron microscopy (SEM), and transmission electron microscopy (TEM) also revealed that fracture strength and strain of ZnO nanowires increase up to ~ 14 GPa and $\sim 7\%$, comparable to

its theoretical values [293–295]. Studies on failure mechanisms of ZnO nanostructures suggested that the surface irregularities and vacancy clusters formed during the nanostructure fabrication process may become stress concentrators for crack nucleation [291]. There is no study on the effects of flash sintering on its mechanical properties. So, this subchapter shows preliminary work on the micromechanical behavior of flash-sintered (FS) ZnO by *in-situ* compression tests inside an SEM microscope at various test temperatures up to 600°C.

Fig. 8.5 shows SEM snapshots of compressed pillars at different strain levels at various temperatures with corresponding stress-strain curves for the FS (red and blue) and CS ZnO (black). For the pillars compressed at room temperature (Fig. 8.5a), the FS ZnO micropillars show flow stress of 1.19 GPa at a strain of 8%, higher than that for the CS ZnO micropillar (~ 0.90 GPa). The FS ZnO micropillars exhibit noticeable crack from a strain of 5% that propagates downward without a significant crack deflection. On the other hand, when tested at 200°C as shown in Fig. 8.5b, the flow stress of the FS ZnO is significantly degraded from 1.19 GPa to 0.71 GPa at a strain of 8% and it became comparable to that of the CS ZnO (0.60 GPa). The cracks were formed at the pillar top and deflected along grain boundaries. After fracture mode changed to intergranular cracking at 200°C, the strength degradation became inconsiderable. For instance, the flow stress of the pillars tested at 400°C was 0.60 GPa which is compared to the value for 200°C tests (0.71 GPa) as shown in Fig. 8.5c. However, a higher degree of intergranular cracking at the surface of the pillars was observed to the point where individual grains are revealed. When compressed at 600°C, the flow stress was 0.58 GPa, comparable to that for 400°C tests (0.60 GPa), but a higher density of intergranular cracks than 400°C test was observed. On the other hand, Fig. 8.6 shows SEM micrographs of the CS ZnO micropillars before and after compression tests at each temperature. For the CS ZnO pillar tested at room temperature, no high density of crack is observed similarly to the FS ZnO case. After compression test of the CS ZnO at 200°C, both intergranular crack and shear-offset formation are observed. Especially, the intergranular crack was concentrated near pillar top. Unlike the FS ZnO pillar tested at 400°C, The CS ZnO pillar shows intergranular fracture, transgranular fracture, and severe dilation of the pillar at pillar bottom (Fig. 8.6c). For the CS ZnO pillar tested at 600°C, fracture occurred along grain boundaries similar to FS ZnO.

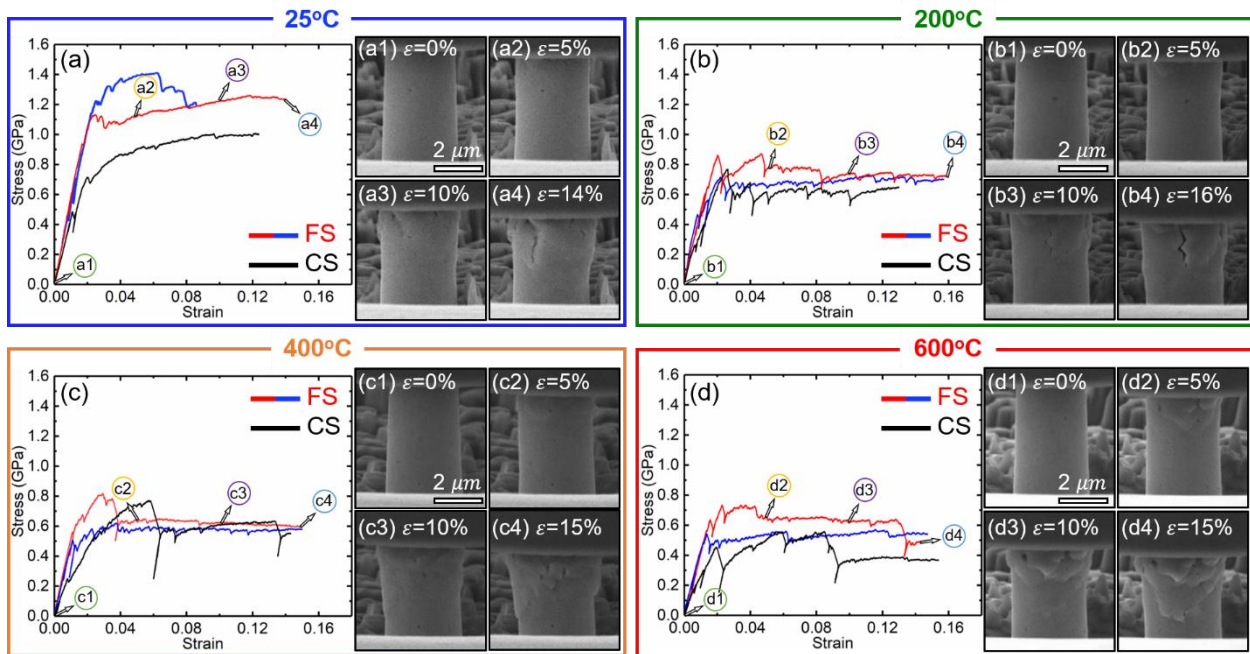


Figure 8.5. *In-situ* microcompression tests on flash-sintered (FS) and conventionally sintered (CS) ZnO at 25, 200, 400, and 600°C. (a) The FS ZnO micropillars have higher flow stress (1.2 GPa) than that of the CS ZnO micropillar at 25°C. SEM snapshots of the FS ZnO pillar reveal cracks generated at a strain of 10% and their downward propagation without a significant crack deflection. (b) The flow stress of the FS ZnO decreased to 0.7 GPa when tested at 200°C. The flow stress of the FS ZnO micropillars tested at 200°C is comparable to that of the CS ZnO micropillar. SEM snapshots show the crack deflections along grain boundaries. (c) The CS and FS pillars tested at 400°C show similar flow stress, ~ 0.6 GPa and the stress-strain curves of the FS pillars have much less serrations. Multiple small cracks along grain boundaries were observed. (d) At 600°C, significant serrations were observed on the flow stress-strain curve of the CS pillars. Whereas there are much less serrations on the flow stress of FS ZnO pillars, and intergranular cracks emerged when $\varepsilon = 5\%$. Crack density increased rapidly when $\varepsilon = 5\%$.

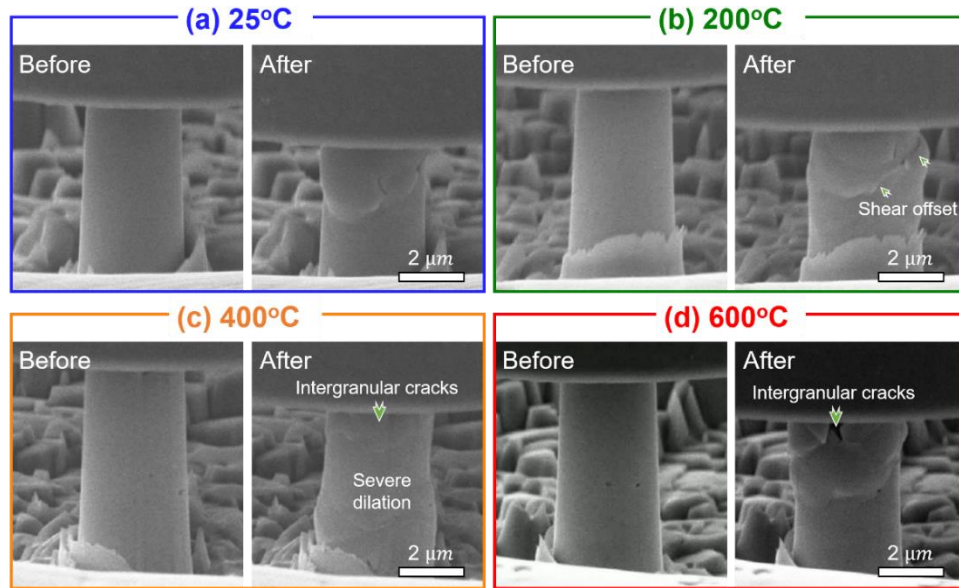


Figure 8.6. SEM micrographs of the CS ZnO micropillars before and after compression tests at room temperature to 600°C. (a) SEM image shows pillar morphology after compression at room temperature. No high density of crack was observed. (b) After compression at 200°C, both intergranular crack and shear-offset formation were observed. (c) The pillar tested at 400°C shows intergranular fracture near top and severe dilation of the pillar at bottom. (d) After 600°C test, intergranular fracture near top was observed.

8.3.1.3. Post-mortem TEM analysis

After the compression test of the FS ZnO at room temperature, microstructure and crystallographic information were obtained by TEM and ASTAR as shown in Fig. 8.7. The bright-field TEM image in Fig. 8.7a shows a significant density of defects with an obvious transgranular cracking in the upper half of the fractured pillar. On the other hand, grains in the lower half of the pillar remain relatively clear and intact. Fig. 8.7b shows a dark-field TEM image of grain in the upper half with $g(\bar{1}101)$ revealing a high density of dislocations near a grain boundary. High-resolution TEM study along $[1\bar{2}13]$ zone axis shows the existence of low angle grain boundary (9°) with a high density of dislocations, confirmed in FFT processed high-resolution TEM image (Fig. 8.7d). The inverse pole figure of the fractured pillar in Fig. 8.7e shows cracks penetrating grain interiors and no obvious change in texture. Kernel average misorientation (KAM) map in Fig. 8.7f shows a high degree of misorientation (bright green) near the fracture surface. GND map in Fig. 8.7e reveals a significant increase in average GND density to $1.97 \times 10^{12} m^{-2}$ after the compression test. A high density of GNDs (yellow and red) is decorated along the fracture surface and crack-tips indicated by orange arrows. For comparison, CS ZnO micropillar compressed at

room temperature was also investigated by TEM as shown in Fig. 8.8. Bright-field TEM (Fig. 8.8a) shows that a high density of defects with transgranular fracture exists in the upper half of the pillar. Dark-field TEM, high-resolution TEM, FFT processed TEM micrographs (Fig. 8.8b-f) show that the existence of abundant dislocations. High degree of misorientation and curved grain boundaries were found in grains near fracture surface and crack-tip as shown in Fig. 8.8g. In addition, high density of GND was decorated near crack-tip indicated by a green arrow and average GND density was calculated to be $1.24 \times 10^{12} m^{-2}$.

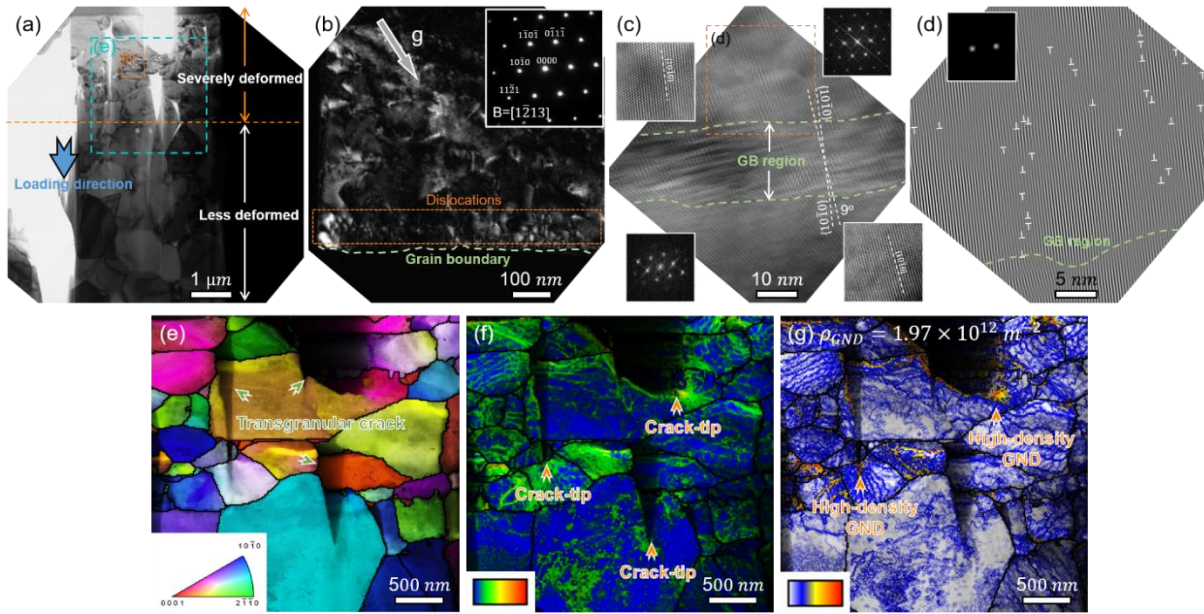


Figure 8.7. Microstructure of the FS ZnO micropillar compressed at room temperature (to a strain of 14%). (a) Bright-field (BF) TEM image shows the upper half of the pillar exhibits a high density of defects and transgranular cracks. The lower half of the pillar remains relatively intact. (b) Dark-field (DF) TEM image of a grain in the upper region of the pillar shows a high density of dislocations near a grain boundary. (c) High resolution TEM micrograph along the $[1\bar{2}13]$ zone axis shows the low angle grain boundary (9°) with a high density of dislocations. (d) Processed high resolution TEM image shows the existence of abundant dislocations along $(10\bar{1}0)$ planes near the grain boundary. (e) Inverse pole figure of the fractured pillar confirms the transgranular cracking and polycrystalline grains. (f) Kernel average misorientation (KAM) map shows high degree of misorientation within grains near the fracture surface. (g) GND map shows the average GND density of $1.97 \times 10^{12} m^{-2}$ after the compression test. A high density of GNDs is observed near the fracture surface, crack tips, and grain boundaries.

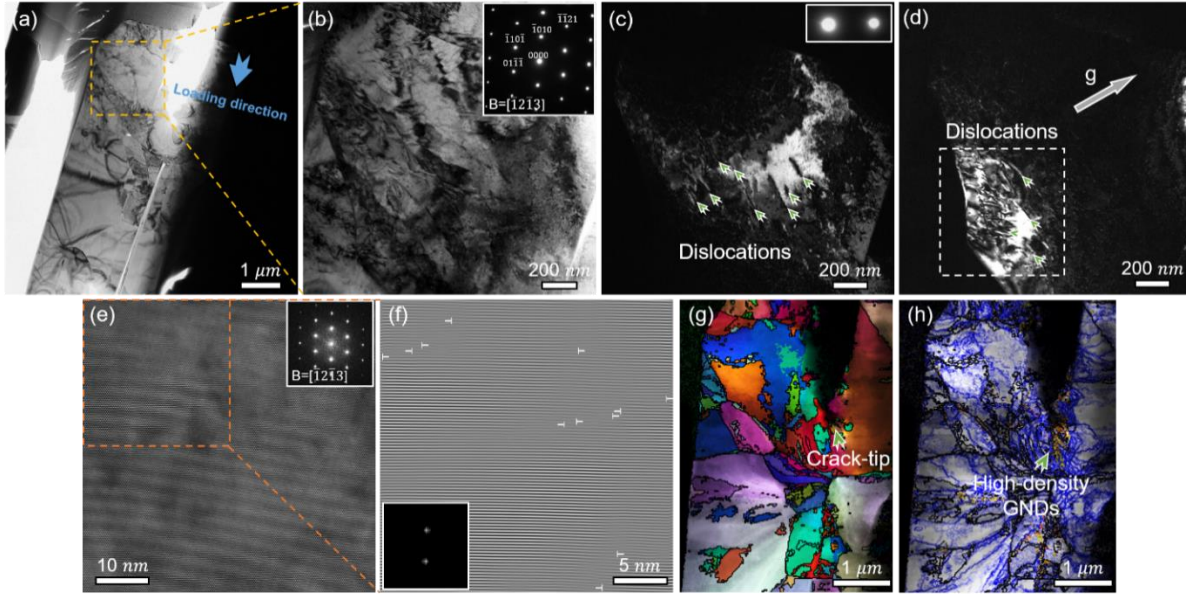


Figure 8.8. TEM post-analyses of the CS ZnO micropillar compressed at room temperature. (a) BF TEM micrograph shows an obvious transgranular crack. (b) A grain near the pillar top has a high density of defects. (c) Weak-beam DF TEM image reveals that the high-density dislocations. (d) DF TEM image also shows dislocations near a grain boundary. (e-f) High resolution and processed TEM micrographs confirm the presence of dislocations. (g-h) Inverse pole figure and GND map of CS ZnO micropillar showing high density of GND near a crack-tip. Average GND density is determined to be $1.24 \times 10^{12} m^{-2}$.

The FS ZnO micropillar tested at 400°C also exhibits a high density of defects in the dilated upper half as seen in Fig. 8.9a. Grains remain equiaxed and local grain separations are occasionally found and indicated by green arrows. Fig. 8.9b shows a high density of dislocations in the severely deformed region taken by dark-field TEM image with $g(\bar{1}100)$. A high density of dislocations was confirmed by high resolution and FFT processed TEM micrographs along a zone axis of [0001] in Fig. 8.9c and d. The inverse pole figure in Fig. 8.9e shows no significant changes in grain shape and texture. KAM map shows that a significant degree of misorientation within grains highlighted in bright green occurs in the upper half of the pillar (Fig. 8.9e). Fig. 8.9f shows that a high density of GND is decorated in the upper half. The average GND density of the pillar was calculated to be $1.65 \times 10^{12} m^{-2}$.

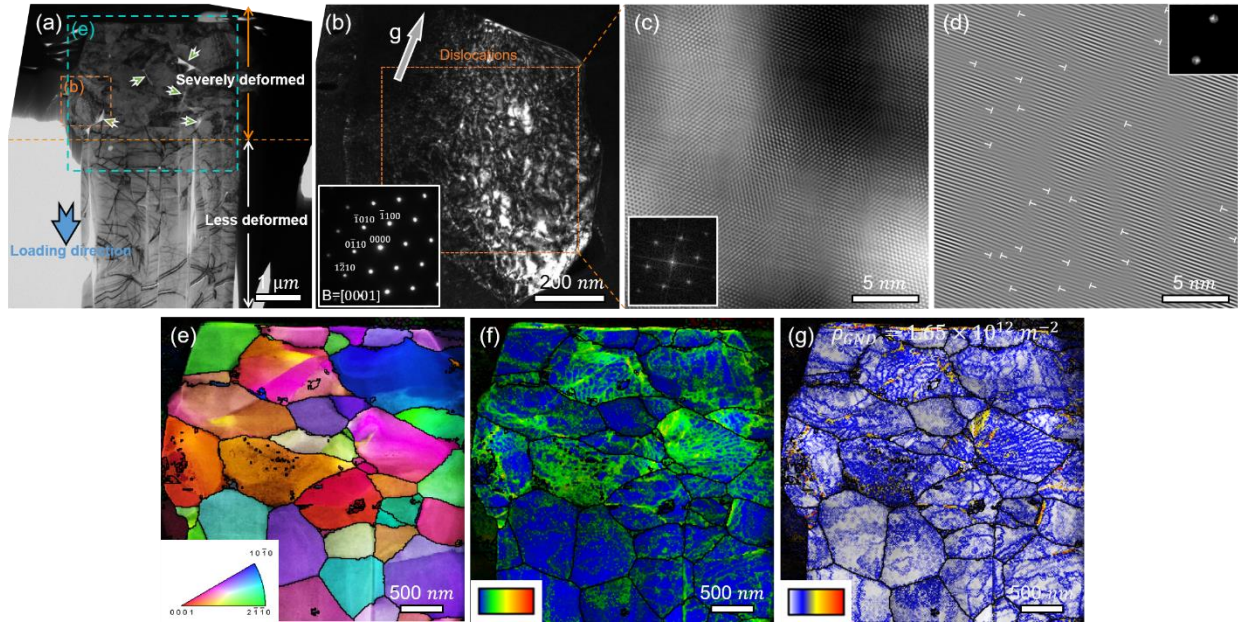


Figure 8.9. TEM analyses of the FS ZnO micropillar compressed at 400°C. (a) BF TEM image shows prominent dilation of the upper half of the tested pillar. Local grain separations are indicated by green arrows. (b) DF TEM image of a grain in the upper deformed region shows a high density of dislocations. (c-d) High resolution and FFT processed TEM micrographs along the [0001] zone axis show high-density dislocations. (e) Inverse pole figure of the compressed pillar shows insignificant changes in the grain shape after the compression test. (f) KAM map shows a high degree of misorientation within grains in the upper half of the deformed pillar. (g) The average GND density of the pillar is $1.65 \times 10^{12} m^{-2}$ when tested at 400°C.

A post-mortem TEM micrograph of the FS ZnO micropillar tested at 600°C in Fig. 8.10a shows the significant dilation at the pillar top, but no local grain separation is observed. Fig. 8.10b and c show bright-field TEM micrographs of several grains near pillar top retaining dislocation network and dislocation arrays. Also, stacking faults were occasionally found (Fig. 8.10d). The Inverse pole figure in Fig. 8.10e shows the presence of elongated grains indicated by green arrows and slightly improved texture. KAM map in Fig. 8.10f shows that misoriented grains are present near the pillar top. GND map reveals that there exist no regions with a high density of dislocations (Fig. 6e) and the average GND density was determined to be $1.16 \times 10^{12} m^{-2}$ which is comparable to that of as-sintered ZnO. Fig. 8.11 shows post-mortem TEM micrographs of the CS ZnO micropillar tested at 600°C. Similar to the FS ZnO micropillars tested at 600°C, CS ZnO micropillar also shows the dilated pillar top to accommodate 16% strain without cracking (Fig. 8.11a). A high density of dislocations and cellular structure were observed by bright-field TEM and scanning TEM (STEM) micrographs, respectively, near a top portion of the compressed pillar. Inverse pole figure of the

deformed pillar reveals that high density of nanograins exists near pillar top. The average GND density is determined to be $1.08 \times 10^{12} m^{-2}$, comparable to that of CS ZnO before deformation. Fig. 8.12a shows critical strain at which the first crack nucleates and GND density as a function of test temperature. As test temperature increases, both critical strain and GND density monotonically decrease. GND density of the pillar tested at 600°C becomes comparable to the reference line (orange) for that of as-sintered ZnO. Fig. 8.12b compares flow stress collected at a strain of 8% for FS and CS ZnO at each test temperature. Flow stress at room temperature shows a considerable difference between the two samples, but the difference becomes insignificant with increasing test temperature. Also, there exists significant strength degradation when the test temperature increases to 200°C. Once the test temperature is above after 200°C, no considerable degradation is observed.

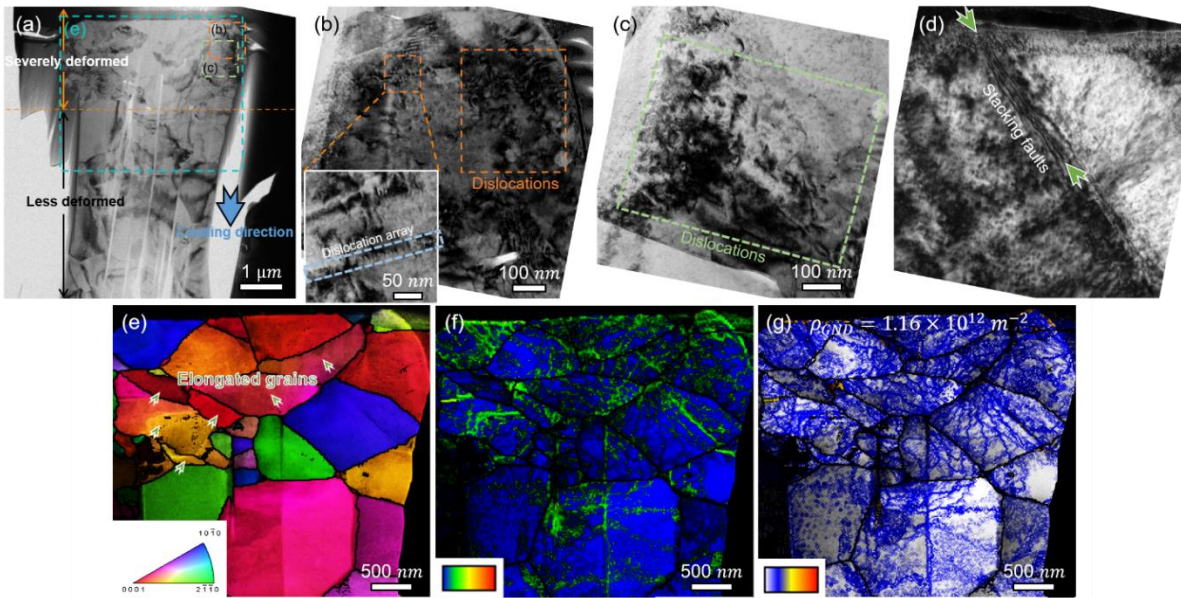


Figure 8.10. Microstructure of the FS ZnO micropillar deformed at 600°C. (a) TEM micrograph shows obvious dilation of the pillar top. No significant grain separation was observed. (b-d) TEM micrographs near the pillar top show dislocation networks, dislocation arrays, and stacking faults. (e) Inverse pole figure reveals elongated grains (indicated by green arrows) at the upper half of the pillar. (f) KAM map shows misorientation within the grains localized near the pillar top. (g) Average GND density of the deformed pillar is $1.16 \times 10^{12} m^{-2}$, comparable to that of as-sintered ZnO.

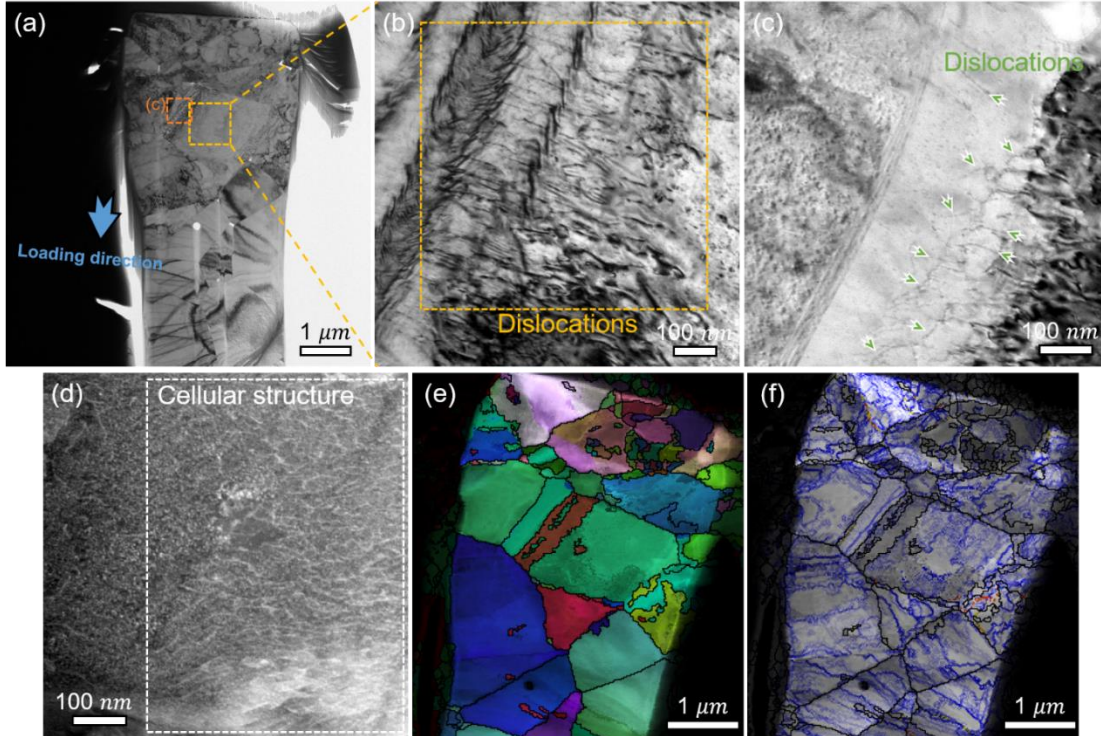


Figure 8.11. TEM post-analyses of the CS ZnO micropillar compressed at 600°C. (a) BF TEM micrograph of the tested pillar shows the overall pillar morphology and obvious dilation at the pillar top. (b-d) A high density of dislocations was observed by BF TEM and STEM micrographs near a top portion of the compressed pillar. (e-f) Inverse pole figure and GND map of the CS micropillar showing the presence of nanograins near pillar top. Average GND density is calculated to be $1.08 \times 10^{12} \text{ m}^{-2}$.

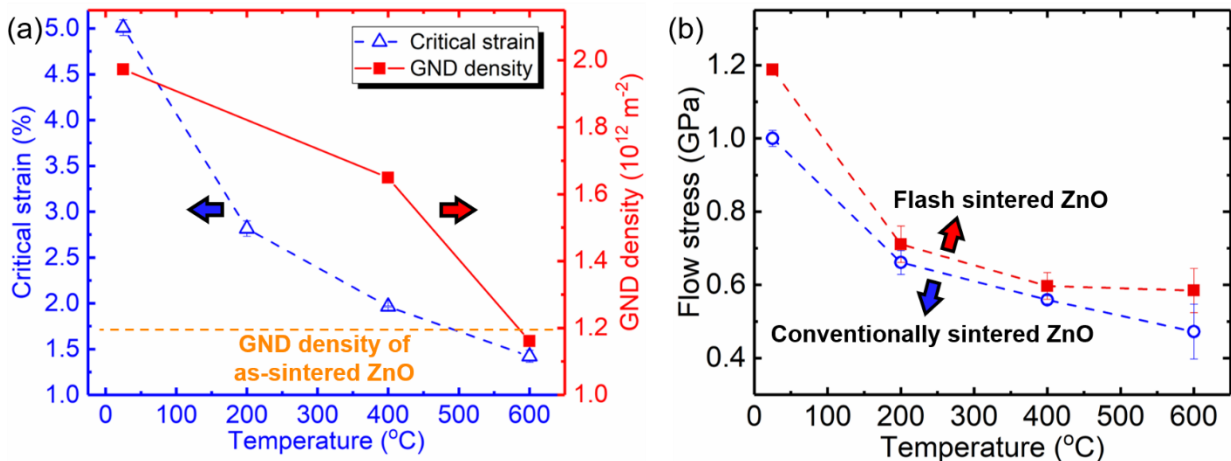


Figure 8.12. Variations of critical strain, GND density, and flow stress with test temperatures. (a) The critical strain to detect cracks (blue triangle) and GND density (red square) decrease as test temperature increases. (b) Flow stress (at a strain of 8%) for the flash-sintered and conventional ZnO decreases with increasing test temperature. After 200°C, strength reduction is insignificant for both types of ZnO specimens.

REFERENCES

- [1] R.H.J. Hannink, P.M. Kelly, B.C. Muddle, "Transformation Toughening in Zirconia-Containing Ceramics," *J. Am. Ceram. Soc.* **83** (2000) 461–487.
- [2] R.C. Garvie, R.H. Hannink, R.T. Pascoe, "Ceramic steel?," *Nature*. **258** (1975) 703–704.
- [3] D.L. Porter, A.H. Heuer, "Mechanisms of Toughening Partially Stabilized Zirconia (PSZ)," *J. Am. Ceram. Soc.* **60** (1977) 183–184.
- [4] R.C. Garvie, P.S. Nicholson, "Structure and Thermomechanical Properties of Partially Stabilized Zirconia in the CaO-ZrO₂ System," *J. Am. Ceram. Soc.* **55** (1972) 152–157.
- [5] J. Goff, W. Hayes, S. Hull, M. Hutchings, K. Clausen, "Defect structure of yttria-stabilized zirconia and its influence on the ionic conductivity at elevated temperatures," *Phys. Rev. B*. **59** (1999) 14202–14219.
- [6] S. Fabris, A.T. Paxton, M.W. Finnis, "A stabilization mechanism of zirconia based on oxygen vacancies only," *Acta Mater.* **50** (2002) 5171–5178.
- [7] J.R. Kelly, I. Denry, "Stabilized zirconia as a structural ceramic: An overview," *Dent. Mater.* **24** (2008) 289–298.
- [8] R.O. Ritchie, "The conflicts between strength and toughness," *Nat. Mater.* **10** (2011) 817–822.
- [9] P.E. REYES-MOREL, I. CHEN, "Transformation Plasticity of CeO₂-Stabilized Tetragonal Zirconia Polycrystals: I, Stress Assistance and Autocatalysis," *J. Am. Ceram. Soc.* **71** (1988) 343–353.
- [10] G. Witz, V. Shklover, W. Steurer, S. Bachegowda, H.P. Bossmann, "Phase evolution in yttria-stabilized zirconia thermal barrier coatings studied by rietveld refinement of X-ray powder diffraction patterns," *J. Am. Ceram. Soc.* **90** (2007) 2935–2940.
- [11] A.G. Evans, A.H. Heuer, "REVIEW- Transformation Toughening in Ceramics: Martensitic Transformations in Crack-Tip Stress Fields," *J. Am. Ceram. Soc.* **63** (1980) 241–248.
- [12] N.P. Padture, M. Gell, E.H. Jordan, "Thermal Barrier Coatings for Gas-Turbine Engine Applications," *Science*. **296** (2012) 280–285.
- [13] S.C. Singhal, "Solid oxide fuel cells for stationary, mobile, and military applications," *Solid State Ionics*. **152–153** (2002) 405–410.

- [14] A. Lai, Z. Du, C.L. Gan, C.A. Schuh, "Shape Memory and Superelastic Ceramics at Small Scales," *Science*. **341** (2013) 1505–1508.
- [15] X. Ren, W. Pan, "Mechanical properties of high-temperature-degraded yttria-stabilized zirconia," *Acta Mater.* **69** (2014) 397–406.
- [16] K. Matsui, H. Horikoshi, N. Ohmichi, M. Ohgai, H. Yoshida, Y. Ikuhara, "Cubic-Formation and Grain-Growth Mechanisms in Tetragonal Zirconia Polycrystal," *J. Am. Ceram. Soc.* **86** (2003) 1401–1408.
- [17] P.F. Becher, M. V. Swain, "Grain-Size-Dependent Transformation Behavior in Polycrystalline Tetragonal Zirconia," *J. Am. Ceram. Soc.* **75** (1992) 493–502.
- [18] F.F. Lange, "Transformation toughening Part 1 Size effects associated with the thermodynamics of constrained transformations," *J. Mater. Sci.* **17** (1982) 225–234.
- [19] D.J. Kim, "Effect of Ta₂O₅, Nb₂O₅, and HfO₂ Alloying on the Transformability of Y₂O₃-Stabilized Tetragonal ZrO₂," *J. Am. Ceram. Soc.* **73** (1990) 115–120.
- [20] A. Bravo-Leon, Y. Morikawa, M. Kawahara, M.J. Mayo, "Fracture toughness of nanocrystalline tetragonal zirconia with low yttria content," *Acta Mater.* **50** (2002) 4555–4562.
- [21] D.L. Porter, A.H. Heuer, "Microstructural Development in MgO-Partially Stabilized Zirconia (Mg-PSZ)," *J. Am. Ceram. Soc.* **62** (1978) 298–305.
- [22] R.R. Hughan, R.H.J. Hannink, "Precipitation During Controlled Cooling of Magnesia-Partially-Stabilized-Zirconia," *J. Am. Ceram. Soc.* **69** (1986) 556–563.
- [23] G.S.A.M. Theunissen, J.S. Bouma, A.J.A. Winnubst, A.J. Burggraaf, "Mechanical properties of ultra-fine grained zirconia ceramics," *J. Mater. Sci.* **27** (1992) 4429–4438.
- [24] D. Kim, T.-Y. Tien, "Phase Stability and Physical Properties of Cubic and Tetragonal ZrO₂ in the System ZrO₂-Y₂O₃-Ta₂O₅," *J. Am. Ceram. Soc.* **74** (1991) 3061–3065.
- [25] B.C. Mercer, J.R. W, D.R. Clarke, A.G. Evans, "On a ferroelastic mechanism governing the toughness of metastable tetragonal-prime (t') yttria-stabilized zirconia," *Proc. R. Soc. A Math. Phys. Eng. Sci.* **463** (2007) 1393–1408.
- [26] T.A. Schaedler, R.M. Leckie, S. Krämer, A.G. Evans, C.G. Levi, "Toughening of nontransformable t'-YSZ by addition of titania," *J. Am. Ceram. Soc.* **90** (2007) 3896–3901.
- [27] A. V. Virkar, "Role of ferroelasticity in toughening of zirconia ceramics," *Key Eng. Mater.* (1998) 183–210.

- [28] D. Baither, M. Bartsch, B. Baufeld, A. Tikhonovsky, A. Foitzik, M. Rühle, U. Messerschmidt, "Ferroelastic and Plastic Deformation of t'-Zirconia Single Crystals," *J. Am. Ceram. Soc.* **84** (2001) 1755–1762.
- [29] B. -S Li, J. -S Cherng, K.J. Bowman, I. -W Chen, "Domain Switching as a Toughening Mechanism in Tetragonal Zirconia," *J. Am. Ceram. Soc.* **71** (1988) C-362-C-364.
- [30] T.A. Schaedler, O. Fabrichnaya, C.G. Levi, "Phase equilibria in the TiO₂-YO_{1.5}-ZrO₂ system," *J. Eur. Ceram. Soc.* **28** (2008) 2509–2520.
- [31] D.P.H. Hasselman, L.F. Johnson, L.D. Bentsen, R. Syed, H.L.I.M. Lee, M. V Swain, M. Science, "Thermal Diffusivity and Conductivity of Dense Polycrystalline ZrO₂ Ceramics : A Survey," **66** (1987) 799–806.
- [32] P.G. Klemens, M. Gell, "Thermal conductivity of thermal barrier coatings," *Mater. Sci. Eng. A.* **245** (1998) 143–149.
- [33] D.R. Clarke, "Materials selection guidelines for low thermal conductivity thermal barrier coatings," *Surf. Coat. Technol.* **163** (2003) 67–74.
- [34] R. Mévrel, J.C. Laizet, A. Azzopardi, B. Leclercq, M. Poulain, O. Lavigne, D. Demange, "Thermal diffusivity and conductivity of Zr_{1-x}Y_xO_{2-x/2} (x = 0, 0.084 and 0.179) single crystals," *J. Eur. Ceram. Soc.* **24** (2004) 3081–3089.
- [35] K. Tsukuma, T. Takahata, "Mechanical Property and Microstructure of TZP and TZP_Al₂O₃ Composites," *Mater. Res. Soc. Symp. Proceeding.* **78** (1987) 123–135.
- [36] M. V. Swain, "Inelastic deformation of Mg-PSZ and its significance for strength-toughness relationship of zirconia toughened ceramics," *Acta Metall.* **33** (1985) 2083–2091.
- [37] J. Lankford, "Plastic Deformation of Partially Stabilized Zirconia," *J. Am. Ceram. Soc.* **66** (1983) c212–c213.
- [38] P.C. Maxwell, A. Goldberg, J.C. Shyne, "Influence of Martensite Formed During Deformation on the Mechanical Behavior of Fe-Ni-C Alloys," *Met. Trans.* **5** (1974) 1319–1324.
- [39] J. Lankford, R.A. Page, "Deformation mechanisms in yttria-stabilized zirconia," *J. Mater. Sci.* **23** (1988) 4144–4156.
- [40] M.V. Swain, "Shape memory behaviour in partially stabilized zirconia ceramics," *Nature.* **322** (1986) 234–236.

- [41] Z. Du, X.M. Zeng, Q. Liu, C.A. Schuh, C.L. Gan, “Superelasticity in micro-scale shape memory ceramic particles,” *Acta Mater.* **123** (2017) 255–263.
- [42] X.M. Zeng, Z. Du, C.A. Schuh, N. Tamura, C.L. Gan, “Microstructure, crystallization and shape memory behavior of titania and yttria co-doped zirconia,” *J. Eur. Ceram. Soc.* **36** (2016) 1277–1283.
- [43] E. Camposilvan, M. Anglada, “Size and plasticity effects in zirconia micropillars compression,” *Acta Mater.* **103** (2016) 882–892.
- [44] I. -W Chen, L.A. Xue, “Development of Superplastic Structural Ceramics,” *J. Am. Ceram. Soc.* **73** (1990) 2585–2609.
- [45] Z. Du, X.M. Zeng, Q. Liu, A. Lai, S. Amini, A. Miserez, C.A. Schuh, C.L. Gan, “Size effects and shape memory properties in ZrO₂ ceramic micro- and nano-pillars,” *Scr. Mater.* **101** (2015) 40–43.
- [46] X.M. Zeng, A. Lai, C.L. Gan, C.A. Schuh, “Crystal orientation dependence of the stress-induced martensitic transformation in zirconia-based shape memory ceramics,” *Acta Mater.* **116** (2016) 124–135.
- [47] X.M. Zeng, Z. Du, N. Tamura, Q. Liu, C.A. Schuh, C.L. Gan, “In-situ studies on martensitic transformation and high-temperature shape memory in small volume zirconia,” *Acta Mater.* **134** (2017) 257–266.
- [48] J.M. San Juan, M.L. Nó, C.A. Schuh, “Superelasticity and shape memory in micro- and nanometer-scale pillars,” *Adv. Mater.* **20** (2008) 272–278.
- [49] S. Korte, J.S. Barnard, R.J. Stearn, W.J. Clegg, “Deformation of silicon - Insights from microcompression testing at 25-500 C,” *Int. J. Plast.* **27** (2011) 1853–1866.
- [50] S. Korte, W.J. Clegg, “Micropillar compression of ceramics at elevated temperatures,” *Scr. Mater.* **60** (2009) 807–810.
- [51] E. Camposilvan, M. Anglada, “Micropillar compression inside zirconia degraded layer,” *J. Eur. Ceram. Soc.* **35** (2015) 4051–4058.
- [52] G.N. Morscher, P. Pirouz, A.H. Heuer, “Temperature Dependence of Hardness in Yttria-Stabilized Zirconia Single Crystals,” *J. Am. Ceram. Soc.* **74** (1991) 491–500.
- [53] Y. Gaillard, M. Anglada, E. Jiménez-Piqué, “Nanoindentation of yttria-doped zirconia: Effect of crystallographic structure on deformation mechanisms,” *J. Mater. Res.* **24** (2009) 719–727.

- [54] N. Zhang, M. Asle Zaeem, “Competing mechanisms between dislocation and phase transformation in plastic deformation of single crystalline yttria-stabilized tetragonal zirconia nanopillars,” *Acta Mater.* **120** (2016) 337–347.
- [55] Y. Sakka, T.S. Suzuki, T. Matsumoto, K. Morita, K. Hiraga, Y. Moriyoshi, “Effect of titania and magnesia addition to 3 mol% yttria doped tetragonal zirconia on some diffusion related phenomena,” *Solid State Ionics.* **172** (2004) 499–503.
- [56] F.R. Chien, F.J. Uvic, V. Prakash, A.H. Heuer, “Stress-induced martensitic transformation and ferroelastic deformation adjacent microhardness indents in tetragonal zirconia single crystals,” *Acta Mater.* **46** (1998) 2151–2171.
- [57] P.E. REYES-MOREL, J. -S CHERNG, I. -W CHEN, “Transformation Plasticity of CeO₂-Stabilized Tetragonal Zirconia Polycrystals: II, Pseudoelasticity and Shape Memory Effect,” *J. Am. Ceram. Soc.* **71** (1988) 648–657.
- [58] M. Cologna, B. Rashkova, R. Raj, “Flash sintering of nanograin zirconia in <5 s at 850°C,” *J. Am. Ceram. Soc.* **93** (2010) 3556–3559.
- [59] H. Charalambous, S.K. Jha, R.T. Lay, A. Cabales, J. Okasinski, T. Tsakalagos, “Investigation of temperature approximation methods during flash sintering of ZnO,” *Ceram. Int.* (2018) 1–8.
- [60] H.. Gao, T.J.. Asel, J.W.. Cox, Y.. Zhang, J.. Luo, L.J. Brillson, “Native point defect formation in flash sintered ZnO studied by depth-resolved cathodoluminescence spectroscopy,” *J. Appl. Phys.* **120** (2016) 1–7.
- [61] A. Karakuscu, M. Cologna, D. Yarotski, J. Won, J.S.C. Francis, R. Raj, B.P. Uberuaga, “Defect Structure of Flash-Sintered Strontium Titanate,” *J. Am. Ceram. Soc.* **95** (2012) 2531–2536.
- [62] W. Rheinheimer, X. Phuah, H. Wang, F. Lemke, M.J. Hoffmann, H. Wang, “The role of point defects and defect gradients in flash sintering of perovskite oxides,” *Acta Mater.* **165** (2019) 398–408.
- [63] S.K. Jha, R. Raj, “The effect of electric field on sintering and electrical conductivity of Titania,” *J. Am. Ceram. Soc.* **97** (2014) 527–534.
- [64] L.A.. Perez-maqueda, E.. Gil-Gonzalez, A.. Perejon, J.M.. Lebrun, P.E.. Sanchez-Jimenez, R.. Raj, “Flash sintering of highly insulating nanostructured phase-pure BiFeO₃,” *J. Am. Ceram. Soc.* **100** (2017) 3365–3369.

- [65] X. Su, G. Bai, J. Zhang, J. Zhou, Y. Jia, "Preparation and flash sintering of MgTiO₃ nanopowders obtained by the polyacrylamide gel method," *Appl. Surf. Sci.* **442** (2018) 12–19.
- [66] M. Biesuz, V.M. Sglavo, "Liquid phase flash sintering in magnesia silicate glass-containing alumina," *J. Eur. Ceram. Soc.* **37** (2017) 705–713.
- [67] M. Biesuz, V.M. Sglavo, "Flash sintering of alumina: Effect of different operating conditions on densification," *J. Eur. Ceram. Soc.* **36** (2016) 2535–2542.
- [68] D. Kok, S. Jha, R.. Raj, M.. Mecartney, "Flash sintering of a three-phase alumina, spinel, and yttria-stabilized zirconia composite," *J. Am. Ceram. Soc.* **100** (2017) 3262–3268.
- [69] M. Biesuz, V.M. Sglavo, "Flash sintering of ceramics," *J. Eur. Ceram. Soc.* **39** (2019) 115–143.
- [70] R. Raj, "Analysis of the Power Density at the Onset of Flash Sintering," *J. Am. Ceram. Soc.* **99** (2016) 3226–3232.
- [71] R.I. Todd, R.S. Bonilla, T. Sneddon, P.R. Wilshaw, "Electrical characteristics of flash sintering : thermal runaway of Joule heating," *J. Eur. Ceram. Soc.* **35** (2015) 1865–1877.
- [72] Y. Zhang, J. Jung, J. Luo, "Thermal runaway, flash sintering and asymmetrical microstructural development of ZnO and ZnO – Bi₂O₃ under direct currents," *Acta Mater.* **94** (2015) 87–100.
- [73] S.K. Jha, X.L. Phuah, J. Luo, C.P. Grigoropoulos, H. Wang, E. García, B. Reeja-Jayan, "The effects of external fields in ceramic sintering," *J. Am. Ceram. Soc.* **102** (2019) 5–31.
- [74] S. Grasso, Y. Sakka, N. Rendtorff, C. Hu, G. Maizza, H. Borodianska, O. Vasylykiv, "Modeling of the temperature distribution of flash sintered zirconia," *J. Ceram. Soc. Japan.* **119** (2011) 144–146.
- [75] M. Cologna, J.S.C. Francis, R. Raj, "Field assisted and flash sintering of alumina and its relationship to conductivity and MgO-doping," *J. Eur. Ceram. Soc.* **31** (2011) 2827–2837.
- [76] J.S.C. Francis, M. Cologna, D. Montinaro, R. Raj, "Flash sintering of anode-electrolyte multilayers for SOFC applications," *J. Am. Ceram. Soc.* **96** (2013) 1352–1354.
- [77] J.S.C. Francis, R. Raj, "Flash-Sinterforging of Nanograin Zirconia: Field Assisted Sintering and Superplasticity," *J. Am. Ceram. Soc.* **95** (2012) 138–146.

- [78] J.G.P. Silva, J. Lebrun, H.A. Al-Qureshi, R. Janssen, R. Raj, "Temperature Distributions During Flash Sintering of 8% Yttria-Stabilized Zirconia," *J. Am. Ceram. Soc.* **98** (2015) 3525–3528.
- [79] K. Terauds, J.M. Lebrun, H.H. Lee, T.Y. Jeon, S.H. Lee, J.H. Je, R. Raj, "Electroluminescence and the measurement of temperature during Stage III of flash sintering experiments," *J. Eur. Ceram. Soc.* **35** (2015) 3195–3199.
- [80] S.K. Jha, K. Terauds, J. Lebrun, R. Raj, "Beyond flash sintering in 3 mol % yttria stabilized zirconia," *J. Ceram. Soc. Japan.* **124** (2016) 283–288.
- [81] R. Chaim, C. Estournès, "On thermal runaway and local endothermic/exothermic reactions during flash sintering of ceramic nanoparticles," *J. Mater. Sci.* **53** (2018) 6378–6389.
- [82] G. Corapcioglu, M. Ali Gulgun, K. Kisslinger, S. Sturm, S.K. Jha, R. Raj, "Microstructure and microchemistry of flash sintered $K_{0.5}Na_{0.5}NbO_3$," *J. Ceram. Soc. Japan.* **124** (2016) 321–328.
- [83] J. Narayan, "A new mechanism for field-assisted processing and flash sintering of materials," *Scr. Mater.* **69** (2013) 107–111.
- [84] H. Yoshida, A. Uehashi, T. Tokunaga, K. Sasaki, T. Yamamoto, "Formation of grain boundary second phase in $BaTiO_3$ polycrystal under a high DC electric field at elevated temperatures," *J. Ceram. Soc. Japan.* **124** (2016) 388–392.
- [85] X. Guo, "Physical origin of the intrinsic grain-boundary resistivity of stabilized-zirconia: Role of the space-charge layers," *Solid State Ionics.* **81** (1995) 235–242.
- [86] R. Chaim, G. Chevallier, A. Weibel, C. Estournès, "Flash sintering of dielectric nanoparticles as a percolation phenomenon through a softened film," *J. Appl. Phys.* **121** (2017) 1–6.
- [87] S. Ghosh, A.H. Chokshi, P. Lee, R. Raj, "A huge effect of weak dc electrical fields on grain growth in zirconia," *J. Am. Ceram. Soc.* **92** (2009) 1856–1859.
- [88] N. Morisaki, H. Yoshida, T. Tokunaga, K. Sasaki, T. Yamamoto, "Consolidation of undoped, monoclinic zirconia polycrystals by flash sintering," *J. Am. Ceram. Soc.* **100** (2017) 3851–3857.
- [89] A. Uehashi, K. Sasaki, T. Tokunaga, H. Yoshida, T. Yamamoto, "Formation of second phase at grain boundary of flash-sintered $BaTiO_3$," *Microscopy.* **63** (2014) i19–i20.

- [90] M. Biesuz, L. Pinter, T. Saunders, M. Reece, J. Binner, V.M.S. Id, S. Grasso, “Investigation of Electrochemical , Optical and Thermal Effects during Flash Sintering of 8YSZ,” *Materials (Basel)*. **11** (2018) 1–15.
- [91] J. Janek, C. Korte, “Electrochemical blackening of yttria-stabilized zirconia - Morphological instability of the moving reaction front,” *Solid State Ionics*. **116** (1999) 181–195.
- [92] M. Yoshida, S. Falco, R.I. Todd, “Measurement and modelling of electrical resistivity by four-terminal method during flash sintering of 3YSZ,” *J. Ceram. Soc. Japan*. **126** (2018) 579–590.
- [93] W. Qin, H. Majidi, J. Yun, K. Benthem, “Electrode Effects on Microstructure Formation During Flash Sintering of Yttrium-Stabilized Zirconia,” *J. Am. Ceram. Soc.* **99** (2016) 2253–2259.
- [94] C. Bonola, P. Camagni, P. Chiodelli, G. Samoggia, “Study of Defects Introduced by Electroreduction in YSZ,” *Radiat. Eff. Defects Solids*. **119–121** (1991) 457–462.
- [95] S.W. Kim, S.G. Kim, J.J. I., S.J.L. Kang, I.W. Chen, “Enhanced Grain Boundary Mobility in Yttria-Stabilized Cubic Zirconia under an Electric Current,” *J. Am. Ceram. Soc.* **94** (2011) 4231–4238.
- [96] Z.A. Munir, U. Anselmi-Tamburini, M. Ohyanagi, “The effect of electric field and pressure on the synthesis and consolidation of materials: A review of the spark plasma sintering method,” *J. Mater. Sci.* **41** (2006) 763–777.
- [97] E.A. Olevsky, S. Kandukuri, L. Froyen, “Consolidation enhancement in spark-plasma sintering: Impact of high heating rates,” *J. Appl. Phys.* **102** (2007) 1–12.
- [98] R. Orrù, J. Woolman, G. Cao, Z.A. Munir, “Synthesis of dense nanometric MoSi₂ through mechanical and field activation,” *J. Mater. Res.* **16** (2001) 1439–1448.
- [99] F. Bernard, F. Charlot, E. Gaffet, Z.A. Munir, “One-Step Synthesis and Consolidation of Nanophase Iron Aluminide,” *J. Am. Ceram. Soc.* **84** (2001) 910–914.
- [100] D. Zhang, L. Zhang, Z. Fu, J.K. Guo, W.H. Tuan, “Enhance the heating rate of the PECS process by inserting a conducting body into BN powder compact,” *J. Mater. Sci.* **41** (2006) 293–295.

- [101] S. Decker, L. Krüger, “Influence of high-energy ball milling on Mg-PSZ-reinforced TRIP steel-matrix composites synthesized by FAST / SPS,” *Mater. Sci. Eng. A*. **761** (2019) 137974.
- [102] A. Miriyev, A. Stern, E. Tuval, S. Kalabukhov, Z. Hooper, N. Frage, “Titanium to steel joining by spark plasma sintering (SPS) technology,” *J. Mater. Process. Technol.* **213** (2013) 161–166.
- [103] B. Basu, J.H. Lee, K.D. Y., “Development of Nanocrystalline Wear-Resistant Y-TZP Ceramics,” *J. Am. Ceram. Soc.* **87** (2004) 1771–1774.
- [104] M. Yue, J.X. Zhang, W.Q. Liu, G.P. Wang, “Chemical stability and microstructure of Nd-Fe-B magnet prepared by spark plasma sintering,” *J. Magn. Magn. Mater.* **271** (2004) 364–368.
- [105] X.-L. Su, P.-L. Wang, W. Chen, “Optical properties of SPS-ed Y- and (Dy, Y)-alpha-sialon ceramics,” *J. Mater. Sci.* **39** (2004) 6257–6262.
- [106] Y.H. Han, M. Nagata, N. Uekawa, K. Kakegawa, “Eutectic Al₂O₃-GdAlO₃ composite consolidated by combined rapid quenching and spark plasma sintering technique,” *Br. Ceram. Trans.* **103** (2004) 219–222.
- [107] Y.S. Kwon, D. V. Dudina, M.A. Korchagin, O.I. Lomovsky, “Microstructure changes in TiB₂-Cu nanocomposite under sintering,” *J. Mater. Sci.* **39** (2004) 5325–5331.
- [108] X.J. Chen, K.A. Khor, S.H. Chan, L.G. Yu, “Overcoming the effect of contaminant in solid oxide fuel cell (SOFC) electrolyte: Spark plasma sintering (SPS) of 0.5 wt.% silica-doped yttria-stabilized zirconia (YSZ),” *Mater. Sci. Eng. A*. **374** (2004) 64–71.
- [109] L. Zhou, Z. Zhao, A. Zimmermann, F. Aldinger, M. Nygren, “Preparation and properties of lead zirconate stannate titanate sintered by spark plasma sintering,” *J. Am. Ceram. Soc.* **87** (2004) 606–611.
- [110] L.A. Stanciu, V.Y. Kodash, J.R. Groza, “Effects of heating rate on densification and grain growth during field-assisted sintering of α -Al₂O₃ and MoSi₂ powders,” *Metall. Mater. Trans. A Phys. Metall. Mater. Sci.* **32** (2001) 2633–2638.
- [111] Z. Shen, M. Johnsson, Z. Zhao, M. Nygren, “Spark plasma sintering of alumina,” *J. Am. Ceram. Soc.* **85** (2002) 1921–1927.
- [112] Y. Zhou, K. Hirao, Y. Yamauchi, S. Kanzaki, “Densification and grain growth in pulse electric current sintering of alumina,” *J. Eur. Ceram. Soc.* **24** (2004) 3465–3470.

- [113] B.N. Kim, K. Hiraga, K. Morita, H. Yoshida, “Effects of heating rate on microstructure and transparency of spark-plasma-sintered alumina,” *J. Eur. Ceram. Soc.* **29** (2009) 323–327.
- [114] N. Murayama, W. Shin, “Effect of rapid heating on densification and grain growth in hot pressed alumina,” *J. Ceram. Soc. Japan.* **108** (2000) 799–802.
- [115] S. Gephart, J. Singh, A. Kulkarni, “Field assisted sintering of SiC using extreme heating rates,” *J. Mater. Sci.* **46** (2011) 3659–3663.
- [116] Y. Zhou, K. Hirao, M. Toriyama, H. Tanaka, “Very Rapid Densification of Nanometer Silicon Carbide Powder by Pulse Electric Current Sintering,” *J. Am. Ceram. Soc.* **83** (2004) 654–656.
- [117] U. Anselmi-Tamburini, J.E. Garay, Z.A. Munir, A. Tacca, F. Maglia, G. Chiodelli, G. Spinolo, “Spark plasma sintering and characterization of bulk nanostructured fully stabilized zirconia: Part II. Characterization studies,” *J. Mater. Res.* **19** (2004) 3263–3269.
- [118] U. Anselmi-Tamburini, J.E. Garay, Z.A. Munir, A. Tacca, F. Maglia, G. Spinolo, “Spark plasma sintering and characterization of bulk nanostructured fully stabilized zirconia: Part I. Densification studies,” *J. Mater. Res.* **19** (2004) 3255–3262.
- [119] G. Skandan, H. Hahn, B.H. Kear, M. Roddy, W.R. Cannon, “The effect of applied stress on densification of nanostructured zirconia during sinter-forging,” *Mater. Lett.* **20** (1994) 305–309.
- [120] U. Anselmi-Tamburini, J.E. Garay, Z.A. Munir, “Fast low-temperature consolidation of bulk nanometric ceramic materials,” *Scr. Mater.* **54** (2006) 823–828.
- [121] M. Nygren, Z. Shen, “On the preparation of bio-, nano- and structural ceramics and composites by spark plasma sintering,” *Solid State Sci.* **5** (2003) 125–131.
- [122] M. Omori, “Sintering, consolidation, reaction and crystal growth by the spark plasma system (SPS),” *Mater. Sci. Eng. A.* **287** (2000) 183–188.
- [123] S.W. Wang, L.D. Chen, T. Hirai, Y.S. Kang, “Microstructure inhomogeneity in Al₂O₃ sintered bodies formed during the plasma-activated sintering process,” *J. Mater. Sci. Lett.* **18** (1999) 1119–1121.
- [124] H. Tomino, H. Watanabe, Y. Kondo, “Electric current path and temperature distribution for spark sintering,” *J. Japan Soc. Powder Powder Metall.* **44** (1997) 974–979.
- [125] Y. Makino, “Characteristics of sintering process based on pulsed high current,” *New Ceram.* **10** (1997) 39–42.

- [126] P. Asokakumar, M. Alatalo, V. Ghosh, A. Kruseman, B. Nielsen, K. Lynn, "Increased Elemental Specificity of Positron Annihilation Spectra," *Phys. Rev. Lett.* **77** (1996) 2097–2100.
- [127] J.E. Garay, S.C. Glade, U. Anselmi-Tamburini, P. Asoka-Kumar, Z.A. Munir, "Electric current enhanced defect mobility in Ni 3Ti intermetallics," *Appl. Phys. Lett.* **85** (2004) 573–575.
- [128] U. Anselmi-Tamburini, J.E. Garay, Z.A. Munir, "Fundamental investigations on the spark plasma sintering/synthesis process III. Current effect on reactivity," *Mater. Sci. Eng. A.* **407** (2005) 24–30.
- [129] G.J. Oudemans, "Continuous hot pressing," *Philips Tech. Rev.* **2** (1968) 45–54.
- [130] R. Chaim, M. Levin, A. Shlayer, C. Estournes, "Sintering and densification of nanocrystalline ceramic oxide powders: A review," *Adv. Appl. Ceram.* **107** (2008) 159–169.
- [131] R. Suryanarayanan Iyer, S.M.L. Sastry, "Consolidation of nanoparticles - development of a micromechanistic model," *Acta Mater.* **47** (1999) 3079–3098.
- [132] B.-B.M. H., "Hot Isostatic Pressing (HIP) technology and its applications to metals and ceramics," *J. Mater. Sci.* **39** (2004) 6399–6420.
- [133] G. Bernard-Granger, C. Guizard, S. Surblé, G. Baldinozzi, A. Addad, "Spark plasma sintering of a commercially available granulated zirconia powder-II. Microstructure after sintering and ionic conductivity," *Acta Mater.* **56** (2008) 4658–4672.
- [134] G. Bernard-Granger, A. Addad, G. Fantozzi, G. Bonnefont, C. Guizard, D. Vernat, "Spark plasma sintering of a commercially available granulated zirconia powder: Comparison with hot-pressing," *Acta Mater.* **58** (2010) 3390–3399.
- [135] G. Bernard-Granger, C. Guizard, "Spark plasma sintering of a commercially available granulated zirconia powder: I. Sintering path and hypotheses about the mechanism(s) controlling densification," *Acta Mater.* **55** (2007) 3493–3504.
- [136] J. Langer, M.J. Hoffmann, O. Guillon, "Electric field-assisted sintering in comparison with the hot pressing of yttria-stabilized zirconia," *J. Am. Ceram. Soc.* **94** (2011) 24–31.
- [137] K. Matsui, K. Tanaka, T. Yamakawa, M. Uehara, N. Enomoto, J. Hojo, "Sintering kinetics at isothermal shrinkage: II, effect of Y₂O₃ concentration on the initial sintering stage of fine zirconia powder," *J. Am. Ceram. Soc.* **90** (2007) 443–447.

- [138] D.P.H. Hasselman, L.F. Johnson, L.D. Bentsen, R. Syed, H.L. Lee, M. V. Swain, "THERMAL DIFFUSIVITY AND CONDUCTIVITY OF DENSE POLYCRYSTALLINE ZrO₂ CERAMICS: A SURVEY," *Am. Ceram. Soc. Bull.* **66** (1987) 799–806.
- [139] J. Luo, R. Stevens, "Porosity-dependence of elastic moduli and hardness of 3Y-TZP ceramics," *Ceram. Int.* **25** (1999) 281–286.
- [140] T.N. Rhys-Jones, "The use of thermally sprayed coatings for compressor and turbine applications in aero engines," *Surf. Coatings Technol.* **42** (1990) 1–11.
- [141] H. Herman, S. Sampath, R. Mccune, "Thermal Spray: Current Status and Future Trends," *MRS Bull.* **25** (2000) 17–25.
- [142] A. Feuerstein, J. Knapp, T. Taylor, A. Ashary, A. Bolcavage, N. Hitchman, "Technical and Economical Aspects of Current Thermal Barrier Coating Systems for Gas Turbine Engines by Thermal Spray and EBPVD : A Review," *J. Therm. Spray Technol.* **17** (2008) 199–213.
- [143] J. Singh, D.E. Wolfe, "Nano and macro-structured component fabrication by electron beam-physical vapor deposition (EB-PVD)," *J. Mater. Sci.* **40** (2005) 1–26.
- [144] L. Singh, V. Chawla, J.S. Grewal, "A Review on Detonation Gun Sprayed Coatings," *J. Miner. Mater. Charact. Eng.* **11** (2012) 243–265.
- [145] J.I. Goldstein, D.E. Newbury, J.R. Michael, N.W.M. Ritchie, J.H.J. Scott, D.C. Joy, *Scanning Electron Microscopy and X-Ray Microanalysis*, Fourth, Springer Nature, NY, 2017.
- [146] D.B. Williams, C.B. Carter, *Transmission electron microscopy*, Second, Springer US, NY, 1996.
- [147] J. Gong, J. Wu, Z. Guan, "Examination of the indentation size effect in low-load vickers hardness testing of ceramics," *J. Eur. Ceram. Soc.* **19** (1999) 2625–2631.
- [148] K.W. Schlichting, N.P. Padture, P.G. Klemens, "Thermal conductivity of dense and porous yttria-stabilized zirconia," *J. Mater. Sci.* **36** (2001) 3003–3010.
- [149] M. Cain, R. Morrell, "Nanostructured ceramics: A review of their potential," *Appl. Organomet. Chem.* **15** (2001) 321–330.
- [150] R.W. Cahn, "Nanostructured materials," *Nature.* **348** (1990) 389–390.
- [151] M. Belmonte, "Advanced ceramic materials for high temperature applications," *Adv. Eng. Mater.* **8** (2006) 693–703.

- [152] J. Luo, S. Adak, R. Stevens, “Microstructure evolution and grain growth in the sintering of 3Y-TZP ceramics,” *J. Mater. Sci.* **33** (1998) 5301–5309.
- [153] J.C. M’Peko, J.S.C. Francis, R. Raj, “Impedance spectroscopy and dielectric properties of flash versus conventionally sintered yttria-doped zirconia electroceramics viewed at the microstructural level,” *J. Am. Ceram. Soc.* **96** (2013) 3760–3767.
- [154] Y. Zhang, J. Luo, “Promoting the flash sintering of ZnO in reduced atmospheres to achieve nearly full densities at furnace temperatures of <120 °C,” *Scr. Mater.* **106** (2015) 26–29.
- [155] Y. Zhang, J. Nie, J.M. Chan, J. Luo, “Probing the densification mechanisms during flash sintering of ZnO,” *Acta Mater.* **125** (2017) 465–475.
- [156] J. Luo, “The scientific questions and technological opportunities of flash sintering: From a case study of ZnO to other ceramics,” *Scr. Mater.* **146** (2018) 260–266.
- [157] J. Nie, Y. Zhang, J.M. Chan, S. Jiang, R. Huang, J. Luo, “Two-step flash sintering of ZnO: Fast densification with suppressed grain growth,” *Scr. Mater.* **141** (2017) 6–9.
- [158] J. Li, L. Guan, W. Zhang, M. Luo, J. Song, X. Song, S. An, “Sintering behavior of samarium doped ceria under DC electrical field,” *Ceram. Int.* **44** (2018) 2470–2477.
- [159] A.C.E. Reid, R.C. Lua, R.E. García, V.R. Coffman, S.A. Langer, “Modelling microstructures with OOF2,” *Int. J. Mater. Prod. Technol.* **35** (2009) 361–373.
- [160] R.I. Todd, Flash sintering of ceramics: A short review, in: B. Lee, V. Mitic, R. Gadow (Eds.), Proc. IV Adv. Ceram. Appl. Conf., Atlantis Press, Paris, 2017: pp. 1–12.
- [161] V. Mote, Y. Purushotham, B. Dole, “Williamson-Hall analysis in estimation of lattice strain in nanometer-sized ZnO particles,” *J. Theor. Appl. Phys.* **6** (2012) 2–9.
- [162] X. Liu, Q. Feng, B. Tang, J. Zheng, Z. Zheng, W. Zhou, J. Tian, J. Wang, “First-principles calculations of mechanical and thermodynamic properties of tetragonal Be₁₂Ti,” *RSC Adv.* **9** (2019) 5302–5312.
- [163] G.P. Cousland, X.Y. Cui, A.E. Smith, A.P.J. Stampfl, C.M. Stampfl, “Mechanical properties of zirconia, doped and undoped yttria-stabilized cubic zirconia from first-principles,” *J. Phys. Chem. Solids.* **122** (2018) 51–71.
- [164] H. Abrams, “Grain size measurement by the intercept method,” *Metallography.* **4** (1971) 59–78.
- [165] T. Sakuma, Y.I. Yoshizawa, H. Suto, “The microstructure and mechanical properties of yttria-stabilized zirconia prepared by arc-melting,” *J. Mater. Sci.* **20** (1985) 2399–2407.

- [166] M. Peach, J.S. Koehler, “The Forces Exerted on Dislocations and the Stress Fields Produced by Them,” *Phys. Rev.* **80** (1950) 436–439.
- [167] X.S. Zhao, S.L. Shang, Z.K. Liu, J.Y. Shen, “Elastic properties of cubic, tetragonal and monoclinic ZrO₂ from first-principles calculations,” *J. Nucl. Mater.* **415** (2011) 13–17.
- [168] K. Morita, K. Hiraga, “Deformed substructures in fine-grained tetragonal zirconia,” *Philos. Mag. Lett.* **81** (2001) 311–319.
- [169] J.D. Eshelby, F.C. Frank, F.R.N. Nabarro, “XLI. The equilibrium of linear arrays of dislocations.,” *London, Edinburgh, Dublin Philos. Mag. J. Sci.* **42** (1951) 351–364.
- [170] A. Montagne, S. Pathak, X. Maeder, J. Michler, “Plasticity and fracture of sapphire at room temperature: Load-controlled microcompression of four different orientations,” *Ceram. Int.* **40** (2014) 2083–2090.
- [171] S. Kiani, K.W.K. Leung, V. Radmilovic, A.M. Minor, J.M. Yang, D.H. Warner, S. Kodambaka, “Dislocation glide-controlled room-temperature plasticity in 6H-SiC single crystals,” *Acta Mater.* **80** (2014) 400–406.
- [172] E.Y. Fogaing, Y. Lorgouilloux, M. Huger, C.P. Gault, “Young’s modulus of zirconia at high temperature,” *J. Mater. Sci.* **41** (2006) 7663–7666.
- [173] G. Subhash, S. Nemat-Nasser, “Dynamic Stress-Induced Transformation and Texture Formation in Uniaxial Compression of Zirconia Ceramics,” *J. Am. Ceram. Soc.* **76** (1993) 153–165.
- [174] G.R. Dickinson, C. Petorak, K. Bowman, R.W. Trice, “Stress Relaxation of Compression Loaded Plasma-Sprayed 7 Wt% Y₂O₃–ZrO₂ Stand-Alone Coatings,” *J. Am.* **88** (2005) 2202–2208.
- [175] O. Guillon, J. Gonzalez-Julian, B. Dargatz, T. Kessel, G. Schierning, J. Räthel, M. Herrmann, “Field-assisted sintering technology/spark plasma sintering: Mechanisms, materials, and technology developments,” *Adv. Eng. Mater.* **16** (2014) 830–849.
- [176] M. Cologna, A.L.G. Prette, R. Raj, “Flash-sintering of cubic yttria-stabilized zirconia at 750°C for possible use in SOFC manufacturing,” *J. Am. Ceram. Soc.* **94** (2011) 316–319.
- [177] R. Ramamoorthy, P.K. Dutta, S. a Akbar, “Oxygen sensors : Materials , methods , designs,” *J. Mater. Sci.* **38** (2003) 4271–4282.
- [178] S. Tao, J.T.S. Irvine, “A redox-stable efficient anode for solid-oxide fuel cells,” *Nat. Mater.* **2** (2003) 320–323.

- [179] J. Cho, J. Li, Q. Li, J. Ding, H. Wang, S. Xue, T.B. Holland, A.K. Mukherjee, H. Wang, X. Zhang, “In-situ high temperature micromechanical testing of ultrafine grained yttria-stabilized zirconia processed by spark plasma sintering,” *Acta Mater.* **155** (2018) 128–137.
- [180] J. Cho, Q. Li, H. Wang, Z. Fan, J. Li, S. Xue, S. Karra, H. Wang, T.B. Holland, A.K. Mukherjee, R.E. García, X. Zhang, “High temperature deformability of ductile flash sintered ceramics via in-situ compression,” *Nat. Commun.* **9** (2018) 2063.
- [181] J.S. Carpenter, A. Misra, M.D. Uchic, P.M. Anderson, “Strain rate sensitivity and activation volume of Cu/Ni metallic multilayer thin films measured via micropillar compression,” *Appl. Phys. Lett.* **101** (2012).
- [182] Q. Wei, S. Cheng, K.T. Ramesh, E. Ma, “Effect of nanocrystalline and ultrafine grain sizes on the strain rate sensitivity and activation volume: Fcc versus bcc metals,” *Mater. Sci. Eng. A.* **381** (2004) 71–79.
- [183] A.K. Mukherjee, “The Rate Controlling Mechanism in Superplasticity,” *Mater. Sci. Eng.* **8** (1971) 83–89.
- [184] X. Zhang, H. Wang, R.O. Scattergood, J. Narayan, C.C. Koch, A. V Sergueeva, A.K. Mukherjee, “Studies of deformation mechanisms in ultra-fine grained and nanostructured zinc,” *Acta Mater.* **50** (2002) 4823–4830.
- [185] N. Balasubramanian, T.G. Langdon, “Flow processes in superplastic yttria-stabilized zirconia: A Deformation Limit Diagram,” *Mater. Sci. Eng. A.* **409** (2005) 46–51.
- [186] I. Charit, A.H. Chokshi, “Experimental evidence for diffusion creep in the superplastic 3 mol% yttria-stabilized tetragonal zirconia,” *Acta Mater.* **49** (2001) 2239–2249.
- [187] K. Morita, K. Hiraga, “Reply to ‘comment on the role of intragranular dislocations in superplastic yttria-stabilized zirconia,’” *Scr. Mater.* **48** (2003) 1402–1407.
- [188] R.S. Mishra, A.K. Mukherjee, “On superplasticity in silicon carbide reinforced aluminum composites,” *Scr. Metall. Mater.* **25** (1991) 271–275.
- [189] A.K. Mishra, R.S., Bieler, T.R., Mukherjee, “On the superplastic behaviour of mechanically alloyed aluminum alloys,” *Scr. Metall. Mater.* **26** (1992) 1605–1608.
- [190] A.K. Mishra, R.S., Bieler, T.R., Mukherjee, “Superplasticity in powder metalurgy aluminum alloys and composites,” *Acta Metall. Mater.* **43** (1995) 877–891.
- [191] T.E. Mitchell, J.P. Hirth, A. Misra, “Apparent activation energy and stress exponent in materials with a high Peierls stress,” *Acta Mater.* **50** (2002) 1087–1093.

- [192] T.E. Mitchell, A.H. Heuer, Dislocations and mechanical properties of ceramics, Elsevier B.V., 2005.
- [193] Y. Kamimura, K. Edagawa, A.M. Iskandarov, M. Osawa, Y. Umeno, S. Takeuchi, “Peierls stresses estimated via the Peierls-Nabarro model using ab-initio γ -surface and their comparison with experiments,” *Acta Mater.* **148** (2018) 355–362.
- [194] B. Baufeld, B. V. Petukhov, M. Bartsch, U. Messerschmidt, “Transition of mechanisms controlling the dislocation motion in cubic ZrO₂ below 700°C,” *Acta Mater.* **46** (1998) 3077–3085.
- [195] A.. Dominguez-Rodriguez, A.H. Heuer, J. Castaing, “Dislocations and the mechanical properties of stabilized ZrO₂,” *Radiat. Eff. Defects Solids.* **119–1212** (1991) 759–769.
- [196] J. Lankford, W.W. Predebon, J.M. Staehler, G. Subhash, B.J. Pletka, C.E. Anderson, “The role of plasticity as a limiting factor in the compressive failure of high strength ceramics,” *Mech. Mater.* **29** (1998) 205–218.
- [197] M.F. Ashby, R.A. Verrall, “Diffusion-accommodated flow and superplasticity,” *Acta Metall.* **21** (1973) 149–163.
- [198] N. Wakiya, N. Tajiri, T. Kiguchi, N. Mizutani, J.S. Cross, K. Shinozaki, “Activation energy of oxygen vacancy diffusion of yttria-stabilized-zirconia thin film determined from DC current measurements below 150°C,” *Japanese J. Appl. Physics, Part 2 Lett.* **45** (2006).
- [199] Y. Dong, I. Chen, “Onset Criterion for Flash Sintering,” *J. Am. Ceram. Soc.* **3627** (2015) 3624–3627.
- [200] R. Ramamoorthy, D. Sundararaman, S. Ramasamy, “Ionic conductivity studies of ultrafine-grained yttria stabilized zirconia polymorphs,” *Solid State Ionics.* **123** (1999) 271–278.
- [201] U. Brossmann, G. Knöner, H.E. Schaefer, R. Würschum, “Oxygen diffusion in nanocrystalline ZrO₂,” *Rev. Adv. Mater. Sci.* **6** (2004) 7–11.
- [202] R. Kirchheim, “Reducing grain boundary, dislocation line and vacancy formation energies by solute segregation. I. Theoretical background,” *Acta Mater.* **55** (2007) 5129–5138.
- [203] R. Kirchheim, “Reducing grain boundary, dislocation line and vacancy formation energies by solute segregation. II. Experimental evidence and consequences,” *Acta Mater.* **55** (2007) 5139–5148.
- [204] M.K. Miller, “Atom probe tomography characterization of solute segregation to dislocations,” *Microsc. Res. Tech.* (2006) 359–365.

- [205] R. Fuentes-samaniego, R. Gasca-Neri, J.P. Hirth, "Solute drag on moving edge dislocations," *Philos. Mag. A Phys. Condens. Matter, Struct. Defects Mech. Prop.* **49** (1984) 31–43.
- [206] H. Yoshinaga, S. Morozumi, "The solute atmosphere round a moving dislocation and its dragging stress," *Philos. Mag.* **23** (1971) 1367–1385.
- [207] Y. Wang, D.J. Srolovitz, J.M. Rickman, R. Lesar, "Dislocation motion in the presence of diffusing solutes: A computer simulation study," *Acta Mater.* **48** (2000) 2163–2175.
- [208] J.H. Gittus, "Theoretical equation for steady state dislocation creep: Effect of solute drag," *Acta Metall.* **22** (1974) 1179–1181.
- [209] Cahn JW, "The impurity-drag effect in grain boundary motion," *Acta Metall.* **10** (1962) 789–798.
- [210] S. Lartigue-Korinek, C. Carry, L. Priester, "Multiscale aspects of the influence of yttrium on microstructure sintering and creep of alumina," *J. Eur. Ceram. Soc.* **22** (2002) 1525–1541.
- [211] C.R. Nerikar, P. V. ; Casillas Trujillo, L. A. ; Andersson, D. A. ; Unal, C. ; Uberuaga, B. P. ; Stanek, "Segregation of xenon to dislocations and grain boundaries in uranium dioxide," *Phys. Rev. B.* **84** (2011) 174105.
- [212] T. Suzuki, Toshimasa ; Ueno, Mitsuo ; Nishi, Yuji ; Fujimoto, Masayuki ; Suzuki, "Dislocation Loop Formation in Nonstoichiometric (Ba,Ca)TiO₃ and BaTiO₃ Ceramics," *J. Am. Ceram. Soc.* **84** (2001) 200–206.
- [213] L. Sun, D. Marrocchelli, B. Yildiz, "Edge dislocation slows down oxide ion diffusion in doped CeO₂ by segregation of charged defects," *Nat. Commun.* **6** (2015) 1–10.
- [214] N. Feng, Bin ; Lugg, Nathan R ; Kumamoto, Akihito ; Ikuhara, Yuichi ; Shibata, "Direct Observation of Oxygen Vacancy Distribution across Yttria-Stabilized Zirconia Grain Boundaries," *ACS Nano.* **11** (2017) 11376–11382.
- [215] S.P.S.Badwall, "SOLID STATE Zirconia-based solid electrolytes : microstructure , stability and ionic conductivity," *Solid State Ionics.* **52** (1992) 23–32.
- [216] Y. Sakka, Y. Oishi, K. Ando, "Zr-Hf interdiffusion in polycrystalline Y₂O₃-(Zr+Hf)O₂," *J. Mater. Sci.* **17** (1982) 3101–3105.
- [217] D. DIMOS, D.L. KOHLSTEDT, "Diffusional Creep and Kinetic Demixing in Yttria-Stabilized Zirconia," *J. Am. Ceram. Soc.* **70** (1987) 531–536.

- [218] A. Jiménez-Melendo, Manuel; Domínguez-Rodríguez, Arturo; Bravo-León, “Superplastic Flow of Fine-Grained Ytria-Stabilized Zirconia Polycrystals: Constitutive Equation and Deformation Mechanisms,” *J. Am. Ceram. Soc.* **81** (1998) 2761–2776.
- [219] K. Hiraga, H.Y. Yasuda, Y. Sakka, “The tensile creep behavior of superplastic tetragonal zirconia doped with small amounts of SiO₂,” *Mater. Sci. Eng. A.* **234–236** (1997) 1026–1029.
- [220] G. Schoeck, “The Activation Energy of Dislocation Movement,” *Phys. Status Solidi.* **8** (1965) 499–507.
- [221] B. Baufeld, M. Bartsch, U. Messerschmidt, D. Baither, “Plastic deformation of cubic zirconia at temperatures between 1150 and 700°C,” *Acta Metall. Mater.* **43** (1995) 1925–1933.
- [222] T. Shimada, M.; Matsushita, K.; Kuratani, S.; Taira, O.; Koizumi, M.; Tsukuma, K.; Tsukidate, “Temperature Dependence of Young’s Modulus and Internal Friction in Alumina, Silicon Nitride, and Partially Stabilized Zirconia Ceramics,” *J. Am. Ceram. Soc.* (1984) C23–C24.
- [223] I. Karaman, B. Basaran, H.E. Karaca, A.I. Karsilayan, Y.I. Chumlyakov, “Energy harvesting using martensite variant reorientation mechanism in a NiMnGa magnetic shape memory alloy,” *Appl. Phys. Lett.* **90** (2007) 1–4.
- [224] A. Nespoli, D. Rigamonti, E. Villa, F. Passaretti, “Design, characterization and perspectives of shape memory alloy elements in miniature sensor proof of concept,” *Sensors Actuators, A Phys.* **218** (2014) 142–153.
- [225] P.F. Becher, M. V. Swain, M.K. Ferber, “Relation of transformation temperature to the fracture toughness of transformation-toughened ceramics,” *J. Mater. Sci.* **22** (1987) 76–84.
- [226] P.E. Becher, K.B. Alexander, A. Bleier, S.B. Waters, W.H. Wanvick, “Influence of ZrO₂ Grain size and Content on the Transformation Response in the Al₂O₃-ZrO₂ (12 mol% CeO₂) System,” *J. Am. Ceram. Soc.* **76** (1993) 657–663.
- [227] F.F. Lange, “Transformation toughening - Part 3 Experimental observations in the ZrO₂-Y₂O₃ system,” *J. Mater. Sci.* **17** (1982) 255–263.
- [228] E. Camposilvan, O. Torrents, M. Anglada, “Small-scale mechanical behavior of zirconia,” *Acta Mater.* **80** (2014) 239–249.

- [229] R.P. Ingel, R.W. Rice, D. Lewis, "Room-Temperature Strength and Fracture of ZrO₂-Y₂O₃ Single Crystals," *J. Am. Ceram. Soc.* **65** (1982) c108–c109.
- [230] I.I.E. Procedure, "Young's Modulus, Flexural Strength, and Fracture of Yttria-Stabilized Zirconia versus Temperature," *J. Am. Ceram. Soc.* **80** (1997) 903–908.
- [231] T.C. Lindley, C.E. Richards, R.O. Ritchie, "Mechanics and Mechanisms of Fatigue Crack Growth in Metals: a Review," *Metallurgia.* **43** (1976) 1–29.
- [232] J.W.W. Edington, K.N.N. Melton, C.P.P. Cutler, "Superplasticity," *Prog. Mater. Sci.* **21** (1976) 61–170.
- [233] S. Tekeli, T.J. Davies, "Comparative study of superplastic deformation and cavitation behaviour in 3 and 8 mol.% yttria-stabilized zirconia," *Mater. Sci. Eng. A.* **297** (2001) 168–175.
- [234] S.X. McFadden, R.S. Mishra, R.Z. Valiev, A.P. Zhilyaev, A.K. Mukherjee, "Low-temperature superplasticity in nanostructured nickel and metal alloys," *Nature.* **398** (1999) 684–686.
- [235] M. Mabuchi, K. Higashi, T.G. Langdon, "An investigation of the role of a liquid phase in Al-Cu-Mg metal matrix composites exhibiting high strain rate superplasticity," *Acta Metall. Mater.* **42** (1994) 1739–1745.
- [236] D.M. Owen, A.H. Chokshi, "The high temperature mechanical characteristics of superplastic 3 mol% yttria stabilized zirconia," *Acta Mater.* **46** (1998) 667–679.
- [237] K.R. Venkatachari, R. Raj, "Superplastic flow in fine-grained alumina," *J Am Ceram Soc.* **69** (1986) 135–138.
- [238] K.C. Chan, G.F. Wang, C.L. Wang, K.F. Zhang, "Low temperature and high strain rate superplasticity of the electrodeposited Ni/Si₃N₄(W)composite," *Scr. Mater.* **53** (2005) 1285–1290.
- [239] S. Stemmer, J. Vleugels, O. Van Der Biest, "Grain boundary segregation in high-purity, yttria-stabilized tetragonal zirconia polycrystals (Y-TZP)," *J. Eur. Ceram. Soc.* **18** (1998) 1565–1570.
- [240] K. Wakai, F., Kodama, Y., Sakaguchi, S., Murayama, N., Izaki, K., Niihara, "A superplastic covalent crystal composite," *Nature.* **344** (1990) 421–423.

- [241] A. Jimenez-melendo, M., Dominguez-rodriguez, “High Temperature Mechanical Characteristics of superplastic yttria-stabilized zirconia. An examination of the flow process,” *Acta Metall.* **48** (2000) 3201–3210.
- [242] A. Nez-melendo, A., Jimenez-melendo, M., Dominguez-rodriguez, “Mechanical and Microstructural Aspects of the High Temperature Plastic Deformation of Yttria-Stabilized Zirconia Polycrystals,” *Acta Metall. Mater.* **40** (1992) 2717–2726.
- [243] B.N. Kim, K. Hiraga, K. Morita, Y. Sakka, “A high-strain-rate superplastic ceramic,” *Nature.* **413** (2001) 288–291.
- [244] H. Yoshida, Y. Sasaki, “Low temperature and high strain rate superplastic flow in structural ceramics induced by strong electric-field,” *Scr. Mater.* **146** (2018) 173–177.
- [245] A.H. Heuer, F.F. Lange, M. V. Swain, A.G. Evans, “Transformation Toughening: An Overview,” *J. Am. Ceram. Soc.* **69** (1986) i–iv.
- [246] C.G. Levi, “Emerging materials and processes for thermal barrier systems,” *Curr. Opin. Solid State Mater. Sci.* **8** (2004) 77–91.
- [247] B. Gleeson, “Thermal Barrier Coatings for Aeroengine Applications,” *J. Propuls. Power.* **22** (2006) 375–383.
- [248] D.R. Clarke, C.G. Levi, “Materials Design for the Next Generation Thermal Barrier Coatings,” *Annu. Rev. Mater. Res.* **33** (2003) 383–417.
- [249] A.G. Evans, D.R. Clarke, C.G. Levi, “The influence of oxides on the performance of advanced gas turbines,” *J. Eur. Ceram. Soc.* **28** (2008) 1405–1419.
- [250] S.M. Lakiza, M.I. Grechanyuk, O.K. Ruban, V.P. Redko, M.S. Glabay, O.B. Myloserdov, O. V. Dudnik, S. V. Prokhorenko, “Thermal Barrier Coatings: Current Status, Search, and Analysis,” *Powder Metall. Met. Ceram.* **57** (2018) 82–113.
- [251] R. Darolia, “Thermal barrier coatings technology: critical review, progress update, remaining challenges and prospects,” *Int. Mater. Rev.* **58** (2013) 315–348.
- [252] S. Stecura, “New ZrO₂-Yb₂O₃ plasma-sprayed coatings for thermal barrier applications,” *Thin Solid Films.* **150** (1987) 15–40.
- [253] S. Stecura, “Two-layer thermal barrier coating for high temperature components,” *Am. Ceram. Soc. Bull.* **56** (1977) 1082–1085.
- [254] S.. Stecura, “Optimization of the Ni-Cr-Al-Y/ZrO₂-Y₂O₃ thermal barrier system,” *Adv. Ceram. Mater.* **1** (1986) 68–76.

- [255] D.R. Clarke, M. Oechsner, N.P. Padture, “Thermal-barrier coatings for more efficient gas-turbine engines,” *MRS Bull.* **37** (2012) 891–898.
- [256] C. Mercer, J.R. Williams, D.R. Clarke, A.G. Evans, “On a ferroelastic mechanism governing the toughness of metastable tetragonal-prime (t’) yttria-stabilized zirconia,” *Proc. R. Soc. A Math. Phys. Eng. Sci.* **463** (2007) 1393–1408.
- [257] A.V. Virkar, “Role of Ferroelasticity in Toughening of Zirconia Ceramics,” *Key Eng. Mater.* **153–154** (1998) 183–210.
- [258] Ro.L.K. Virkar, ANIL V. ; Matsumoto, “Ferroelastic Domain Switching as a Toughening Mechanism in Tetragonal Zirconia,” *J. Am. Ceram. Soc.* **69** (1986) C-224-C–226.
- [259] M. Peters, K. Fritscher, G. Staniek, W. a. Kaysser, U. Schulz, “Design and Properties of Thermal Barrier Coatings for advanced turbine engines,” *Materwiss. Werksttech.* **28** (1997) 357–362.
- [260] C.A. Johnson, J.A. Ruud, R. Bruce, D. Wortman, “Relationships between residual stress, microstructure and mechanical properties of electron beam-physical vapor deposition thermal barrier coatings,” *Surf. Coatings Technol.* **108–109** (1998) 80–85.
- [261] G. Gregori, L. Li, J.A. Nychka, D.R. Clarke, “Vibration damping of superalloys and thermal barrier coatings at high-temperatures,” *Mater. Sci. Eng. A.* **466** (2007) 256–264.
- [262] T.E. Strangman, “Thermal barrier coatings for turbine airfoils,” *Thin Solid Films.* **127** (1985) 93–106.
- [263] J.R. Davis, Handbook of Thermal Spray Technology, First, ASM International, OH, 2004.
- [264] A.G. Evans, N.A. Fleck, S. Faulhaber, N. Vermaak, M. Maloney, R. Darolia, “Scaling laws governing the erosion and impact resistance of thermal barrier coatings,” *Wear.* **260** (2006) 886–894.
- [265] A.G. Evans, J.W. Hutchinson, “The mechanics of coating delamination in thermal gradients,” *Surf. Coatings Technol.* **201** (2007) 7905–7916.
- [266] Y. Wang, M.X. Li, H.L. Suo, “Mechanical properties of YSZ thermal barrier coatings with segmented structure,” *Surf. Eng.* **28** (2012) 329–332.
- [267] M. Keshavarz, M.H. Idris, N. Ahmad, “Mechanical properties of stabilized zirconia nanocrystalline EB-PVD coating evaluated by micro and nano indentation,” *J. Adv. Ceram.* **2** (2013) 333–340.

- [268] E.O. Hall, "The Deformation and Ageing of Mild Steel: III Discussion of Results," *Proc. Phys. Soc. Sect. B.* **64** (1951) 747.
- [269] N.J. Petch, "The Cleavage Strength of Polycrystals," *J. Iron Steel Inst.* **174** (1953) 25–28.
- [270] J. Cho, J. Li, H. Wang, Q. Li, Z. Fan, A.K. Mukherjee, H. Wang, X. Zhang, "Study of deformation mechanisms in flash-sintered yttria-stabilized zirconia by in-situ micromechanical testing at elevated temperatures," *Mater. Res. Lett.* **7** (2019) 194–202.
- [271] C.J. Chan, F.F. Lange, M. Ruhle, J.F. Jue, a. V. Virkar, "Ferroelastic Domain Switching in Tetragonal Zirconia Single-Crystals Microstructural Aspects," *J. Am. Ceram. Soc.* **74** (1991) 807–813.
- [272] R.W. Cahn, "Twinned crystals," *Adv. Phys.* **3** (1954) 363–445.
- [273] J. Cho, J. Li, Z. Shang, J.M. Lopez, W.J. Jarosinski, M.M. Gentleman, V. Viswanathan, S. Xue, H. Wang, X. Zhang, "Comparison of temperature dependent deformation mechanisms of 8YSZ thermal barrier coatings prepared by air-plasma-spray and D-gun thermal spray: An in situ study," *J. Eur. Ceram. Soc.* **39** (2019) 3120–3128.
- [274] R.H.J. Hannink, C.J. Howard, E.H. Kisi, M.V. Swan, "Relationship between Fracture Toughness and Phase Assemblage in Mg-PSZ," *J. Am. Ceram. Soc.* **77** (1994) 571–579.
- [275] M. Zhang, L. Gao, J. Kang, J. Pu, J. Peng, M. Omran, G. Chen, "Stability optimisation of CaO-doped partially stabilised zirconia by microwave sintering," *Ceram. Int.* **45** (2019) 23278–23282.
- [276] M.E. Hilley, Residual Stress Measurement by X-ray Diffraction, SAE J784a, Society of Automotive Engineers, Warrendale, PA, 1971.
- [277] J. Lankford, "Indentation microfracture in the Palmqvist crack regime: implications for fracture toughness evaluation by the indentation method," *J. Mater. Sci. Lett.* **1** (1982) 493–495.
- [278] R.R. Hughan, R.H. Hannink, "Precipitation During Controlled Cooling of Magnesia-Partially-Stabilized Zirconia," *J. Am. Ceram. Soc.* **69** (1986) 556–563.
- [279] R. Chaim, D.G. Brandon, "Microstructure evolution and ordering in commercial Mg-PSZ," *J. Mater. Sci.* **19** (1984) 2934–2942.
- [280] N. Huber, J. Heerens, "On the effect of a general residual stress state on indentation and hardness testing," *Acta Mater.* **56** (2008) 6205–6213.

- [281] J. Chevalier, S. Deville, E. Munch, R. Jullian, F. Lair, “Critical effect of cubic phase on aging in 3 mol % yttria-stabilized zirconia ceramics for hip replacement prosthesis,” *Biomaterials*. **25** (2004) 5539–5545.
- [282] R.H.J. Hannink, “Microstructural development of sub-eutectoid aged MgO-ZrO₂ alloys,” *J. Mater. Sci.* **18** (1983) 457–470.
- [283] Z. Liu, A.E.C. Spargo, “High-resolution transmission electron microscopy and electron-energy-loss spectroscopy study of the phase Mg₂Zr₅O₁₂ in MgO-partially stabilized zirconia,” *Philos. Mag. A Phys. Condens. Matter, Struct. Defects Mech. Prop.* **81** (2001) 625–636.
- [284] E.H. Kisi, J. Christopher, R.J. Hill, “Crystal Structure of Orthorhombic Zirconia in Partially Stabilized Zirconia,” *J. Am. Ceram. Soc.* **72** (1989) 1757–1760.
- [285] D.B. Marshall, M.R. James, J.R. Porter, “Structural and Mechanical Property Changes in Toughened Magnesia-Partially-Stabilized Zirconia at Low Temperatures,” *J. Am. Ceram. Soc.* **72** (1989) 218–227.
- [286] Z. Liu, Y. Bando, J. Drennan, A.E.C. Spargo, “HRTEM study of orthorhombic zirconia in MgO-PSZ,” *J. Appl. Crystallogr.* **36** (2003) 1026–1029.
- [287] F. Liang, C. Laird, “Control of Intergranular Fatigue Cracking by Slip Homogeneity in Copper I: Effect of Grain Size,” *Mater. Sci. Eng. A*. **A117** (1989) 95–102.
- [288] C. Schmerbauch, J. Gonzalez-Julian, R. Röder, C. Ronning, O. Guillon, “Flash sintering of nanocrystalline zinc oxide and its influence on microstructure and defect formation,” *J. Am. Ceram. Soc.* **97** (2014) 1728–1735.
- [289] H. Bicer, B. Beyoglu, T.E. Ozdemir, J. Okasinski, T. Tsakalakos, “Direct in situ observation of electric field assisted densification of ZnO by energy dispersive X-ray diffraction,” *Ceram. Int.* **45** (2019) 7614–7618.
- [290] X.L. Phuah, H. Wang, H. Charalambous, S.K. Jha, T. Tsakalakos, X. Zhang, H. Wang, “Comparison of the grain growth behavior and defect structures of flash sintered ZnO with and without controlled current ramp,” *Scr. Mater.* **162** (2019) 251–255.
- [291] H.D. Espinosa, R.A. Bernal, M. Minary-jolandan, “A Review of Mechanical and Electromechanical Properties of Piezoelectric Nanowires,” *Adv. Mater.* **24** (2012) 4656–4675.

- [292] R. Agrawal, B. Peng, E.E. Gdoutos, H.D. Espinosa, "Elasticity Size Effects in ZnO Nanowires - A Combined Experimental-Computational Approach," *Nano Lett.* **8** (2008) 3668–3674.
- [293] M.R. He, P. Xiao, J. Zhao, S. Dai, F. Ke, J. Zhu, "Quantifying the defect-dominated size effect of fracture strain in single crystalline ZnO nanowires," *J. Appl. Phys.* **109** (2011) 1–5.
- [294] M. He, J. Zhu, "Defect-dominated diameter dependence of fracture strength in single-crystalline ZnO nanowires: In situ experiments," *Phys. Rev. B.* **83** (2011) 1–4.
- [295] F. Xu, Q. Qin, A. Mishra, Y. Gu, Y. Zhu, "Mechanical Properties of ZnO Nanowires Under Different Loading Modes," *Nano Res.* **3** (2010) 271–280.